

Atomic Scale Investigations into the Origins of Ductility in Mg Alloys

Présentée le 30 octobre 2020

à la Faculté des sciences et techniques de l'ingénieur
Laboratoire de modélisation mécanique multi-échelle
Programme doctoral en mécanique

pour l'obtention du grade de Docteur ès Sciences

par

Rasool AHMAD

Acceptée sur proposition du jury

Prof. T. Schneider, président du jury
Prof. W. Curtin, directeur de thèse
Prof. M. Ghazisaeidi, rapporteuse
Prof. D. Warner, rapporteur
Prof. J.-F. Molinari, rapporteur

All I know that I know nothing
— Socrates in *Plato's Apology*

To my family...

Acknowledgements

Performing cutting-edge research and contributing to the existing knowledge base of humanity can be daunting and exciting at the same time for someone initiating in a research area. I consider myself extremely fortunate to have Prof. William Curtin as my PhD thesis supervisor who provided me the guidance to navigate through the research path, granted me enough freedom to set my own goals, and assisted me in every possible way to achieve them. He let me join his research group ‘Laboratory for Multiscale Mechanics Modeling (LAMMM)’ as a doctoral student, introduced me to the exciting field of nano-scale crystal plasticity, taught me the nuances of atomistic modeling of materials, and was always eager to clear any doubt and engage in a stimulating discussion on a wide range of topics. I am pretty confident one cannot hope for a better supervisor than Prof William Curtin who is always there to back you up.

I would like to thank all the past and present members of LAMMM who constituted a scientifically stimulating atmosphere for conducting research: Zhaoxuan Wu, Binglun Yin, Satish Rao, Mostafa Khosrownejad, Ali Tehranchi, Max Hodapp, Wolfram Noehring, Predrag Andric, Nikolaos Bouklas, Francesco Maresca, Markus Stricker, Till Junge, Albert Glensk, Xiao Zhou, Abhinav Jain, Carolina Baruffi, Shankha Nag, Yi Hu, Eleanor Mak, Daniel Marchand, Ankit Gupta, Alireza Ghafarollahi, Ali Falsafi, and Ekin Kubilay. I want to especially thank Zhaoxuan for profusely helping me understand various aspects of Mg plasticity and atomistic simulations, and Binglun for always willing to discuss the subtleties of a concept and making it easy for me to grasp. These two persons were constant collaborators and sources of help during my PhD. I would also like to thank Predrag for assisting me during my initial PhD days and teaching me how to obtain the basic properties of crystals using atomistic simulations. I also express my gratitude to Madam Geraldine Palaj, our group administrator, for continuously warding me off the tedious official works and putting up with the numerous delays that I caused.

I want to express my gratitude to the jury members of my PhD oral examination: Prof. Tobias Schneider, Prof. Jean Francois Molinari, Prof. Maryam Ghazisaeidi, and Prof. Derek Warner. Their expert comments and suggestions lead to the improvement in the final draft of the thesis.

During my stay in Switzerland, I came across many great friends who were central in providing a comfortable and supportive environment. Mukesh Thakur, Ankit, Nihar, Vijay, Gauri, Yash , Mukesh Tripathi, Bhusan, Shankha, Rishabh, Richa, Moulik, and Harshvardhan, I will always cherish our memories of mountain hiking, dinner, traveling, insightful discussions, and other innumerable activities we did together. I am grateful to Mukesh, Ankit, Richa, and Eleanor for

Acknowledgements

proofreading part of the thesis, and Nihar, Carolina Baruffi and Madam Geraldine Palaj for translating the abstract into French.

I also want to thank all my friends across the world. Especially, I am indebted to our Y11-3Top, Hall 3 group from IITK including Akash, Hemant, Indra, Rishabh D, Rishabh G, Unnat, Shubham, Abhishek, Sarthak, Amandeep, Jai, Harsh, Brahma, Yagvendra, Aditya, Deepu, ANS Karthik, Sandesh, Naseer, Rohan, Sriram, Samyak, Rohan, Anil, Rajesh, Yashwanth, Anshul, Chndrakanth, Ayush, Anurag D, Manzar, Anurag B, and Chetan for providing unparalleled support and unmatched memories to be treasured for the whole life. I also want to thank Sultan, Noor, Amwar, Mubashshar, Ghazi, Usloob, Imran, Shahanwaz, and many other friends I was fortunate enough to have at different stages of my life.

I also want to express my respect for my two childhood teachers, Mohammad Yunus and Om Prakash Sharma, and my M.Tech. advisor Prof. Sumit Basu who played significant roles in motivating me to pursue higher educations.

I want to express my unutterable respect to my parents, Naseema Khatoon and Mohammad Athar, and my brothers, Abrar, Irshad, Zeeshan, and Enayat, my sister-in-law Asma-ul-Husna for all their countless sacrifices, continuous encouragement, and unconditional support. I want to thank my niece Zehra for bringing me moments of joy and happiness through her ineffable innocence.

This thesis owes its materialization to and imprinted by the persons mentioned above, and several others whom I apologize for forgetting to mention.

Lausanne, October 14, 2020

Rasool Ahmad.

Abstract

The development of energy-efficient transport vehicles is crucial in combating the impending problem of global warming. Employing light-weight structural materials in automobile and aerospace industries, until the transition to fully renewable energy sources, is one way towards countering the global warming threat. Magnesium (Mg), the lightest structural metal and abundant in Earth's crust, can prove to be a key material in this regard. Large scale industrial application of pure Mg is, nonetheless, hampered by low intrinsic ductility and low fracture toughness at room temperature which is attributed to the underlying less symmetric and plastically anisotropic hexagonal-close-packed (hcp) crystal structure. The edge/mixed part of the pyramidal $\langle c + a \rangle$ dislocations are metastable on the easy-glide pyramidal planes and undergo a thermally activated pyramidal-to-basal (PB) transition into lower energy immobile basal-dissociated dislocations. The PB transition is driven by a net energy difference between the high-energy pyramidal-dissociated and the low-energy basal-dissociated $\langle c + a \rangle$ dislocations, occurs rapidly at room temperature and renders pure Mg devoid of slip-systems that can accommodate the $\langle c \rangle$ axis plastic strain. The lack of pyramidal $\langle c + a \rangle$ slip results in the strong basal texture, pronounced plastic anisotropy, high hardening rate, and low ductility in wrought pure Mg components. The PB transition, thus, lies at the heart of low ductility in pure Mg.

Solid solution alloying by adding small amounts of rare-earth elements (RE = Y, Gd, Ce, Nd, Er, Dy, etc.) and other solutes such as Ca, Mn, and Zr have been shown experimentally to improve ductility by a substantial amount. Increased ductility in these Mg alloys is, furthermore, observed to be accompanied by the activation of much-required pyramidal $\langle c + a \rangle$ slip systems that were absent in pure Mg. The research work presented in this thesis aims to uncover, via conducting molecular dynamics/statics (MD/MS) simulations, the atomic-scale dislocation mechanisms responsible for the enhanced activation of the pyramidal $\langle c + a \rangle$ dislocations in certain ductile Mg alloys; and leverage the gleaned insight to devise a strategy for designing new ductile Mg alloys.

This work focuses on the Mg-Y system as a representative of ductile Mg-RE alloys to perform MD/MS simulations in order to reveal the distinct atomic-scale effects of RE solutes on various mechanisms associated with the pyramidal $\langle c + a \rangle$ dislocations. We start by testing the hypothesis that RE solutes might stabilize the edge/mixed pyramidal $\langle c + a \rangle$ dislocations on the easy-glide pyramidal planes by increasing the energy barrier of the detrimental PB transition. The large scale finite temperature MD simulations in Mg-Y alloys, employing a newly developed MEAM potential, clearly show that Y solute atoms are unable to alter the

energy barrier and transition time associated with the PB transition.

We, next, propose a new solute accelerated cross-slip based mechanistic theory to explain the increased activity of the pyramidal $\langle c + a \rangle$ dislocations in ductile solid solution Mg alloys. Cross-slip and double cross-slip of screw part of the pyramidal $\langle c + a \rangle$ dislocation loops are capable of acting as a natural dislocation source, and thus a much faster cross-slip process can extenuate the dislocation immobilization effects of the relatively slower PB transition. The energy difference between the low-energy pyramidal II and the high-energy pyramidal I $\langle c + a \rangle$ dislocations in pure Mg leads to a slow cross-slip process which is ineffective in circumventing the PB transition. We show that small addition of certain favorable solute elements can reduce the pyramidal $\langle c + a \rangle$ dislocations energy difference and accelerate the cross-slip process to the levels much faster than the PB transition, and thus enable the enhanced slip of the pyramidal $\langle c + a \rangle$ dislocations with a concomitant increase in ductility. The evidence for the solute enhanced cross-slip process is presented from the transmission electron microscopy (TEM) observations in Mg-Y alloys. We, furthermore, develop a quantitative model to establish the conditions for ductility as a function of alloys compositions.

With increasing concentration of favorable solutes, the pyramidal I $\langle c + a \rangle$ screw dislocations can become energetically more stable than the pyramidal II $\langle c + a \rangle$ screw dislocations which can significantly change the cross-slip path. The transition paths and energetics for double cross-slip of the pyramidal I $\langle c + a \rangle$ dislocations are analyzed in the regime where the pyramidal I $\langle c + a \rangle$ dislocations are energetically more favorable than the pyramidal II. This is achieved by conducting the nudged-elastic-band (NEB) simulations using a proxy MEAM potential for Mg designed to favor the pyramidal I over the pyramidal II $\langle c + a \rangle$ dislocation. In light of the obtained NEB results, the quantitative mechanistic model is extended into the pyramidal I favorable regime.

We then apply the developed quantitative model to the binary, ternary, quaternary, and higher-order dilute solid solution Mg alloys containing Ag, Zn, Al, Li, K, Sn, Mn, Sr, Ca, Zr, and RE as solute elements. The predictions of the model are compared with the experimentally observed ductility in a wide range of Mg alloys and found to be in an excellent agreement. The theory, in particular, identifies Mn, Li, Sn, K, Ca, Sr, RE, and Zr solutes as effective in lowering the pyramidal $\langle c + a \rangle$ dislocation energy difference, accelerating the cross-slip process, randomizing the basal texture, and improving ductility in resulting alloys. The model further predicts an upper limit of concentrations of strongly favorable solutes such as REs, beyond which ductility again begins to deteriorate in Mg alloys.

The research work performed in this thesis provides us an insight into the atomic-scale origins of ductility in various solid solution Mg alloys and enables the computationally guided systematic search for new compositions of high-ductile and high-formable Mg alloys.

Keywords: Mg alloys, ductility, pyramidal $\langle c + a \rangle$ dislocations, cross-slip, NEB, molecular dynamics, MEAM potential.

Résumé

Le développement de véhicules de transport efficaces d'un point de vue énergétique est crucial pour lutter contre le problème imminent du réchauffement climatique. L'utilisation de matériaux structuraux légers dans les industries automobiles et aérospatiales, jusqu'à la transition vers des sources d'énergie entièrement renouvelables, est un moyen de contrer la menace du réchauffement climatique. A cet égard, le magnésium (Mg), qui est, le métal à utilisation structurale le plus léger et abondant dans la croûte terrestre, peut s'avérer être un élément clé. L'application industrielle à grande échelle du Mg pur est néanmoins entravée par une faible ductilité intrinsèque et une faible ténacité à la rupture à température ambiante attribuée à sa structure hexagonale compacte (hcp), moins symétrique et plus plastiquement anisotrope que d'autres structures cristallines. Les arrêtes/composantes mixtes des dislocations pyramidales $\langle c + a \rangle$ sont métastables sur la pente douce et subissent une transition thermique activée 'pyramidal-basal' (PB), vers une faible énergie de dislocations immobilisées et basales-dissociées. La transition PB est liée au coût énergétique élevé des dislocations $\langle c + a \rangle$ pyramidales dissociées par rapport aux mêmes dislocations basales dissociées; elle se produit rapidement à température ambiante et elle rend le magnésium pur dépourvu de systèmes de glissement qui peuvent assister la déformation plastique le long de l'axe $\langle c \rangle$. L'absence des systèmes de glissement pyramidal $\langle c + a \rangle$ implique une forte texture basale, une forte anisotropie dans le comportement plastique, un taux de durcissement élevé et une faible ductilité dans les pièces forgées en magnésium pur. La transition PB est donc au cœur de la faible ductilité du magnésium pur.

Il a été montré expérimentalement que la création des solutions solides par ajout de petites quantités d'éléments de terres rares (RE = Y, Gd, Ce, Nd, Er, Dy, etc.) et d'autres solutés tels que Ca, Mn et Zr, a permis d'améliorer substantiellement la ductilité. Par ailleurs, on observe que la ductilité accrue de ces alliages de magnésium s'accompagne de l'activation de systèmes de glissement pyramidal $\langle c + a \rangle$ nécessaires mais absents dans le magnésium pur. Les travaux de recherche présentés dans cette thèse visent à découvrir, en conduisant des simulations de dynamique/statique moléculaire (DM/SM), les mécanismes à l'échelle atomique responsables de l'activation accrue des dislocations sur le plan pyramidal $\langle c + a \rangle$ dans certains alliages ductiles de Mg et, utiliser les connaissances ainsi acquises pour concevoir une stratégie de conception de nouveaux alliages de magnésium à haute ductilité.

Ce travail se concentre sur le système Mg-Y en tant que représentant des alliages ductiles Mg-RE pour effectuer des simulations de DM/SM afin de révéler les différents effets à l'échelle atomique des solutés RE sur divers mécanismes associés aux dislocations sur le plan pyramidal

$\langle c + a \rangle$. Nous commençons par tester l'hypothèse que les solutés RE pourraient stabiliser les arêtes/composantes mixtes des dislocations pyramidales $\langle c + a \rangle$ en augmentant la barrière énergétique de la transition PB désavantageuse. Les simulations en DM des alliages Mg-Y à grande échelle et à température déterminée, pour lesquelles on utilise un potentiel MEAM nouvellement développé, montrent clairement que les atomes de soluté Y sont incapables de modifier la barrière énergétique et les temps de transition associés avec la transition PB.

Nous proposons ensuite une nouvelle théorie mécanique basée sur un glissement dévié accéléré par la présence des solutés pour expliquer l'augmentation de l'activité des dislocations pyramidales $\langle c + a \rangle$ dans les alliages de magnésium ductiles. Le glissement dévié simple et double de la partie filetée des boucles de dislocation pyramidales $\langle c + a \rangle$ peuvent agir comme une source naturelle de dislocations. Par conséquent, un processus de glissement dévié accéléré par rapport à la vitesse de la transition PB, peut atténuer l'immobilisation des dislocations causée par la transition PB. La différence entre la basse l'énergie des dislocations pyramidales II $\langle c + a \rangle$ et l'énergie élevée des dislocations pyramidales I $\langle c + a \rangle$ dans le magnésium pur entraîne un processus lent de glissement dévié qui est inefficace contre la transition PB. Nous montrons que l'ajout de certains éléments solutés favorables, en petite quantité, peut réduire la différence d'énergie des dislocations sur les différents plans pyramidaux $\langle c + a \rangle$ et accélérer le processus de glissement dévié en le rendant beaucoup plus rapide que la transition PB, permettant ainsi un glissement facilité des dislocations pyramidales $\langle c + a \rangle$ avec une augmentation concomitante de la ductilité. La preuve expérimentale du processus de glissement dévié favorisé par la présence des solutés dans les alliages Mg-Y est obtenue par microscopie électronique à transmission (MET). Nous développons ensuite un modèle quantitatif pour établir les conditions de ductilité en fonction de la composition des alliages.

En augmentant la concentration des solutés favorables, les dislocations en vis pyramidales I $\langle c + a \rangle$ peuvent devenir énergétiquement plus stables que les dislocations en vis pyramidales II $\langle c + a \rangle$, ce qui peut modifier considérablement le chemin de réaction du glissement dévié. Les vitesses de transition et l'énergétique pour le double glissement dévié des dislocations pyramidales I $\langle c + a \rangle$ sont analysées au régime où elles sont énergétiquement plus favorables que les dislocations pyramidales II. L'analyse est réalisée par simulation avec la méthode « Nudged Elastic Band » (NEB), en utilisant un potentiel MEAM pour le magnésium, conçu spécialement pour favoriser les dislocations pyramidales I par rapport aux dislocations pyramidales II. Sur la base des résultats obtenus avec les simulations NEB, le modèle mécanique quantitatif est étendu au régime pyramidal I favorable.

Nous appliquons ensuite le modèle quantitatif développé aux alliages de magnésium binaires, ternaires, quaternaires et plus, contenant Ag, Zn, Al, Li, K, Sn, Mn, Sr, Ca, Zr et RE comme éléments solutés. Les prédictions du modèle sont comparées aux mesures de ductilité obtenues expérimentalement pour une large gamme d'alliages de magnésium et avérées être en excellent accord avec les données expérimentales. La théorie, en particulier, identifie les solutés Mn, Li, Sn, K, Ca, Sr, RE et Zr comme efficaces pour abaisser la différence d'énergie entre les dislocations $\langle c + a \rangle$, en accélérant ainsi le processus de glissement dévié, en randomisant la texture basale et en améliorant la ductilité des alliages résultantes. Le modèle prédit, en outre, une limite supérieure de concentrations de solutés fortement favorables tels que les RE

au-delà de la quelle la ductilité recommence à diminuer.

Le travail de recherche réalisé dans cette thèse nous donne un aperçu des phénomènes à l'échelle atomique qui sont à l'origine de la ductilité dans divers alliages de magnésium en solution solide et permet la conception, d'une façon systématique et computationnelle, de nouveaux alliages de magnésium à haute ductilité et formabilité.

Mots clés : alliages de magnésium, ductilité, dislocations pyramidales $\langle c + a \rangle$, glissement dévié, NEB, dynamique moléculaire, potentiel MEAM.

Contents

Acknowledgements	i
Abstract (English/Français)	iii
List of Figures	xiii
List of Tables	xvii
1 Introduction and Background	1
1.1 Dislocation: carrier of plasticity in crystalline materials	2
1.2 Crystal structure, dislocation systems and stacking faults in Mg	3
1.3 Energy of a straight dissociated dislocation	6
1.4 Dislocation controlled temperature-dependent plasticity	9
1.5 Mechanistic origins of low ductility and emergence of strong basal texture in wrought Mg	10
1.6 Enhanced ductility in wrought Mg alloys containing rare earth solute elements	12
1.7 Scope and structure of the thesis	15
2 Computational Methods	17
2.1 Elements of molecular dynamics and static simulations	18
2.2 Transition state theory and the Nudged Elastic Band method	19
2.2.1 Transition state theory	20
2.2.2 Nudged elastic band method	22
3 Interatomic potentials employed in the atomistic simulations	25
3.1 Two pure Mg MEAM interatomic potentials: MEAM_I and MEAM_II	26
3.2 Mg-Y MEAM interatomic potential	27
3.2.1 Misfit strain and misfit volume	29
3.2.2 Solute-stacking fault interaction energy	30
3.2.3 Y interactions with the pyramidal II $\langle c + a \rangle$ edge dislocation	34
3.2.4 Discussion on the applicability of the Mg-Y MEAM potential	38
4 Pyramidal-to-Basal Transition of $\langle c + a \rangle$ Dislocations in Mg-Y Alloys	41
4.1 Computational details	41
4.2 Results	43

Contents

4.2.1	Transition mechanism	43
4.2.2	Transition time	45
4.2.3	Energetic force driving the PB transition	46
5	Cross-Slip Mechanism of Pyramidal $\langle c + a \rangle$ Screw Dislocations in Mg	49
5.1	Cross-slip of $\langle c + a \rangle$ dislocation in pyramidal II favorable regime	50
5.2	Cross-slip of $\langle c + a \rangle$ dislocation in pyramidal I favorable regime	52
5.2.1	Computational details	53
5.2.2	Cross-slip transition paths and barriers	56
5.2.3	Implications for double pyramidal I cross-slip	60
5.3	Model for pyramidal $\langle c + a \rangle$ cross-slip barrier	62
6	Cross-Slip Driven Ductility in Dilute Mg Alloys: Theory	65
6.1	Mechanistic model of enhanced ductility	66
6.2	Solute effects on pyramidal I/II energy difference: dilute limit	67
6.3	Solute-dislocation interaction energies	72
6.4	Net shear stress $\Delta\tau$ driving the cross-slip process	78
6.4.1	Pyramidal II favorable regime	78
6.4.2	Pyramidal I favorable regime	81
6.5	Solute effects on dislocation energy difference ΔE^{I-II} : ultra dilute limit	82
6.5.1	Cross-slip of pyramidal $\langle c + a \rangle$ screw dislocations in the presence of a single solute	84
6.6	Experimental observation of the solute accelerated pyramidal cross-slip in Mg-Y alloys	88
7	Cross-Slip Driven Ductility in Dilute Mg Alloys: Results	91
7.1	Determination of model parameters	91
7.2	Prediction for binary Mg alloys	94
7.3	Predictions for ternary Mg alloys	95
7.4	Predictions for quaternary Mg alloys	102
7.5	Predictions in pyramidal I favorable regime	102
8	Discussion and Conclusion	107
9	Outlook	111
A	The MEAM potential framework for elemental and binary alloy system	113
A.1	Formalism for pure element	113
A.2	Formalism for binary system	116
B	Ultra Dilute Limit for Higher Order Alloys	119
B.1	The ultra dilute limit in ternary alloy	119
B.1.1	Type 1 in the dilute and type 2 in the ultra dilute limit ($c_1 \geq c^*$ and $c_2 < c^*$)	119

B.1.2	Both solutes are in the ultra dilute limit ($c_1 < c^*$ and $c_2 < c^*$)	120
B.2	The ultra dilute limit in quaternary alloy	121
B.2.1	One solute (type 1) in the ultra dilute limit ($c_1 < c^*$, $c_2 \geq c^*$, $c_3 \geq c^*$) . . .	122
B.2.2	Two solutes (type 1 and 2) in the ultra dilute limit ($c_1 < c^*$, $c_2 < c^*$, $c_3 \geq c^*$)	122
C	DFT Computation and Solute-Stacking Fault Interaction Energy	125
C.1	Details of DFT computations	125
C.2	Solute-stacking fault interaction energy	125
D	Dislocation Energy Difference associated with Pyramidal Cross-Slip	129
	Bibliography	131
	Curriculum Vitae	149

List of Figures

1.1	Schematic depiction of dislocations gliding on a slip plane.	3
1.2	Schematic illustration of different crystallographic planes and directions in an hcp crystal.	4
1.3	Basal stacking fault and dissociated basal $\langle \mathbf{a} \rangle$ edge dislocation	5
1.4	Schematic illustration of various components involved in the energy of a straight dissociated dislocation.	6
1.5	Temperature-dependent plastic deformation of crystals	9
1.6	Pyramidal-to-basal (PB) transition of the pyramidal II $\langle \mathbf{c} + \mathbf{a} \rangle$ edge dislocation occurring at 500 K, as observed in the MD simulations.	11
1.7	TEM observation of the basal-oriented $\langle \mathbf{c} + \mathbf{a} \rangle$ dislocations.	12
1.8	Plots of stress versus strain obtained from the tensile tests up to failure at room temperature for pure Mg and Mg-RE solid solution alloys.	13
1.9	Variation of experimentally observed ductility in different Mg alloys as a function of grain size.	14
2.1	An illustration of a thermally activated process between two metastable states.	21
2.2	A schematic illustration of different forces involved in NEB calculation for a two dimensional potential energy surface.	23
3.1	Atomic structures of the pyramidal I and the pyramidal II $\langle \mathbf{c} + \mathbf{a} \rangle$ screw dislocation cores in pure Mg.	29
3.2	Positions of different stable stacking faults in the basal, pyramidal I, and pyramidal II planes.	31
3.3	Schematics of the simulation cells used to compute various stacking fault energies and solute-stacking fault interaction energy.	32
3.4	Interaction energy of Y solute with various stacking faults in Mg.	35
3.5	Interaction energy of Y solute with pyramidal II $\langle \mathbf{c} + \mathbf{a} \rangle$ edge dislocation.	37
4.1	Pyramidal-to-basal (PB) transition of pyramidal II $\langle \mathbf{c} + \mathbf{a} \rangle$ edge dislocation in Mg-3at.%Y alloy at a temperature of 500 K as obtained from the MD simulation.	43
4.2	Mean transition time \bar{t} of the pyramidal-to-basal transition versus temperature for both Mg-3at.%Y and pure Mg.	44
4.3	Energies of pyramidal II dissociated and basal oriented $\langle \mathbf{c} + \mathbf{a} \rangle$ dislocation structures in pure Mg and Mg-3wt.%Y alloy.	45

List of Figures

5.1	Schematic illustration of the pyramidal I and the pyramidal II planes in the hcp crystal structure.	50
5.2	Energetics and mechanism of the $\langle c + a \rangle$ cross-slip from the low-energy pyramidal II to the high-energy pyramidal I plane.	51
5.3	Schematic illustration of possible cross-slip or double cross-slip paths for $\langle c + a \rangle$ screw dislocation between two pyramidal I planes	54
5.4	Core structures of $\langle c + a \rangle$ screw dislocations that are accessible through cross-slip process.	54
5.5	Energy difference versus reaction coordinate, as determined in NEB calculation of the minimum energy path of the cross-slip process between two pyramidal I planes accomplished through the route where the pyramidal I dislocation cross-slips to other accessible pyramidal I plane via a high-energy pyramidal II plane.	57
5.6	Energy difference versus reaction coordinate, as determined in NEB calculation of the minimum energy path of the cross-slip process between two pyramidal I planes accomplished through the route where the pyramidal I dislocation cross-slips directly to other accessible pyramidal I plane by nucleating a pair of jogs and without ever residing on the high-energy pyramidal II plane.	58
5.7	Energy difference versus reaction coordinate, as determined in NEB calculation of the minimum energy path of the cross-slip process between two pyramidal I planes accomplished through the route where the pyramidal I dislocation first cross-slips to a high-energy pyramidal II plane, and goes back to a parallel pyramidal I plane after gliding some distance on a pyramidal II plane.	59
5.8	Energetics and minimum energy path of the most favorable cross-slip path between pyramidal I planes as inferred from the NEB results.	61
5.9	Schematic illustration of cross-slip of $\langle c + a \rangle$ screw dislocation from pyramidal II to pyramidal I plane in pyramidal II favorable regime.	63
6.1	Schematic depiction of the mechanistic theory that involves the PB transition and cross-slip process associated with pyramidal $\langle c + a \rangle$ dislocations.	68
6.2	Change in correspondence of solute positions with respect to the two pyramidal $\langle c + a \rangle$ dislocations during the cross-slip.	73
6.3	Average and fluctuation contributions of solutes in dislocation energy difference.	76
6.4	Representation of coordinate system and applied load during the cross-slip process.	79
6.5	Map of difference between interaction energy ΔU^{I-II} of Y solute atom with pyramidal I and pyramidal II $\langle c + a \rangle$ screw dislocations.	85
6.6	MEPs for the cross-slip of $\langle c + a \rangle$ screw dislocations from pyramidal II to pyramidal I plane in Mg and Mg-Y alloys.	86
6.7	Energy variation along the MEP associated with the pyramidal II-pyramidal I cross-slip of $\langle c + a \rangle$ screw dislocations in pure Mg and Mg-Y.	87

6.8	Experimental results for pure Mg and Mg-Y alloys under tensile deformation at room temperature.	89
7.1	Predictions of the cross-slip barrier ΔG_{XS} , including fluctuation, and ductility index χ in binary Mg alloys containing Zn, Al and Y solutes.	93
7.2	Variation of the cross-slip barrier, including average and fluctuation, and ductility index χ with the concentration of the solutes in binary alloys.	95
7.3	Variation of ductility index χ as a function of the concentrations of solutes in ternary Mg alloys.	96
7.4	Variation of ductility index χ as a function of the concentrations of solutes in ternary Mg alloys.	97
7.5	Variation of ductility index χ as a function of the concentrations of solutes in ternary Mn based Mg alloys.	98
7.6	Prediction of ductility in quaternary alloys based on Al-Zn solutes.	99
7.7	Prediction of ductility in quaternary alloys based on Li-Al solutes.	100
7.8	Prediction of ductility in quaternary alloys based on Li-Al solutes.	101
7.9	Prediction of ductility in Mg-RE binary alloys including the pyramidal I favorable regime.	104
C.1	The single solute-stacking fault interaction energies U_{SF} with pyramidal I and pyramidal II stacking faults are plotted as a function of the solute-stacking fault distance for Ag, Zn, Al, Li, K and Sn.	127
C.2	The single solute-stacking fault interaction energies U_{SF} with pyramidal I and pyramidal II stacking faults are plotted as a function of the solute-stacking fault distance d_i for Mn, Sr, Ca, Y, Nd, Ce and Zr.	128

List of Tables

3.1	Parameters for the MEAM_I and the MEAM_II potentials for pure Mg used in this work.	26
3.2	Properties of the MEAM_I and the MEAM_II interatomic potentials for pure Mg.	28
3.3	Parameters for the MEAM potentials to describe pure Y used in this work.	28
3.4	The MEAM potential parameters developed for the binary Mg-Y alloy system.	29
3.5	Properties of Y solute atom in Mg as calculated by the current MEAM potential, the DFT, and the Kim potential.	36
3.6	Interaction energy of Y with the pyramidal II $\langle c + a \rangle$ edge dislocation in Mg at various atomic sites around the dislocation core, as calculated from the current MEAM potential and the DFT.	38
6.1	Properties of various solutes in Mg relevant for mechanistic theory.	77
7.1	Properties of Mg relevant to the pyramidal I and the pyramidal II stacking faults that are used in the mechanistic model to predict ductility in dilute solid solution Mg alloys.	93

1 Introduction and Background

Magnesium (Mg) is the lightest structural metal with high specific strength and is abundant in the Earth's crust, comprising nearly 2 % of the total weight. The density of Mg, 1.738 gm/cm^3 , is two-third of aluminum and one-fourth of the steel. Thus, Mg can be used in the automotive and aerospace industry to build an energy-efficient transportation system [77, 115, 125, 141, 161], and therefore contribute in combating the imminent problem of global warming. Furthermore, the biocompatibility of Mg renders it very attractive for biomedical applications [190, 195].

The large scale industrial applications of pure Mg are, however, impeded by its poor room-temperature ductility and low fracture toughness. Since manufacturing processes such as forming, extrusion, drawing, forging, etc. require good ductility and fracture toughness, the applications of wrought Mg components are severely limited. Furthermore, the low fracture toughness of Mg renders it unsuitable for use in critical structural components. The ductility of solid solution Mg alloys, however, has been experimentally observed to improve with the small addition of certain solute elements. For instance, Agnew et al. [6] and Sandlöbes et al. [181, 182] show that rare-earth elements (RE = Y, Gd, Dy, Tb, Er, Ho, Ce, Nd), in particular, stand out as very effective solute elements in significantly improving the room temperature ductility of resulting Mg alloys. Moreover, Mg alloys containing Ca, Mn, Zr, Li, and other solute elements also display enhanced room temperature ductility [6, 40, 49, 148, 243, 247]. Obtaining a mechanistic understanding of the specific role of the favorable solutes in enhancing Mg ductility will prove instrumental in designing new Mg alloys tailored to meet various technological applications, and is the main focus of this thesis.

The ductility and toughness of a material depend on the plastic properties, i.e., ability to yield and achieve a suitable level of strain hardening to prevent any localized deformation which can result in catastrophic failure. The plastic deformation of crystalline materials, in turn, is intimately connected with the evolution of dislocation microstructures. For example, the low ductility of pure Mg originates from a detrimental thermally activated pyramidal-to-basal (PB) transition [151, 155, 228] that markedly hinders the mobility of crucial pyramidal $\langle c + a \rangle$ dislocations and exacerbates the plastic anisotropy of Mg crystal (discussed in details in Section 1.5).

Therefore, we first present a brief description of dislocations and Mg crystal structure before we delve into the salient aspects of plasticity in Mg and its alloys. The following Sections 1.3 and 1.4 discuss the energy of a dissociated dislocation and temperature-dependent plasticity originating from various thermally activated dislocation processes. Section 1.5 describes the PB transition of pyramidal $\langle c + a \rangle$ dislocations as a primary cause for low ductility in pure Mg. We, next, present the available experimental results on ductility and active dislocation systems in Mg-RE alloys and evaluate various hypotheses put forward in order to explain the enhanced ductility in these Mg alloys in Section 1.6. The final Section 1.7 of this chapter describes the scope and general structure of the thesis.

1.1 Dislocation: carrier of plasticity in crystalline materials

A dislocation is a linear crystalline defect of which existence was posited to reconcile the discrepancy between the theoretical estimate and experimentally observed strength of crystalline materials [89, 152, 160, 203]. The motion and evolution of these dislocations primarily control plastic properties of metals and other crystalline materials [13, 19, 55, 114, 145, 170]. As depicted in Fig. 1.1, dislocations demarcate the boundary between the slipped and unslipped parts of the crystal. Their motions on specific crystallographic glide planes lead to the progressive shearing of the crystal across the glide plane resulting in the plastic deformation. Dislocations are essentially curved lines that are identified by a line direction ξ . The magnitude and direction of the shear associated with a dislocation are characterized by its Burgers vector b . Depending on the angle between the line direction and the Burgers vector, dislocations are categorized into the edge, screw, and mixed dislocations. In an edge dislocation, Fig. 1.1(a), the Burgers vector is perpendicular to the line direction; in a screw dislocation, Fig. 1.1(b), the Burgers vector and line direction are parallel or anti-parallel to each other; all other intermediate cases belong to mixed dislocations. Dislocations are constrained to move on a glide plane that contains both Burgers vector and line direction. This leads to a well-defined glide plane for edge dislocations. On the other hand screw dislocations, as depicted in Fig. 1.1(b), can glide on multiple planes owing to the fact that its Burgers vector and line direction do not define a unique glide plane. Thus screw dislocations can change their glide planes to overcome an obstacle or in response to the applied stress. This process of screw dislocations changing their glide is termed cross-slip and has important consequences in the plastic deformation of crystals [98, 110, 143, 191]. For a comprehensive exposition of dislocation theory, the readers may consult Refs. [13, 44, 96].

The theory of linear elasticity can accurately describe the influence of a dislocation far from the dislocation line. However, the region around the dislocation line, dislocation core, represents the breakdown of the elasticity theory and is resolved at the discrete atomic level. The atomic structure of dislocation cores strongly affects the mobility and other various properties associated with dislocations. For instance, in a crystal, dislocations glide preferentially on one of the densely packed planes and have one of the lattice vectors of the unit cell as Burgers vector. A dislocation on the closest packed plane with the closest packed lattice vector as its

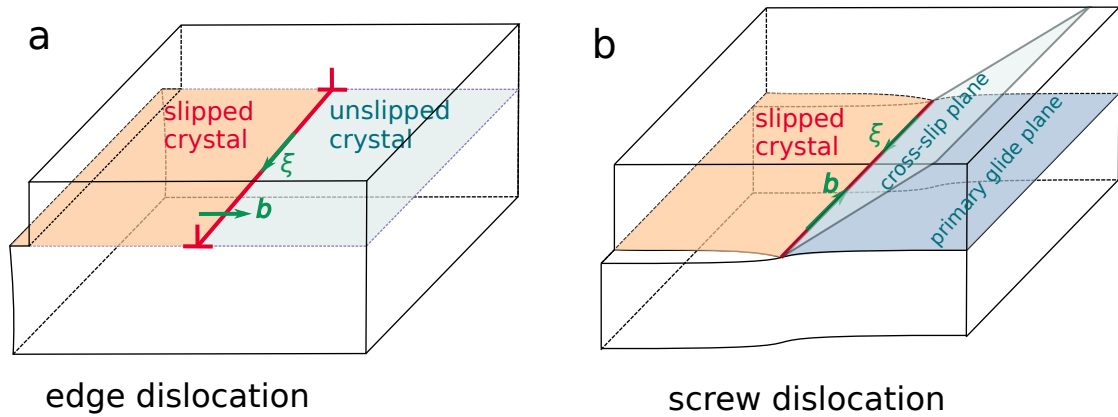


Figure 1.1 – **Schematic depiction of dislocations gliding on a slip plane:** (a) edge and (b) screw dislocation. A dislocation is the boundary line between the slipped and unslipped parts of the crystal. Edge dislocation has Burgers vector \mathbf{b} and dislocation line ξ perpendicular to each other, while these two vectors are parallel or anti-parallel in the case of a screw dislocation. Plastic shear happens in the crystal with the dislocations moving from left to right. Screw dislocation in (b) can continue glide on the primary plane or cross-slip to the plane that also contains the dislocation line ξ and Burgers vector \mathbf{b} .

Burgers vector requires the lowest stress to move. Given the importance of the crystal structure in controlling the dislocation behavior, next Section 1.2 presents a brief description of the crystal structure of Mg and various underlying active dislocation systems.

1.2 Crystal structure, dislocation systems and stacking faults in Mg

Solid-phase Mg has the hexagonal close-packed (hcp) crystal structure. Various crystallographic planes and directions associated with an hcp crystal structure are depicted in Fig. 1.2. Different crystallographic planes and their Miller indices are: basal $\{0001\}$, prismatic I $\{10\bar{1}0\}$, prismatic II $\{11\bar{2}0\}$, pyramidal I $\{10\bar{1}1\}$, and pyramidal II $\{11\bar{2}2\}$. In hcp crystals, there are one basal, three prismatic I, three prismatic II, twelve pyramidal I, and six pyramidal II planes. Additionally, common crystallographic directions contained in these planes are: $\langle \mathbf{a} \rangle$ - $\langle 11\bar{2}0 \rangle$, $\langle \mathbf{c} \rangle$ - $\langle 0001 \rangle$, $\langle \mathbf{c} + \mathbf{a} \rangle$ - $\langle 11\bar{2}3 \rangle$. Three different $\langle \mathbf{a} \rangle$, one $\langle \mathbf{c} \rangle$, and six distinct $\langle \mathbf{c} + \mathbf{a} \rangle$ directions are present in an hcp crystal. During plastic deformation, dislocations may glide on these planes with one of the listed lattice vectors as their Burgers vector.

As discussed previously, dislocations tend to glide on the closest packed plane and prefer the closest packed direction as their Burgers vector. In hcp crystal, only the basal plane is the close-packed plane, and the $\langle \mathbf{a} \rangle$ direction contained within it is the close-packed direction. Thus, the basal $\langle \mathbf{a} \rangle$ dislocations are found to be particularly active in pure Mg and occasionally observed to cross-slip on prismatic I planes. Additionally, dislocations with Burgers vector $\langle \mathbf{c} + \mathbf{a} \rangle$ glide predominantly on pyramidal II planes in pure Mg, and could cross-slip on pyramidal I plane depending on the loading conditions [16, 240]. Compared to the cubic crystal structures –

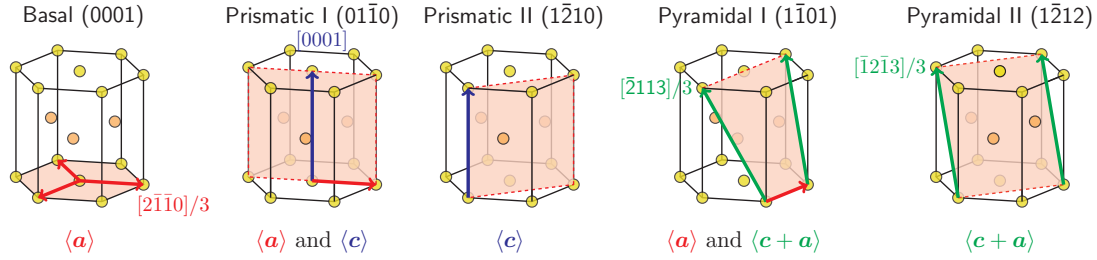


Figure 1.2 – **Schematic illustration of different crystallographic planes and directions in an hcp crystal:** planes - basal, prismatic I, prismatic II, pyramidal I and pyramidal II; directions - $\langle a \rangle$, $\langle c \rangle$, and $\langle c + a \rangle$. The crystallographic directions mentioned below each figure are possible Burgers vector for dislocations gliding on that plane.

face-centered (fcc) and body-centered (bcc) – hcp crystal structure is less symmetric. For instance, hcp crystal has only one close-packed basal plane as opposed to the fcc crystal which has four intersecting close-packed planes. The low symmetry of the hcp crystal structure leads to the activation of multiple dislocation systems and twinning, and thus makes the plastic behavior of Mg complex and scientifically fascinating [1, 23, 238].

Dislocation behavior is further affected by the presence of stable stacking faults in slip planes. Stacking fault is an area defect that disrupts the normal stacking of atomic planes and emerges during the shearing of the crystal across a well-defined crystallographic plane [216, 217]. To understand the concept of stacking fault, we consider the upper half of a crystal as being rigidly shifted with respect to the lower half across a specific crystallographic plane, and measure the resultant additional energy per unit area compared to the original pristine crystal. This additional energy per unit area is termed generalized stacking fault energy γ .

Fig. 1.3(a) demonstrates the generalized stacking fault energy arising from the shifting process across the basal plane in Mg. We observe that a full lattice vector shift recovers the original crystal without any change in the energy. However, as shown in Fig. 1.3(b), we may encounter some fractional lattice vector shifts for which the resulting configuration is locally stable but the energy is higher than the original pristine crystal. This location in the slip plane is called the stable stacking fault. The basal plane contains such stable stacking fault at position $1/3\langle 1\bar{1}00 \rangle$, which is known as I_2 stacking fault. Basal I_2 stacking fault changes the stacking arrangement of the basal planes from ...ABABABAB... to ...ABABCACA..., where A, B, and C denote the sequencing order of close-packed $\{111\}$ planes in fcc crystal. On the basal plane, two additional non-glide type stable stacking faults, i.e. they cannot appear during the shifting process, can also arise from the precipitation of vacancies/interstitials: basal I_1 stacking fault corresponding to the stacking order ...ABABACAC...; basal extrinsic stacking fault corresponding to the stacking order ...ABABCABAB... The existence of a stable stacking fault on a slip plane encourages the dissociation of a dislocation with a full lattice vector as its Burgers vector into two partials having fractional lattice vectors corresponding to the stable stacking fault as their Burgers vectors. The two partials are connected by the

1.2. Crystal structure, dislocation systems and stacking faults in Mg

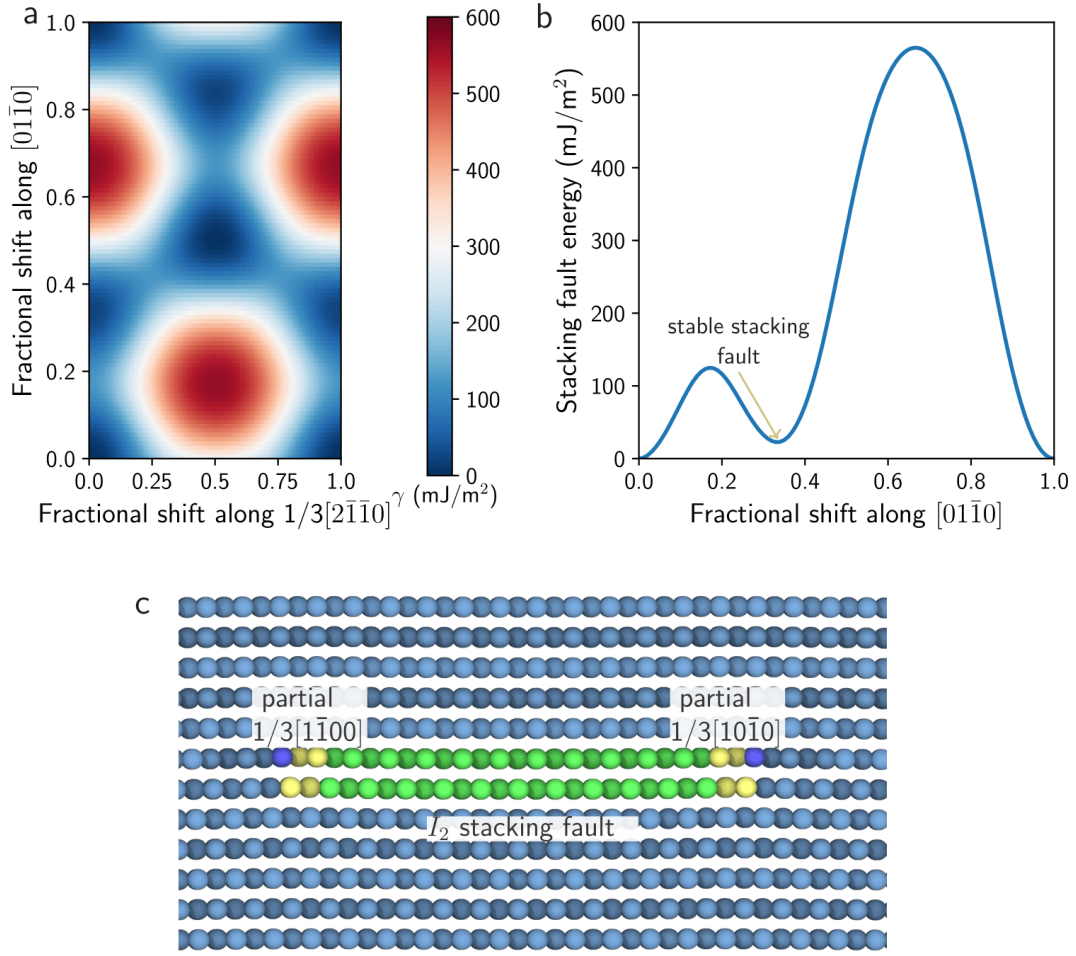


Figure 1.3 – **Basal stacking fault and dissociated basal $\langle a \rangle$ edge dislocation.** (a) Generalized stacking fault energy map γ arising from shifting of the upper half of Mg crystal relative to the lower half across the basal plane. (b) Stacking fault energy curve obtained by relatively shifting the two half of the crystal along $[01\bar{1}1]$ direction. The plot clearly shows that there exists a stable stacking fault at one-third shift along $[01\bar{1}1]$ direction. (c) The atomic core structure of a basal $\langle a \rangle$ dislocation in Mg dissociated into two partials bounded by a basal I_2 stacking fault in between. Atoms in (c) are colored according to its local crystal structure as identified from the common neighbor analysis: blue - hcp; green - fcc; purple - bcc; yellow - unidentified crystal structure.

stacking fault in between. For instance, basal I_2 stacking fault causes the basal $\langle a \rangle$ dislocation to dissociate in two Shockley type partials whose Burgers vectors are related according to: $1/3\langle 2\bar{1}\bar{1}0 \rangle = 1/3\langle 10\bar{1}0 \rangle + I_1 \text{ stacking fault} + 1/3\langle 1\bar{1}00 \rangle$.

Fig. 3.2 shows the positions of the stable stacking faults relevant to dislocation dissociation on the basal, pyramidal I, and pyramidal II plane. The pyramidal I contains three stable stacking faults: SF1 is relevant for $\langle a \rangle$, and SF2 and SF3 are associated with the dissociation of $\langle c + a \rangle$ dislocation. The pyramidal II contains only one stable stacking fault which determines

the dissociation of $\langle c + a \rangle$ dislocations. In Chapter 3, we present the various stable stacking fault energies in pure Mg by using different interatomic potentials employed in this work. For a complete description of the stacking faults in hcp materials, readers are directed to Ref. [236].

1.3 Energy of a straight dissociated dislocation

The transformation of a system is often driven by energetic considerations. The system evolves under external stimuli towards a state that minimizes a specific kind of free energy, e.g., Helmholtz or Gibbs free energy, corresponding to the external constraints. Dislocation is also treated as a physical system, and its transformations can be understood in terms of its tendency to minimize the free energy under external loads. Several transformations under investigations in this thesis, such as the PB transition discussed in Section 1.5 and pyramidal $\langle c + a \rangle$ cross-slip, presented in Chapter 5, belong to this category. We, therefore, briefly present in this section various contributions to the energy of a straight dissociated dislocation by closely following the Stroh formalism of anisotropic elasticity, as presented in Ref. [232].

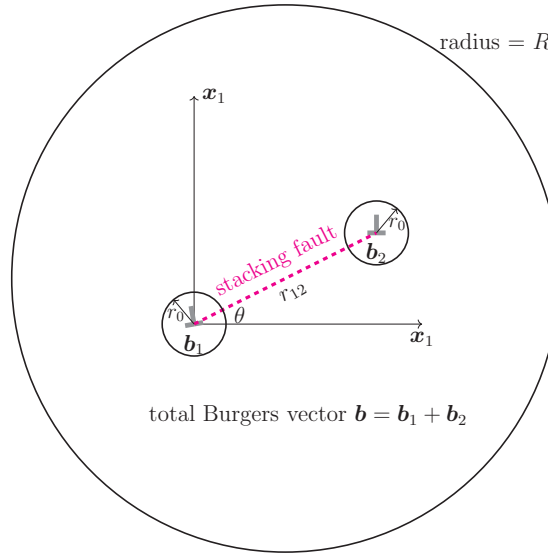


Figure 1.4 – **Schematic illustration of various components involved in the energy of a straight dissociated dislocation.** A straight dislocation of total Burgers vector \mathbf{b} and dislocation line ξ along the normal of the paper is dissociated into two partials of Burgers vectors \mathbf{b}_1 and \mathbf{b}_2 , with $\mathbf{b} = \mathbf{b}_1 + \mathbf{b}_2$. The two partials are connected by an intervening stable stacking fault of width r_{12} . In the main text, we determine the energy per unit dislocation length contained in an arbitrarily large cylinder of radius R .

Fig. 1.4 shows the geometry of a straight dislocation dissociated into two partials separated by r_{12} and bounded by a stable stacking fault of energy per unit area γ . The line connecting the two partials is inclined at an angle θ with respect to a predefined coordinate system. The Burgers vectors of the two partials are \mathbf{b}_1 and \mathbf{b}_2 , with Burgers vector of total dislocation

1.3. Energy of a straight dissociated dislocation

$\mathbf{b} = \mathbf{b}_1 + \mathbf{b}_2$. We are interested in determining the dislocation energy per unit length contained in an arbitrarily large cylinder of radius R .

For the dissociated dislocation, we can write the total energy per unit dislocation length as the sum of the core energies E_c of the two partials, elastic energy comprising self elastic energies E_e of the partials and elastic interaction energy W_{e12} between them, and energy E_{sf} associated with the intervening stacking fault, i.e.,

$$E_{\text{tot}}(r) = (E_{c1} + E_{c2}) + (E_{e1} + E_{e2} + W_{e12}) + E_{sf}. \quad (1.1)$$

The core energy $E_c(r_0)$ contains all the non-linear energy contribution arising due to the discrete atomic structure within a cutoff radius r_0 which can only be faithfully determined from atomistic simulations. The self-energy E_c is the energy contained in the annular cylindrical region beyond cutoff radius r_0 and within R due to the elastic deformation caused by each partial dislocations individually. The self elastic energies of the two partials are given as

$$E_{e1} = K_1 \ln \frac{R}{r_0}, \quad E_{e2} = K_2 \ln \frac{R}{r_0}, \quad (1.2)$$

where self energy prefactors are computed as

$$K_i = \frac{1}{2\pi} \mathbf{b}_i^T \text{Im} \{ \mathbf{B} \mathbf{B}^T \} \mathbf{b}_i, \quad (1.3)$$

where \mathbf{B} is the 3×3 complex matrix determined by the material elastic stiffness tensor, and $\text{Im}\{\}$ function retains only the imaginary part of the complex number.

The elastic interaction energy between the two partials is written as

$$W_{e12} = K_{12} \ln \frac{R}{r_{12}} - E_\theta, \quad (1.4)$$

where the first term on the right-hand side arises due to the radial interaction and the origin of the second terms lies in the angular interaction between the partials. The two terms are calculated by

$$K_{12} = \frac{1}{\pi} \mathbf{b}_2^T \text{Im} \{ \mathbf{B} \mathbf{B}^T \} \mathbf{b}_1, \quad E_\theta = \frac{1}{\pi} \mathbf{b}_2^T \text{Im} \{ \mathbf{B} \langle \ln(\cos \theta + p_\alpha \sin \theta) \rangle \mathbf{B}^T \} \mathbf{b}_1, \quad (1.5)$$

where $\langle f(z_\alpha) \rangle = \text{diag}[f(z_1), f(z_2), f(z_3)]$ denotes a 3×3 diagonal matrix, p_α are the eigenvalues with positive imaginary part which appear in the Stroh Formalism. The derivation and precise expression of all these quantities are not relevant for the current discussion, and we refer the readers to Ref. [205] for a detailed presentation on the Stroh formalism of anisotropic elasticity and to Ref. [232] for its application to computing elastic energy associated with a dislocation.

The final contribution is the energy due to the intervening stacking fault of width r_{12} which is

simply given by

$$E_{\text{sf}} = \gamma r_{12}, \quad (1.6)$$

where γ is the stacking fault energy.

By collecting all the terms together, the total dislocation energy per unit length is expressed as

$$\begin{aligned} E_{\text{tot}}(R) &= E_{c1}(r_0) + E_{c2}(r_0) + K_1 \ln \frac{R}{r_0} + K_2 \ln \frac{R}{r_0} + K_{12} \ln \frac{R}{r_{12}} - E_\theta + \gamma r_{12}, \\ &= E_c(r_0) + K \ln \frac{R}{r_0} - K_{12} \ln \frac{r_{12}}{r_0} - E_\theta + \gamma r_{12}, \end{aligned} \quad (1.7)$$

where $E_c(r_0) = E_{c1}(r_0) + E_{c2}(r_0)$ is the combined core energy of the two partials, and $K = K_1 + K_2 + K_{12} = \frac{1}{2\pi} \mathbf{b}^T \text{Im} \{ \mathbf{B} \mathbf{B}^T \} \mathbf{b}$ is the energy prefactor for the full dislocation. We can further represent the sum of energies $E_c(r_0) - K_{12} \ln(r_{12}/r_0) - E_\theta + \gamma r_{12}$ as structure energy E_{struc} . Then the total dislocation energy per unit length can be rewritten as

$$E_{\text{tot}}(R) = E_{\text{struc}}(r_0) + K \ln \frac{R}{r_0}. \quad (1.8)$$

Written in this form, Eq. 1.8, the total dislocation energy can be interpreted as comprising two parts: structural energy and elastic energy. Structural energy $E_{\text{struc}}(r_0)$ is the energy contained in a cylinder of radius r_0 centered on the dislocation that includes core energy of partials, stacking fault energy, contributions from the interaction between the partials, and near-field elastic energy. Essentially, $E_{\text{struc}}(r_0)$ contains all the structure-specific energy and can only be accessed by the atomistic simulations. The second term in the right-hand side of the Eq. 1.8 is the elastic self-energy due to the total dislocation in the annular cylinder of inner radius r_0 and outer radius R . This implies that r_0 should be large enough such that the elastic description of the dislocation should be valid beyond r_0 . Furthermore, since energy prefactor K only depends on the material elastic constants, Burgers vector, and dislocation line of the total dislocation contained within the radius r_0 , this elastic energy is independent of the exact structure and arrangement of the dislocation. Thus the elastic energy cannot differentiate between the specific dislocation core structures confined within radius r_0 .

In this thesis, we will often encounter dislocation transformations during which the Burgers vector and line direction of the total dislocation content remain unchanged, and only the dislocation core structures alter. The PB transition and the cross-slip are two prominent examples of such dislocation transformations appearing in this thesis. These transformations are driven and controlled by the change in the structure-specific energy $E_{\text{struc}}(r_0)$ of the two dislocation arrangements since the elastic energies of the two dislocation arrangements are the same.

1.4 Dislocation controlled temperature-dependent plasticity

The plastic deformation of crystalline materials is generally temperature-dependent. For instance, as shown in Fig. 1.5(a), the flow stress of bcc iron is experimentally observed to decrease with increasing temperature [45, 116]; yielding of single-crystal Mg by the pyramidal $\langle c + a \rangle$ slip exhibits highly temperature-dependent behavior, i.e., as depicted in Fig. 1.5(b), yield stress increases from 100 K up to 300 K and decreases onward [15, 240]; similarly, the CRSS for the prismatic slips in hcp materials, as Fig. 1.5(c) demonstrates, are temperature dependent [7, 8, 56–58]. Furthermore, atomic-diffusion through the vacancy migration from one atomic site to another in a crystal is also temperature-dependent and plays an important role in material transport and dislocation climb.

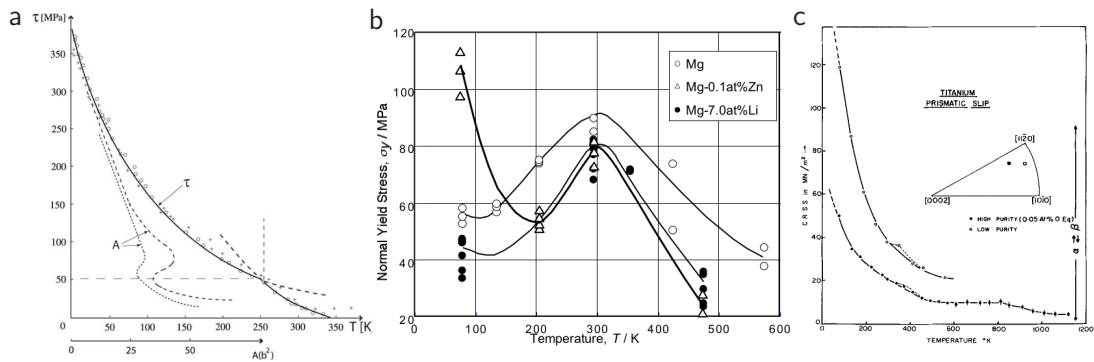


Figure 1.5 – **Temperature-dependent plastic deformation of crystals.** (a) Variation of the yield stress τ in pure bcc Fe as obtained from the tensile tests (from Ref. [45]). (b) Temperature-dependent yield stresses of pure hcp Mg, Mg-7.0at.%Li and Mg-0.1at.%Zn single crystals stretched in the $[11\bar{2}0]$ direction. These single crystals are reported to deform by the pyramidal II $\langle c + a \rangle$ slip (from Ref. [15]). (c) Temperature-dependent CRSS for the prismatic slip in Ti with two levels of interstitial impurities (from Ref. [8]).

As noted in Section 1.1, the plastic properties of crystalline materials are controlled mainly by the motion and evolution of dislocations, and therefore it is natural to look into the influence of temperature on dislocation behaviors in order to gain an insight into the temperature-dependent crystal plasticity. Dislocations glide and evolve in a crystal by overcoming both long-range elastic stress fields arising from the dislocation network and local short-range energy barriers represented by solutes, precipitates, intrinsic lattice resistance, and transformation of dislocation cores [19, 46, 108]. The long-range dislocation stress field depends on the temperature only through the elastic constant of the crystal, and thus this mild temperature dependence can be accounted for in an average way by modifying the elastic constant with temperature.

The prominent effect of temperature on dislocation evolution emanates from overcoming the local energy barriers. The short-range interaction of a dislocation with the local energy barrier involves a relatively small number of atoms and is strongly influenced by the random

atomic vibration caused by the available thermal energy at finite temperature. The thermal fluctuations assist the dislocation to overcome the local energy barrier and decrease the stress level needed to maintain the dislocation glide and strain rate. In a crystal, the dislocations remain trapped in a local energy minimum for a long time until a sufficient nudge from random thermal fluctuation helps the dislocation cross the barrier to get trapped in the next energy minimum. The crystal plasticity is, therefore, a result of the successive thermally assisted overcoming of local energy barrier by dislocations.

The thermally activated processes, thus, are of fundamental importance and underlie almost all the temperature-dependent plastic properties of materials. The most important quantity concerning the thermally activated process is the transition rate at which an energy barrier is overcome as a function of temperature and applied load. This transition rate then determines the flow rate of materials under an applied load and temperature. A systematic characterization of thermally activated processes is performed under the transition state theory and is presented in Section 2.2. For a comprehensive theoretical and experimental coverage of various thermally activated dislocation mechanisms, readers are referred to Ref. [46].

1.5 Mechanistic origins of low ductility and emergence of strong basal texture in wrought Mg

Low ductility of Mg is attributed to the lower symmetry of its underlying hcp crystal structure. As discussed in the previous Section 1.2, plastic deformation in Mg is mainly caused by the slip of the basal $\langle a \rangle$ dislocations. However, the basal $\langle a \rangle$ dislocations by themselves are unable to satisfy the von Mises criterion of homogeneous plasticity in polycrystals. The von Mises criterion demands the activation of at least five independent slip systems to accommodate arbitrary plastic strains and to maintain the strain compatibility in neighboring grains. However, the basal $\langle a \rangle$ dislocation represents two different slip systems, and even the activation of the prismatic I $\langle a \rangle$ and the pyramidal $\langle a \rangle$ can provide at most four independent slip systems [238]. The motion of $\langle a \rangle$ dislocations, furthermore, cannot accommodate the $\langle c \rangle$ -axis plastic strain. Thus, to achieve the homogeneous plastic deformation dislocations having Burgers vectors component in $\langle c \rangle$ direction must be operative. Pyramidal I and pyramidal II $\langle c + a \rangle$ dislocations are such slip systems of which activation can satisfy von Mises criterion and improve ductility.

The pyramidal $\langle c + a \rangle$ dislocations, nevertheless, are not particularly active in pure Mg. This low activity of the pyramidal $\langle c + a \rangle$ dislocations primarily arises from an intrinsic thermally activated pyramidal-to-basal (PB) transition of the pyramidal $\langle c + a \rangle$ dislocations [79, 151, 155, 200, 228, 229, 246]. We briefly present the mechanism and effects of the PB transition on the evolution of the pyramidal II $\langle c + a \rangle$ dislocation loops as recently revealed by Wu and Curtin [228] by conducting molecular dynamics (MD) simulations at temperatures 500 K, 600 K and 700 K. As shown in Fig. 1.6, the pyramidal II dissociated $\langle c + a \rangle$ edge dislocations are metastable on their easy-glide pyramidal II plane. At finite temperatures, the $\langle c + a \rangle$ edge

1.5. Mechanistic origins of low ductility and emergence of strong basal texture in wrought Mg

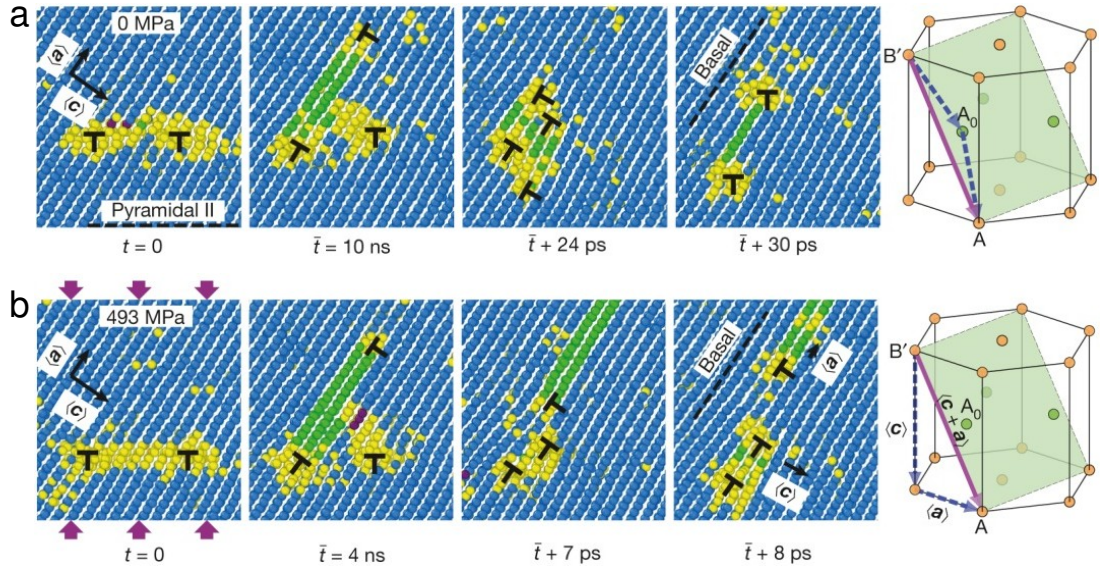


Figure 1.6 – **Pyramidal-to-basal (PB) transition of the pyramidal II $\langle c + a \rangle$ edge dislocation occurring at 500 K, as observed in the MD simulations.** (a) The pyramidal II dissociated $\langle c + a \rangle$ dislocation transforms into the basal-dissociated $\langle c + a \rangle$ dislocation, where the final dislocation structure involves the two $1/2\langle c + a \rangle$ partials connected by a basal I_1 stacking fault. (b) The pyramidal II dissociated $\langle c + a \rangle$ edge dislocation dissociates into the basal $\langle c \rangle$ and the basal $\langle a \rangle$ dislocations. Two partials of the basal $\langle c \rangle$ dislocation are bounded by the basal extrinsic stacking fault, and the two Shockley partials of the basal $\langle a \rangle$ dislocation involve the basal I_2 stacking fault between them. The last schematics in both (a) and (b) show the Burgers vectors of the initial pyramidal II dissociated (in solid red) and final basal dissociated dislocations (in dotted blue). In atomic figures, the colors denote the crystal structure of the atoms as identified from the common neighbor analysis: blue - hcp; green - fcc; purple - bcc; yellow - unidentified crystal structure. Adapted from [228].

dislocations transform into one of the three basal oriented dislocation structures depending on the stresses available to perform work by gliding the basal $\langle a \rangle$ dislocation. Even at zero stress, the pyramidal II $\langle c + a \rangle$ edge dislocations can transform into either the basal-dissociated $\langle c + a \rangle$ dislocation, as depicted in the last frame of Fig. 1.6(a) or the basal dissociated $\langle c \rangle$ and $\langle a \rangle$ as demonstrated in the last frame of Fig. 1.6(b). The PB transition is driven by the energy difference of about $0.3\text{ eV}/\text{\AA}$ between the high-energy pyramidal II and the low-energy basal-dissociated $\langle c + a \rangle$ dislocation structures (see Eq. 1.8). Furthermore, the energy barrier of 0.5 eV associated with the thermally activated PB transition leads to a rapid rate at room temperature.

The transformed basal-oriented dislocations which are capable of accommodating $\langle c \rangle$ axis plastic strain contain non-glide basal stacking faults, i.e., either basal I_1 or extrinsic stacking fault, and therefore, are essentially sessile dislocations. At room temperature, the pyramidal II $\langle c + a \rangle$ edge dislocation glide at around 10 MPa , whereas the basal-oriented $\langle c + a \rangle$ dislocations require about 330 MPa for the glide. The transformed basal-dissociated sessile

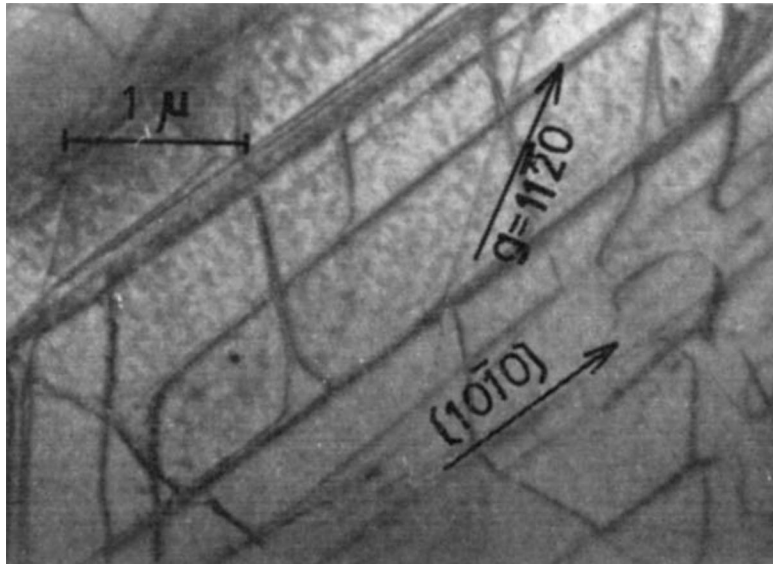


Figure 1.7 – **TEM observation of the basal-oriented $\langle c + a \rangle$ dislocations.** The $\langle c + a \rangle$ dislocations are lying along the directions $\langle 10\bar{1}1 \rangle$ which are the intersection of the basal and the pyramidal II planes. Reprinted from Obara et al. [151].

$\langle c + a \rangle$ dislocations are observed experimentally as straight lines lying along the intersection of the pyramidal II and the basal plane, i.e., $[10\bar{1}0]$ crystallographic direction, as shown in Fig. 1.7.

Because of the deleterious PB transition, the edge part of a pyramidal II $\langle c + a \rangle$ loop prevents the expansion of the loop and undesirably hardens the pyramidal $\langle c + a \rangle$ slip system. This further exacerbates the plastic anisotropy of pure Mg already existing due to the underlying low symmetry hcp crystal structure. Experimentally, the critical resolved shear stress (CRSS) of the pyramidal $\langle c + a \rangle$ are found to be two orders of magnitude higher than that of basal $\langle a \rangle$ slip [206]. Mg, therefore, deforms predominantly by the basal $\langle a \rangle$ dislocations and tension twinning at room temperature that results in the development of strong characteristic basal texture in polycrystal wrought Mg at room temperature [5, 182, 219]. In rolled Mg sheets, the $\langle c \rangle$ -axis of grains align along the normal direction and in extruded Mg products, the $\langle c \rangle$ -axes aligns along the radial direction. These characteristic strong basal textures are the macroscopic manifestations of lack of the pyramidal $\langle c + a \rangle$ slip, and indicative of poor ductility.

1.6 Enhanced ductility in wrought Mg alloys containing rare earth solute elements

Due to the various promising properties of Mg-based alloys, empirically-based metallurgical strategies [9, 32, 117, 154, 157, 241] have been actively pursued with an aim to increase the ductility of Mg alloys. Fig. 1.9 shows the experimentally observed ductility, identified by the failure strain in tensile tests, for a range of Mg alloys. The trend of increase in ductility with

1.6. Enhanced ductility in wrought Mg alloys containing rare earth solute elements

the reduction in grain size is apparent across all Mg alloys. However, even at relatively large grain sizes, rare-earth elements (RE = Y, Ce, Nd, Gd, Er, Ho, Tb, Dy), in particular, stands out as excellent solute elements to improve ductility in Mg alloys [5, 95, 167, 179, 181, 182]. Sandlöbes et al. [181, 182] conduct extensive experiments on Mg-RE alloys and show that even a small amount (3wt.%) of RE elements leads to a substantial increase in ductility of resulting solid solution alloys. Furthermore, this increase in ductility is shown to be accompanied by a low hardening rate and enhanced activity of the $\langle c + a \rangle$ dislocations on both pyramidal I and pyramidal II planes [179, 181]. The pyramidal $\langle c + a \rangle$ slip systems are important and much needed to enable homogeneous plastic deformation and avoid harmful strain localization. The understanding of the activation of the pyramidal $\langle c + a \rangle$ dislocations in Mg-RE alloys is thus crucial in searching for new and cost-effective alloying elements and optimizing the mechanical properties of Mg alloys.

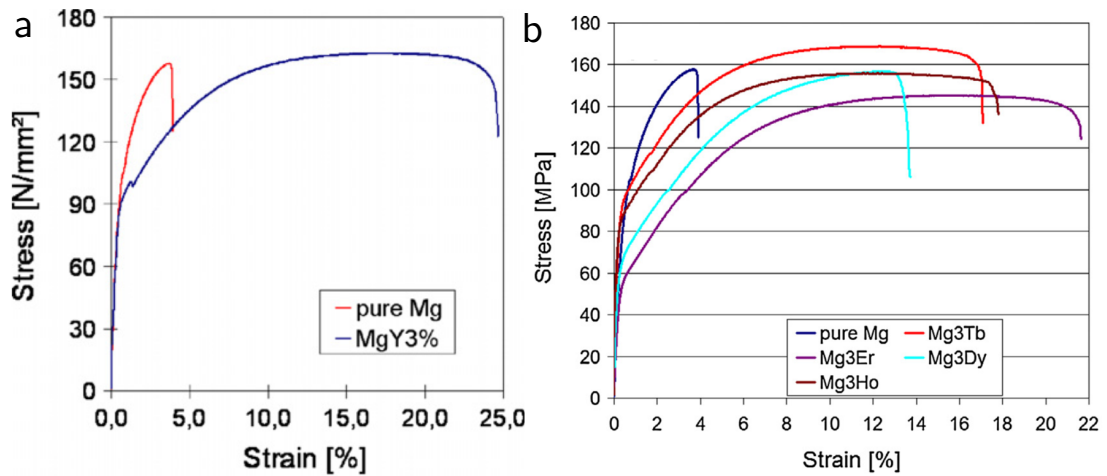


Figure 1.8 – **Plots of stress versus strain obtained from the tensile tests up to failure at room temperature for pure Mg and Mg-RE solid solution alloys.** Fig.(a) shows the result for Mg-3wt.%Y and Fig.(b) shows results for Mg-3wt.%Er, Mg-3wt.%Ho, Mg-3wt.%Tb, and Mg-3wt.%Dy. There is clear evidence of a substantial increase in ductility after the addition of 3 wt.% of RE solute elements. Reprinted (a) from Sandlöbes et al. [182] and (b) from Sandlöbes et al. [181].

Apart from RE solutes, other solutes elements including Ca, Mn, Sr, Sn, Li, Zr etc. have also been identified experimentally as favorable for inducing ductility in resulting solid solution Mg alloys [40, 49, 148, 154, 198, 243, 247].

We now discuss several explanations that have been proposed in the literature to explain the enhanced ductility in Mg-RE alloys. Various thermo-mechanical processing route to produce ductile Mg alloys focus on randomizing the texture away from the strong basal textures. While the basal texture may be used as an indicator of ductility, the development of crystallographic textures itself is the result of the interplay between underlying deformation mechanisms. Specifically, activation of the pyramidal $\langle c + a \rangle$ dislocation can explain the emergence of weak

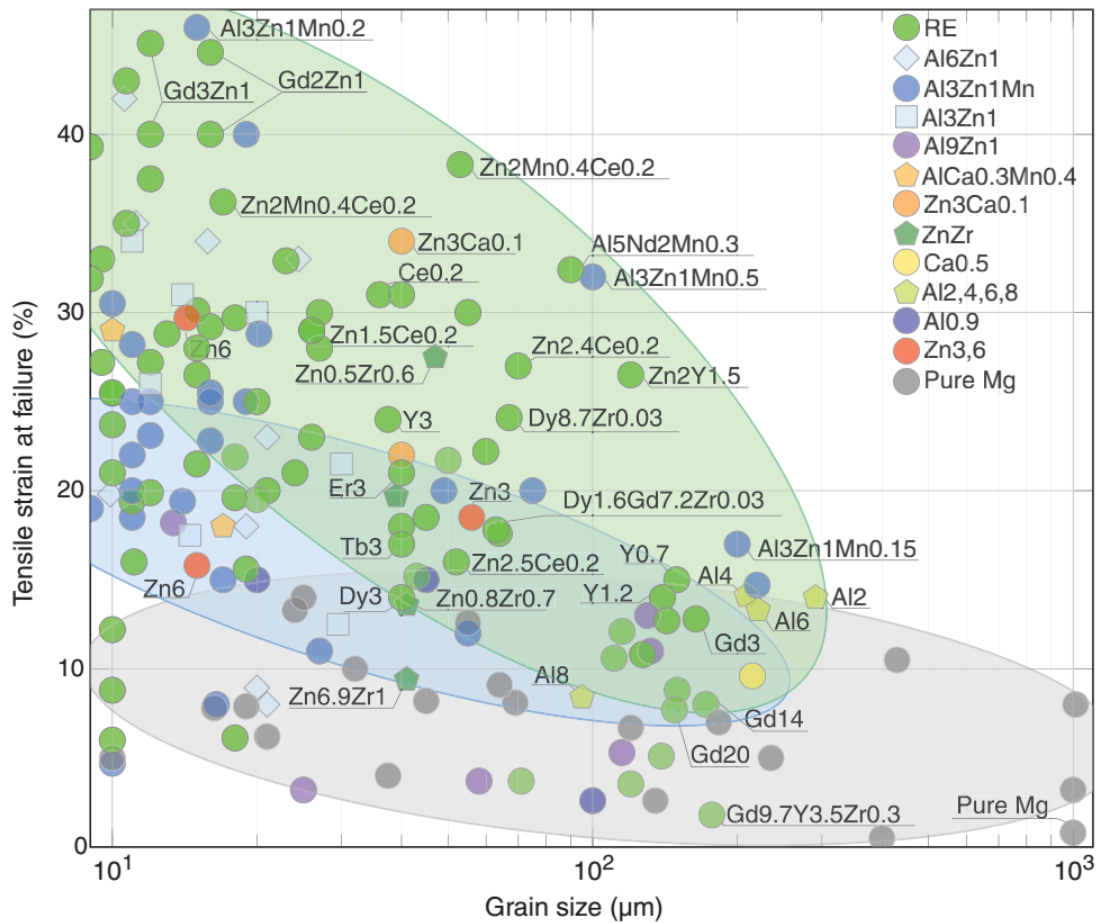


Figure 1.9 – **Variation of experimentally observed ductility in different Mg alloys as a function of grain size.** Pure Mg has low ductility across all grain sizes. Alloys based on Al and Zn show moderate ductility, and Mg-RE alloys show a significant increase in ductility.

basal texture in ductile Mg alloy [6, 219]. Agnew et al. [6] shows that during plane-strain compression, representative of rolling processes, the slip of the pyramidal $\langle c + a \rangle$ dislocations helps rotate the basal pole away from the normal direction towards the rolling direction. Sandlöbes et al. [180, 181] suggest that RE solutes, Y in particular, reduce the basal I_1 stacking fault energy that in turn acts as a heterogeneous source of the pyramidal $\langle c + a \rangle$ dislocations, and then based on this conjecture, propose a Y-like index for other solute elements to determine their potency in inducing ductility [178]. Agnew et al. [2] analyze this mechanism and find that exceedingly high stress is required for the basal I_1 stacking fault to act as a pyramidal $\langle c + a \rangle$ dislocation source, which cannot be met easily in normal conditions. Furthermore, the proposed special role of Y solutes on the basal I_1 stacking faults is not supported by the first principal quantitative comparative studies of the influence of Y (ductilizing), Al (moderately ductile), and Zn (low ductility) solute additions [237]. Yoo et al. [239] suggest that new pyramidal $\langle c + a \rangle$ dislocations can be formed at junctions of the $\langle a \rangle$ and the $\langle c \rangle$ dislocations. However, as already been discussed in the previous Section 1.5, combining the basal-dissociated $\langle c \rangle$ and

$\langle a \rangle$ dislocations to form the pyramidal $\langle c + a \rangle$ dislocation is energetically highly unfavorable. Ando and Tonda [17] suggest that the addition of favorable solutes might suppress the PB transition, and thus promotes the activation of the pyramidal $\langle c + a \rangle$ slips. However, experimental results demonstrate a large number of the basal-dissociated $\langle c + a \rangle$ dislocations present in ductile Mg-RE alloys [179]. Additionally, Agnew et al. [4] proposed a mechanism where solute elements lower the stable pyramidal stacking fault energy and increase the basal stacking fault, thereby decrease the driving force of the PB transition and increase the activation of the pyramidal $\langle c + a \rangle$ dislocation. This mechanism is untested and will be investigated as a part of the research presented in this thesis and presented in Chapter 4.

1.7 Scope and structure of the thesis

As described in the preceding sections, the PB transition of the pyramidal $\langle c + a \rangle$ dislocations has been recognized to lie at the heart of low ductility and high hardening rate in pure Mg. Furthermore, high ductility in certain Mg alloys is observed with a concomitant increase in the activity of the pyramidal $\langle c + a \rangle$ dislocation. A fundamental mechanistic insight into the roles of solute elements in enabling this increased pyramidal $\langle c + a \rangle$ slip would be essential to facilitate designing, optimizing, and manufacturing of new technologically important ductile Mg alloys. Illuminating and uncovering the underlying dislocation mechanisms responsible for causing the ductility in Mg alloys is the central objective of this thesis.

The detrimental PB transition is essentially an atomic scale phenomenon, and thus the ameliorating impacts of the favorable solutes responsible for circumventing the PB transition and activating the pyramidal $\langle c + a \rangle$ dislocations must also exist at the atomic scale. Chapter 2 presents the basics of main computational methods, molecular dynamics simulation, and nudged-elastic-band (NEB), employed in this research to gain insight into the various atomic-scale dislocation mechanisms in pure Mg and Mg alloys.

The availability of a large number of experimental results makes Mg-Y alloys suitable to be used as a representative for ductile Mg alloys in order to unveil the atomic-scale effects of favorable solutes on the pyramidal $\langle c + a \rangle$ dislocation. In atomistic simulations, full information about any material is encoded into the interatomic potential. Chapter 3 discusses the interatomic potentials for pure Mg and Mg-Y alloy used in this work and describes their properties and validity for probing the dislocation mediated plasticity.

Chapter 4 focuses on testing the hypothesis, by conducting finite temperature MD simulations in Mg-3at.%Y alloy, that favorable solute elements might stabilize the pyramidal-dissociated $\langle c + a \rangle$ dislocation, delay the PB transitions by raising the associated energy barrier and thus enable the activation of the $\langle c + a \rangle$ dislocation on the easy-glide pyramidal planes. The simulation results conclusively demonstrate that the energetic drive for the PB transition in solid solution Mg-3at.%Y alloy is essentially unchanged and, hence, some other mechanisms must be operative to enable the enhanced slip of the pyramidal $\langle c + a \rangle$ dislocations.

Chapter 1. Introduction and Background

We, next, propose a new mechanism to explain the ductility of Mg alloys based on solute accelerated cross-slip of the pyramidal $\langle c + a \rangle$ dislocation. To better understand the solute effects on the pyramidal $\langle c + a \rangle$ cross-slip process, Chapter 5 describes the cross-slip processes happening in pure Mg. The energetics and the minimum energy path for the pyramidal $\langle c + a \rangle$ cross-slip processes are computed using the NEB methods, considering both cases: first, the pyramidal II $\langle c + a \rangle$ screw dislocation is energetically more, and the second, the pyramidal I $\langle c + a \rangle$ screw dislocation is more stable. We, however, emphasize that the case of the pyramidal II $\langle c + a \rangle$ screw dislocation being more stable is highly important as in pure Mg, the $\langle c + a \rangle$ screw dislocation predominantly glides on the pyramidal II plane. The pyramidal I favorable case may, nevertheless, arise in certain alloys. In light of the obtained NEB results, a cross-slip model is proposed to compute the activation parameters for the pyramidal $\langle c + a \rangle$ cross-slip process which constitutes one of the key components of the new mechanism.

Chapter 6 expounds in full detail the various elements in the pyramidal $\langle c + a \rangle$ cross-slip based ductility theory and accompanying mathematical model. The ductility mechanism is premised on the ability of the cross-slip and double cross-slip processes to act as a natural source for generating new dislocation loops. Ductility is decided by the competition between the beneficial cross-slip process associated with the screw part and deleterious PB transition associated with the edge/mixed part of the pyramidal $\langle c + a \rangle$ dislocation loop. The dislocation energy difference between the high-energy pyramidal I and the low-energy pyramidal II $\langle c + a \rangle$ screw dislocation renders the cross-slip process ineffective. Particular solute elements, nonetheless, can accelerate the cross-slip process by reducing the dislocation energy difference. This chapter finishes by presenting the experimental observation of increased pyramidal cross-slip process in Mg-Y alloy with increasing concentration of Y solutes.

Chapter 7 presents the prediction of the ductility model for various dilute binary ternary, quaternary Mg alloys comprising mainly a wide spectrum of non-RE solute elements (Al, Zn, Ag, Sn, Ca, Sr, Sn, Zr, K, Mn, Li). The comparison of the ductility prediction by the model in a wide range of Mg alloys are shown to be in remarkable agreement with the available experimental observations. The model predictions are, furthermore, presented in convenient forms to allow the identification of ductile compositions of Mg alloys in a way that could enable the use of other theories and models in order to optimize other properties including ductility, strength, fracture toughness, creep, corrosion, cost, etc.

Chapter 8 recapitulates and discusses the main findings of the research of this thesis, and finally, Chapter 9 discusses the possible ways in which the current research could be extended in the future.

2 Computational Methods

In this chapter, we briefly discuss the computational methods used in conducting the research work presented in this thesis. The multiscale nature of phenomena underpinning materials properties in general, and dislocation mediated plasticity in particular, spans several orders of magnitude in length and time scales, and thus necessitates the development and application of multiple computational tools each focusing on specific scales [38, 59, 76, 201, 211, 222], or coupling several scales in one unified framework [12, 60, 61, 90, 91, 248].

The structure of dislocation cores and chemistry of dislocation-solute interactions are resolved at the electronic level and are accurately computed by employing the density functional theory (DFT) calculations [82, 120, 207]. The mobility and other short-range mechanisms associated with the dislocations are atomic-scale in nature, and so are probed efficiently by using molecular dynamics (MD) or Markov chain Monte Carlo simulations [48, 142, 165, 245]. Furthermore, the kinetics of some thermally activated dislocation processes, such as mobility of screw dislocation in bcc crystals, involve timescale beyond the capability of atomistic simulations. Kinetic Monte Carlo techniques are most suitable to handle these problems [43, 64, 189]. Dislocation dynamics are next in the hierarchy of computational methods that simulate the behavior of an ensemble of dislocation lines evolving under an applied load and provide useful insight into the hardening of single crystals [20, 39, 114]. Crystal plasticity resolves the problem at grain level in a polycrystalline material by considering the evolution of average dislocation populations instead of tracking individual dislocations [92, 109, 174, 175]. Finally, finite element methods reside at the highest level of the hierarchy and deal with the macroscopic plasticity [153].

The choice of a computational tool must be informed by the length and time scale involved in the dislocation mechanisms of interest [59]. Since we know that low ductility of pure Mg arises from the thermally activated PB transition of the pyramidal $\langle c + a \rangle$ dislocations occurring at length and time scale amenable to atomistic simulation, we extensively employ MD, along with its static variant molecular static (MS), simulations in this work. A brief exposition of MD and MS simulation is the subject of Section 2.1

Another important aspect of the crystal plasticity, as discussed in Section 1.4, is the thermally activated dislocation processes occurring at the atomic scale. The PB transition of the pyramidal $\langle c + a \rangle$ dislocations and cross-slip of the screw dislocations, two main dislocation mechanisms of focus in this thesis, are thermally activated. Section 2.2 is devoted to the discussion of the transition state theory which provides a framework to characterize a thermally activated process. This section further provides an introduction to the nudged-elastic-band (NEB) method that is used to determine the energy barrier associated with various thermally activated dislocation processes featuring in this research.

2.1 Elements of molecular dynamics and static simulations

Molecular dynamics (MD) is a simulation method designed to keep track of motion of every atom in a system evolving under prescribed conditions. The core component of the MD simulation is the numerical integration of Newtonian equation of motion. Consider that N atoms are interacting with each other according to an underlying potential energy function $U(\mathbf{r}_1, \mathbf{r}_2, \dots, \mathbf{r}_N)$ that depends on the position of every atom. Further suppose that at time t_n the position and velocity of each atom are $(\mathbf{r}_1^n, \mathbf{r}_2^n, \dots, \mathbf{r}_N^n)$ and $(\mathbf{v}_1^n, \mathbf{v}_2^n, \dots, \mathbf{v}_N^n)$, respectively. MD simulation then enables us to compute the position and velocity of every atom at time $t_{n+1} = t_n + \Delta t$, i.e. after a time step of Δt .

From the knowledge of potential energy function, we first determine the force acting on each atoms at time t_n , which for atom i is given by

$$\mathbf{F}_i^n = - \frac{\partial U(\mathbf{r}_1^n, \mathbf{r}_2^n, \dots, \mathbf{r}_N^n)}{\partial \mathbf{r}_i^n}. \quad (2.1)$$

The acceleration of this atom \mathbf{a}_i at t_n then simply is

$$\mathbf{a}_i^n = \frac{\mathbf{F}_i^n}{m_i}, \quad (2.2)$$

where m_i is the mass of atom with index i . We then obtain the positions and velocity of each atom at time t_{n+1} by using a simple velocity Verlet algorithm as

$$\mathbf{r}_i^{n+1} = \mathbf{r}_i^n + \mathbf{v}_i^n \Delta t + \frac{1}{2} \mathbf{a}_i^n \Delta t^2, \quad (2.3a)$$

$$\mathbf{v}_i^{n+1} = \mathbf{v}_i^n + \left(\frac{\mathbf{a}_i^n + \mathbf{a}_i^{n+1}}{2} \right) \Delta t. \quad (2.3b)$$

It is clear from Eq. 2.3(b), that in order to update the atomic velocities, the information about accelerations at time t_{n+1} is required. To accomplish this we first update the positions according to Eq. 2.3(a), and then compute the updated accelerations by using Eqs. 2.1 and 2.2. The two steps of force computation and update of positions and velocities are iterated for a specified number of time steps. This is the basic machinery of MD simulation, which is

further extended to simulate the canonical and isothermal-isobaric ensembles [201, 210].

Molecular static (MS) simulation, on the other hand, is essentially energy minimization that is employed to find the atomic configurations corresponding to local minima in potential energy surface $U(\mathbf{r}_1, \mathbf{r}_2, \dots, \mathbf{r}_N)$. MS simulations involve one of the widely used minimization algorithms, such as gradient descent, conjugate gradient, and damp dynamics to iteratively update the atomic positions until the force on every atom is less than a predefined cutoff value. MS simulations are extremely useful in obtaining the 0 K properties of the materials and finding the configurations and energetics of dislocations and other crystalline defects. For a more detailed exposition of MD/MS simulations and related statistical mechanical concepts, readers are referred to Refs. [11, 38, 75, 201, 210, 222].

In both MD and MS simulations, the interatomic potential energy function $U(\mathbf{r}_1, \mathbf{r}_2, \dots, \mathbf{r}_N)$ is the most important component. The potential energy function is the representation of the material, and thus the results of simulations are as accurate as the interatomic potential being employed. Although in principle, the potential energy for an atomic configuration can be determined accurately by the first principle methods, such as the DFT, the enormous amount of computational resources required for the DFT calculations makes adopting such paths unfeasible. Therefore, a vast body of research in computational materials science is devoted to designing empirical interatomic potentials that accelerate the force calculation part of MD/MS simulations. These empirical interatomic potentials are functions that map a configuration of atomic positions to the corresponding energy. The commonly used interatomic potentials generally involve several free parameters which are fitted to describe the specific properties of materials under investigation [73, 201]. The embedded-atom method (EAM) and modified embedded-atom method (MEAM) are two widely used frameworks of interatomic potentials to describe metals in MD/MS simulations [28, 62, 63, 137]. We present the details and properties of the interatomic potentials used in this work in the next Chapter 3.

All the MD/MS simulations in this research work are conducted by using an open-source massively parallel MD code LAMMPS [159]; the visualization and post-processing of the results of the atomistic simulations are performed in OVITO [196].

2.2 Transition state theory and the Nudged Elastic Band method

It is often more useful to represent a system comprising N atoms as a point in a $3N$ -dimensional ‘configurational space’ instead of N points in the three-dimensional coordinate space. A point in the configurational space is represented by \mathbf{R} that contains the $3N$ coordinates of the atoms, i.e. $\mathbf{R} = (\mathbf{r}_1, \mathbf{r}_2, \dots, \mathbf{r}_N)$. Thus each axis in the configurational space specifies one Cartesian coordinate of a particular atom.

The potential energy surface $U(\mathbf{R})$ for any real system comprising N atoms is a non-convex hypersurface in the configurational space that contains an exponentially large number of local minima. The potential energy surface can be visualized as a landscape consisting of a

large number of valleys separated by ridges. The states in the valleys represent the different metastable states of the system. At finite temperature, the system remains in one valley for a long time until a random thermal fluctuation provides sufficient energy to cross a ridge-barrier and allows the system to go into the next valley. The path through which the transformation is achieved from initial to final metastable states is called the minimum energy path (MEP). To continue with our landscape analogy, the MEP can be thought of as a mountain pass connecting the two valleys through a saddle point in between. The state associated with the saddle point is called the transition state which has the maximum potential energy on the MEP. The energy barrier or activation energy of the transformation, that controls the transformation rate, is then the energy difference between the initial metastable state and the transition state. Such transformations are called thermally activated transformations/transitions/processes owing to the critical role of the random thermal fluctuations in assisting the transformations [71, 208].

The presence of a relatively large energy barrier prevents the investigation of such thermally activated processes by using plain MD simulations. A thermally activated process with an energy barrier of 0.5 eV would take on average about 50 micro-seconds to take place even once. To gather enough statistics of the transition, at least a hundred times longer simulations are required. Due to the requirement of resolving atomic vibrations, a typical MD simulation would need to perform 10^{11} time-steps to achieve the time-scale of the transition which is beyond the capability of existing computational resources. However, this difference of time-scale between atomic vibration and the thermally activated transition allows one to estimate the transition rate by utilizing the statistical theories [71, 215, 223].

2.2.1 Transition state theory

Transition state theory [71, 215] uses equilibrium statistical mechanics to determine the rate of a thermally activated process occurring between two metastable states in a $3N$ -dimensional configuration space. Fig. 2.1 schematically shows the two such metastable states A and B for a two-dimensional surface. In configurational space, the two metastable states are identified by vectors \mathbf{R}_A and \mathbf{R}_B . The potential energy surface is partitioned into two regions corresponding to the two metastable states with a surface S_D dividing the two regions. The two regions are labeled as region A and region B. The dividing surface S_D passes through the transition state P and is perpendicular to the contour of the potential energy. We consider that the system starts in the region A and transitions into the region B with the help of thermal fluctuations. The transition state theory involves the following assumptions: the system is in thermal equilibrium at temperature T , and spends all the time in either region A or region B with the occasional jump between the two; there is a clear separation between the time scales of the atomic vibration and that of the transition between the two states, i.e. the transition time is much longer than the time period of atomic vibration to enable the equilibration of the system after each transition; a trajectory starting in the region A cannot return in the same region after passing through the dividing surface with velocity directed in the direction of region B.

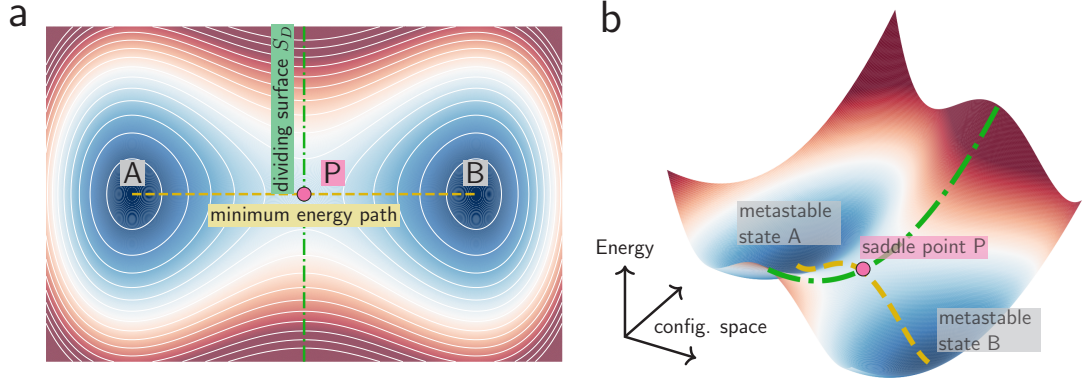


Figure 2.1 – **An illustration of a thermally activated processes between two metastable states.** States A and B are the two metastable states, and P is the transition state situated at the saddle point of the potential energy surface. (a) The contour plot of a two-dimensional potential energy surface demonstrates the metastable states and transition state. The yellow dashed line shows the minimum energy path connecting the two metastable states, and the green dash-dotted line is the surface S_D dividing the potential energy surface into two regions corresponding to the states A and B. (b) A three-dimensional representation of the potential energy surface.

By considering the canonical (NVT) distribution of microstates, Vineyard [215] worked out the following exact expression for the frequency of transition $\nu_{A \rightarrow B}^{\text{TST}}$ from state A to state B happening at temperature T under the transition state theory

$$\nu_{A \rightarrow B}^{\text{TST}} = \sqrt{\frac{kT}{2\pi m}} \frac{\int_{S_D} \exp\left(-\frac{U(\mathbf{R})}{kT}\right) d\mathbf{R}}{\int_A \exp\left(-\frac{U(\mathbf{R})}{kT}\right) d\mathbf{R}}, \quad (2.4)$$

where k is the Boltzmann constant; m is the atomic mass; the numerator of the second term in the right side is obtained by integrating over the dividing surface S_D , and the denominator is obtained by performing integration over the region A. The above expression Eq. 2.4, however, cannot be computed easily for any complex potential energy surface as it requires the information about the shape of the surface. To obtain a tractable expression for the transition rate, Vineyard [215] assumed that the harmonic terms of the potential energy surface near the minimum A and the saddle point P represent the dominant contribution to the two integrals of Eq. 2.4. This harmonic assumption is equivalent to assuming materials properties independent of temperatures which originate from the anharmonic structure of the potential energy surface and considers entropic barrier resulting from harmonic vibrations. The harmonic transition state theory leads to the following simplified expression for the transition frequency

$$\nu_{A \rightarrow B}^{\text{HTST}} = \frac{\prod_{i=1}^{3N} \nu_i^A}{\prod_{i=1}^{3N-1} \nu_i^P} \exp\left(-\frac{\Delta E}{kT}\right), \quad (2.5)$$

where ν_i^A and ν_i^P , respectively, are the normal frequency modes arising from the harmonic

form of the potential surface near initial state A and transition state P, and $\Delta E = U(\mathbf{R}_P) - U(\mathbf{R}_A)$ is the energy barrier associated with the transition and is simply the energy difference between initial and transition states.

Under the harmonic transition state theory, we need the energy barrier ΔE (to be discussed in the next section) and the frequencies of the normal modes near state A and P to determine the transition frequency. To further simplify the expression, the prefactor in Eq. 2.5 is taken to be the Debey frequency $\nu_0 = 10^{13} \text{ s}^{-1}$ for thermally activated transitions happening in crystalline materials [169, 214, 228]. Finally, the transition reduces to the simple Arrhenius form

$$\nu_{A \rightarrow B} = \nu_0 \exp\left(-\frac{\Delta E}{kT}\right). \quad (2.6)$$

The Arrhenius form of Eq. 2.6 has been successfully applied to investigate several thermally activated dislocation mechanisms [69, 70, 99, 169, 221, 228, 249]. The applicability of the Arrhenius expression in dislocation mechanisms is justified by the negligible contribution of entropy in the free energy of a dislocation [55]. In this work we use the Eq. 2.6 to determine the rate of various thermally activated processes associated with dislocations. Some dislocation mechanisms, such as dislocation nucleation, involve significant changes in the atomic arrangements and entropic barrier stemming from the anharmonic effects can no longer be neglected [149, 176, 177, 220].

For more elaborate and detailed discussions on the transition state theory with a focus on thermally activated dislocation mechanisms, the readers are referred to Refs. [108, 162, 185, 186].

2.2.2 Nudged elastic band method

The energy barrier ΔE of a thermally activated process is an important quantity to determine the transition rate, Eqs. 2.5 and 2.6, which requires the information about the initial and associated transition state. We often have access to the initial and the final metastable states involved in the transition and want to find the MEP connecting the two. The MEP then allows us to identify the transition state and, consequently, the energy barrier associated with the transition. Nudged elastic band (NEB) [100], and string methods [68, 212] are two computational techniques widely used in computing the MEP from the knowledge of the initial and the final states. In this work, we use the NEB method for computing the MEP of dislocation processes and is briefly presented bellow following Jónsson et al. [100].

The NEB method provides a discrete representation of the MEP with the help of intermediate replicas (images) connecting the initial and the final metastable states. We consider that the MEP is discretized by using $M + 2$ replicas denoted by positions $\mathbf{R}_0, \mathbf{R}_1, \mathbf{R}_2, \dots, \mathbf{R}_{M+1}$ in the configurational space. In the string of $M + 2$ replicas, first $\mathbf{R}_0 = \mathbf{R}_A$ corresponds to the initial metastable state A and final $\mathbf{R}_{M+1} = \mathbf{R}_B$ corresponds the final metastable state B. The

2.2. Transition state theory and the Nudged Elastic Band method

remaining M intermediate states $\mathbf{R}_1, \mathbf{R}_2, \mathbf{R}_3, \dots, \mathbf{R}_M$ are initialized by using some interpolation scheme. The intermediate replicas are connected to immediate neighbors by a spring of natural length zero. The end replicas are kept fixed and intermediate replicas are allowed to evolve towards the MEP under a combined force arising from the underlying potential energy and connecting springs. The force due to potential energy tries to attract the replica towards the nearest metastable state, and the spring force seeks to maintain equal separation between the replicas. A naive way would be to consider the force on i th ($1 \leq i \leq M$) intermediate replica as

$$\mathbf{F}_i = -\nabla U(\mathbf{R}_i) + \mathbf{F}_i^S \quad \text{for } 1 \leq i \leq M, \quad (2.7)$$

where the first term on the right side represents force due to the potential energy, and the second term $\mathbf{F}_i^S = k^S(\mathbf{R}_{i+1} - 2\mathbf{R}_i + \mathbf{R}_{i-1})$ is force due to the spring having the force constant k^S .

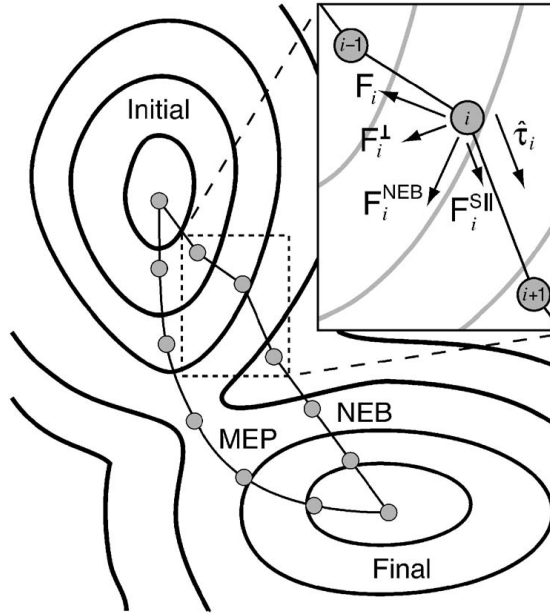


Figure 2.2 – A schematic illustration of different forces involved in NEB calculation for a two dimensional potential energy surface. The total NEB force on i^{th} image $\mathbf{F}_i^{\text{NEB}}$ is composed of perpendicular to tangent $\hat{\mathbf{t}}_i$ component of potential force \mathbf{F}_i^{\perp} and parallel to tangent component of spring force $\mathbf{F}_i^{\text{S}\parallel}$. Under the influence of the NEB force $\mathbf{F}_i^{\text{NEB}}$, the images converge to the MEP of the transition. From Ref. [187].

The naive method of determining the force acting on intermediate replicas leads to undesirable effects on replicas distribution. If the spring constant k^S is too high, the replicas cut the corner and avoid going through the saddle point. However, a small value of spring constant results in a lower resolution of replicas near the saddle point. The NEB method alleviates this shortcoming by keeping a specific projection of the two forces either along or perpendicular to the path

tangent $\hat{\mathbf{t}}_i$ at replica i . The local tangent at replica i can be computed as

$$\hat{\mathbf{t}}_i = \frac{\mathbf{R}_{i+1} - \mathbf{R}_{i-1}}{|\mathbf{R}_{i+1} - \mathbf{R}_{i-1}|} \quad \text{for } 1 \leq i \leq M. \quad (2.8)$$

The form of local tangent influences the convergence of the calculation, and many other improved estimations of the tangent direction have been proposed in the literature [87]. The modified force on the replica i is next computed by retaining the perpendicular component of the force due to the potential and the parallel component of the spring force, i.e.

$$\mathbf{F}_i^{\text{NEB}} = \mathbf{F}_i^\perp + \mathbf{F}_i^{\text{S||}} \quad \text{for } 1 \leq i \leq M, \quad (2.9)$$

where $\mathbf{F}_i^\perp = -\nabla U(\mathbf{R}_i) + (\nabla U(\mathbf{R}_i) \cdot \hat{\mathbf{t}}_i) \hat{\mathbf{t}}_i$ is the component of the potential force perpendicular to the path tangent, and $\mathbf{F}_i^{\text{S||}} = (\mathbf{F}_i^{\text{S}} \cdot \hat{\mathbf{t}}_i) \hat{\mathbf{t}}_i$ is the component of the spring force parallel to the local path tangent on i^{th} image. Finally, a force based minimization algorithm is used to determine the converged replicas representing the MEP of the transition. Fig. 2.2 shows a schematic of the of the various forces involved in the NEB calculations.

We have described only the basic and essential concepts involved in the NEB method above. Several improvements and extensions of the method have been proposed, and we refer to Refs [87, 87, 88, 128, 146, 187] for a comprehensive exposition of the NEB method used in practice. In this work, we use the NEB method as implemented in the MD code LAMMPS.

Numerous thermally activated dislocation mechanisms have been investigated and characterized by using the NEB method. For instance, to report a few, Vegge et al. [214] and Esteban-Manzanares et al. [70] studied the cross-slip processes of screw dislocations; Zhu et al. [249] investigated the mechanism of the surface dislocation nucleation; Rodney [169] characterized the activation parameters of the kink-pair mechanism of the dislocation glide; and Esteban-Manzanares et al. [69] probed the interaction of dislocation with GP zone in Al-Cu alloys. Furthermore, comparative studies of the accuracy and applicability of several transition state methods in application to the dislocation mechanisms can be found in Refs. [183, 184].

3 Interatomic potentials employed in the atomistic simulations

This chapter is in part extracted from the following publications

1. Ahmad R., Groh S., Ghazisaeidi M., and Curtin W. A. (2018). Modified embedded-atom method interatomic potential for Mg-Y alloys. *Modelling Simul. Mater. Sci. Eng.*, 26: 065010.
2. Ahmad R., Wu Z. and Curtin W. A. (2020). Analysis of double cross-slip of pyramidal I $\langle \mathbf{c} + \mathbf{a} \rangle$ screw dislocations and implications for ductility in Mg alloys. *Acta Mater.*, 183: 228-441.

Interatomic potentials are the only description of the materials accessed by an atomistic simulation. Thus a reasonably accurate interatomic potential is essential for understanding, investigating, characterizing, and uncovering various atomistic mechanisms and phenomena associated with the material under consideration. This chapter presents the interatomic potentials to study Mg and Mg-Y alloys, and their predictions related to properties important for plastic behavior.

Numerous efforts to understand various atomic-level mechanisms underlying mechanical properties have spawned several interatomic potentials for both Mg and Mg-RE alloys. For example, Liu et al. [122] Sun et al. [199] and Pei et al. [156] developed pure Mg interatomic potential in the EAM framework. However, these EAM potentials fall short of describing the generalized stacking fault energy, dislocation core structure, Peierls barrier, twinning dislocation, and basal surface energy [81, 188, 231, 235]. The EAM potential developed by Pei et al. [156] predicts the fcc phase of Mg to be more stable than the hcp phase. Kim et al. [105] proposed a new pure Mg interatomic potential in the framework of MEAM that is capable of producing reasonable core structures of various dislocations but fails in the investigation of fracture properties. Wu et al. [231] presented a new and improved MEAM interatomic potential for the study of plasticity and fracture properties of pure Mg. This work extensively employs the MEAM potential of Wu et al. [231] in conducting the atomistic simulations in

pure Mg.

Similarly, many interatomic potentials have been proposed for various Mg alloys [102, 103, 105, 156] in the MEAM framework. However, all of these potentials are largely untested for plastic properties. Since we focus on the Mg-Y as a model for the Mg-RE alloy system to gain insight into the influence of RE solute elements on the various dislocation mechanisms, we focus on the recent Mg-Y potential developed by Kim et al. [102], hereafter referred to as Kim potential. The misfit volume of Y solute in Mg is predicted to be much smaller than experiments and DFT. The Kim potential is also unable to capture the interaction of Y solute with various stacking faults. All these properties are crucial in dictating the dislocation behavior in Mg-Y alloys. The limitations of Kim potential justify the development of a new and well-validated interatomic potential to investigate the plastic properties of Mg-Y alloys, and is presented in Section 3.2.

All the atomistic simulations performed in this work use the MEAM framework to describe the interactions between atoms in both pure Mg and Mg-Y solid solutions alloys. Therefore, a brief description of the MEAM formalism for pure element and binary alloy system has been provided in Appendix A. We here present different parameters of MEAM potentials for pure Mg and Mg-Y alloys along with their selected predictions.

3.1 Two pure Mg MEAM interatomic potentials: MEAM_I and MEAM_II

1

A full description of a pure element in the MEAM framework requires 16 parameters (see Appendix A for detail). Four parameters (cohesive energy E_c , equilibrium nearest-neighbor distance r_e , bulk modulus B , and an adjustable parameter d to fit $\partial B/\partial P$) are obtained from the universal equation of state [172]. Seven parameters (decay lengths $\beta^{(0)}, \beta^{(1)}, \beta^{(2)}, \beta^{(3)}$, and weight factors $(t^{(1)}, t^{(2)}, t^{(3)})$) describe the electron density for embedding. One parameter A is used in the embedding function, and two parameters (C_{\min}, C_{\max}) account for many-body screening effects. Cutoff radius, r_c and smoothing radius Δr control the extent and decay of the potential near cutoff radius, respectively.

Table 3.1 – Parameters for the MEAM_I and the MEAM_II potentials for pure Mg used in this work. The units of E_c , r_e , r_c and Δr are eV, Å, Å and Å, respectively.

	E_c	r_e	α	A	$\beta^{(0)}$	$\beta^{(1)}$	$\beta^{(2)}$	$\beta^{(3)}$	$t^{(1)}$	$t^{(2)}$	$t^{(3)}$	C_{\min}	C_{\max}	d	r_c	Δr
MEAM_I	1.51	3.18	5.59	0.52	2.00	1.30	1.30	1.00	5.55	3.00	-7.40	0.49	2.80	0.00	5.88	1.88
MEAM_II	1.52	3.18	5.61	0.79	2.35	1.46	2.30	1.15	6.82	1.50	-7.09	0.36	2.38	0.00	7.89	6.60

In this work, we use two different MEAM potentials to describe the interatomic interaction in pure Mg. The first one is that presented in Wu et al. [231], and we refer to it by MEAM_I potential hereafter. This MEAM_I potential has been well validated and shown to predict

¹The MEAM_II potential is developed in collaboration with Prof Zhaoxuan Wu from City University Hongkong, China.

the pure Mg properties pertaining to plasticity and fracture in good agreement with the DFT calculations. In particular, the MEAM_I potential predictions of the lattice and elastic constants, generalized stacking fault energies on different planes, core structure, and Peierls stress of various dislocations in Mg are in excellent accord with the DFT computations. The second MEAM potential used in this work for pure Mg is obtained by reparameterization of the MEAM_I potential. We refer to this new Mg potential as MEAM_II potential hereafter in this thesis. The parameters for both the MEAM_I and MEAM_II potentials are listed in Table 3.1.

Different properties of pure Mg, as predicted by both the MEAM_I and the MEAM_II potentials, are shown in Table 3.2, and compared with the corresponding DFT values. The values of the lattice and elastic constants as predicted by the two potentials are very close to each other and consistent with the first principle values. Both potentials predict similar stable basal I_2 stacking fault energy which are smaller than the DFT value.

The two potential, however, differ with each other in the prediction of the pyramidal I and the pyramidal II stable stacking faults, and also in the prediction of the relative stability of the two pyramidal $\langle c + a \rangle$ screw dislocations. Since the two pyramidal $\langle c + a \rangle$ screw dislocations have the same Burgers and the line direction, the dislocation energy difference will arise, as discussed in Section 1.3, due to the different dislocation core structures, and would be constant per unit dislocation length. The MEAM_I potential yields the pyramidal II $\langle c + a \rangle$ screw dislocation to be more stable than the pyramidal I $\langle c + a \rangle$ screw dislocation, with energy difference $E_{\text{Mg}}^{\text{I-II}} = 27\text{meV/nm}$; and the MEAM_II potential predicts the $\langle c + a \rangle$ screw dislocation to be more stable on pyramidal I than on pyramidal II plane, with energy difference $E_{\text{Mg}}^{\text{I-II}} = -28\text{meV/nm}$. The core structures of the pyramidal I and the pyramidal II $\langle c + a \rangle$ screw dislocations, obtained from the two potentials, are shown in Fig. 3.1(a) which agree quite well with each other and with those obtained from the DFT [81, 231].

We will be using the MEAM_I potential extensively in this work to investigate the properties of the pyramidal $\langle c + a \rangle$ screw dislocation, as numerous experimental observations point towards the $\langle c + a \rangle$ screw dislocation being more stable on the pyramidal II plane than on the pyramidal I plane [17, 155, 200]. On the other hand, the MEAM_II potential will be employed specifically in Chapter 5 in order to understand and elucidate the cross-slip process of the pyramidal $\langle c + a \rangle$ screw dislocation in the case where the pyramidal I $\langle c + a \rangle$ screw dislocation is more stable than the pyramidal II $\langle c + a \rangle$ screw dislocation. This reversal of relatively dislocation stability is particularly relevant for various Mg alloys.

3.2 Mg-Y MEAM interatomic potential²

In this section, we present a new MEAM interatomic potential for Mg-Y alloys. Description of a binary alloy within the MEAM formalism first requires interatomic potentials of the constituent elements. For pure Mg, we use the MEAM_I potential presented in the previous

²The Mg-Y potential is developed in collaboration with Dr Sébastien Groh from University of Basel, Switzerland.

Chapter 3. Interatomic potentials employed in the atomistic simulations

Table 3.2 – Properties of the MEAM_I and the MEAM_II interatomic potentials for pure Mg including lattice constants (a and c/a), cohesive energy (E_c), elastic constants ($C_{11}, C_{12}, C_{13}, C_{33}, C_{44}$), various stable stacking fault energies(SFE) and dislocation energy difference between the pyramidal I and the pyramidal II dissociated $\langle c + a \rangle$ screw dislocations ($\Delta E_{\text{Mg}}^{\text{I-II}}$). The potential predictions are compared with the corresponding DFT results from Ref. [236]

Properties	MEAM_I	MEAM_II	DFT[236]
a (Å)	3.187	3.187	3.189
c/a	1.623	1.622	1.627
E_c (eV/atom)	-1.51	-1.51	-1.51
C_{11} (GPa)	64.3	65.4	61
C_{12} (GPa)	25.5	24.8	26
C_{13} (GPa)	20.3	21.9	20
C_{33} (GPa)	70.9	69.4	63
C_{44} (GPa)	18.0	19.5	18
SFE (basal I_2) (mJ m ⁻²)	23	21	34
SFE (pyramidal I) (mJ m ⁻²)	169	161	161
SFE (pyramidal II) (mJ m ⁻²)	200	188	165
$\Delta E_{\text{Mg}}^{\text{I-II}}$ (meV/nm)	27	-28	—

section. An MEAM potential for pure Y was developed by Ko and Lee [106] and describes structural and mechanical properties in good agreement with experimental data. We retain all the parameters of Y potential with the exception of the decay parameters $\beta^{(1)}$ and $\beta^{(3)}$ which are adjusted to better describe the interaction energies of Y solutes with the various stacking faults of Mg.

Table 3.3 – Parameters for the MEAM potentials to describe pure Y used in this work. The units of E_c , r_e , r_c and Δr are eV, Å, Å and Å, respectively.

	E_c	r_e	α	A	$\beta^{(0)}$	$\beta^{(1)}$	$\beta^{(2)}$	$\beta^{(3)}$	$t^{(1)}$	$t^{(2)}$	$t^{(3)}$	C_{\min}	C_{\max}	d	r_c	Δr
Y	4.37	3.607	4.37	0.90	2.00	5.00	1.00	1.00	8.00	8.00	-8.50	0.36	2.80	0.00	5.88	1.88

To describe the interaction between the two elements of binary alloys, 13 additional parameters are needed. Four parameters (E_c , r_e , B , d) are related to the universal equation of state for a reference intermetallic compound. Eight parameters related to screening (C) and one parameter related to the electron density scaling parameter ($\rho_0^{\text{Mg}}; \rho_0^{\text{Y}}$) are introduced. Potential parameters are fitted using structural and elastic properties of reference B2-MgY structure, the heat of formation of B2-MgY, and the position-dependent single-solute interaction energies with the stable stacking faults on the basal (I_2), the pyramidal II, and the pyramidal I (SF2) planes. The fitted parameters for the binary Mg-Y system are shown in Table 3.4. We use radial cutoff distance r_c of 5.875 Å and smoothing radius Δr of 1.875 Å. In the following sections, we analyze the properties of the potential against available experimental and DFT data.

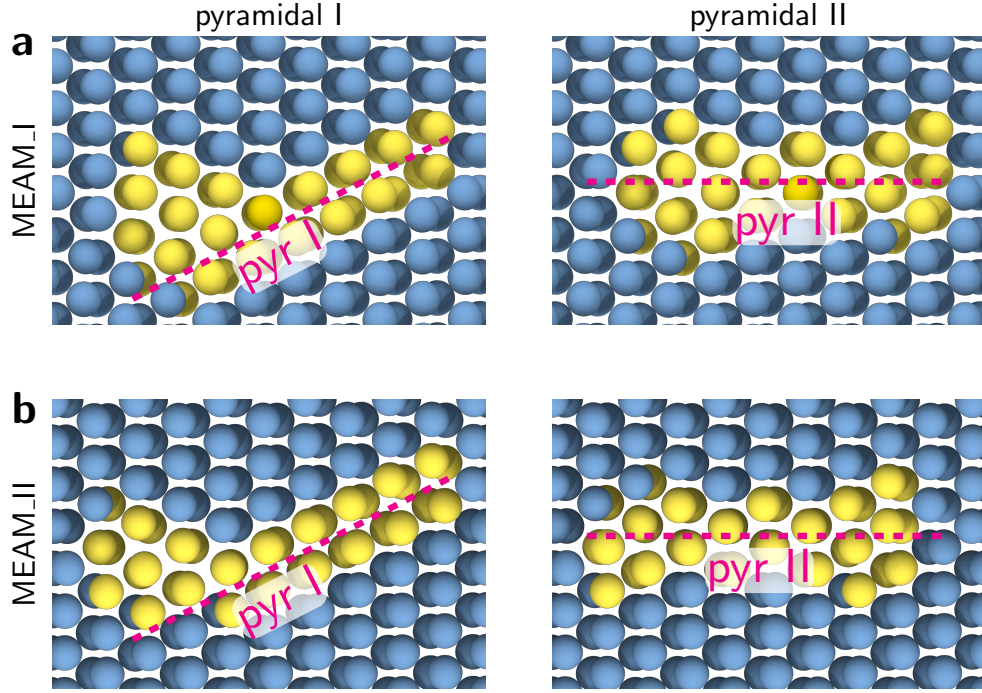


Figure 3.1 – Atomic structures of the pyramidal I and the pyramidal II $\langle c + a \rangle$ screw dislocation cores in pure Mg, as obtained from (a) the MEAM_I and (b) the MEAM_II interatomic potentials. The MEAM_I predicts that the pyramidal II $\langle c + a \rangle$ screw dislocation is more stable, whereas the MEAM_II predicts the $\langle c + a \rangle$ screw dislocation is more stable on the pyramidal I plane. Atoms are colored according to their local crystal structures as identified by the common neighbor analysis: blue, hcp; yellow, other.

Table 3.4 – The MEAM potential parameters developed for the binary Mg-Y alloy system. The units of E_c , r_e and are eV and Å, respectively.

Parameters	Values	Parameters	Values
Reference	B2-type Mg-Y	$C_{\min}(\text{Mg}, \text{Y}, \text{Mg})$	0.60
E_c	3.075	$C_{\min}(\text{Y}, \text{Mg}, \text{Y})$	0.36
r_e	3.2575	$C_{\min}(\text{Mg}, \text{Mg}, \text{Y})$	0.00
α	4.46	$C_{\min}(\text{Mg}, \text{Y}, \text{Y})$	1.20
d	0.00	$C_{\max}(\text{Mg}, \text{Y}, \text{Mg})$	2.80
$\rho_0^{\text{Mg}}: \rho_0^{\text{Y}}$	1:1.4	$C_{\max}(\text{Y}, \text{Mg}, \text{Y})$	2.80
		$C_{\max}(\text{Mg}, \text{Mg}, \text{Y})$	1.63
		$C_{\max}(\text{Mg}, \text{Y}, \text{Y})$	2.80

3.2.1 Misfit strain and misfit volume

The first important property of a solute related to the mechanical properties of alloys is the solute misfit strain tensor and the associated solute misfit volume. Following Refs. [22, 54, 213], misfit strains are calculated using the dipole tensor. In simulations, one Mg atom in the perfect hcp lattice is replaced by one Y atom, and all atomic positions are then relaxed keeping the

periodic cell vectors fixed using periodic boundary conditions. The relaxation leads to the development of stress σ_{ij} in the simulation box containing a solute. The dipole tensor P_{ij} of the solute is related to stress σ_{ij} and total volume of the simulation box V as

$$P_{ij} = -V\sigma_{ij}. \quad (3.1)$$

The misfit strain of the solute $\epsilon_{ij}^{\text{misfit}}$ is then computed from dipole tensor P_{ij} using anisotropic elasticity as

$$\epsilon_{ij}^{\text{misfit}} = \frac{1}{V_0} S_{ijkl} P_{kl}, \quad (3.2)$$

where S_{ijkl} is the anisotropic compliance tensor of Mg, and V_0 is the volume of one Mg atom in its hcp bulk. The misfit strains are calculated in the coordinate system where \mathbf{x}_1 is along $[2\bar{1}\bar{1}0]$, \mathbf{x}_2 along $[01\bar{1}0]$, and \mathbf{x}_3 is along $[001]$ direction. The misfit volume of the solute, normalized by the atomic volume of Mg, $\Delta V/V_0$ is the trace of the misfit strain tensor, i.e. $\Delta V/V_0 = \text{tr}(\epsilon^{\text{misfit}})$.

For the current MEAM potential, we obtain the non-zero misfit strain components $\epsilon_{11}^{\text{misfit}} = \epsilon_{22}^{\text{misfit}} = 0.205$ and $\epsilon_{33}^{\text{misfit}} = 0.183$ for Y in Mg. As reported in Table 6.1, the DFT misfit strain components of Y in Mg, in the same coordinate system, are $\epsilon_{11}^{\text{misfit}} = \epsilon_{22}^{\text{misfit}} = 0.223$ and $\epsilon_{33}^{\text{misfit}} = 0.120$. The DFT misfit strain tensor is thus slightly more anisotropic than that of the MEAM. Previous works on Y usually report only the misfit volume. For the current MEAM potential, the misfit volume is $\Delta V/V_0 = 0.593$, in good agreement with the DFT values of 0.567 [237], 0.580 [181], and 0.636 [234]. In contrast, the Kim potential yields a value of only 0.240, less than one-half the DFT value. Since the misfit volume is related to the interaction energy of a dislocation with the solute, it is necessary that the potential predicts this quantity accurately for application to many problems in plasticity.

3.2.2 Solute-stacking fault interaction energy

The interaction of solute atoms with stacking fault constitutes an appreciable part of solute interaction with a dissociated dislocation. The solutes situated between the two partials interact with the intervening stacking fault and influence the energetics of different dislocation mechanisms.

Computational details

To compute solute-stacking fault interaction energies, we adopt the simulation box geometry and methodology used in recent DFT studies of the same problem by Yin et al. [237]. For each slip system, a primitive cell is defined by a set of three vectors ($\mathbf{a}_1, \mathbf{a}_2, \mathbf{a}_3$) as shown in Figure 3.2 with ($\mathbf{a}_1, \mathbf{a}_2$) defining the stacking fault plane and $\mathbf{a}_1, \mathbf{a}_2$ and \mathbf{a}_3 usually not mutually orthogonal. A periodic simulation cell of pure Mg is built by replicating the primitive cell N_i times in the \mathbf{a}_i ($i = 1, 2, 3$) directions to obtain a parallelepiped simulation cell with periodic

repeat vectors ($N_1 \mathbf{a}_1, N_2 \mathbf{a}_2, N_3 \mathbf{a}_3$). The N_i s are chosen large enough such that periodic solute-solute interactions are negligible in order to remain in the limit of dilute concentrations. We use the coordinate system such that the $\mathbf{x}_1 - \mathbf{x}_2$ plane lie in stacking fault plane, and the \mathbf{x}_3 axis is normal to the stacking fault plane.

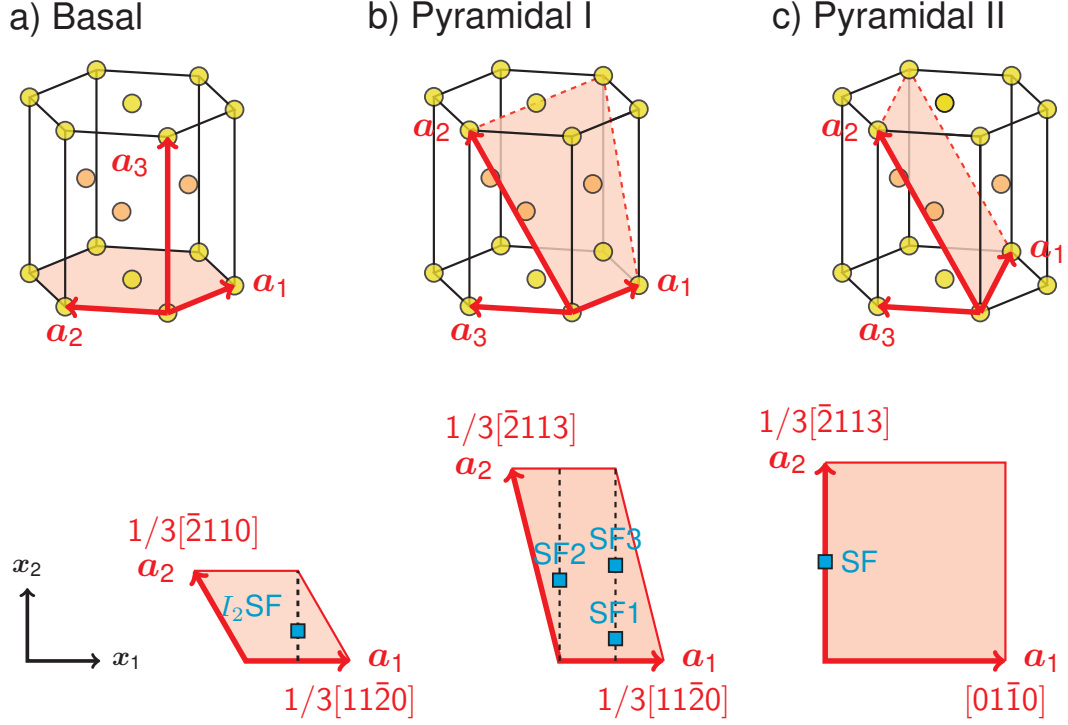


Figure 3.2 – **Positions of different stable stacking faults in the basal, pyramidal I, and pyramidal II planes.** The upper row shows the three lattice vectors \mathbf{a}_1 , \mathbf{a}_2 and \mathbf{a}_3 used to build the simulation boxes. The lower row depicts the coordinate system used in the simulation, (a) basal, (b) pyramidal I, and (c) pyramidal II slip planes along with positions of stable stacking faults contained within.

We consider the intrinsic Basal I_1 fault and the extrinsic E stacking fault, neither of which can be generated by slip processes, and the intrinsic basal I_2 , pyramidal I, and pyramidal II faults that are formed by slip processes. Simulation cells for the basal I_1 and E stacking faults are constructed by arranging close-packed basal planes as $(AB)_{N_3/2}-(AC)_{N_3/2}$ and $(AB)_{N_3/2}-C-(AB)_{(N_3-2)/2}-C$, respectively, where A,B and C are the stacking sequence of close-packed (111) planes in fcc crystals (...ABCABC...). As shown in Figure 3.3a, two such stacking faults are generated in each simulation box because of the periodic boundary condition used. The relaxed structures of these stacking faults are obtained by relaxing the simulation cell only in direction \mathbf{x}_3 normal to the fault plane. The slip stacking faults are generated using the tilted-box method [236] in which the simulation cell vector $N_3 \mathbf{a}_3$ is shifted laterally by the stacking fault vector \mathbf{t} , as depicted in Figure 3.3b. Relaxation of the simulation cell is subject to $\sigma_{i3} = 0$ ($i = 1,2,3$) while holding the $N_1 \mathbf{a}_1$ and $N_2 \mathbf{a}_2$ repeat vectors fixed. The in-plane positions

of the various stable stacking faults are depicted in Figure 3.2. An important advantage of the tilted-box method is that it allows full relaxation of all atoms, in contrast to solely out of stacking fault plane relaxation in the conventional method. The tilted-box method yields only stable stacking faults, if they exist, in the corresponding stacking fault plane.

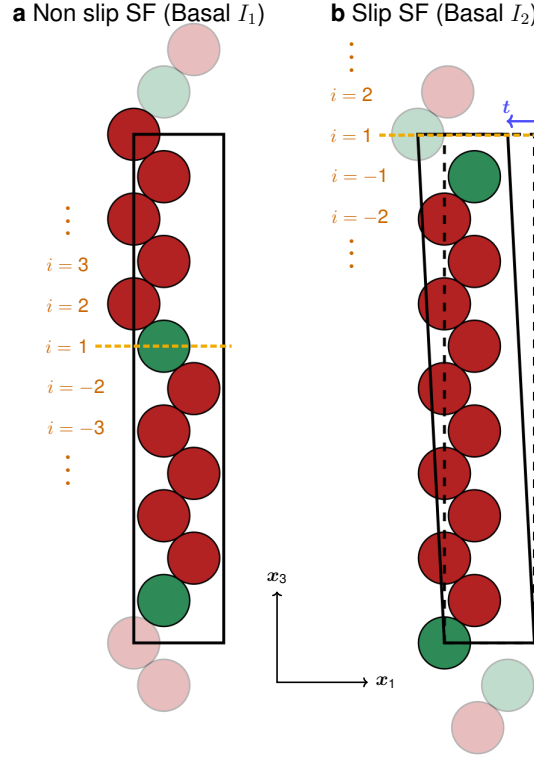


Figure 3.3 – **Schematics of the simulation cells used to compute various stacking fault energies and solute-stacking fault interaction energy.** (a) Basal I_1 stacking fault as a representative non-slip stacking fault. (b) Basal I_2 stacking fault as an example using the tilted box method for creating slip stacking faults. In (b), the solid black lines denote the initial simulation cell of perfect Mg and the dashed lines show the simulation box tilted by the stacking fault vector t , leading to the formation of stacking fault. Index i refers to the solute position with respect to the stacking fault plane. Red and green atoms denote the hcp and fcc atoms, respectively.

To measure the solute-stacking fault interaction energies, we start with the corresponding relaxed stacking fault structure in the pure Mg. One Mg is then replaced by one Y solute atom at each unique atomic position at height r_i with respect to stacking fault plane as shown in Figure 3.3. The simulation box is then relaxed only in the out-of-plane x_3 direction; this prevents the motion of the stacking fault. The interaction energy $E_{\text{int}}(r_i)$ of a solute at distance r_i from the stacking fault plane is then computed as

$$E_{\text{int}}(r_i) = (E_{\text{SF}}^{\text{A}} - E_{\text{B}}^{\text{A}}) - (E_{\text{SF}}^{\text{Mg}} - E_{\text{B}}^{\text{Mg}}), \quad (3.3)$$

where E_{SF}^{A} and $E_{\text{SF}}^{\text{Mg}}$ are the energies of the alloy (one Y atom at r_i from stacking fault) and

pure Mg with the stacking fault, respectively. Note that these energies are total energies, not energies per unit area. E_B^A and E_B^{Mg} are the bulk energies of the hcp structure with and without the Y solute, respectively.

In the dilute limit (neglecting solute-solute interaction), we use the interaction energies to calculate the average stacking fault energy γ^A (energy per unit area) in the alloy as follows. The absence of any interaction between the solutes would lead to the uniform random distribution of solutes. For a solute concentration of $c \ll 1$, every atomic site is equally likely to be occupied by the solute, with a probability c . Thus, the stacking fault energy of the alloy can be written as

$$\begin{aligned}\tilde{\gamma}^A &= \frac{E_{SF}^A - E_B^A}{A}, \\ &= \frac{E_{SF}^{Mg} - E_B^{Mg} + \sum_i \sum_j s_i^j E_{int}(r_i)}{A}, \\ &= \frac{E_{SF}^{Mg} - E_B^{Mg}}{A} + \frac{1}{A} \sum_i \sum_j s_i^j E_{int}(r_i),\end{aligned}\tag{3.4}$$

where E_B^A and E_{SF}^A are the total energies of bulk alloy and alloy with the stacking fault and A is the total area of the stacking fault. In the second line of the above equation, we make use of Eq. 3.3 to write the change in alloy energy due to the introduction of the stacking fault in terms of the change in pure Mg energy upon creating the stacking fault and solutes-stacking fault interaction energies. s_i^j is the occupation variable which is 1 if the atomic site identified by the indices i and j is occupied by the solute, and 0 otherwise. Index i identifies the planes with respect to the stacking fault, and index j denotes the atomic site within the i^{th} plane. Thus, i run over all the plane and j runs over the number of atoms contained within the plane which is A/A_0 , with A_0 being the effective atomic area of one Mg atom corresponding to the stacking fault plane. Further, recognizing that $E_{SF}^{Mg} - E_B^{Mg} / A = \gamma^{Mg}$ is the stacking fault energy in the pure Mg, we can express the alloy stacking fault energy as

$$\tilde{\gamma}^A = \gamma^{Mg} + \frac{1}{A} \sum_{i=-\infty}^{\infty} \sum_{j=1}^{A/A_0} s_i^j E_{int}(r_i).\tag{3.5}$$

We now compute the average stacking fault energy in the alloys by noting that s_i^j is a Bernoulli random variable which is 1 with probability equal to the solute concentration c and 0 with probability $1 - c$, which leads to the average value of $\langle s_i^j \rangle = c$. Then, the average alloy stacking fault energy is computed as

$$\begin{aligned}\gamma^A &= \langle \tilde{\gamma}^A \rangle = \gamma^{Mg} + \frac{1}{A} \sum_{i=-\infty}^{\infty} \sum_{j=1}^{A/A_0} \langle s_i^j \rangle E_{int}(r_i), \\ &= \gamma^{Mg} + \frac{c}{A} \frac{A}{A_0} \sum_{i=-\infty}^{\infty} E_{int}(r_i), \\ &= \gamma^{Mg} + \frac{c}{A_0} \sum_{i=-\infty}^{\infty} E_{int}(r_i).\end{aligned}\tag{3.6}$$

Above Eq. 3.6 can be written as

$$\gamma^A = \gamma^{\text{Mg}} + kc, \quad (3.7)$$

where $k = (\sum_{i=-\infty}^{\infty} E_{\text{int}}(r_i)) / A_0$ is the coefficient characterizing the effects of solutes on the the stacking fault energy.

Results

The interactions of Y atoms versus position for each of the stable basal (I_1 , I_2 and E), pyramidal I (SF2 and SF3), and pyramidal II stacking faults in Mg are shown in Figure 3.4. Also shown are the DFT results of Yin et al. [237] that were used for fitting of the MEAM Mg-Y potential. Also shown in each figure is the coefficient k as computed using the MEAM potential and DFT. For all planes, the interaction between a Y atom and the stacking fault becomes negligible after a few atomic layers from the stacking fault plane. For basal stacking faults, the MEAM energies are always negative (attraction) whereas the DFT energies are negative for the first few planes but then become positive at larger distances. The basal intrinsic I_1 , I_2 and extrinsic E stacking fault energies decrease with Y concentration but the MEAM potential yields k values that are approximately 50% smaller than the DFT results. The Y interactions with the pyramidal I SF2 show the same alternation in sign with positions in alternate layers, consistent with the variations in out-of-plane atomic relaxation in successive atomic layers in pure Mg [236]. But the MEAM values are again smaller in magnitude than the DFT values, leading to a smaller value of the coefficient k . There are no DFT results for the basal E and pyramidal I SF3 stacking faults. The Y interactions with the Pyramidal II stacking fault are in reasonably good agreement with the DFT results in trend and magnitude. However, the MEAM value in the first plane is somewhat lower than the DFT value. This leads to a value for the coefficient k that is slightly smaller than, but comparable to, the DFT value. The MEAM and DFT values of k for the various stacking faults are shown again in Table 3.5 along with the predictions of the Kim potential. The new MEAM potential is generally more accurate than the Kim potential in terms of signs and magnitudes, especially for the pyramidal I faults.

3.2.3 Y interactions with the pyramidal II $\langle c + a \rangle$ edge dislocation

Slip of the $\langle c + a \rangle$ dislocations in Mg is crucial for achieving plastic strain in the $\langle c \rangle$ direction. This motivated a recent DFT study of the interaction of Y solutes with the pyramidal II edge core [36].

Computational details

In the DFT study, the simulation box has a periodic length of $\sim 1\text{nm}$ along the line direction [36]. The computation yields the total energy $E_{\text{tot}}(x_{i,1}, x_{i,2})$ of the DFT cell containing the Mg dislocation and a solute at position $(x_{i,1}, x_{i,2})$ relative to the center of the dislocation core.

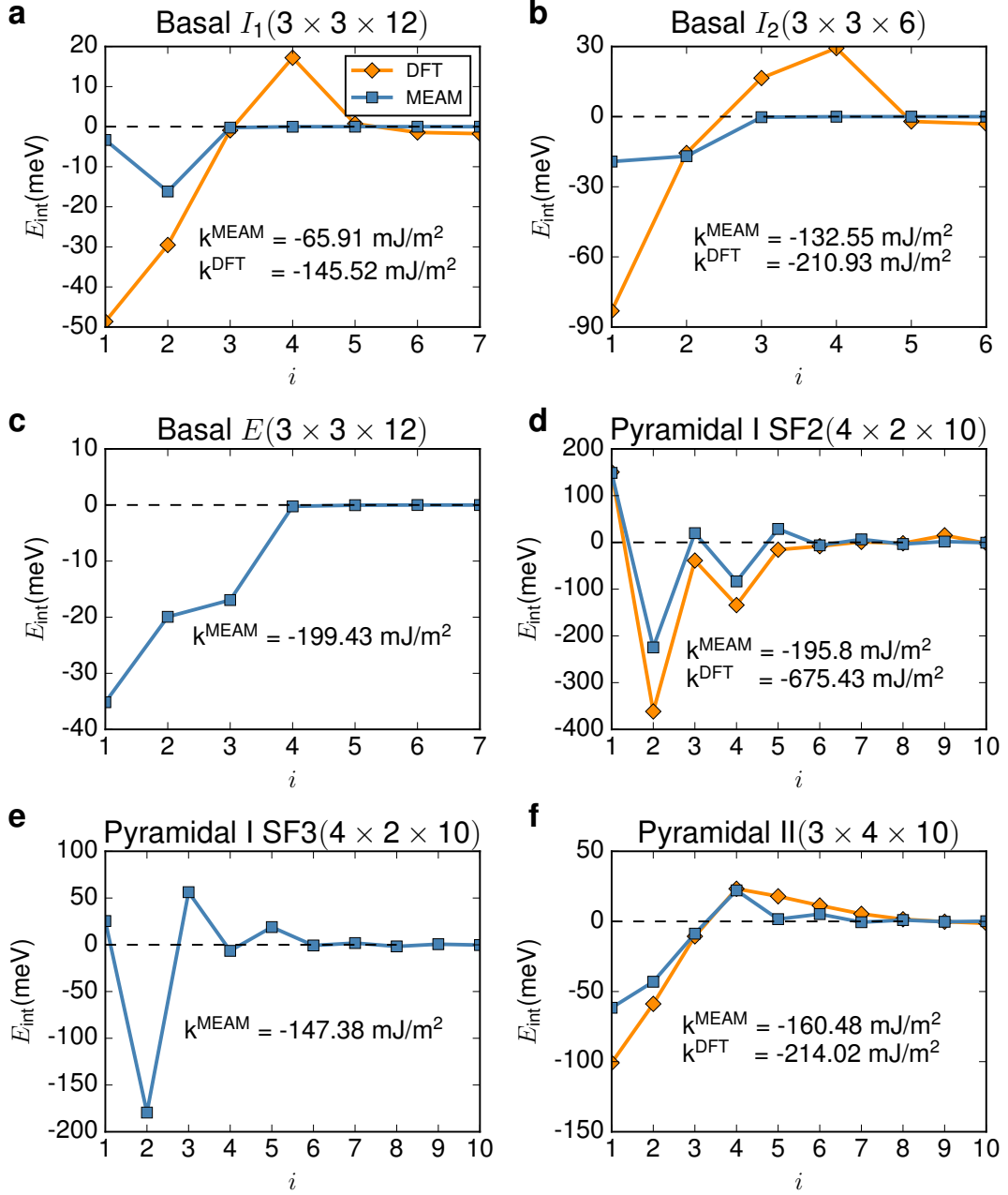


Figure 3.4 – **Interaction energy of Y solute with various stacking faults in Mg**, as computed using the current MEAM potential and using the DFT [237], as a function of distance from stacking fault plane: (a) basal I_1 (b) basal I_2 (c) basal E (d) pyramidal I SF2 (e) pyramidal I SF3 (f) pyramidal II. The size of the simulation cell $N_1 \times N_3 \times N_3$ for the corresponding stacking fault, used in MEAM calculation, is indicated in parentheses.

The interaction energy is the difference between the solute at $(x_{i,1}, x_{i,2})$ and the reference energy E_{ref} of a solute far from the dislocation in the perfect crystal Mg lattice, $E_{\text{int}}(x_{i,1}, x_{i,2}) =$

Chapter 3. Interatomic potentials employed in the atomistic simulations

Table 3.5 – Properties of Y solute atom in Mg as calculated by the current MEAM potential, the DFT, and the Kim potential. $\Delta V / V_0$ is the normalized Y misfit volume of Y and k is the coefficient for the average effect of solute concentration on the stacking fault energy (units of mJ/m²).

	MEAM	Kim Potential	DFT
$\Delta V / V_0$	0.593	0.240	0.567 ^a , 0.580 ^b , 0.636 ^c
$k(\text{basal } I_1)$	-65.83	-2.41	-145.52 ^a
$k(\text{basal } I_2)$	-132.54	-5.33	-210.93 ^a
$k(\text{basal } E)$	-199.22	-8.26	
$k(\text{pyramidal I SF2})$	-187.34	-19.08	-675.43 ^a
$k(\text{pyramidal I SF3})$	-140.74	73.32	
$k(\text{pyramidal II})$	-163.92	-250.45	-214.02 ^a

^a : Yin et al. [237]

^b : Sandlöbes et al. [181]

^c : Yasi et al. [234]

$E_{\text{tot}}(x_{i,1}, x_{i,2}) - E_{\text{ref}}$. Due to the small size of the DFT computational cell, it is not possible to compute E_{ref} in the same geometry. Uncertainties in the total energy computation also make it inaccurate to use a separate simulation of a solute in a periodic perfect crystal as the reference energy. A reference energy is therefore estimated by averaging the energies of the dislocation with solutes at all sites on the two planes on either side of the dislocation slip plane, $E_{\text{ref}} = (1/N) \sum_i E_{\text{tot}}(x_{i,1}, x_{i,2})$. For interaction energies governed only by the elastic interaction between the edge dislocation pressure field p and the solute misfit volume ΔV , $E_{\text{int}}(x_{i,1}, x_{i,2}) = p(x_{i,1}, x_{i,2})\Delta V$, the sum above should be nearly zero. Consistency of the estimated value of E_{ref} and the DFT results can be further assessed by comparing the DFT energies to the elasticity predictions for atomic sites away from the core, where the elasticity prediction becomes increasingly accurate and the field of interaction energies versus atomic position should be smooth. The use of the short periodic length combined with the low Peierls stress of the dislocation (and presumably of the individual partial dislocations) also leads to an inability to measure the interaction energy $E_{\text{int}}(x_{i,1}, x_{i,2})$ at sites whose neighbors along the glide plane have much lower (more negative) interactions. When a solute is placed in such a site, one or both partials glide such that the solute position relative to the dislocation core is in the energetically-favorable site.

Simulation of the dislocation using the MEAM potential follows a standard method. We start with a large pure Mg simulation cell ($l_{x_1} \times l_{x_2} \times l_{x_3} \sim 30\text{nm} \times 30\text{nm} \times 1\text{nm}$) with $\mathbf{x}_1 - \mathbf{x}_3$ as the glide plane, \mathbf{x}_3 axis parallel to the dislocation line, and \mathbf{x}_2 axis normal to the glide plane. A straight dislocation is introduced at the origin by applying the anisotropic elastic displacement field [13] corresponding to the Volterra dislocation. Relaxation of atomic positions is then carried out while holding fixed those atoms within two times the cutoff radius ($2r_c$) from the outer boundary. Periodic boundary conditions are used in the dislocation line direction. Relaxation is performed using the conjugate gradient method until the forces on all atoms are less than 10^{-6} eV/Å. A single solute is then introduced at $(x_{i,1}, x_{i,2})$, the system is relaxed and the total energy is computed. The interaction energy is then computed as

$E_{\text{int}}(x_{i,1}, x_{i,2}) = E_{\text{tot}}(x_{i,1}, x_{i,2}) - E_{\text{ref}}$. Here, E_{ref} can be computed either by placing a solute far from the dislocation (but not near the outer boundary) or in a separate perfect-crystal simulation. As in the DFT simulations, the high-energy solute sites are not always measurable because the dislocation can glide such that the solute resides in a lower energy site relative to the final position of the dislocation. In atomistic simulations, which are not limited to small sizes, this issue can sometimes be mitigated by using a longer dislocation line length. However, for longer line lengths, the dislocation may still glide locally near the solute while remaining in the original locations further away, i.e. the dislocation becomes bowed. Thus, the computed energy may still not reflect the true interaction energy of a solute with a straight dislocation.

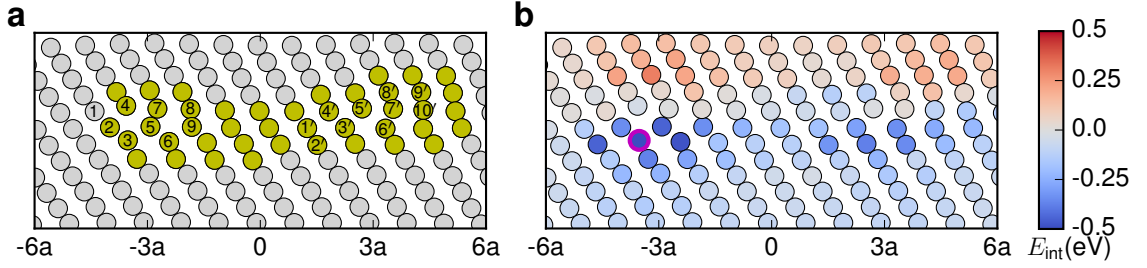


Figure 3.5 – **Interaction energy of Y solute with pyramidal II $\langle c + a \rangle$ edge dislocation.** (a) Core structure of pyramidal II $\langle c + a \rangle$ edge dislocation in pure Mg obtained from the MEAM potential. Yellow atoms correspond to non-hcp core atoms as identified from common neighbor analysis. Atomic sites are marked for which interaction energies are listed in Table 3.6. (b) Interaction energy map for different atomic sites around the dislocation with $l_{x_3} \sim 6.5$ nm, as computed from the MEAM potential. For the site highlighted by the cyan outline, the interaction energy of -0.563 eV is beyond the range of the indicated scale.

Results³

The interaction energies of Y solutes for all of the atomic sites around the edge dislocation as computed using the Mg-Y MEAM potential are shown in Figure 3.5a for dislocation line length ~ 6.5 nm. Specific MEAM and DFT values for the sites studied by DFT are listed in Table 3.6. The table indicates those sites that are unstable and the final relative position of the solute due to dislocation glide during relaxation. MEAM computations are carried out for two lengths, $l_{x_3} \sim 1, 6.5$ nm. For cases where solutes are stable at both lengths, the difference reflects solute-solute interactions at a separation of ~ 1 nm. For cases where the solutes are unstable at $l_{x_3} \sim 1$ nm, the energies at $l_{x_3} \sim 6.5$ nm are estimates including energy of a possible local dislocation bowing.

The interaction energies calculated from the MEAM potential with $l_{x_3} \sim 6.5$ nm are generally in good agreement with the DFT values. The sign of interaction energies – indicating the attractive and repulsive sites – at each site are the same in both DFT and MEAM calculations

³The DFT values presented in this section were provided by Prof. Maryam Ghazisaeidi from the Ohio State University, USA.

Chapter 3. Interatomic potentials employed in the atomistic simulations

except for the site 4. Moreover, in both DFT and MEAM calculations, the most stable sites around both partials (site 3 around left partial and site 6' around right partial) are the same. In DFT, site number 7' has a very large positive interaction energy which is unusual given that the neighboring sites (4', 10') have negative interaction energies and so the dislocation would be expected to glide to one of these substantially lower-energy sites. The typical absolute deviation in interaction energy, excluding sites 4 and 7', is ~ 0.04 eV, with a maximum of 0.107 eV for site 2'. The absence of any systematic difference suggests that the reference energy used in the DFT is reasonable. The deviations also might not be crucial because dislocation properties are influenced by the collective solute field in a random alloy [121]. Finally, the interactions of Y with the left partial dislocation (around $x_1 = -3a$ in Figure 3.5b) are observed to be stronger than around the right partial dislocation (at around $x_1 = 3a$ in Figure 3.5b), which is consistent with the wider spreading of the right partial dislocation core. The wider spreading of the right partial core is also presumably associated with a lower Peierls stress that leads to a larger number of atomic sites being unstable to glide that partial.

Table 3.6 – Interaction energy, in eV, of Y with the pyramidal II $\langle c + a \rangle$ edge dislocation in Mg at various atomic sites around the dislocation core, as calculated from the current MEAM potential and using DFT for $l_{x_3} \sim 1$ nm. The atomic sites of Y solute are marked in Figure 3.5a. Asterisk(*) means that the dislocation configuration is unstable for solutes at that site, and the dislocation partial glides to put the solute on the site mentioned in parentheses.

Site#	Interaction Energy (eV)			Site#	Interaction Energy (eV)		
	MEAM		DFT		MEAM		DFT
	$l_{x_3} \sim 1$ nm	$l_{x_3} \sim 6.5$ nm	$l_{x_3} \sim 1$ nm		$l_{x_3} \sim 1$ nm	$l_{x_3} \sim 6.5$ nm	$l_{x_3} \sim 1$ nm
1	*($\rightarrow 4$)	0.034	0.081	1'	*($\rightarrow 6'$)	-0.187	-0.211
2	*($\rightarrow 5$)	-0.344	*	2'	*($\rightarrow 11'$)	-0.327	-0.220
3	-0.558	-0.563	-0.475	3'	*($\rightarrow 6'$)	-0.289	-0.278
4	-0.056	-0.033	0.180	4'	-0.095	-0.068	-0.090
5	-0.445	-0.446	-0.385	5'	*($\rightarrow 4'$)	-0.011	*
6	*($\rightarrow 3$)	-0.482	*	6'	-0.333	-0.340	-0.280
7	*($\rightarrow 4$)	-0.003	*	7'	*($\rightarrow 4'$)	0.022	1.183
8	0.043	0.017	0.054	8'	*($\rightarrow 12'$)	0.074	0.048
9	-0.341	-0.342	-0.308	9'	*($\rightarrow 13'$)	0.135	0.074
				10'	*($\rightarrow 14'$)	-0.099	-0.074
				11'	-0.384	-0.376	
				12'	-0.111	-0.112	
				13'	0.047	0.042	
				14'	-0.147	-0.151	

3.2.4 Discussion on the applicability of the Mg-Y MEAM potential

The Mg-Y MEAM potential makes predictions that are generally in reasonable agreement with experiments and/or DFT. However, as with all potentials, the agreement is not perfect. Since plastic deformation in Mg involves many different dislocation phenomena (solute strengthening of various slip systems, pyramidal-to-basal transformation, pyramidal cross-slip), it is thus important to carefully identify those problems for which the potential is useful

and those problems where the potential remains insufficient for obtaining realistic semi-quantitative results.

First, the MEAM solute misfit volume is well-captured. This is important for solute interactions with the pressure field of a dislocation. These interactions tend to dominate solute strengthening [120, 121, 234]. The role of the solute interaction with the basal I_2 stacking fault in the solute strengthening of basal slip appears small [204], suggesting that the potential is suitable for the study of basal solute strengthening. The full interactions with the pyramidal II $\langle c + a \rangle$ edge dislocation around the core are also reasonably good (with the exception of one unusual site energy in the DFT results). Along with the good misfit volume, this indicates that the potential should be suitable for semi-quantitative assessment of pyramidal II solute strengthening. Together, these enable some assessment of the plastic anisotropy as characterized by the ratio of pyramidal II to basal Peierls stresses. The interactions of Y with the pyramidal I $\langle c + a \rangle$ and prismatic $\langle a \rangle$ dislocations have not been examined, and so applications to the strengthening of these slip systems are not yet validated.

The solute interactions with the pyramidal II stacking fault are also well-captured. This is encouraging since the pyramidal II $\langle c + a \rangle$ dislocations are energetically preferred to the pyramidal I $\langle c + a \rangle$ dislocations, such that the study of the pyramidal II $\langle c + a \rangle$ is probably more important than the study of the pyramidal I $\langle c + a \rangle$. The MEAM solute interactions with the basal faults are reasonable, but not quite strong enough. The resulting k values are then too small in comparison to the corresponding value for the pyramidal II stacking fault. This suggests some inaccuracy in using the potential to examine the PB transition of the pyramidal II edge dislocation. However, at low solute concentrations, the absolute difference in basal stacking fault energy will be small and the pyramidal-to-basal transition is not dominated by the energy of the I_1 stacking fault [232]. Thus, the potential may provide some insights into any role of Y solutes in modifying the energy barrier for this transformation.

The major deviation for the Mg-Y MEAM potential is in the value of k for the pyramidal I SF2 stacking fault. The MEAM potential predicts this value to be comparable to the k value for the pyramidal II, whereas the DFT value for the pyramidal I k is approximately 3 times larger than that of the pyramidal II. The MEAM potential therefore cannot be used to fully investigate the change in the pyramidal II to the pyramidal I cross-slip energy barrier, which holds the key to understanding ductility in Mg alloys, as will be discussed in Chapter 6. However, the potential can be used to assess the role of specific solute configurations in reducing the pyramidal II-I cross-slip barrier. Specifically, since the solute-stacking fault interactions at individual sites around the pyramidal II and the pyramidal I faults can be computed with reasonable accuracy using the MEAM potential, the energies of the pyramidal II and the pyramidal I screw dislocations in the presence of specific solute configurations can be analyzed, and the cross-slip barrier between the pyramidal II and the pyramidal I computed. The correlation of local solute energies, even if approximate, with a corresponding change in the cross-slip barrier, would enable testing of assumptions underlying the model presented in Chapter 6.

The application of any interatomic potential must always be undertaken with care. Researchers may identify other valuable phenomena for which atomistic studies of Mg-Y could be insightful. The current potential may be useful for examining such problems, especially for testing mechanistic models. However, we advocate that researchers examine the properties of this Mg-Y potential in detail to validate, quantitatively, or qualitatively, its applicability to any specific phenomenon. We also encourage further validation and testing of the potential to reveal any additional positive features or to expose any flaws that would make the potential unsuitable for certain problems.

4 Pyramidal-to-Basal Transition of $\langle c + a \rangle$ Dislocations in Mg-Y Alloys

This chapter is extracted from the following publication

1. Ahmad R., Wu Z., Groh S. and Curtin W. A. (2018). Pyramidal II to basal transformation of $\langle c + a \rangle$ edge dislocations in Mg-Y alloys. *Scr. Mater.*, 155: 114-118.

Experimental studies on Mg-RE alloys, discussed in Section 1.6, show that enhanced ductility of Mg-RE alloys is caused by the increased activity of $\langle c + a \rangle$ dislocations on pyramidal planes that enable the plastic deformation in $\langle c \rangle$ axis direction. Understanding the origins of the activation of pyramidal $\langle c + a \rangle$ dislocations in Mg-RE alloys, thus, is the key to lay out a path for designing new high ductile Mg alloys. Previous research works [4, 228] have suggested a plausible explanation that increased activation of pyramidal $\langle c + a \rangle$ dislocation might result from RE solutes affecting the stability of the easy-glide pyramidal $\langle c + a \rangle$ dislocations against the PB transition. If RE solute-dislocation interaction decreases the energy difference between the easy-glide pyramidal dissociated and the sessile basal-oriented $\langle c + a \rangle$ structures, it would typically decrease the energetic driving force and increase the energy barrier for the deleterious PB transformation. This would delay the transformation to longer times or higher temperatures, allowing much more glide of $\langle c + a \rangle$ dislocation on the easy-glide pyramidal planes, a reduced apparent CRSS for $\langle c + a \rangle$ slip, and an increase in $\langle c \rangle$ axis strain and overall ductility. A comprehensive investigation into this proposed mechanism by performing finite temperature MD simulations in Mg-3at.%Y, a model for Mg-RE alloys, is the focus of the present chapter.

4.1 Computational details

Here, we examine the stability of edge $\langle c + a \rangle$ dislocation on the pyramidal II plane in a model Mg-3at.%Y alloy. We focus on the pyramidal II $\langle c + a \rangle$ dislocation as Mg is observed to deform predominantly by $\langle c + a \rangle$ dislocations moving on pyramidal II plane [17, 155, 200]. Additionally, since pyramidal I $\langle c + a \rangle$ mixed dislocation is more susceptible to the PB transition [229],

$\langle c + a \rangle$ dislocations have a higher probability to be stabilized on easy-glide pyramidal II plane by RE solutes. We use three times the concentration of Y solutes at which enhanced ductility is observed in experiments to magnify any effects of Y on the PB transformation. To describe the interatomic interaction, We use the MEAM interatomic potential for Mg-Y alloys presented in Section 3.2. As shown in Table 3.5 and Fig. 3.4, this Mg-Y MEAM potential yields a larger negative k (solute effect on stacking fault energy) than that of DFT for pyramidal II stacking faults and a smaller negative k for the basal faults; these differences favor the stability of the pyramidal II easy-glide dislocation structure as compared to the basal-oriented dislocation structures. The MEAM potential for Mg-Y is thus suitable for investigating the concerned mechanism.

MD simulations are performed using the procedures similar to those used previously [227, 228]. Initial cells are perfect hcp lattice of size $\sim 60 \text{ nm} \times 60 \text{ nm} \times 2 \text{ nm}$ oriented with $\langle c + a \rangle$ direction along x axis, the pyramidal II plane normal along y axis, and $\langle \bar{1}010 \rangle$ along z axis. The simulation cell size along the dislocation line direction is large enough to accommodate the critical 3D nucleus of the thermally activated PB transition state [228]. Mg-3at.%Y is created by randomly substituting 3 % of the Mg atoms with Y atoms. A $\langle c + a \rangle$ edge dislocation with Burgers vector in x and line direction in z is created by displacing all atoms according to the anisotropic linear elastic Volterra solution [13] with periodicity along z . The system is then relaxed using the conjugate gradient method while holding all atoms within $2r_c$ (r_c = potential cutoff radius) of the outer boundary fixed.

In dilute random solid solution alloys under quasi-static loading at room temperature, plasticity is generated as the easy-glide dislocations move, via thermal activation, from one local favorable solute environment to another. The local favorable solute environments lower the total energy of the dislocation, which may then also energetically stabilize the easy-glide dislocations relative to the sessile basal-oriented structure. To capture these local favorable solute environments, we introduce the dislocation line at 30 successive locations separated by 1 nm along the glide direction, relax the entire simulation cell as described above, and measure the energy within a cylinder of radius $6|c + a|$ centered on the core and aligned along z . We select the lowest-energy configuration as the starting configuration for subsequent MD simulations of the PB transformation.

For MD simulations at finite temperatures of 500, 600, and 700 K, we extract a cylindrical simulation cell of radius 15 nm centered at the dislocation core from the initial larger cell, rescale the simulation cell size and atom positions to match the finite-temperature lattice parameters of Mg-3at.%Y, fix the boundary atoms and initialize atom velocities using a Gaussian distribution corresponding the desired temperature. The integration of the equations of motion is then performed using the velocity-Verlet algorithm with a time-step of 1 fs and a Nose-Hoover thermostat to maintain the temperature [159]. All simulations are performed under zero applied stress.

4.2 Results

In this section, we report the results obtained from the MD simulations carried out in Mg-3at.%Y alloy and compare them with that in pure Mg. We consider seven Mg-3at.%Y samples with different random Y distributions and corresponding favorable pyramidal II $\langle c + a \rangle$ edge dislocation configurations.

4.2.1 Transition mechanism

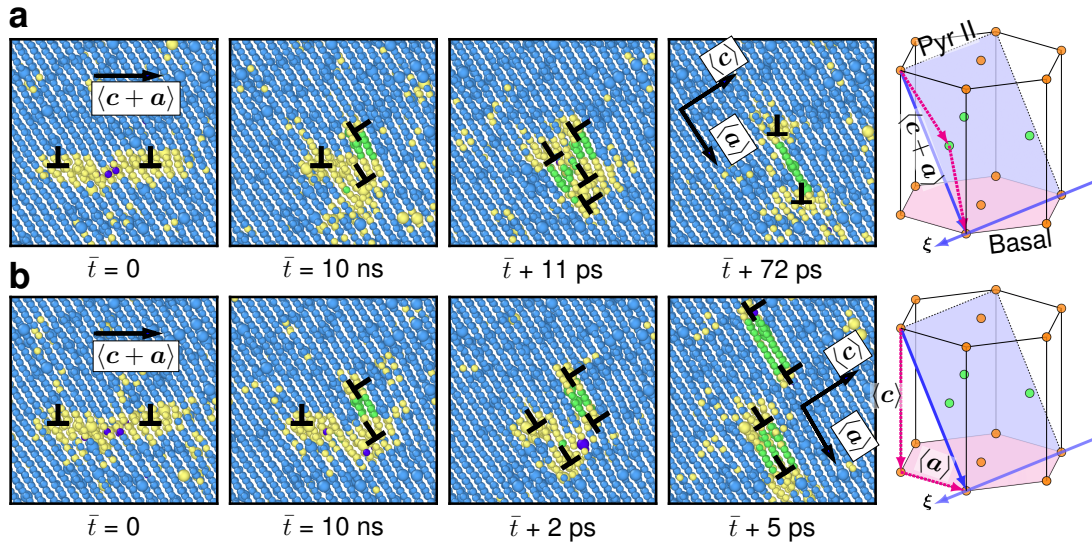


Figure 4.1 – **Pyramidal-to-basal (PB) transition of pyramidal II $\langle c + a \rangle$ edge dislocation in Mg-3at.%Y alloy at a temperature of 500 K** leading to (a) basal-dissociated $\langle c + a \rangle$ dislocation and (b) basal-dissociated $\langle c \rangle + \langle a \rangle$ dislocation. Smaller atoms are Mg and bigger atoms are Y. Atoms are colored according to their local crystal structures identified by the common neighbor analysis (CNA) [72]: blue - hcp, green - fcc, purple - bcc, yellow - others; occasional appearances of yellow atoms away from the dislocation core structure are due to temporary changes of CNA values caused by atomic vibrations at 500 K.

In all cases, the $\langle c + a \rangle$ edge dislocation dissociated on the pyramidal II plane undergoes a transformation to one of the two basal-dissociated structures (basal-dissociated $\langle c \rangle + \langle a \rangle$ and dissociated $\langle c + a \rangle$ connected by a basal I_1 stacking fault) as shown in Fig. 4.1. Transitions to the final structure are always preceded by the nucleation of a Shockley partial $\langle a \rangle$ dislocation on the basal plane from one of the pyramidal II $\langle c + a \rangle$ partial dislocations as shown in the second column of both rows of Fig. 4.1. This is the main rate-limiting process in the entire PB transition. The nucleated Shockley partial is connected to the rest of the dislocation structures by an I_2 stacking fault on the basal plane. Subsequently, another Shockley $\langle a \rangle$ partial dislocation is nucleated from the remaining dislocation structure. The next stage of the PB transition may happen in two ways. First, the nucleated dislocations stay close to each other and combine to form climb dissociated $\langle c + a \rangle$ dislocation partials connected by an

I_1 stacking fault on the basal plane as shown in Fig. 4.1(a). The separation between the two partials and thus the width of I_1 stacking fault is kinetically limited and varies from $1.5b$ to $5b$ among different simulation runs. It should be noted that equilibrium separation between the climb dissociated partial is much larger, but increasing the partial separation requires a self-compensated climb. In the second transformation route shown in Fig. 4.1(b), the second nucleation of Shockley $\langle a \rangle$ partial leads to the clear separation of $\langle c \rangle$ from $\langle a \rangle$ dislocation. The whole dissociated $\langle a \rangle$, comprising the two Shockley partials connected by an I_2 stacking fault, glides away leaving behind the $\langle c \rangle$ dislocation. The remaining $\langle c \rangle$ dislocation is dissociated into two half $\langle c \rangle$ dislocations that are delimited by an extrinsic basal stacking fault. Both the rate-limiting process and final structures are those observed in pure Mg [228]. Y solutes thus have no systematic effects on either the PB transition mechanism or the final dislocation core structures.

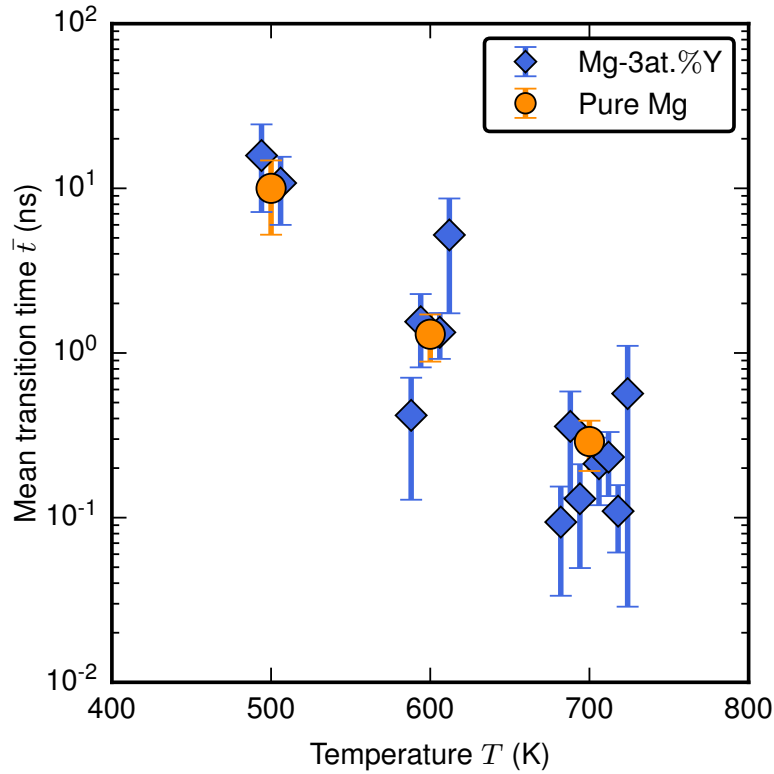


Figure 4.2 – Mean transition time \bar{t} of the pyramidal-to-basal transition versus temperature for both Mg-3at.%Y and pure Mg. The simulations are performed at 500 K, 600 K, and 700 K temperatures, and plots are shifted around those temperatures for clarity purpose only. Each diamond marker corresponds to a different random spatial distribution of Y solutes. Error bars show the 95% confidence interval of mean transition times for each random solute distribution.

4.2.2 Transition time

We measure the mean transition time as the average of ten nominally identical MD simulations for each sample, using different random initial atom velocity assignments. Fig. 4.2 shows the mean transition time \bar{t} measured in various Mg-3at.%Y samples at three temperatures. The results of pure Mg are also shown for comparison. No significant effect of Y on the average transition time is seen. Small fluctuations are found among the different random alloy realizations. The 95% confidence interval indicated are associated with the stochastic nature of thermally-activated transitions, and are similar to those in pure Mg. We observed no systematic effect of Y on stabilizing the easy-glide $\langle c + a \rangle$ edge dislocation dissociated on the pyramidal II plane.

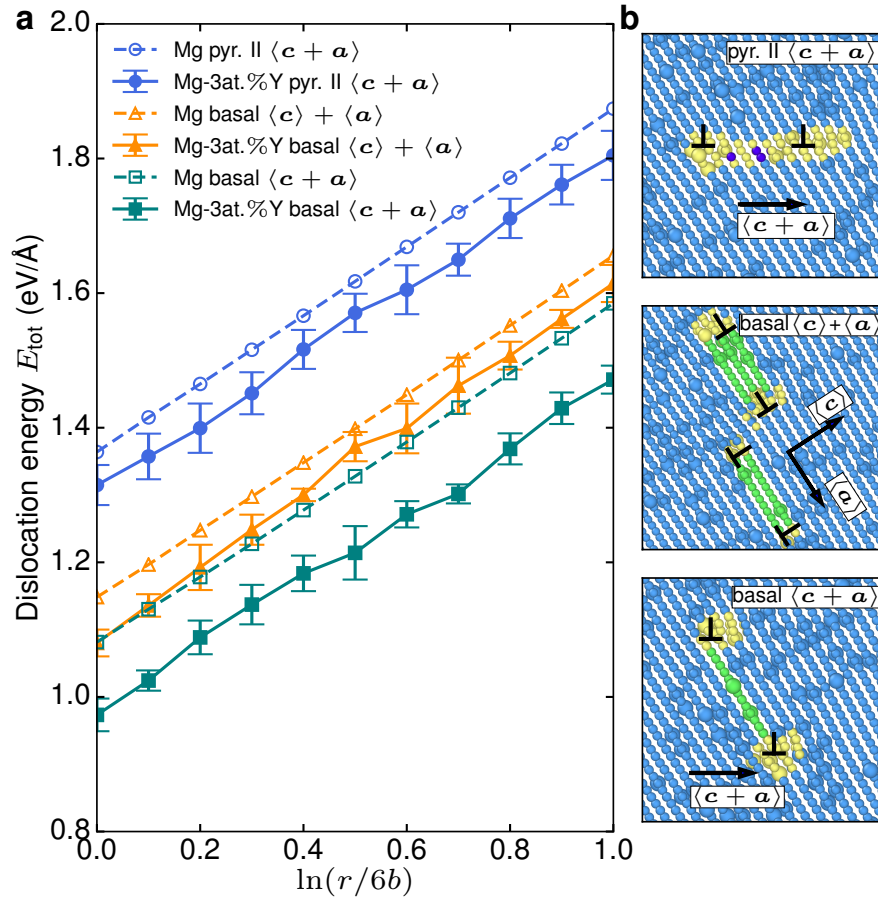


Figure 4.3 – **Energies of the pyramidal II dissociated and the basal-oriented $\langle c + a \rangle$ dislocation structures in pure Mg and Mg-3wt.%Y alloy.** (a) Dislocation energy within a radius of cylinder r for different dislocation structures in both Mg-3at.%Y and pure Mg, and (b) corresponding dislocation structures in Mg-3at.%Y. Error bars show the standard deviation of dislocation energy measured in alloys with different random Y distributions. For color scheme in (b), refer to Fig. 4.1.

4.2.3 Energetic force driving the PB transition

The thermally-activated PB transition is driven by the reduction of the total dislocation energy upon transformation into different core structures. As shown in Section 1.3, the energy per unit dislocation length within a cylinder of radius r can be divided into two parts

$$E_{\text{tot}}(r) = E_{\text{struc}} + E_{\text{elastic}}(r), \quad (4.1)$$

where E_{struc} is the energy within a distance r_{min} from the center of the dislocation and includes the core energy, stacking fault energy, interaction energy between partials, near-core elastic energy, and near-field solute energies. $E_{\text{elastic}}(r)$ is the far-field elastic energy outside of r_{min} ad given by

$$E_{\text{elastic}}(r) = K \ln(r/r_{\text{min}}), \quad (4.2)$$

where K is a function of the total Burgers vector \mathbf{b} , the dislocation line direction $\boldsymbol{\xi}$, and the anisotropic elastic constants [232]. $E_{\text{elastic}}(r)$ is thus independent of the core structure within r_{min} and so is identical for all cores. The total energy differences among dislocations with different core configurations then depends on ΔE_{struc} , which is equal to the difference in total energy $\Delta E_{\text{tot}}(r)$ at any $r > r_{\text{min}}$, aside from small effects of solute fluctuations.

Fig. 4.3 shows $E_{\text{tot}}(r)$ versus $\ln(r/r_{\text{min}})$ with $r_{\text{min}} = 6b$ for the different structures when quenched to $T = 0$ K for both Mg-3at.%Y and pure Mg. For the alloys, the average and standard deviation across the seven different solute environments are shown. The total energy $E_{\text{tot}}(r)$ scales linearly with $\ln(r/r_{\text{min}})$ as expected, aside from some fluctuations due to the random Y solute distributions. In pure Mg, $\Delta E_{\text{struc}} \approx -0.3$ eV/Å between the initial and lowest-energy transformed structures [228]. The favorable solutes interacting with the initial pyramidal II dissociated $\langle c + a \rangle$ dislocation do lower the energy. However, perhaps surprisingly, for the same spatial solute distribution, the transformed structure can also find a lower-energy position. The total energies of the basal-oriented sessile dislocations are thus also reduced relative to pure Mg. At 3 at.% Y with this Mg-Y potential, the average energy reductions are ~ 0.06 eV/Å (initial pyramidal-dissociated $\langle c + a \rangle$), ~ 0.11 eV/Å (basal-dissociated $\langle c + a \rangle$), and ~ 0.05 eV/Å (basal dissociated $\langle c \rangle + \langle a \rangle$). Evidently, while the initial dislocation was chosen specifically as a local low-energy configuration, the transformation process at finite temperatures enables the final dislocation to find a comparably lower-energy final state. Thus, Y solutes lower the energy of *all* relevant dislocation structures and therefore do not reduce the average driving force for the transition process. There is then no expectation that the average energy barrier should be changed, consistent with the direct simulations of the transition time.

We conclude that the mechanism of increased Mg ductility via stabilization of the easy-glide $\langle c + a \rangle$ through favorable solute fluctuations is thus unlikely to operate. Since experiments on Mg-3wt.%RE alloys show increased $\langle c + a \rangle$ activity and ductility, some other, dominant mechanism(s) must be activated upon addition of dilute RE solutes. In the following chapters, we present a cross-slip based mechanism to explain the enhanced slip of the pyramidal

$\langle c + a \rangle$ dislocations and experimental observations of ductility in different Mg alloys.

5 Cross-Slip Mechanism of Pyramidal $\langle c + a \rangle$ Screw Dislocations in Mg

This chapter is in part extracted from the following publication

1. Ahmad R., Wu Z. and Curtin W. A. (2020). Analysis of double cross-slip of pyramidal I $\langle c + a \rangle$ screw dislocations and implications for ductility in Mg alloys. *Acta Mater.*, 183: 228-241.

Before expounding on the full mechanistic theory responsible for the activation of the pyramidal $\langle c + a \rangle$ dislocations and resultant increased ductility in certain Mg alloys, we first need to understand the energetics and mechanisms associated with the cross-slip of the pyramidal $\langle c + a \rangle$ screw dislocations in Mg that help circumvent the detrimental PB transition and forms the core component of the ductility theory to be presented in Chapter 6.

The $\langle c + a \rangle$ screw dislocations can dissociate and glide either on the pyramidal I or on the pyramidal II planes of the hcp crystal structure. Due to residing on different crystallographic planes, the two $\langle c + a \rangle$ screw dislocations have different dislocation core structures and different energies. Experimental observations and results from atomistic simulations demonstrate that in pure Mg, the $\langle c + a \rangle$ dislocations is more stable on the pyramidal II than on the pyramidal I plane. Furthermore as shown in Fig. 5.1, no two pyramidal II planes in hcp crystal intersect with each other along a common $\langle c + a \rangle$ direction, and thus cross-slip of the pyramidal II $\langle c + a \rangle$ screw dislocation in pure Mg can be accomplished only by going through the high-energy pyramidal I plane. The atomistic mechanism underlying the pyramidal II-pyramidal I cross-slip has been investigated in detail through NEB computations by Wu and Curtin [230] and presented briefly below in Section 5.1.

The energy difference between the high-energy pyramidal I and the low-energy pyramidal II $\langle c + a \rangle$ dislocations is 27 meV/nm in pure Mg and the relative stability between the two dislocations can be altered by introducing solute elements which will be discussed in Section 6.2. Therefore, to understand the cross-slip behavior of the pyramidal $\langle c + a \rangle$ dislocations in Mg alloys, we also need to gain an insight into the cross-slip mechanism when pyramidal I

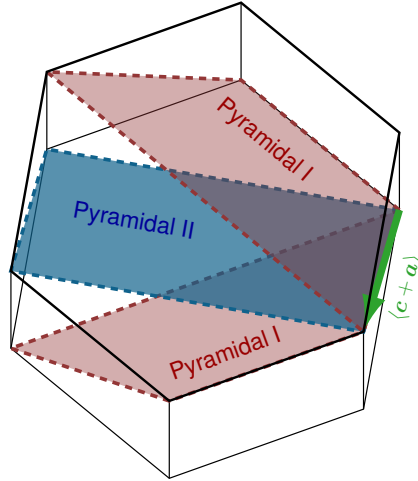


Figure 5.1 – **Schematic illustration of the pyramidal I and the pyramidal II planes in the hcp crystal structure.** The planes shown here intersect each other along a common $\langle c + a \rangle$ direction and thus are accessible to the pyramidal $\langle c + a \rangle$ dislocations through the cross-slip process. The cross-slip of the $\langle c + a \rangle$ screw dislocations residing on the pyramidal II plane is accomplished by going through the pyramidal I plane. On the other hand, the $\langle c + a \rangle$ screw dislocation residing on the pyramidal I plane has the option to cross-slip either directly to the pyramidal I plane or to the pyramidal II plane.

$\langle c + a \rangle$ screw dislocation is more stable than pyramidal II. The existence of the two pyramidal I and one pyramidal II planes intersecting with each other along the $\langle c + a \rangle$ direction leads to the various possible paths for the cross-slip process. We present and analyze various possible routes of the cross-slip process in the pyramidal I favorable regime by means of NEB calculations in Section 5.2. We, however, emphasize that the pyramidal II favorable regime is more important due to the pyramidal II $\langle c + a \rangle$ screw dislocation being more stable in pure Mg. The pyramidal I favorable regime is relevant only at higher concentrations of the solutes that reduce the energy difference between the pyramidal I and the pyramidal II $\langle c + a \rangle$ screw dislocations.

Based on the results gleaned from the NEB calculations, a model for computing the activation parameters of the pyramidal $\langle c + a \rangle$ cross-slip process is presented in Section 5.3.

5.1 Cross-slip of $\langle c + a \rangle$ dislocation in pyramidal II favorable regime

Wu and Curtin [230] perform extensive NEB computations to reveal and elucidate the atomistic mechanism associated with the cross-slip of $\langle c + a \rangle$ dislocations in the pyramidal II favorable regime. They employ the pure Mg potential MEAM_I presented in Table 3.1 that predicts pyramidal II $\langle c + a \rangle$ screw dislocation more stable than pyramidal I.

Fig. 5.2 shows the mechanism and energetics associated with cross-slip of $\langle c + a \rangle$ dislocation in the pyramidal II favorable regime. The atomic configurations along the MEP of the

5.1. Cross-slip of $\langle c + a \rangle$ dislocation in pyramidal II favorable regime

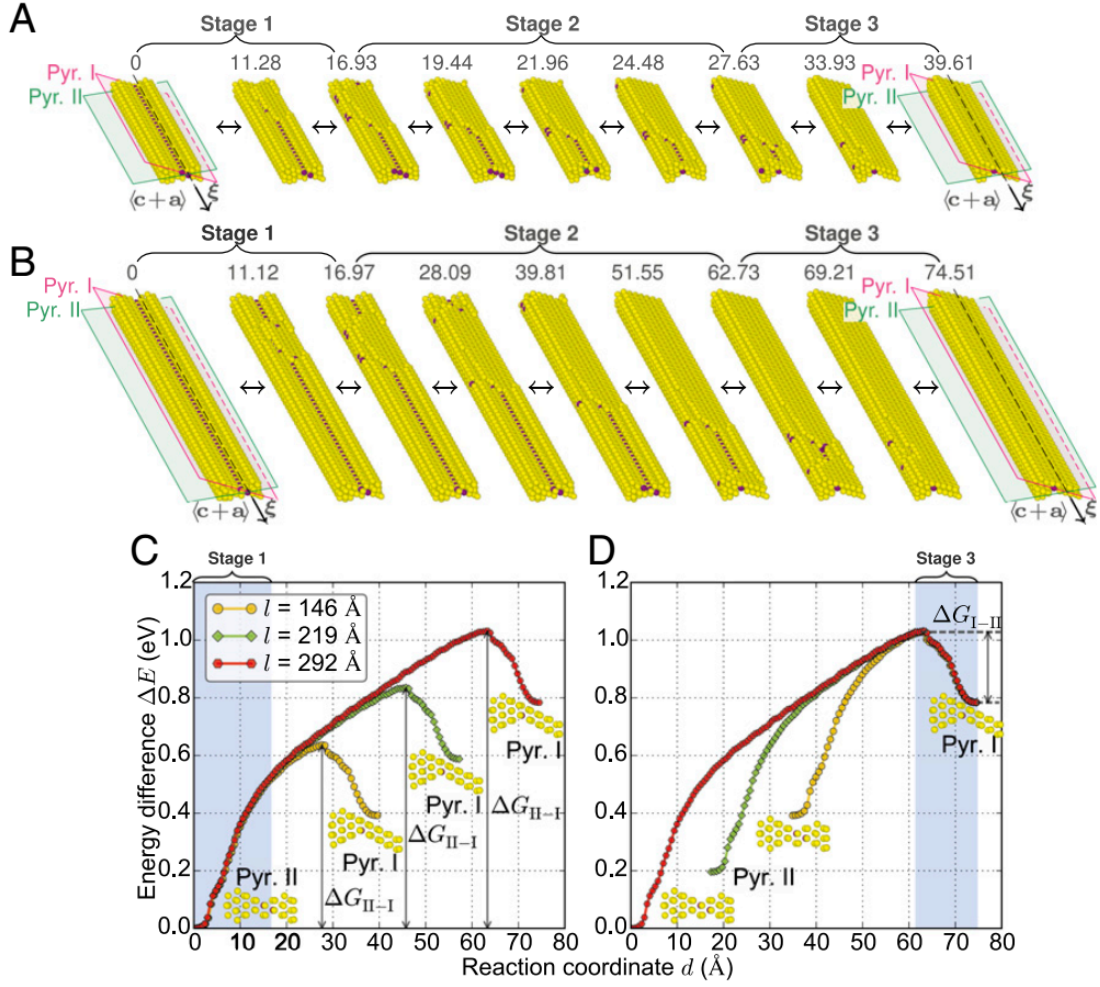


Figure 5.2 – **Energetics and mechanism of the $\langle c + a \rangle$ cross-slip from the low-energy pyramidal II to the high-energy pyramidal I plane.** Atomic configurations of dislocation encountered during the NEB calculations are shown for (a) dislocation length of 146 Å, (b) dislocation length of 292 Å. The numbers above atomic configurations indicate the reaction coordinates shown in (c) and (d). Various cross-slip stages are marked in both (a) and (b). Energy-changes during the cross-slip processes for various dislocation lengths as a function of reaction coordinate are shown with (c) pyramidal II and (d) pyramidal I $\langle c + a \rangle$ screw dislocation as reference. In (c) and (d), the cross-slip barrier associated with different dislocation lengths are denoted as ΔG_{II-I} and ΔG_{I-II} . Only non-hcp atoms involved in dislocations cores are shown. The atoms are colored according to local crystal structure identified by the common neighbor analysis: purple, bcc; yellow, others. From Wu and Curtin [230].

cross-slip process from pyramidal II to pyramidal I plane is shown in Fig. 5.2(a) and (b) for dislocation lengths of 146 and 292 Å, respectively. Fig. 5.2(c) and (d) present the energy change of dislocation structures as a function of reaction coordinate during the cross-slip process with pyramidal II and pyramidal I $\langle c + a \rangle$ dislocations as reference states, respectively. The reaction coordinate (RC) is a measure of the cumulative distance of the replicas along the MEP

starting from 0 at replica $k=1$. For replica $k > 1$, $RC(k) = \sum_{j=2}^k |\mathbf{R}_j - \mathbf{R}_{j-1}|$ where \mathbf{R}_j is the $3N$ dimensional vector in configuration space of the atomic positions in replica j and N is the total number of atoms in each replica.

The NEB results show that the cross-slip mechanism is accomplished in three stages marked in Fig. 5.2(a) and (b): nucleation, propagation, and annihilation. The first stage ($0 < RC < 17$) is the nucleation of jog/kink pair that transfers a part of the pyramidal II $\langle c + a \rangle$ dislocation on the pyramidal I plane. The energy change associated with this stage is length independent and depicted in Fig. 5.2(c) as the shaded region. During the second stage ($17 < RC < 63$ for dislocation length 292 Å), the incipient jog/kink pair move in opposite directions along the dislocation length gradually transferring the increasing length of the $\langle c + a \rangle$ dislocation from the pyramidal II to the pyramidal I plane. The energy change during this stage is length-dependent and arises solely due to the energy difference between the two pyramidal $\langle c + a \rangle$ screw dislocations. In the last stage ($17 < RC < 63$ for dislocation length 292 Å), the two ends of the jog/kink pair come very close to each other due to the periodic boundary condition, and annihilate each other. The energy change in this stage is length independent, and the same as that associated with the first stage.

The main findings of the NEB calculations are following. First, the cross-slip of pyramidal $\langle c + a \rangle$ proceeds via a unique mechanism that does not involve any dislocation constriction as in the Friedel-Escaig mechanism of cross-slip in fcc metals [74, 173]. Secondly, the total energy barrier for $\langle c + a \rangle$ cross-slip from the low-energy pyramidal II to the high-energy pyramidal I plane is length-dependent and can only be accomplished in presence of a driving stress that reduces the cross-slip free energy by performing work on the cross-slipped dislocation as discussed in Section 5.3. Thirdly, the energy barrier involved in the $\langle c + a \rangle$ cross-slip from the high-energy pyramidal I to the low-energy pyramidal II is length independent and is the intrinsic barrier associated with the nucleation of jog/kink pair. Thus, the double cross-slip of $\langle c + a \rangle$ dislocation from one pyramidal II to another pyramidal II plane is controlled by the energy barrier of the cross-slip from pyramidal II to pyramidal I plane.

5.2 Cross-slip of $\langle c + a \rangle$ dislocation in pyramidal I favorable regime

In the solute regime where $\langle c + a \rangle$ screw dislocation is more stable on pyramidal I than on the pyramidal II plane, the cross-slip behavior could become much more interesting due to the fact that as shown in Fig. 5.1, two pyramidal I and one pyramidal II planes contain a common $\langle c + a \rangle$ Burgers vector. Due to the availability of two equivalent pyramidal I planes for cross-slip, $\langle c + a \rangle$ dislocation residing on the low-energy pyramidal I plane may not necessarily be required to cross-slip first onto the high-energy pyramidal II plane.

In the pyramidal I plane favorable regime, there are four possible $\langle c + a \rangle$ double cross-slip paths, as shown in Fig. 5.3. The first possible path (Fig. 5.3(a)) requires cross-slip onto a higher-energy pyramidal II plane, glide by some distance on the pyramidal II plane, and then cross-slip back to a pyramidal I plane parallel to the original plane. A second plausible cross-

slip path (Fig. 5.3(b)) is similar to the first except that the dislocation cross-slips onto the other accessible pyramidal I plane after some glide on the pyramidal II plane. The third possibility is that the dislocation gliding on a pyramidal I plane cross-slips directly onto the next adjacent parallel pyramidal I plane shifted by only the pyramidal I interplanar distance, as shown in Fig. 5.3(c). In this cross-slip mechanism, the dislocation thus has to form a pair of atomic-scale jogs on the pyramidal II plane connecting the two pyramidal I planes. Unlike the case in Fig. 5.3(a), the dislocation does not fully dissociate onto the pyramidal II plane during the cross-slip process. Therefore, the energy barriers for the cases in Fig. 5.3(a) and 5.3(c) are different. The fourth possibility (Fig. 5.3 (d)) involves $\langle c + a \rangle$ dislocation cross-slipping directly from the original pyramidal I plane to the other accessible pyramidal I plane by forming a jog/kink pair. Since the cross-slip paths are different, solute effects could change dramatically along the different paths and in the two regimes. Quantitative prediction thus first requires detailed calculations of these possible transition paths and associated energy barriers, followed by an analysis of the rates of the cross-slip and PB transition in the regime where pyramidal I slip is dominant (i.e., in Mg alloys with some sufficiently high concentrations of solutes strongly favoring the pyramidal I $\langle c + a \rangle$ screw dislocation).

In this section, we examine and compare the energetics of these four possible cross-slip paths using the NEB calculations. We show that the first path (Fig. 5.3(a)) has the lowest cross-slip barrier so that the cross-slip process is simply the reverse of the process in the pyramidal II favorable regime.

5.2.1 Computational details

For the mechanism of interest in this work, we are interested in the potential for which the pyramidal I screw is favorable relative to the pyramidal II screw. In a real alloy, this condition is created by the average effects of the solutes on the two pyramidal stacking fault energies [237]. Thus the MEAM_II potential provided in Table 3.1 is the most suitable one for this work. This MEAM_II potential yields an energy difference $\Delta E_{\text{Mg}}^{\text{I-II}} \approx -28$ meV/nm, as compared to the value $\Delta E_{\text{Mg}}^{\text{I-II}} \approx +27$ meV/nm given by the MEAM_I potential. Thus, essentially, this potential is a proxy for average Mg-Y alloy regarding pyramidal $\langle c + a \rangle$ cross-slip. The core structures of the two pyramidal I and one pyramidal II $\langle c + a \rangle$ screw dislocations, accessible to each other by the cross-slip process, are shown in Fig. 5.4.

Introducing solutes into pure Mg has two effects on the cross-slip barrier. The first effect, mentioned above, is a change in the average dislocation energy difference $\Delta E_{\text{Mg}}^{\text{I-II}}$ which scales linearly with solute concentrations [237]. The interatomic potential used here is thus equivalent to an alloy with solutes at concentrations that would give an average effect of $\Delta E_{\text{Mg}}^{\text{I-II}} \approx -28$ meV/nm. One such alloy would be, according to the DFT predictions, Mg-1.3at%Y. The second effect of solutes is associated with fluctuations in the local solute concentration that lead to an additional change in the local cross-slip barrier. This is not captured by the present interatomic potential, but in fact, need not be. The path and the intrinsic barrier of the un-

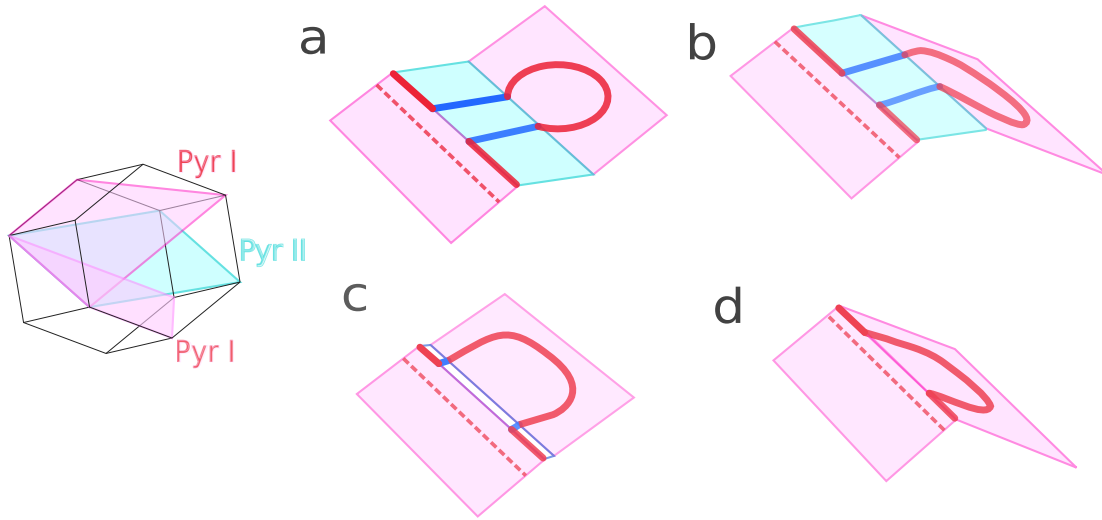


Figure 5.3 – **Schematic illustration of possible cross-slip or double cross-slip paths for $\langle c + a \rangle$ screw dislocation between two pyramidal I planes.** The crystallographic relation among the different pyramidal I and pyramidal II planes accessible through the cross-slip process, i.e. containing a common $\langle c + a \rangle$ direction, is also shown. The color code is: pyramidal I (red), pyramidal II (blue). Dashed lines in (a), (b), (c), and (d) represent the configuration of $\langle c + a \rangle$ dislocation lying on the primary pyramidal I plane just before cross-slip, and solid lines show the dislocation lines during the cross-slip process. (a) and (b), respectively, show the possibility of $\langle c + a \rangle$ dislocation cross-slipping from one pyramidal I plane to the parallel and other accessible pyramidal I planes after gliding on the high-energy pyramidal II plane. (c) and (d) depict the accomplishment of the cross-slip from one pyramidal I plane to the parallel and other accessible pyramidal I planes, respectively, without going through the pyramidal II plane.

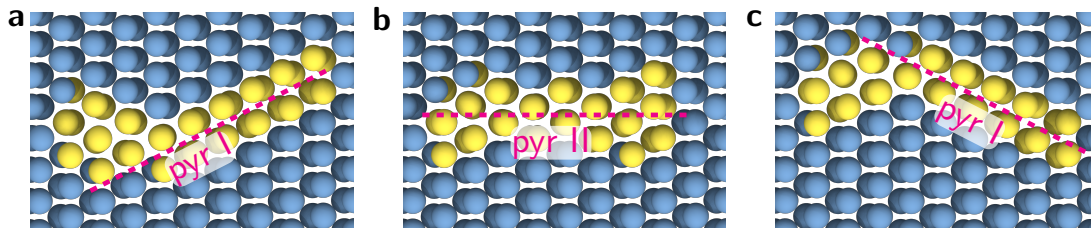


Figure 5.4 – **Core structures of $\langle c + a \rangle$ screw dislocations that are accessible through the cross-slip process,** i.e. having common Burgers vector, as determined from the MEAM_II potential. Dislocation cores shown in (a) and (c) are of equal energy and dissociated on the two distinct intersecting pyramidal I planes; and dislocation core in (b) is dissociated on the only intersecting pyramidal II plane. Blue atoms denote atoms with hcp lattice environment and yellow atoms represent the non-hcp environment as identified from the common-neighbor analysis [72, 197]. The magenta line in all three figures indicates the pyramidal I or pyramidal II slip plane on which dislocation is dissociated.

5.2. Cross-slip of $\langle c + a \rangle$ dislocation in pyramidal I favorable regime

derlying cross-slip process can be identified only by the average solute effects. The effects of fluctuations in the random alloy are added subsequently as discussed in Section 6.2. We also note that the applicability of an effective single atom potential to represent a random alloy has already been demonstrated and applied to study dislocation cross-slip in random FCC solid solution alloys [150].

Typical NEB calculations to obtain the minimum energy path (MEP) and associated energy barrier require the configurations of the initial and final states. Here, the initial state is a fully-relaxed $\langle c + a \rangle$ screw dislocation dissociated on the initial pyramidal I plane. The final state is a fully relaxed $\langle c + a \rangle$ screw dislocation dissociated on the final pyramidal I plane. For the processes shown in Fig. 5.3(a) and (b), the final plane could be at some arbitrary glide distance away from the initial plane. NEB calculations are performed at temperature $T = 0$ K, and hence the MEP and barriers will also involve the (high) Peierls barrier for the glide of the pyramidal II screw dislocation at $T = 0$ K. Such barriers are not small but are not relevant for the real problem of interest. Under realistic conditions, the glide of the pyramidal II dislocation occurs over a Peierls barrier that is reduced by whatever applied resolved shear stress needed to enable plastic flow at experimental strain rates and temperatures. The reduced glide barriers are much smaller than the cross-slip barriers. Therefore, in our NEB computations at $T = 0$ K, the final pyramidal I plane is chosen such that the glide distance on the pyramidal II plane is minimal. In NEB calculations for the case of Fig. 5.3(a), the glide of pyramidal II $\langle c + a \rangle$ dislocation is restricted to the adjacent pyramidal I planes. Furthermore, the glide of the pyramidal II dislocation in Fig. 5.3(b) is eliminated entirely, and cross-slip of the $\langle c + a \rangle$ dislocation from the initial pyramidal I to pyramidal II, and then to the final pyramidal I plane, is accomplished at the same position. Finally, the cross-slip path shown in Fig. 5.3(d) does not involve glide on the pyramidal II plane.

Since the cross-slip paths in Fig. 5.3(b), after elimination of pyramidal II glide, and Fig. 5.3(d) do not entail dislocation glide and occur at the same position, we study these two cross-slip cases in a simulation supercell with periodic boundary conditions in the dislocation line direction and fixed boundary conditions in the other two directions. We first create the pyramidal II $\langle c + a \rangle$ screw dislocation in an effectively infinite elastic medium by applying the anisotropic displacement field of the corresponding Volterra dislocation, followed by minimizing the system energy using the conjugate gradient algorithm while keeping the boundary atoms (within twice the potential cut-off radius from the outer boundary) fixed. We then perform MD simulations at 100 K and the $\langle c + a \rangle$ screw dislocation cross-slips to the lower energy pyramidal I plane as given by the MEAM_II potential. The $\langle c + a \rangle$ dislocation on the other accessible pyramidal I plane is obtained by running MD simulations at 100 K and with a non-glide shear stress of ≈ 200 MPa applied in the direction that promotes dissociation of the dislocation on the other pyramidal I plane orientation [230]. The pyramidal I $\langle c + a \rangle$ dislocation cores thus obtained are further relaxed using the same initial boundary conditions as that of the pyramidal II dislocation. Thus we obtain three $\langle c + a \rangle$ screw dislocations which are shown in Fig. 5.4: one on the high-energy pyramidal II plane and two of equal energy on the low-energy pyramidal I planes. The three screw dislocations have the same Burgers vector, share the same

boundary conditions, and are thus accessible to each other by cross-slip processes.

The minimum energy paths and associated energy barriers of the cross-slip processes are next probed using the NEB method as implemented in LAMMPS [87, 88, 128, 146, 159]. The size of the simulation box for these cases is $l_x \times l_y \times l_z \approx 40 \times 40 \times 21 \text{ nm}^3$, where the x axis is along the $[10\bar{1}0]$ direction, z axis along the dislocation line direction $[11\bar{2}3]$, and y axis along the normal of the pyramidal II plane. For the case in Fig. 5.3(b), with pyramidal II glide eliminated, we use 128 replicas in which two pyramidal I $\langle c + a \rangle$ screw dislocations are at the initial and final replicas with the intermediate replicas initialized by linearly interpolating the atomic positions of the two end replicas. In the case of Fig. 5.3(d), we use 64 replicas that are created by splicing the initial and final configurations of different lengths such that the replicas gradually transform from the initial configuration to the final configurations. We run the NEB minimization in the two cases until the maximum force on any atom across all replicas falls below 2 meV/\AA .

On the other hand, the cross-slip process shown in Fig. 5.3(a) requires gliding of the dislocation along the pyramidal II plane. To eliminate the image forces due to the fixed boundary conditions, we investigate this cross-slip path in a simulation box periodic in both the dislocation line and glide directions, i.e. along the $x - z$ pyramidal II glide plane, and with traction free boundary conditions in the direction (y) perpendicular to the pyramidal II plane. The coordinate system used in this case is the same as that described above, and the size of the simulation box is $l_x \times l_y \times l_z \approx 50 \times 32 \times 21 \text{ nm}^3$. We first create two configurations each containing a $\langle c + a \rangle$ dislocation on the pyramidal II plane shifted by the minimum glide distance of $\sqrt{3}a$, a being the lattice constant, along the x direction. The initial and final configurations, each with a $\langle c + a \rangle$ screw dislocation on the pyramidal I plane, are obtained by performing MD simulations of the two pyramidal II configurations at 100 K. The two pyramidal I $\langle c + a \rangle$ screw dislocations obtained in this way are dissociated on the same type of parallel adjacent pyramidal I planes and are connected by the glide of $\sqrt{3}a$ on the pyramidal II plane. For the NEB calculations here, we use a total of 64 replicas with intermediate replicas initialized by linearly interpolating the atomic positions of the initial and final replicas. This setup of the NEB calculation also enables us to gauge the feasibility of the cross-slip path shown in the Fig. 5.3(c), since the minimum energy path will select whether to first cross-slip onto the pyramidal II plane or directly cross-slip to the adjacent parallel pyramidal I plane.

5.2.2 Cross-slip transition paths and barriers

The results of the NEB calculations are presented as the total excess system energy versus the reaction coordinate (RC) along the MEP path.

Fig. 5.5 shows the MEP and corresponding energies of the intermediate dislocation structures for the case shown in Fig. 5.3(b) with glide on the pyramidal II plane eliminated. In this case the $\langle c + a \rangle$ screw dislocation cross-slips from one pyramidal I plane to the other accessible pyramidal I plane via the pyramidal II plane. The cross-slip occurs in many stages and involves

5.2. Cross-slip of $\langle c + a \rangle$ dislocation in pyramidal I favorable regime

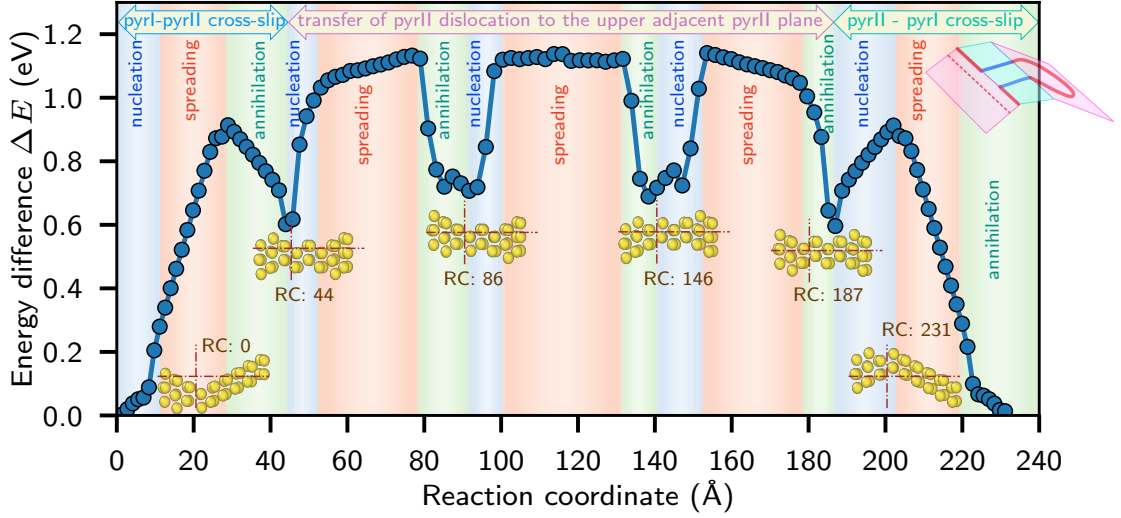


Figure 5.5 – Energy difference versus reaction coordinate, as determined in NEB calculation of the minimum energy path of the cross-slip process between two pyramidal I planes accomplished through the route where the pyramidal I dislocation cross-slips to other accessible pyramidal I plane via a high-energy pyramidal II plane. The cross-slip process is accomplished in three stages as mentioned at the top of the figure. Three steps involved in each transformation stages are shown: nucleation is the formation of the incipient jog/kink pairs; spreading is the lateral motion of the kink/jog pair along dislocation length and energy change in this step is dislocation length dependent; annihilation is the mutual cancellation of the kink/jog pair forced by the periodic boundary along dislocation length. Atomistic pictures of intermediate metastable dislocation core structures encountered during the cross-slip process –with their reaction coordinates – are shown by drawing only non-hcp near core atoms identified using common neighbor analysis. The brown cross-hairs plotted on the dislocation cores are for the purpose of indicating the motion/glide/transformation of dislocation cores against a static background. A schematic diagram of the cross-slip process, i.e. Fig. 5.3(b), is depicted in the upper right corner.

several intermediate metastable dislocation structures. Fig. 5.5 also identifies the nucleation, spreading along dislocation line length, and annihilation of kink/jog pair which accompany every stage. The intrinsic barrier is involved in these nucleation and annihilation steps. Energy changes in the nucleation and annihilation steps are dislocation length independent, while that in the spreading step may depend on the dislocation length (controlled by the energy difference of the two connected metastable core structures). Furthermore, the enthalpy change in the spreading part can be reduced by applying a resolved shear stress which does work in the bowing out of the dislocation. In the first stage, the pyramidal I dislocation transforms onto the pyramidal II plane (at RC \approx 44). This process is essentially the same as that of the cross-slip of the low-energy pyramidal II $\langle c + a \rangle$ dislocation to the high-energy pyramidal I $\langle c + a \rangle$ dislocation in pure Mg [230]. The energy barrier in this stage depends on the dislocation length and is \approx 0.9 eV for the dislocation length used here (21 nm). This dislocation core obtained at RC 44 could glide on pyramidal II plane under resolved shear

stresses which is not considered in the present calculations. The next stage involves the shuffling of atoms in order to migrate the pyramidal II $\langle c + a \rangle$ dislocation from one pyramidal II plane to the adjacent pyramidal II plane just above (RC 44 to 187). The energy barrier (≈ 0.55 eV) for this stage depends weakly on the dislocation length as it goes through slightly higher-energy metastable dislocation structures (at RC $\approx 86, 146$). In the final stage, the pyramidal II $\langle c + a \rangle$ dislocation cross-slips back to the pyramidal I plane with an associated length-independent, the intrinsic energy barrier of ≈ 0.3 eV required to form the cross-slip jog. For cross-slip of the current dislocation of length 21 nm, the total energy barrier is ≈ 1.15 eV.

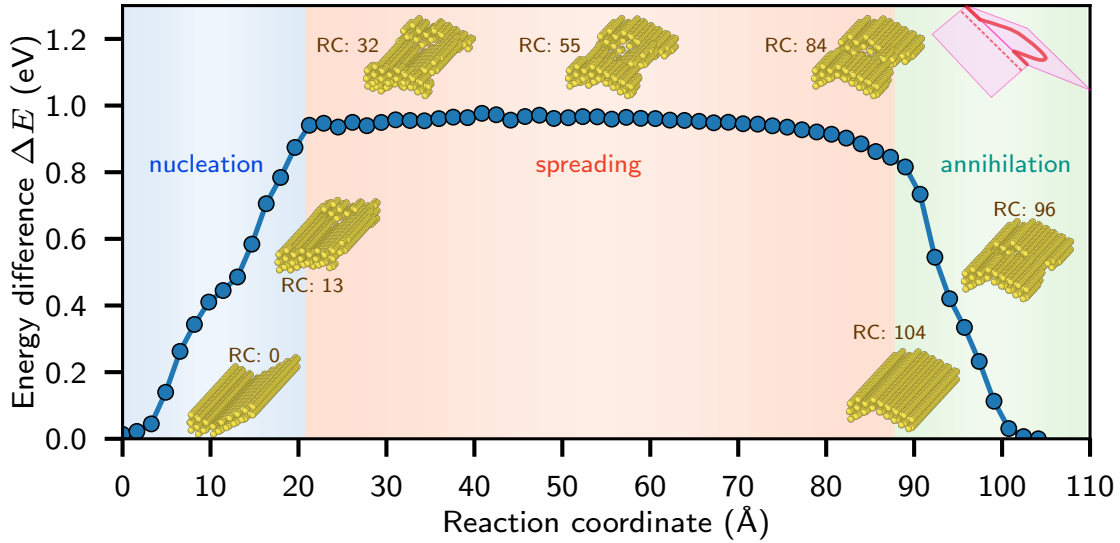


Figure 5.6 – Energy difference versus reaction coordinate, as determined in NEB calculation of the minimum energy path of the cross-slip process between two pyramidal I planes accomplished through the route where the pyramidal I dislocation cross-slips directly to other accessible pyramidal I plane by nucleating a pair of jogs and without ever residing on the high-energy pyramidal II plane. Three steps of the cross-slip process are shown: nucleation is the formation of the incipient jog/kink pairs; spreading is the lateral motion of the kink/jog pair along dislocation length and energy change in this step is dislocation length dependent; annihilation is the mutual cancellation of the kink/jog pair forced by the periodic boundary along dislocation length. Atomistic pictures of intermediate metastable dislocation core structures encountered during the cross-slip process – with their reaction coordinates – are shown by drawing only non-hcp near core atoms identified using common neighbor analysis. A schematic diagram of the cross-slip process, i.e. Fig. 5.3(d), is depicted in the upper right corner.

Fig. 5.6 shows the second possible MEP and associated energetics for cross-slip between two different pyramidal I planes as shown Fig. 5.3(d). In this MEP, the first step (RC 1-20) is the nucleation of a pair of dislocation jogs which transforms a small dislocation segment from the primary pyramidal I plane to the cross-slip pyramidal I plane. During the second step (RC 20-84), the cross-slipped jogs expand laterally along the dislocation line and gradually transforming the dislocation in the process. In the third and last step (RC 84-105), due to the

5.2. Cross-slip of $\langle c + a \rangle$ dislocation in pyramidal I favorable regime

periodic boundary conditions, the two jogs come very close and finally annihilate each other, transforming the whole dislocation to the cross-slip pyramidal I plane. The energy barrier of this MEP is the intrinsic energy of formation of the initial cross-slip jogs, ≈ 1.0 eV, and hence is independent of the dislocation length.

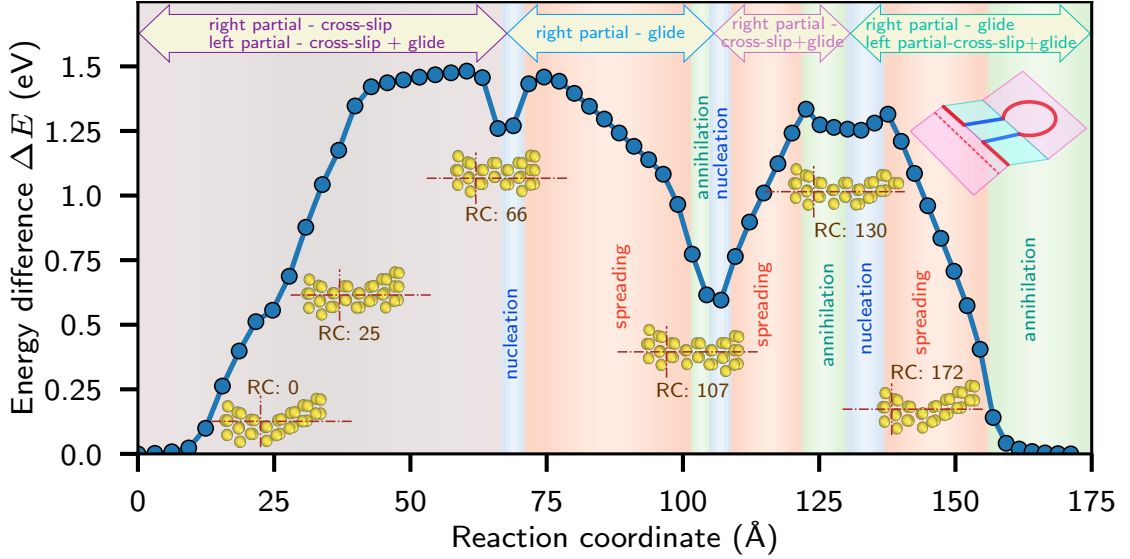


Figure 5.7 – **Energy difference versus reaction coordinate, as determined in NEB calculation of the minimum energy path of the cross-slip process between two pyramidal I planes accomplished through the route where the pyramidal I dislocation first cross-slips to a high-energy pyramidal II plane, and goes back to a parallel pyramidal I plane after gliding some distance on a pyramidal II plane.** The cross-slip process is accomplished in four stages as mentioned at the top of the figure. The first stage (cross-slip of right partial, and cross-slip and glide of left partial) is completed by multiple nucleation events which are not well separated from each other. Three steps involved in other three transformation stages are shown: nucleation is the formation of the incipient jog/kink pairs; spreading is the lateral motion of the kink/jog pair along dislocation length and energy change in this step is dislocation length dependent; annihilation is the mutual cancellation of the kink/jog pair forced by the periodic boundary along dislocation length. Atomistic pictures of intermediate metastable dislocation core structures encountered during the cross-slip process –with their reaction coordinates – are shown by drawing only non-hcp near core atoms identified using common neighbor analysis. The brown cross-hairs plotted on the dislocation cores are for the purpose of indicating the motion/glide/transformation of dislocation cores against a static background. A schematic diagram of the cross-slip process, i.e. Fig. 5.3(a), is depicted in the upper right corner.

Fig. 5.7 shows the variation of the energy and the transformation of the dislocation structures for the cross-slip path in Fig. 5.3(a), where the initial pyramidal I dislocation cross-slips onto, and glides on, a pyramidal II plane and then cross-slips back onto a pyramidal I plane parallel to the original pyramidal I plane. The whole process is accomplished in multiple stages as indicated in Fig. 5.7. We observe that during the first stage (RC from 0 to 66), the right partial of the $\langle c + a \rangle$ screw dislocation cross-slips to the pyramidal II plane, and the left partial

dislocation cross-slips to and glides on the pyramidal II plane. This stage involves multiple nucleation events that are not sharply demarcated from each other, thus we cannot determine the intrinsic barrier for this forward process. This nucleation process is length-dependent with an intrinsic barrier of at least ≈ 0.23 eV which is the energy change during the RC 63-66. In the second stage of the process (RC from 66 to ~ 107), the right partial glides on the pyramidal II plane. Because the dislocation goes from a low-energy configuration to high-energy configurations, the energy barrier in this stage is dislocation-length dependent with an intrinsic barrier of ≈ 0.23 eV. The third stage (RC from 107 to 130) involves the transfer and a little glide of right partial on the final pyramidal I plane. The energy barrier in this stage is length-dependent with a small intrinsic barrier of ≈ 0.06 eV. In the last stage (RC from 130 to 172), the right partial further glides on the pyramidal I plane, and the left partial glides on the pyramidal II plane followed by transfer onto the pyramidal I plane. The intrinsic barrier of this last stage is ≈ 0.06 eV. The total energy barrier for the overall process is ≈ 1.49 eV.

5.2.3 Implications for double pyramidal I cross-slip

As briefly discussed in the Introduction and presented in detail in the next Chapter 6, the ductility-enhancement mechanism envisions that high ductility can be achieved by sustained plastic strain in the $\langle c \rangle$ direction through the generation of $\langle c + a \rangle$ dislocation loops at a rate fast enough to counter the immobilization of $\langle c + a \rangle$ dislocations due to the PB transition. The generation of $\langle c + a \rangle$ dislocation loops is accomplished by the double cross-slip of the screw segments of each dislocation loop. Here, we analyse the cross-slip barriers when the solute concentration is high enough such that for the $\langle c + a \rangle$ screw dislocation, the pyramidal I plane is energetically more favorable than the pyramidal II plane. In this case, cross-slip occurs by one of the processes examined using NEB in the previous section.

The cross-slip process shown in Fig. 5.5 involves cross-slip onto the higher-energy pyramidal II plane followed by cross-slip back onto another available pyramidal I plane. The barrier for this process includes an intrinsic barrier of at least ≈ 0.45 eV, associated with the initial cross-slip to the pyramidal II plane and the migration of the pyramidal II dislocation one layer above the original plane, plus an additional barrier arising from the pyramidal II/I energy difference per unit dislocation length. The latter length-dependent part of the barrier can be reduced by the application of a resolved shear stress on the glide plane but the intrinsic barrier remains. Therefore, this double cross-slip path is not effective in alleviating the deleterious effects of the PB transition that has a barrier of only 0.3 eV [229].

Two distinct pyramidal I planes intersect each pyramidal II plane along a common $\langle c + a \rangle$ direction, as shown in Fig. 5.3. Therefore, starting from a pyramidal II $\langle c + a \rangle$ dislocation, there are two different pyramidal I planes available for the cross-slip process. It can be inferred from Fig. 5.5 that the two pyramidal I planes associated with a pyramidal II plane are not equivalent with respect to the cross-slip of the $\langle c + a \rangle$ screw dislocation. For instance, beginning from the pyramidal II $\langle c + a \rangle$ dislocation at RC 44, the energy barrier to the pyramidal I dislocation at

5.2. Cross-slip of $\langle c + a \rangle$ dislocation in pyramidal I favorable regime

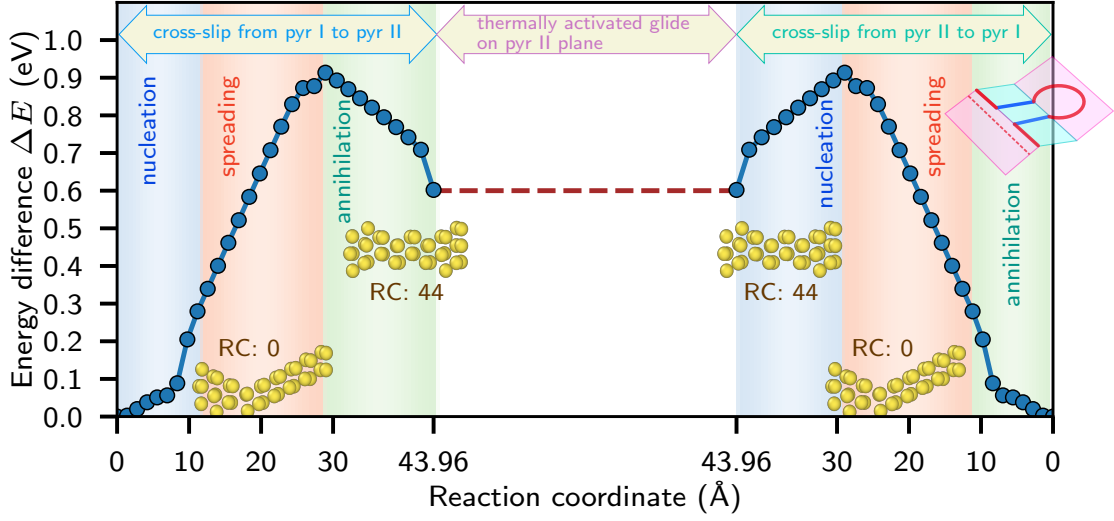


Figure 5.8 – **Energetics and minimum energy path of the most favorable cross-slip path between pyramidal I planes**, as inferred from the NEB results shown in Figs. 5.5, 5.6 and 5.7. The pyramidal I $\langle c + a \rangle$ dislocation cross-slips first to the pyramidal II plane and after gliding some distance on a high-energy pyramidal II plane, again cross-slips back to a parallel pyramidal I plane. Three steps involved in the two cross-slip stages are shown: nucleation is the formation of the incipient jog/kink pairs; spreading is the lateral motion of the kink/jog pair along dislocation length and energy change in this step is dislocation length dependent; annihilation is the mutual cancellation of the kink/jog pair forced by the periodic boundary along dislocation length. Atomistic pictures of intermediate metastable dislocation core structures encountered during the cross-slip process –with their reaction coordinates – are shown by drawing only non-hcp near core atoms identified using common neighbor analysis. A schematic diagram of the cross-slip process, i.e. Fig. 5.3(a), is depicted in the upper right corner.

RC 0 (≈ 0.3 eV) is significantly lower than that on the other pyramidal I plane at 230 (≈ 0.5 eV). In the same way, for the pyramidal II dislocation at RC 187, the energy barrier to the pyramidal I dislocation at RC 230 is smaller (≈ 0.3 eV) than that on the pyramidal I plane at RC 0 (≈ 0.5 eV). This should be a general conclusion regardless of the specific interatomic potential because of the fact that the pyramidal II plane lacks mirror symmetry across the slip plane.

The direct cross-slip between two pyramidal I planes without ever residing on a higher-energy pyramidal II plane (Fig. 5.6) has an energy barrier of ≈ 1 eV, which is more than three times that of the corresponding PB transition barrier on pyramidal I planes. Therefore, this path is not effective in circumventing the detrimental PB transition either.

The cross-slip process shown in Fig. 5.7 involves cross-slip onto a pyramidal II plane followed by cross-slip back onto a parallel pyramidal I plane. The processes of cross-slip and glide on pyramidal II are accomplished simultaneously for each partial successively. This particular energy path includes the rather high Peierls barrier of the screw $\langle c + a \rangle$ dislocation on the

pyramidal II plane at 0 K temperature. A separate NEB calculation (not shown here) computes a Peierls barrier of ≈ 1 eV for the screw $\langle c + a \rangle$ dislocation of ≈ 21 nm gliding on the pyramidal II plane. At non-zero temperatures under applied glide shear stresses, the glide of the screw dislocation is expected to have much lower energy barriers. The independent cross-slip of the individual partials is also caused by the nearly identical Burgers vectors and cores of the partials dissociated on the pyramidal I and pyramidal II planes [97]. Thus, the barrier for cross-slip onto the pyramidal II plane is the controlling barrier for double cross-slip with an intrinsic barrier of ≈ 0.3 eV. This process is basically the same as that occurring when the pyramidal II plane is energetically favorable, and so is suitable for mitigating the detrimental effects of the PB transition. To be effective, however, this process must be assisted by a net resolved shear stress acting on the pyramidal II plane to remove the length-dependent portion of the energy barrier. Since the initial pyramidal I dislocation does not go directly to the adjacent parallel pyramidal I plane, this computation further indicates the implausibility of the cross-slip path shown schematically in Fig. 5.3(c).

On the basis of the above discussion, we conclude that in the regime where solutes make the pyramidal I $\langle c + a \rangle$ dislocations energetically more favorable, cross-slip to generate new $\langle c + a \rangle$ dislocation loops occurs by the process shown in Fig. 5.8. Specifically, the pyramidal I dislocation first cross-slips onto a pyramidal II plane following the path of RC from 0 to 44 (pyramidal I to pyramidal II $\langle c + a \rangle$ cross-slip) of Fig. 5.5. Subsequently, after an arbitrary amount of thermally activated glide along the pyramidal II plane, $\langle c + a \rangle$ screw dislocation cross-slips back onto the similarly orientated pyramidal I plane, which is essentially the reverse of the forward cross-slip process from pyramidal I to pyramidal II plane.

5.3 Model for pyramidal $\langle c + a \rangle$ cross-slip barrier

Based on the results obtained from the NEB computations of pyramidal $\langle c + a \rangle$ dislocation, we now present a model for computing the energy barrier for $\langle c + a \rangle$ cross-slip happening from lower energy plane to higher energy plane. We note that the energy barrier associated with the cross-slip occurring from the higher energy plane onto the lower energy plane is the intrinsic energy change involved with the nucleation of the jog/kink pair. Thus, the energy barrier for cross-slip from lower to higher energy plane is the rate-controlling process, and its computation is the goal of the proposed model.

The cross-slip model presented here is applicable in both pyramidal II and pyramidal I favorable regime. We, here, however, consider the pyramidal II favorable regime to explain the essential feature of the model, and application of the model to pyramidal I favorable regime is straightforward.

Cross-slip of a $\langle c + a \rangle$ screw dislocation from the low-energy pyramidal II slip plane to the high-energy pyramidal I slip plane cannot occur spontaneously, because the final state (a long straight pyramidal I screw dislocation) has hugely higher energy (increasing in proportion to the dislocation length) than the original pyramidal II screw dislocation. The cross-slip

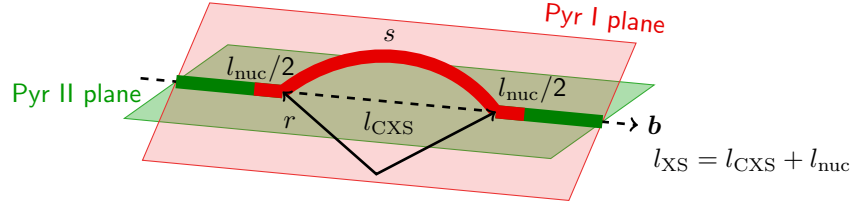


Figure 5.9 – Schematic illustration of cross-slip of $\langle c + a \rangle$ screw dislocation from pyramidal II to pyramidal I plane in pyramidal II favorable regime. Quantities relevant to the analysis of the cross-slip barrier ΔG_{XS} are indicated. Note that l_{nuc} is the length of the cross-slipped pyramidal I dislocation at the pyramidal I/pyramidal II junction that does not bow out under driving stress $\Delta\tau$.

must thus be driven by a *net* resolved shear stress $\Delta\tau$ on the pyramidal I plane [230]; this driving/net stress is essentially the local resolved shear stress above the Peierls stress for pyramidal I $\langle c + a \rangle$ screw dislocation. When a nascent pyramidal I loop is created along the pyramidal II dislocation, the net resolved shear stress $\Delta\tau$ can do work by bowing-out the pyramidal I segment, reducing the total energy of the system and allowing the loop to expand. However, the creation of the initial loop requires energy to form two pyramidal II/pyramidal I intersections/jogs and to pay the energy cost of the pyramidal I segment relative to the original pyramidal II segment. As the loop bows out, there is an additional elastic energy cost for the additional pyramidal I line length and an energy gain by the work done by the applied stress acting over the area of the bow-out. Fig. 5.9 shows a schematic of the nucleation process. All of the above processes are captured by expressing the cross-slip barrier, as a function of cross-slipped length, within a line tension model following Refs. [164, 230] as

$$\Delta G_{\text{XS}}(l) = \Delta G_{\text{XS},i} + \Delta E^{\text{I-II}}(l + l_{\text{nuc}}) + \Gamma \Delta s(l) - \Delta\tau b A(l), \quad (5.1)$$

where $l + l_{\text{nuc}}$ is the initial length of the cross-slipped pyramidal I segment before bowing-out. The intrinsic nucleation length $l_{\text{nuc}} = 2.5$ nm is the length of $\langle c + a \rangle$ screw dislocation that has cross-slipped to the pyramidal I plane at the conclusion of formation of the initial cross-slip jog/step, corresponding to reaction coordinate of ≈ 10 (Fig. 6.6(a)). And l is the length of the pyramidal I dislocation which bows-out under the influence of resolved shear stress $\Delta\tau$. $\Delta G_{\text{XS},i} = 0.23$ eV [230] is the intrinsic cross-slip barrier associated with initial nucleation of the cross-slipped segment including the two pyramidal II-pyramidal I intersections, $\Delta E^{\text{I-II}}$ is the energy difference per unit dislocation length between the pyramidal I and pyramidal II $\langle c + a \rangle$ screw dislocations, $\Gamma = \mu b^2/4$ is the screw dislocation line tension [101] with μ the shear modulus, $\Delta s(l)$ is the increase in pyramidal I line length due to bowing out of the cross-slipped segment of length l and $A(l)$ is the area swept out during bowing-out. In the line-tension model, the bow-out configuration is a circular arc having radius of curvature r satisfying the

equilibrium condition $r = \Gamma / (b\Delta\tau)$. $\Delta s(l)$ and $A(l)$ are then determined by geometry as

$$\Delta s(l) = 2r \sin^{-1} \left(\frac{l}{2r} \right) - l, \quad (5.2a)$$

$$A(l) = r^2 \sin^{-1} \left(\frac{l}{2r} \right) - \frac{rl}{2} \sqrt{1 - \left(\frac{l}{2r} \right)^2}, \quad (5.2b)$$

The critical bowed-out cross-slip length l_{CXS} , at a given stress $\Delta\tau$, is the value of l that minimizes $\Delta G_{\text{XS}}(l)$. Once the barrier is reached, the cross-slipped segment on pyramidal I can expand indefinitely, lowering the total energy of the system due to the work done by the applied stress. Setting $\partial \Delta G_{\text{XS}} / \partial l_{\text{XS}} = 0$, l_{CXS} is found to be

$$l_{\text{CXS}} = \frac{2\sqrt{\Delta E^{\text{I-II}}(2\Gamma - \Delta E^{\text{I-II}})}}{b\Delta\tau}. \quad (5.3)$$

The total operative critical cross-slip length, including bowed-out length and nucleation length, is $l_{\text{XS}} = l_{\text{CXS}} + l_{\text{nuc}}$. The cross-slip barrier is then

$$\Delta G_{\text{XS}} = \Delta G_{\text{XS,i}} + \Delta E^{\text{I-II}} l_{\text{XS}} + \Gamma \Delta s(l_{\text{CXS}}) - \Delta\tau b A(l_{\text{CXS}}). \quad (5.4)$$

To apply the model in the pyramidal I favorable regime, we need to make sure that $\Delta E^{\text{I-II}} < 0$, and then use the absolute value of energy difference in Eqs. 5.3 and 5.4. Another quantity to modify is $\Delta\tau$, which now is the local resolved shear stress minus the critical resolved shear stress for cross-slipped pyramidal II $\langle c + a \rangle$ screw dislocation. Thus we need to have the information about the dislocation energy difference and driving-stress in order to compute the cross-slip barrier. The extension of the model in random solid solution Mg alloy and estimation of the quantities involved in the model are discussed in the following Chapter 6.

6 Cross-Slip Driven Ductility in Dilute Mg Alloys: Theory

This chapter is in part extracted from the following publications

1. Wu Z., Ahmad R., Yin B., Sandlöbes S., and Curtin W. A. (2018). Mechanistic origin and prediction of enhanced ductility in magnesium alloys. *Science*, 359: 447-452.
2. Ahmad R., Yin B., Wu Z. and Curtin W. A. (2019). Designing high ductility in magnesium alloys. *Acta Mater.*, 172: 161-184.
3. Ahmad R., Wu Z. and Curtin W. A. (2020). Analysis of double cross-slip of pyramidal I $\langle c + a \rangle$ screw dislocations and implications for ductility in Mg alloys. *Acta Mater.*, 183: 228-241.

It is established, both experimentally and computationally as discussed in Section 1.5, that low ductility in pure Mg originates primarily from the immobilization of the pyramidal $\langle c + a \rangle$ dislocations caused by the PB transition. In order to enhance the pyramidal $\langle c + a \rangle$ slip, a mechanism is required that can circumvent/overcome the harmful PB transition and enable the pyramidal $\langle c + a \rangle$ dislocation systems to operate. Cross-slip and double cross-slip of screw dislocations between the pyramidal I and pyramidal II planes represent such mechanisms that can naturally act as the multiplying source for dislocations. The PB transition and cross-slip are both thermally activated processes and the ductility is then controlled by the competition between them. If the cross-slip process is rapid enough to defeat the PB transition, new pyramidal $\langle c + a \rangle$ dislocations would be generated faster than PB transition could arrest them, enabling enhanced ductility. Different solute elements then alter the energy difference between the two pyramidal $\langle c + a \rangle$ dislocations, affects the cross-slip rate, and thus change the ductility level of resulting solid solution alloys.

In this chapter, we present a novel cross-slip based ductility model that successfully rationalizes broad experimental observations of ductility in a range of dilute solid solution Mg alloys.

6.1 Mechanistic model of enhanced ductility

We first outline the mechanistic model and the resulting ductility condition. To explain the essential concepts involved in the model, we choose to work here in pyramidal II favorable regime, however, the model can readily be extended into the pyramidal I favorable regime. We will describe along the way the necessary modifications for the model to be applied in the pyramidal I favorable regime. To start, we consider a pyramidal II $\langle c + a \rangle$ dislocation loop of arbitrary dimensions $L \times L$ as shown in Fig. 6.1. The edge-like segments of the loop are susceptible to the PB transition to sessile structures. If this transition is nucleated along an edge segment, it will expand immediately along the entire edge portion because the basal-oriented structure has a much lower energy [228]. Growth of the loop, and hence plastic strain, will be limited to motions of the screw-like segments while near-edge segments, as they are created by such motion, will quickly rotate and convert to the sessile basal-oriented structure. The result of the above PB-transition is long, straight, basal-oriented, immobile edge $\langle c + a \rangle$ dislocations, as reported in many experiments [79, 151, 155]. Some experiments [79, 80] also show a very high density of basal-oriented $\langle c + a \rangle$ dislocation loops; the mechanistic origin by which the loops form remains largely unknown at this time but is not important for the present problem.

The screw segments of the loop can undergo cross-slip onto the coincident pyramidal I plane, followed by cross-slip back onto another pyramidal II plane (Fig. 6.1). This double-cross-slip process is inhibited by the high energy cost of the pyramidal I screw relative to that of the pyramidal II screw, and so is not fast in pure Mg. However, if this process can be accelerated, dislocation loops can then multiply, and these loops can expand and generate $\langle c + a \rangle$ plastic strain contributing slips in the $\langle c \rangle$ direction. Furthermore, the individual pyramidal II loops are now isolated from one another by the intervening pyramidal I segments remaining after the double cross-slip. Thus, the PB transition in one loop does not lead to starvation of mobile $\langle c + a \rangle$ dislocations or immobilization of other loops. While all loops are susceptible to the PB transition, the isolation means that, even in the presence of the same total dislocation density, many more PB transition events are required to immobilize that density.

Therefore, to sustain $\langle c + a \rangle$ slip and achieve high plastic strains and consequent ductility, we assert that the cross-slip rate of the screw segments must be much faster than the rate of the PB transition. Both processes are thermally activated with activation energies ΔG_{XS} and ΔE_{PB} , respectively, and initiated by nucleation over critical nucleation lengths l_{XS} and l_{PB} (see below), respectively. High ductility can be achieved if the total cross-slip nucleation rate R_{XS} , due to all possible L/l_{XS} nucleation sites along the screw segment, is much faster than the total PB transition rate R_{PB} , due to all possible L/l_{PB} nucleation segments along the edge segment. Using Arrhenius expression for the two rates, enhanced ductility at temperature T is thus predicted to be achievable when

$$R_{XS} \gg R_{PB},$$

$$v_0 \frac{L}{l_{XS}} \exp\left(-\frac{\Delta G_{XS}}{kT}\right) \gg v_0 \frac{L}{l_{PB}} \exp\left(-\frac{\Delta E_{PB}}{kT}\right), \quad (6.1)$$

6.2. Solute effects on pyramidal I/II energy difference: dilute limit

where v_0 is attempt frequency, k is the Boltzmann constant and T is the absolute temperature.

To quantify the ductility potency of any alloy composition, we introduce a “ductility index” χ such that the cross-slip rate R_{XS} exceeds the PB transition rate R_{PB} by a factor of 10^χ , i.e. $R_{XS} = 10^\chi R_{PB}$. Eq. 6.1 can then be rewritten to compute χ as

$$\chi = \frac{1}{\ln 10} \left[\ln \left(\frac{l_{PB}}{l_{XS}} \right) + \frac{\Delta E_{PB} - \Delta G_{XS}}{kT} \right]. \quad (6.2)$$

We consider $\chi = 1$ sufficient for ductility, i.e. a cross-slip rate that is ten times as fast as the PB transition rate can enable sufficient $\langle \mathbf{c} + \mathbf{a} \rangle$ plastic slip and ductility. For $\chi > 1$, high ductility is also achieved. However, much larger χ does not imply higher ductility; once the ductility condition is satisfied, the actual ductility is determined by many other factors, and primarily the work hardening rate that is not studied here. Once the ductility condition is achieved, the alloy is expected to fail in a normal “ductile” manner according to, for instance, the Considère criterion for the onset of necking in elastic-plastic materials. Conversely, $\chi < 0$ corresponds to poor ductility, i.e. the rate of cross-slip is slower than that of PB transition and so is insufficient to create enough plastic strain to overcome the detrimental immobilization caused by the PB transition.

The ductility index χ can be increased either by increasing ΔE_{PB} or by decreasing ΔG_{XS} . The PB transition is so energetically favorable (~ 0.3 eV/Å [228]) that alloying with a dilute solute is very unlikely to sufficiently increase ΔE_{PB} . As shown in Chapter 4, there is no systematic change in the average PB transition time across various realizations of a model Mg-3at.%Y random alloy, and thus the PB energy barrier remains close to that in pure Mg. In fact, there are perhaps larger variations in the transition time suggesting that solute fluctuations could slightly accelerate the process. Therefore in subsequent calculations, we use $\Delta E_{PB} = 0.5$ eV and $l_{PB} = 2$ nm [228] for pyramidal II favorable regime. In pyramidal I favorable regime, the cross-slip process need to compete with PB transition associated with pyramidal I $\langle \mathbf{c} + \mathbf{a} \rangle$ mixed dislocation, which has even lower energy barrier $\Delta E_{PB} = 0.3$ eV and the same critical length $l_{PB} = 2$ nm [229].

We thus aim to increase the ductility index χ by lowering the cross-slip barrier ΔG_{XS} by means of solid solution alloys. The solutes alter the dislocation energy difference ΔE^{I-II} by interacting with the two pyramidal dislocations participating in the cross-slip process. As described in Section 5.3, the cross-slip barrier is sensitively dependent on the energy difference, and therefore, certain solutes could enable high ductility in Mg alloys by lowering the energy difference ΔE^{I-II} . The effects of solutes on dislocation energy difference ΔE^{I-II} , affecting the cross-slip barrier ΔG_{XS} and ductility index χ , is the focus of following sections.

6.2 Solute effects on pyramidal I/II energy difference: dilute limit

The cross-slip barrier ΔG_{XS} , Eq. 5.4, is controlled by some intrinsic properties of Mg and by the pyramidal I/II screw dislocation energy difference ΔE^{I-II} . In pure Mg, ΔE^{I-II} is small (e.g.

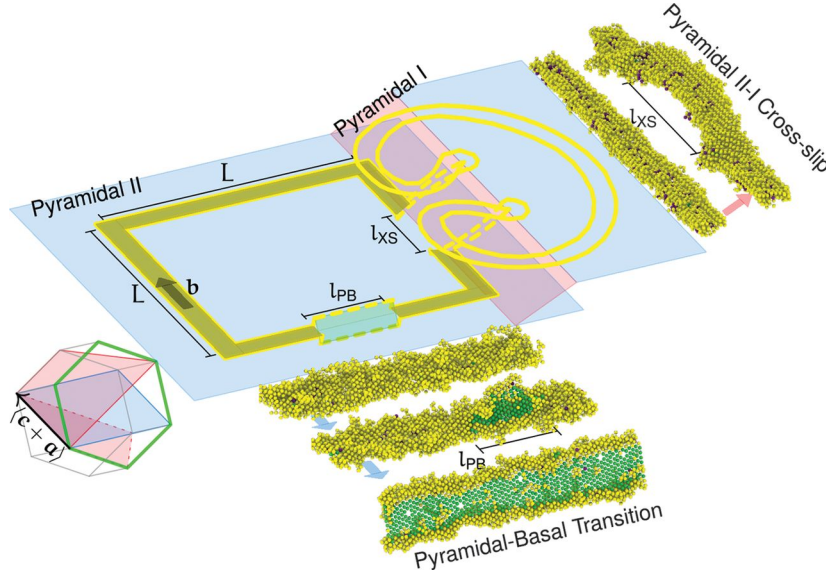


Figure 6.1 – **Schematic depiction of the mechanistic theory that involves the PB transition and cross-slip process associated with pyramidal $\langle c + a \rangle$ dislocations.** The two thermally activated processes operate during the expansion of a $\langle c + a \rangle$ dislocation loop of size $L \times L$ lying on the pyramidal II plane, and the competition between them determines the ductility. The detrimental PB transition of the edge segment locks the loop by generating a basal oriented sessile segment. Cross-slip of the screw part from pyramidal II to pyramidal I, and again double cross-slip back to pyramidal II, generates a new dislocation loop that can expand and counteract the effect of the PB transition on the original loop. Accompanying atomistic figures show non-hcp coordinated atoms colored by common-neighbor analysis with green = face-centered cubic, purple = body-centered cubic, and yellow = all others.

$\Delta E^{I-II} = 27$ meV/nm predicted by an accurate MEAM interatomic potential [230] and $\Delta E^{I-II} = 7 \pm 20$ meV/nm estimated from DFT studies) but crucial in increasing the cross-slip barrier ΔG_{XS} . At the relevant stress $\Delta \tau$ (see Section 6.4), the cross-slip barrier ΔG_{XS} in pure Mg is 0.6-0.9 eV, significantly exceeding the PB transition barrier ΔE_{PB} . Thus, $\chi < 0$ and the ductility in pure Mg is predicted, and observed to be, poor. However, if this energy difference ΔE^{I-II} can be reduced by introducing appropriate solute elements at sufficient concentrations, then the cross-slip rate is enhanced and the ductility condition $\chi > 1$ can be achieved. We thus consider a random substitutional multicomponent solid solution Mg alloy comprising solutes of types m solute having atomic concentrations c_m in the dilute limit $c_m \ll 1$ and $\sum_m c_m \ll 1$.

In the random solid solution alloy, the total system energy is modified by the interactions between the solute atoms and the dislocations. This interaction can have contributions from the solute interactions with the dislocation elastic stress field, the stacking fault in between the two dissociated partials of the $\langle c + a \rangle$ dislocation, and the cores of the two partials. We neglect the solute-solute interaction due to the dilute concentrations of solute elements. In the present problem, we have two different dislocations, pyramidal I and pyramidal II screw $\langle c + a \rangle$ dislocations. For a solute of type m at atomic site j , we denote the interaction energies

6.2. Solute effects on pyramidal I/II energy difference: dilute limit

with the pyramidal I and pyramidal II screw dislocations as $U_j^{I,m}$ and $U_j^{II,m}$, respectively. The cross-slip process transforms the pyramidal II dislocation into a pyramidal I dislocation, occurring within the pre-existing field of random solutes at the atomic sites j . Thus, for a segment of length l , there is a change in the total system energy $\Delta E_{\text{tot}}^{I-II}$ due to both the fundamental difference in pyramidal I and II energies and the solute/dislocation interactions that can be expressed as

$$\Delta E_{\text{tot}}^{I-II} = \Delta E_{\text{Mg}}^{I-II} l + \sum_m \sum_j s_j^m \Delta U_j^{I-II,m}, \quad (6.3)$$

where $\Delta U_j^{I-II,m} = U_j^{I,m} - U_j^{II,m}$. Here, s_j^m is a site-occupancy variable for a type m solute, with $s_j^m = 1$ if a solute of type m exists at atomic site j and 0 otherwise. The sum is performed over all sites j within an arbitrarily large cylinder centered on the dislocation having an axis of length l along the dislocation line direction. In the random alloy, the average of s_j^m over all sites j is the concentration c_m . c_m is also the probability of finding any one particular site occupied by a type m solute.

Far from cross-slip/dislocation core sites, the interaction between dislocation and a solute is purely elastic. Having the same Burgers vector and line direction, both pyramidal I and pyramidal II $\langle \mathbf{c} + \mathbf{a} \rangle$ screw dislocations have the same far-field elastic stresses due to the partial dislocations, and hence have the same interaction energies with the solutes. Therefore, solutes that are far from the dislocations do not affect the dislocation energy difference or the cross-slip barrier. There are then only some finite number of distinct atomic sites – here denoted by N_T – per unit b of line length that contribute to the dislocation energy difference. The sum over j in the above can thus be restricted to the N_T different sites per b , with l/b identical sites of each type along the line length l .

We can rewrite the above energy in terms of an average effect, in which there is a probability c_m of finding an m atom on every possible site j around the dislocation, plus a fluctuation associated with the actual random distribution of solutes along any one segment of length l . Eq. 6.3 is thus written as

$$\begin{aligned} \Delta E_{\text{tot}}^{I-II} &= \Delta E_{\text{Mg}}^{I-II} l + \underbrace{\sum_m \sum_j c_m \Delta U_j^{I-II,m}}_{\text{average effect}} + \underbrace{\sum_m \sum_j (s_j^m - c_m) \Delta U_j^{I-II,m}}_{\text{fluctuation effect}}, \\ &= \Delta E_{\text{Mg}}^{I-II} l + \frac{l}{b} \sum_m \sum_{i \in N_T} c_m \Delta U_i^{I-II,m} + \sum_m \sum_j (s_j^m - c_m) \Delta U_j^{I-II,m}, \\ &= \langle \Delta E^{I-II} \rangle l + \mathbb{F} [\Delta E^{I-II}(l)], \end{aligned} \quad (6.4)$$

where

$$\langle \Delta E^{I-II} \rangle = \Delta E_{Mg}^{I-II} + \frac{1}{b} \sum_m c_m \sum_{i \in N_T} \Delta U_i^{I-II,m} \quad (6.5)$$

is the average energy difference per unit length between the pyramidal I and pyramidal II $\langle \mathbf{c} + \mathbf{a} \rangle$ screw dislocations in the alloy, and

$$\mathbb{F} [\Delta E^{I-II}(l)] = \sum_m \sum_j (s_j^m - c_m) \Delta U_j^{I-II,m}. \quad (6.6)$$

The sum over i in the Eqs. 6.4 and 6.5 is over the distinct N_T atom sites within one Burgers vector b of dislocation length.

During cross-slip of dislocations in an alloy, the critical cross-slip length l_{XS} must enable the cross-slipped dislocation to expand. Local fluctuations in solutes could assist nucleation locally but the cross-slip nucleus would be unable to expand into the surrounding higher-energy regions. Thus, the relevant cross-slip nucleation length must be computed based only on the average effect of the solute atoms. Local fluctuations will then lower the barrier, but the nucleated segment will be able to expand through other local environments where nucleation would not typically be possible. The nucleation length is thus computed using only the average term $\langle \Delta E^{I-II} \rangle$ in Eq. 6.5, and the cross-slip length l_{XS} is then given by Eq. 5.3. Since there are L/l_{XS} statistically independent cross-slip nucleation segments across the entire screw part of the dislocation loop of length L , the total rate of cross-slip is

$$R_{XS} = \sum_{k=1}^{L/l_{XS}} v_0 \exp \left(-\frac{\Delta G_{XS}^k}{kT} \right), \quad (6.7)$$

where ΔG^k is the cross-slip barrier of the k^{th} segment

$$\begin{aligned} \Delta G_{XS}^k &= \Delta G_{XS,i} + \langle \Delta E^{I-II} \rangle l_{XS} + \mathbb{F}^k [\Delta E^{I-II}(l_{XS})] + \Gamma \Delta s - \Delta \tau b A, \\ &= \langle \Delta G_{XS} \rangle + \mathbb{F}^k [\Delta E^{I-II}(l_{XS})]. \end{aligned} \quad (6.8)$$

The quantity $\langle \Delta G_{XS} \rangle = \Delta G_{XS,i} + \langle \Delta E^{I-II} \rangle l_{XS} + \Gamma \Delta s - \Delta \tau b A$ is the average cross-slip barrier and is the same for all segments. The quantity $\mathbb{F}^k [\Delta E^{I-II}(l_{XS})]$ is the fluctuation contribution arising from the local spatial configuration of solutes in segment k . The total cross-slip rate can then be written as

$$R_{XS} = v_0 \exp \left(-\frac{\langle \Delta G_{XS} \rangle}{kT} \right) \sum_{k=1}^{L/l_{XS}} \exp \left(-\frac{\mathbb{F}^k [\Delta E^{I-II}(l_{XS})]}{kT} \right). \quad (6.9)$$

The fluctuation contribution $\mathbb{F}^k [\Delta E^{I-II}(l_{XS})]$, Eq. 6.6, depends on the actual random occupancy of the solutes in the atomic sites j by solute atoms m around the k^{th} cross-slip segment. The distribution of these fluctuation is a Gaussian distribution with zero mean and standard

6.2. Solute effects on pyramidal I/II energy difference: dilute limit

deviation $\sigma(\mathbb{F})$ given as

$$\sigma(\mathbb{F}) = \sqrt{\frac{l_{\text{XS}}}{b} \sum_m \sum_{i \in N_T} \sigma^2[s_i^m] (\Delta U_i^{\text{I-II},m})^2}. \quad (6.10)$$

Inserting the definition of \mathbb{F} , with only the Bernoulli random variables s_i^m and the l_{XS}/b identical sites of each type along the length l_{XS} , leads to

$$\sigma[l_{\text{XS}}] = \sigma(\mathbb{F}) = \sqrt{\frac{l_{\text{XS}}}{b} \sum_m c_m \sum_{i \in N_T} (\Delta U_i^{\text{I-II},m})^2}. \quad (6.11)$$

Here, we use the variance of s_i^m given by $\sigma^2[s_i^m] = c_m(1 - c_m) \approx c_m$ in the dilute limit.

Across the screw dislocation, there are L/l_{XS} independent dislocation segments where cross-slip nucleation can initiate. The thermally activated cross-slip at one segment can trigger the cross-slip process across the entire dislocation length. The cross-slip barrier, therefore, is controlled by those segments having the most favorable fluctuation of solutes for reducing the barrier. Thus, the cross-slip might be an extreme value problem but here we consider only typical frequent fluctuations by considering barriers reduced by one standard deviation $\sigma[l_{\text{XS}}]$, which occurs on average in $\approx 1/6$ of the segments and is a conservative measure. Our final expression for cross-slip rate of a length L of screw dislocation is then, using Eqs. 6.9 and 6.11,

$$R_{\text{XS}} = v_0 \frac{L}{l_{\text{XS}}} \exp\left(-\frac{\langle \Delta G_{\text{XS}} \rangle - \sigma[l_{\text{XS}}]}{kT}\right). \quad (6.12)$$

Recalling the ductility index χ defined as $R_{\text{XS}} = 10^\chi R_{\text{PB}}$, the ductility index χ including average and fluctuation effect is

$$\chi = \frac{1}{\ln 10} \left[\ln\left(\frac{l_{\text{PB}}}{l_{\text{XS}}}\right) + \frac{\Delta E_{\text{PB}} - (\langle \Delta G_{\text{XS}} \rangle - \sigma[l_{\text{XS}}])}{kT} \right]. \quad (6.13)$$

In the pyramidal I favorable regime of solute concentration, i.e. when $\langle \Delta E^{\text{I-II}} \rangle < 0$, we use absolute value of $\langle \Delta E^{\text{I-II}} \rangle$ in Eqs. 5.3 and 6.8 to determine the barrier for the cross-slip from pyramidal I to pyramidal II plane. The contribution from the fluctuation of the solute elements, nevertheless, remains same as computed by Eq. 6.11.

The above analysis pertains to the dilute limit, $c_m \ll 1$ as noted earlier. However, there is a lower limit to the concentration at which our statistical analysis above applies. The limit is easily identified in a binary alloy as follows. At a solute concentration $c^* = b/(l_{\text{XS}} N_T)$, there is, on average, only one solute among all the N_T type-sites over the entire critical cross-slip dislocation length l_{XS} . The statistical analysis above only applies to concentrations above this limit. The concentration c^* is thus the boundary between the dilute limit and the ultra dilute limit. The ultra dilute limit can be one of technological relevance, recalling that ductility is achieved in Mg-Ce alloys at ≈ 0.03 at.% Ce that is deep into the ultra dilute limit [138]. We thus address the ultra dilute limit in Section 6.5.

6.3 Solute-dislocation interaction energies

The mechanistic theory developed in previous subsections requires, as inputs, the site-specific solute-dislocation interaction energies. These energies can be computed, in principle, by atomistic simulations using semi-empirical potentials or first-principles methods such as DFT. However, there are no existing interatomic potentials for Mg alloys that have anywhere near the accuracy and scope needed for implementing the theory fully. In addition, the computational cost of DFT is prohibitive given the number of atomic sites that must be explored and the number of different solute elements that are of interest. This motivates careful consideration of the different possible contributions to the solute-dislocation interaction energies and approaches for their calculations.

Solute-dislocation interactions can be envisioned to arise from three main contributions: solutes interacting with the dislocation cores, elastic stress field, and stacking fault. Fig. 6.2 (a), (b) show the atomistic structures of the pyramidal II and pyramidal I screw dislocations, respectively, as computed using the MEAM_I interatomic potential for pure Mg. Despite different glide planes and stacking faults, the cores have nearly the same partial Burgers vectors and are quite similar. Comparing Figs. 6.2 (a), (b), which indicate non-hcp atoms as determined by common neighbor analysis [72, 209], the pyramidal I and pyramidal II core structures differ only by non-hcp atoms at the peripheries of the cores. The solute-core interactions, which are by far the most difficult to compute [36], may thus be similar and are, also, restricted to a limited number of atoms compared to the overall number of atomic sites around the entire dislocation structure.

The solute-stacking fault interaction is well-defined and computable in DFT. For the pyramidal faults in Mg, these interactions extend several atomic layers above and below the stacking fault plane [237]. A solute in each distinct plane has specific interaction energy with the fault. Figs. 6.2 (a), (b) indicate the planes above and below the two dislocations, respectively, noting that the pyramidal I plane has pairs of closely-spaced atom layers. The net solute-stacking fault interaction, per unit stacking fault area, is the sum of the interactions of the solutes on all planes near the fault plane. In the dilute limit, solute-solute interactions are neglected and each solute contributes independently from the other solutes. Ignoring the dislocation for the moment, the solute-stacking fault interactions change the average stacking fault energy as

$$\gamma(c) = \gamma_{\text{Mg}} + kc, \quad (6.14)$$

where γ_{Mg} is the stacking fault energy in pure Mg and k characterizes the average effect of the solute on the stacking fault [237]. The quantity k is computed as $k = 1/A_0 \sum_i U_{\text{SF}}(d_i)$ where $U_{\text{SF}}(d_i)$ is the interaction energy of a single solute in the layer at d_i^{th} plane from the stacking fault/slip plane (see Appendix C.2), and A_0 is the unit atomic area in the stacking fault plane. The values of k^{I} and k^{II} for the pyramidal I and II stacking faults, respectively, are computed in this manner for each solute using $U_{\text{SF}}(d_i)$ from DFT. The details of the DFT computations and results for solute-stacking fault interaction energies for various solutes are presented in

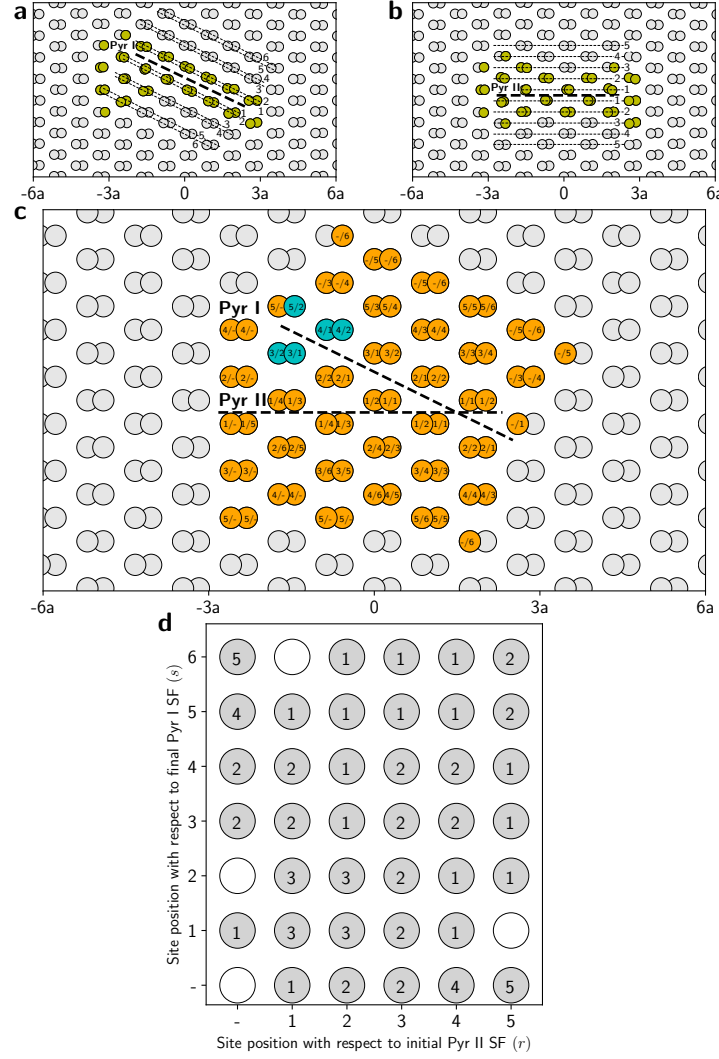


Figure 6.2 – **Change in correspondence of solute positions with respect to the two pyramidal $\langle c + a \rangle$ dislocations during the cross-slip.** The core structure of (a) $\langle c + a \rangle$ screw dislocation dissociated on the pyramidal I plane and on (b) the pyramidal II plane as obtained from the MEAM_I potential. Non-hcp core atoms, identified by the cna analysis, are colored in yellow. The dashed lines denote the position of atomic layers with respect to the stacking faults. $a = 3.19 \text{ \AA}$ is lattice parameter of Mg. (c) Atom correspondences with respect to initial pyramidal II and final cross-slipped pyramidal I dislocation in pure Mg. In the calculation of fluctuation and ultra dilute solute concentrations, the near core atoms consist mainly of those colored in orange and cyan. Atoms colored in cyan designate the atomic sites for which interaction energies in the ultra dilute limit require modification (see text). The first and second number of the number pair (r/s) placed on each atom denote, respectively, its position with respect to initial pyramidal II and final pyramidal I stacking fault planes, both of which are indicated by dashed lines. (d) The degeneracy $g(r/s)$ of each pair (r/s) as determined from Fig. (c).

Appendix C.

For cross-slip, we require the change in dislocation energy upon cross-slip. Fig. 6.2(c) shows the pyramidal II and I dislocations together, which are connected through the cross-slip. The notation r/s indicates the change in identification of a given atom position from being associated with the stacking fault plane r in the pyramidal II fault to plane s in the pyramidal I fault that occurs due to cross-slip. Sites with no r/s , or with $r/-$ or $-/s$, designation are considered outside the influence of the stacking fault(s). Each atomic site i thus has an associated pair of initial/final planes r/s . Different physical sites i can have the same r/s , and Fig. 6.2(d) shows the number of sites, or degeneracy $g(r/s)$, for each r/s for the atomistic structure of the MEAM_I Mg dislocations in Figs. 6.2 (a), (b), and (c). The change in total solute-dislocation interaction energy due to the cross-slip can then be written as

$$\sum_{i \in N_T} \Delta U_{SF,i}^{I-II,m} = \sum_{(r/s)} g(r/s) \Delta U_{SF,(r/s)}^{I-II,m}, \quad (6.15)$$

where $\Delta U_{SF,(r/s)}^{I-II,m} = U_{SF,s}^{I,m} - U_{SF,r}^{II,m}$ is the difference in interaction energies of type m solute with pyramidal I and pyramidal II stacking faults, with solute being at s^{th} plane from pyramidal I fault and at r^{th} plane from pyramidal II fault.

The above specific results pertain to the core structure of the MEAM_I interatomic potential. The pure Mg stacking fault energies in the MEAM_I potential are close to but not precisely those computed by more-accurate DFT (see Table 3.2), however, so that the partial dislocation spacing in the MEAM_I potential differs slightly from the spacing observed in DFT studies/elasticity calculations. Thus, while illustrative (and used below for some atomistic studies for single solutes), this does not quite capture the expected Mg stacking fault contribution fully. We thus adopt a continuum description of the average energy difference as follows. As stated above, we consider here only the solute/stacking fault interaction. Using anisotropic elasticity [232], we compute the partial separation distance w_{SF} (stacking fault width), for both pyramidal I and pyramidal II screw dislocations. The energy due to the stacking fault is then $w_{SF}\gamma(c)$ for each dislocation. In the dilute limit, the results can be expanded to lowest order in the solute concentration, using Eq. 6.14, as $w_{SF}(\gamma_{Mg} + kc)$. Thus the solutes lead to additional energy of $w_{SF}kc$ relative to pure Mg. In pure Mg, the stacking fault width w_{SF} is $w_{SF} = K_{12}/\gamma_{Mg}$ where K_{12} is an anisotropic elasticity energy prefactor completely determined by the anisotropic elastic constants, Burgers vector, and dislocation line direction. The effect of dilute solutes in changing the partial separation is second order in concentration, hence neglected. As detailed in Appendix D, considering only the stacking fault contribution to the pyramidal I/II energy difference, we obtain

$$\begin{aligned} \langle \Delta E^{I-II} \rangle &= \Delta E_{Mg}^{I-II} + \sum_m \left[\frac{K_{12}^I k_m^I}{\gamma_{Mg}^I} - \frac{K_{12}^{II} k_m^{II}}{\gamma_{Mg}^{II}} \right] c_m, \\ &= \Delta E_{Mg}^{I-II} + \sum_m \Delta E_{avg,SF}^{I-II,m} c_m, \end{aligned} \quad (6.16)$$

where we have generalized to multiple solutes in the dilute limit, and $\Delta E_{\text{avg,SF}}^{\text{I-II},m} = \left[\frac{K_{12}^{\text{I}} k_m^{\text{I}}}{\gamma_{\text{Mg}}^{\text{I}}} - \frac{K_{12}^{\text{II}} k_m^{\text{II}}}{\gamma_{\text{Mg}}^{\text{II}}} \right]$ represents the average effect on the dislocation energy difference due to interactions of stacking fault and solute type m . The random spatial distribution of solutes leads to fluctuations in the energy difference due to solute-stacking fault energies. Following the notation introduced earlier, the standard deviation of the energy difference $\sigma[l_{\text{XS}}]$ within dislocation length l_{XS} is obtained by

$$\begin{aligned} \sigma[l_{\text{XS}}] &= \sqrt{\frac{l_{\text{XS}}}{b} \sum_m c_m \sum_{(r/s)} g(r/s) \left(\Delta U_{\text{SF},(r/s)}^{\text{I-II},m} \right)^2}, \\ &= \sqrt{\frac{l_{\text{XS}}}{b} \sum_m c_m \left(\Delta E_{\text{fluc,SF}}^{\text{I-II},m} \right)^2}, \end{aligned} \quad (6.17)$$

where $\Delta E_{\text{fluc,SF}}^{\text{I-II},m} = \sqrt{\sum_{(r/s)} g(r/s) \left(\Delta U_{\text{SF},(r/s)}^{\text{I-II},m} \right)^2}$ characterizes the intrinsic fluctuation of solute type m contributing in the cross-slip barrier. We report the characteristic average effect $\Delta E_{\text{avg,SF}}^{\text{I-II},m}$ and fluctuation effect $\Delta E_{\text{fluc,SF}}^{\text{I-II},m}$ of various solutes, considered in this work, in Table 6.1, obtained from DFT computations of $U_{\text{SF}}(d_i)$.

The elastic interaction of the solute misfit strain tensor with the dislocation elastic stress field is frequently the most important contribution for solid solution strengthening [234], and even in the core regions. In principle, the elastic contributions can be computed using the elastic field created by the Burgers vector distribution of slip, as in a Peierls-Nabarro model. This elastic energy is then added to the contribution from the solute/stacking fault interactions [36, 204, 234]. However, in practice, the pyramidal stacking faults have a significant out-of-plane dilation and in-plane strains relative to the perfect hcp crystal. These strain fields generate additional elastic stresses around the actual dislocation but they cannot easily be disentangled from the computation of solute-stacking fault interactions. Hence, the simple addition of energies due to solute elastic (mechanical) and stacking fault (chemistry) interactions involves some uncontrolled double-counting of the elastic effects. It is thus not reliable to additively include the elastic interactions into the model. Fortunately, for most solutes, the elastic interaction energy is small compared to the stacking fault interaction energy.

While not generally included in the model, we show here the calculations of the solute-dislocation elastic interaction energy for hcp Mg. A solute of type m generates a tetragonal misfit strain $\epsilon_m^{\text{misfit}}$ when introduced into the bulk hcp lattice. In the coordinate system of the standard hcp unit cell where \mathbf{x}_1 is along $[1\bar{2}10]$, \mathbf{x}_2 along $[10\bar{1}0]$ and \mathbf{x}_3 along $[0001]$ directions, there are then three misfit strain compents $\epsilon_{11,m}^{\text{misfit}} = \epsilon_{22,m}^{\text{misfit}}$ and $\epsilon_{33,m}^{\text{misfit}}$. These misfit strain components have been computed via first-principles DFT and are presented in Table 6.1.

A solute at site i has an elastic interaction energy with the dislocation stress field $\boldsymbol{\sigma}_i$ of $-V_0 \boldsymbol{\sigma}_i : \epsilon_m^{\text{misfit}}$ where V_0 is the atomic volume of bulk Mg. For a random distribution of solutes, the average and fluctuation of pyramidal I/II energy difference induced by the solute misfit strain-dislocation interaction are then the averaged sum and fluctuation of the differences over all

sites,

$$\langle \Delta E_P \rangle = -\frac{V_0}{b} \sum_m \sum_{i \in N_T} c_m \left[\left(\Delta \sigma_{11,i}^{I-II} + \Delta \sigma_{22,i}^{I-II} \right) \epsilon_{11,m}^{\text{misfit}} + \Delta \sigma_{33,i}^{I-II} \epsilon_{33,m}^{\text{misfit}} \right], \quad (6.18)$$

$$\sigma[l_{XS}] = \sqrt{\frac{l_{XS} V_0^2}{b} \sum_m \sum_{i \in N_T} c_m \left[\left(\Delta \sigma_{11,i}^{I-II} + \Delta \sigma_{22,i}^{I-II} \right) \epsilon_{11,m}^{\text{misfit}} + \Delta \sigma_{33,i}^{I-II} \epsilon_{33,m}^{\text{misfit}} \right]^2}, \quad (6.19)$$

where $\Delta \sigma_i^{I-II} = \sigma_i^I - \sigma_i^{II}$, and the summation over i includes all distinct N_T atomic sites within one Burgers vector length b of dislocation line.

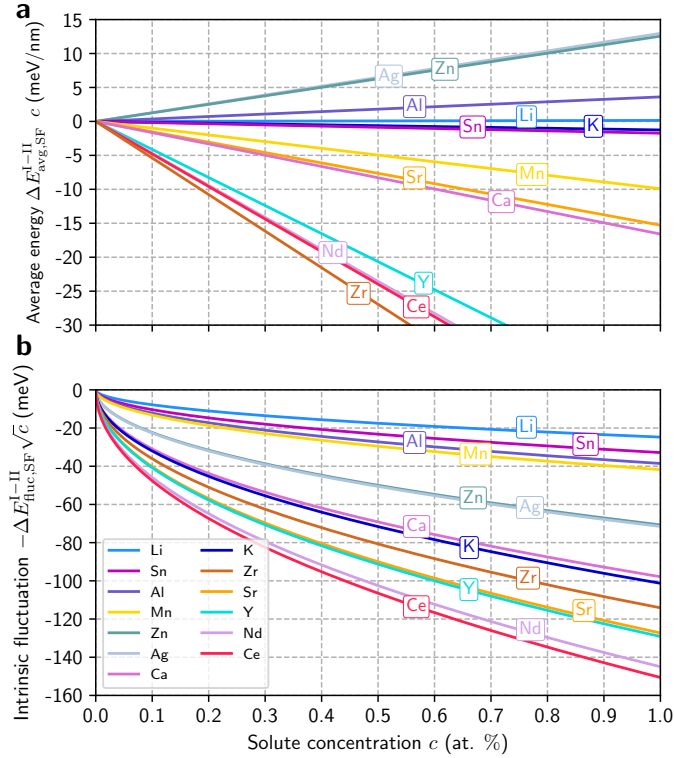


Figure 6.3 – Average and fluctuation contributions of solutes in dislocation energy difference. Fig. (a) presents the variation of the average effect, and Fig. (b) shows the variation of the intrinsic fluctuation with various solutes concentrations. In (a), slopes of Zn, Sn, and Ce are decreased marginally for clarity, as their curves coincide with that of Ag, K, and Nd, respectively. Moreover, the precise values of slopes are presented in Table 6.1. For all solutes, except Al, the interaction is approximated by solute/stacking fault interaction; for Al, solute misfit/dislocation interaction is considered in determining the average and fluctuation effect.

As an example, the total stress difference $\sum_{i \in N_T} \Delta \sigma_i$ computed for the dislocations predicted by the MEAM_I potential (see Fig. 6.2(a), (b)), using the atomic virial stress and the reference perfect-crystal atomic volume, are $(V_0/b) \sum_{i \in N_T} \left[\Delta \sigma_{i,11}^{I-II} + \Delta \sigma_{i,22}^{I-II} \right] = -6.107$ eV/nm, and $(V_0/b) \sum_{i \in N_T} \Delta \sigma_{i,33}^{I-II} = 7.317$ eV/nm. For an isotropic misfit strain, the two contributions nearly cancel. However, the misfit strain tensor for solutes in Mg is generally tetragonal, leading to

6.3. Solute-dislocation interaction energies

less cancellation. With the misfit strain components shown in Table 6.1, the elastic interaction is found to be small in comparison to the solute-stacking fault interaction for most solutes, and thus can be neglected. For those solutes where the average solute-stacking fault interaction is small (Al, Li, K, Sn), the elastic contribution, although still small, is not negligible by comparison. However, due to an unknown degree of double-counting of the elastic effects, the elastic contribution should not be added to the stacking fault contribution.

We further compare the solute-stacking-fault interaction energy for each solute position, as computed by DFT, with the interaction energy arising from the interaction of the solute misfit strain with the stacking fault stress. The solute misfit strain is determined from DFT computations, and the local stacking fault stresses are computed using the MEAM_I potential. Among Al, Li, K, and Sn, the DFT results and elastic results match well only for Al, as shown in Fig. C.1. Therefore, in Al and only in Al, we can neglect the DFT solute-stacking fault interaction and use the solute misfit strain-dislocation stress contribution for the total interaction energy. For all other solutes, only solute-stacking fault interaction can be used, which automatically contains the misfit strain-stacking fault stress interaction energy.

Table 6.1 – Properties of various solutes in Mg. Characteristic average $\Delta E_{\text{avg,SF}}^{\text{I-II}}$ and fluctuation $\Delta E_{\text{fluc,SF}}^{\text{I-II}}$ contribution, as defined in Eqs. 6.16 and 6.17, of all solutes, except Al, are determined using DFT computed solute/stacking fault interaction. For Al, we employ solute misfit/dislocation stress interaction energy. Misfit strain and misfit volume are computed from DFT.

Solute	$\Delta E_{\text{avg,SF}}^{\text{I-II}}$ (meV/nm)	$\Delta E_{\text{fluc,SF}}^{\text{I-II}}$ (meV)	Misfit strain ($\epsilon_{11}^{\text{misfit}}, \epsilon_{33}^{\text{misfit}}$)	Misfit volume
Ag	1297	715	(-0.179, -0.168)	-0.526
Zn	1295	707	(-0.151, -0.166)	-0.468
Al	361	386	(-0.108, -0.139)	-0.355
Li	15	247	(-0.055, -0.069)	-0.179
K	-126	1013	(0.394, 0.370)	1.158
Sn	-134	328	(0.030, -0.020)	0.040
Mn	-991	418	(-0.173, -0.255)	-0.601
Sr	-1528	1273	(0.425, 0.368)	1.218
Ca	-1659	978	(0.265, 0.223)	0.753
Y	-4131	1291	(0.223, 0.120)	0.566
Nd	-4711	1450	(0.307, 0.191)	0.805
Ce	-4754	1506	(0.355, 0.232)	0.942
Zr	-5386	1141	(0.046, -0.148)	-0.056

Fig. 6.3(a) shows the effects of various solutes on the average energy difference of pyramidal $\langle \mathbf{c} + \mathbf{a} \rangle$ screw dislocations. Solute decreasing the energy difference would promote the cross-slip process, enabling ductility. Thus, on the basis of the average effect we can readily categorize Ag and Zn as strongly unfavorable; Sr, Ca, REs and Zr as highly favorable; and Mn as moderately favorable. Solute such as Al, Li, Sn, K have very weak effects on the average energy difference, and therefore, fluctuation effects could prove to be crucial in deciding the overall ductility at a particular concentration. Furthermore, since Al, on average, tends to increase the energy difference, we expect low ductility at high Al concentrations. Fig. 6.3(b)

shows the concentration-dependent favorable intrinsic fluctuation of the same solutes, which is identified as $-\Delta E_{\text{fluc,SF}}^{\text{I-II}} \sqrt{c}$. This plot demonstrates the relative fluctuation effect of the solutes. We use negative sign to stress that fluctuation is always favorable in assisting the cross-slip process. REs, Sr, Zr, and Ca have large fluctuation which further shows the potency of these solutes in achieving ductility. One interesting case is that of K, which has almost no average effect but large fluctuation, making it a favorable solute. Zn and Ag have intermediate fluctuation which could mitigate the detrimental average effect at smaller concentrations. Al, Sn, and Li have weaker average as well as fluctuation effects of which combined effect may produce ductility at some intermediate concentration ranges. Mn is the solute with a moderate average and relatively small fluctuation effects. Nonetheless, it could be effective in enabling ductility. These plots help us roughly identify unfavorable and favorable solutes, which agree with broad experimental observations. However, precise quantitative prediction requires additional information and consideration, and is presented in the next Chapter 7.

6.4 Net shear stress $\Delta\tau$ driving the cross-slip process

The cross-slip model the cross-slip model requires, as input, the value of resolved shear stress $\Delta\tau$ that drives bow-out of the $\langle \mathbf{c} + \mathbf{a} \rangle$ screw dislocation on higher energy slip-plane. This section determines $\Delta\tau$, for both pyramidal II and pyramidal I favorable regimes, in relation to the pyramidal I and pyramidal II Peierls stresses and the texture, for uniaxial loading along the rolling direction for common rolling textures.

For plastic deformation at quasi-static strain rates, dislocations are always nearly stationary at positions of local equilibrium (zero *net* resolved shear stress on each segment), independent of the applied stress. The applied stress τ_{app} can increase above the fundamental lattice Peierls stress τ_{P} and additional stresses due to pinning by forest dislocation junctions, precipitates, solute fields, and long-range dislocation interactions. For forest junctions and precipitates, the dislocation is pinned only in certain segments but then bows out until all segments along the line experience zero force (equilibrium). These additional stresses are collectively represented by a local “backstress” τ_{b} acting on the dislocation segment. Dislocations then move, and plasticity occurs, by thermal activation of the dislocations over the barriers created by these obstacles and fields. “Dislocation dynamics”, i.e. the kinetics of dislocation glide, is thus rarely actually important, except in situations where dislocation mobilities are very slow (such as bcc crystals at low temperatures).

6.4.1 Pyramidal II favorable regime

In the pyramidal II favorable regime, we assume that $\langle \mathbf{c} + \mathbf{a} \rangle$ screw dislocation glides on pyramidal II in local equilibrium. At local equilibrium, the total shear stress on a pyramidal II dislocation segment due to the applied resolved shear stress and all backstresses is then equal to the Peierls stress,

$$\tau_{\text{II}} = \tau_{\text{app}} - \tau_{\text{b}} = \tau_{\text{II,P}}. \quad (6.20)$$

When the pyramidal II dislocation is in equilibrium, cross-slip is driven by the net resolved shear stress $\Delta\tau$ acting on a possible pyramidal I dislocation at the same position. As shown in Fig. 6.4 (a), we consider one pyramidal II and two cross-slip pyramidal I planes described in a coordinate system where x_1 , x_2 and x_3 are oriented along a ($[2\bar{1}\bar{1}0]$), $c \times a$ ($[01\bar{1}0]$) and c ($[0001]$) directions, respectively.

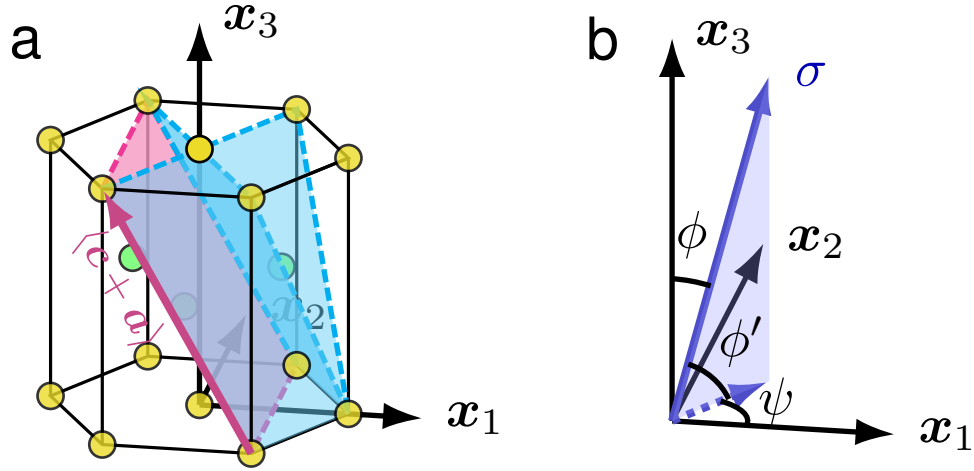


Figure 6.4 – **Representation of coordinate system and applied load during the cross-slip process.** (a) Schematic of the pyramidal I and the pyramidal II planes available to the $\langle c + a \rangle$ dislocations for cross-slip. (b) The coordinate system and direction of applied uniaxial stress σ are used in the calculation of net driving stress. The coordinate system is the same as that used in (a).

A uniaxial stress of magnitude σ is assumed to be applied as shown in Fig. 6.4(b). This uniaxial stress σ – generating shear stresses τ_{app} and τ_b – is at an angle ϕ from x_3 ($\langle c \rangle$) axis and whose projection on basal plane ($x_1 - x_2$) is at angle ψ from the x_1 ($\langle a \rangle$) axis. The resolved shear stress on the shown pyramidal II plane is

$$\tau_{II} = \sigma (0.446 \sin^2 \phi \cos^2 \psi - 0.452 \sin \phi \cos \phi \cos \psi - 0.446 \cos^2 \phi), \quad (6.21)$$

and the resolved shear stresses acting on the cross-slip pyramidal I planes accessible to this pyramidal II segment are

$$\tau_I = \sigma (0.4 \sin^2 \phi \cos^2 \psi - 0.405 \sin \phi \cos \phi \cos \psi - 0.4 \cos^2 \phi \pm 0.231 \sin^2 \phi \sin \psi \cos \psi \mp 0.376 \sin \phi \cos \phi \sin \psi). \quad (6.22)$$

Substituting Eq. 6.29 and $\tau_{II} = \tau_{II,P}$ into the above, and denoting the pyramidal I Peierls stress as $\tau_{I,P}$, lead to the net driving stress acting on the pyramidal I plane, for the shown triplets, as a function of orientation of load axis (ϕ, ψ)

$$\Delta\tilde{\tau}(\phi, \psi) = 0.89\tau_{II,P} - \tau_{I,P} + \sigma |0.231 \sin^2 \phi \sin \psi \cos \psi - 0.376 \sin \phi \cos \phi \sin \psi|, \quad (6.23)$$

where we consider the pyramidal I plane with the larger of the two possible stresses, leading to the absolute value term. Furthermore, we note that there are other five similar triplets of pyramidal II/pyramidal I planes, situated $\pi/3$ degrees apart about \mathbf{x}_3 axis. Thus for a given orientation of load (ϕ, ψ) , the net resolved shear stress is the maximum of all six triplets, which is

$$\Delta\tau(\phi, \psi) = \max\{\Delta\tilde{\tau}(\phi, \psi + k\pi/3) : k = 0, 1, \dots, 5\}. \quad (6.24)$$

The typical net driving shear stress $\Delta\tau$ for pyramidal II/I cross-slip in a polycrystalline sample then depends on the polycrystalline texture.

We first consider strong basal texture, typical of rolled Mg [84, 219], where the $\langle \mathbf{c} \rangle$ axes of the grains are predominantly aligned along the normal direction of the sheet. The uniaxial load σ is applied along the rolling direction, which lies along some random directions in the basal plane. For this case, $\phi = \pi/2$ while $\psi \in (-\pi, \pi]$ varies randomly from grain to grain. The net driving shear stress is then estimated by averaging over the angle ψ which, due to symmetry of the six triplets of pyramidal II/I planes, reduces to

$$\begin{aligned} \Delta\tau &= \frac{3}{\pi} \int_{-\pi/6}^{\pi/6} \Delta\tau(\phi = \pi/2, \psi) d\psi, \\ &= 0.89\tau_{II,P} - \tau_{I,P} + 0.11\sigma. \end{aligned} \quad (6.25)$$

At the onset of yielding, $\sigma = \tau_{II,P}/0.446$ and hence

$$\Delta\tau = 0.89\tau_{II,P} - \tau_{I,P} + 0.247\tau_{II,P} = 1.137\tau_{II,P} - \tau_{I,P}. \quad (6.26)$$

The MEAM_I Peierls stresses for the screw dislocation at $T=300$ K are $\tau_{II,P} \approx 45$ MPa and $\tau_{I,P} \approx 35$ MPa. These lead to single crystal $\langle \mathbf{a} \rangle$ axis tension yield stress of 100 MPa comparable to experiments [18]. For these values, we obtain $\Delta\tau = 16$ MPa. As an example, for lower values $\tau_{II,P} \approx 20$ MPa and $\tau_{I,P} \approx 10$ MPa, we estimate $\Delta\tau = 13$ MPa.

We next consider a polycrystal with basal texture split into two lobes and tilted toward the rolling direction - so called DPRD (double-peak basal pole tilted in the rolling direction) texture - which is commonly observed in Mg alloys [3, 6, 84, 126, 182]. For a basal pole tilted at $\pm 15^\circ$ towards the rolling direction, $\phi = 75^\circ$. Again, averaging over the in-plane angle $\psi \in (-\pi/6, \pi/6]$ and using $\sigma = \tau_{II,P}/0.446$, yields

$$\Delta\tau = 1.269\tau_{II,P} - \tau_{I,P}. \quad (6.27)$$

For the same values $\tau_{II,P} = 45$ MPa and $\tau_{I,P} = 35$ MPa, we obtain $\Delta\tau = 22$ MPa. This value is rather larger than the value of $\Delta\tau = 16$ MPa obtained for the strong basal texture, indicating that cross-slip should be much more favorable, and ductility much higher, in polycrystals possessing the DPDR texture. In fact, we would argue that it is the solute-accelerated double cross-slip process itself that enables the $\langle \mathbf{c} + \mathbf{a} \rangle$ slip that creates the DPDR texture, which is

then naturally leading to enhanced ductility.

The above analysis also highlights that increasing the stress level could increase the $\Delta\tau$, and thus decrease the cross-slip barrier, and in turn, initiate increased slip of pyramidal I $\langle c + a \rangle$ dislocations. This may explain the observed onset of pyramidal I slip in single-crystal deformation of pure Mg at stresses somewhat above the initial yield stress [14, 167]. Furthermore, the tilting of basal pole due to DPRD texture results in higher net driving shear stress $\Delta\tau$, which can enable the cross-slip process even in alloys possessing DPRD texture and unfavorable solutes such as Zn.

6.4.2 Pyramidal I favorable regime

We now estimate the driving stress $\Delta\tau$ when pyramidal I is more stable than pyramidal II $\langle c + a \rangle$ screw dislocation. We assume the pyramidal I glide to happen in equilibrium, i.e., at zero net stress. At equilibrium, the total shear stress on a pyramidal I dislocation segment due to applied stresses and backstresses τ_b is equal to the Peierls stress,

$$\tau_I = \tau_{\text{app}} - \tau_b = \tau_{I,P}. \quad (6.28)$$

Following the same coordinate system shown in Fig. 6.4, the resolved shear stress on the shown pyramidal II plane is

$$\tau_{II} = \sigma (0.446 \sin^2 \phi \cos^2 \psi - 0.452 \sin \phi \cos \phi \cos \psi - 0.446 \cos^2 \phi), \quad (6.29)$$

and the resolved shear stresses acting on the cross-slip pyramidal I planes accessible to this pyramidal II segment are

$$\tau_I = \sigma (0.4 \sin^2 \phi \cos^2 \psi - 0.405 \sin \phi \cos \phi \cos \psi - 0.4 \cos^2 \phi) \quad (6.30)$$

$$\pm 0.231 \sin^2 \phi \sin \psi \cos \psi \mp 0.376 \sin \phi \cos \phi \sin \psi, \quad (6.31)$$

Substituting Eq. 6.31 and $\tau_I = \tau_{I,P}$ into the $\Delta\tilde{\tau} = \tau_{II} - \tau_{II,P}$, and denoting the pyramidal II Peierls stress as $\tau_{II,P}$, lead to the net driving stress acting on the pyramidal II plane, for the shown triplets, as a function of orientation of load axis (ϕ, ψ)

$$\Delta\tilde{\tau}(\phi, \psi) = 1.125\tau_{I,P} - \tau_{II,P} + 1.125\sigma |0.231 \sin^2 \phi \sin \psi \cos \psi - 0.376 \sin \phi \cos \phi \sin \psi|, \quad (6.32)$$

where we consider the pyramidal I plane with the larger of the two possible stresses, leading to the absolute value term. Following the same procedure, as was performed in pyramidal II favorable regime, i.e. averaging over the angle ψ , we obtain the driving stress for strong basal texture as

$$\begin{aligned} \Delta\tau(\phi, \psi) &= \max\{\Delta\tilde{\tau}(\phi, \psi + k\pi/3) : k = 0, 1, \dots, 5\}, \\ \Delta\tau &= \frac{3}{\pi} \int_{-\pi/6}^{\pi/6} \Delta\tau(\phi = \pi/2, \psi) d\psi, \\ &= 1.125\tau_{I,P} - \tau_{II,P} + 0.124\sigma. \end{aligned} \quad (6.33)$$

For $\sigma = 100$ MPa, which is comparable to experimental yield stresses of Mg alloys, the net resolved shear stress on pyramidal II plane is $\Delta\tau = 1.125\tau_{I,P} - \tau_{II,P} + 12.4$. The MEAM_I Peierls stresses for the screw dislocation at $T=300$ K leads to $\Delta\tau \approx 7$ MPa. At higher stress level of $\sigma = 200$ MPa, the net resolved shear stress becomes $\Delta\tau \approx 19$ MPa. Furthermore, solute strengthening on dislocations in Mg-Y alloy would modify the net resolved shear stress. Since the interaction of RE solutes with pyramidal I stacking fault is stronger than that with pyramidal II stacking fault, we expect the net resolved shear stress to increase with solute concentrations.

Next, for the basal pole tilted $\pm 15^\circ$ towards the rolling direction, $\phi = 75^\circ$. Again averaging over $\psi \in (-\pi/6, \pi/6]$ yields

$$\Delta\tau = 1.125\tau_{I,P} - \tau_{II,P} + 0.19\sigma. \quad (6.34)$$

For the tilted basal pole using $\tau_{II,P} \approx 45$ MPa, $\tau_{I,P} \approx 35$ MPa and $\sigma = 100$ MPa, we obtain $\Delta\tau = 13$ MPa.

The magnitude of the driving stress $\Delta\tau$ is estimated to be close in both pyramidal I and pyramidal II favorable cases, and so $\Delta\tau = 20$ MPa is used in the subsequent calculations presented in Chapter 7.

6.5 Solute effects on dislocation energy difference ΔE^{I-II} : ultra dilute limit

Any single solute within the N_T distinct types of sites around the pyramidal II/I dislocations can change the dislocation energy difference and thus change the cross-slip barrier. $N_T = 45$ is taken in this work which is estimated by looking at the number of sites around dislocations having appreciable interaction energy difference ΔU_i^{I-II} . Single solute arises in the ultra dilute limit and requires special treatment because the previous statistical analyses in the dilute limit fail. To clearly demonstrate the effects of solutes in the ultra dilute limit, the discussion here focuses on binary alloys; ternary and quaternary alloys are discussed in the Appendix B. Similar reasoning can be easily extended to analyze other higher-order alloys.

At solute concentrations below c^* , i.e. the ultra dilute limit, there will be one solute or no solute among the N_T sites, on average, somewhere within each cross-slip length l_{XS} . For a dislocation of length L with L/l_{XS} cross-slip nucleation segments, a fraction c/c^* contain one solute while the remaining fraction $(1 - c/c^*)$ are solute-free. The latter have a cross-slip activation barrier equal to that of pure Mg, ΔG_{XS}^{Mg} . The cross-slip rate R_{XS} in the dislocation

6.5. Solute effects on dislocation energy difference ΔE^{I-II} : ultra dilute limit

length L is then the sum of the rates over all segments,

$$R_{XS} = \underbrace{\sum_{k=1}^{(1-\frac{c}{c^*})\frac{L}{l_{XS}}} v_0 \exp\left(-\frac{\Delta G_{XS}^{Mg}}{kT}\right)}_{\text{pure Mg}} + \underbrace{\sum_{k=1}^{\frac{c}{c^*}\frac{L}{l_{XS}}} v_0 \exp\left(-\frac{\Delta G_{XS}^k}{kT}\right)}_{\text{segments containing on solute}}, \quad (6.35)$$

$$= \left(1 - \frac{c}{c^*}\right) \frac{L}{l_{XS}} v_0 \exp\left(-\frac{\Delta G_{XS}^{Mg}}{kT}\right) + \sum_{k=1}^{\frac{c}{c^*}\frac{L}{l_{XS}}} v_0 \exp\left(-\frac{\Delta G_{XS}^k}{kT}\right).$$

For the cross-slip segments containing one solute, the probability of containing two solutes is $\sim c^2$, which is negligible. Thus, it suffices to examine one segment of length l_{XS} containing a single solute. The total energy difference between pyramidal I and II dislocations of length l_{XS} having one solute among N_T sites is

$$\Delta E_{\text{tot}}^{I-II} = \Delta E_{Mg}^{I-II} l_{XS} + \sum_{i \in N_T} s_i \Delta U_i^{I-II}, \quad (6.36)$$

where $s_i = 1$ for the site i containing the solute and $s_i = 0$ for all other sites ($\langle s_i \rangle = 1/N_T$ and $\sigma^2[s_i] \approx 1/N_T \forall i$). To be consistent with the dilute limit, we separate this into average and fluctuation parts as

$$\begin{aligned} \Delta E_{\text{tot}}^{I-II} &= \Delta E_{Mg}^{I-II} l_{XS} + \frac{1}{N_T} \sum_{i \in N_T} \Delta U_i^{I-II} + \sum_{i \in N_T} \left(s_i - \frac{1}{N_T}\right) \Delta U_i^{I-II}, \\ &= \langle \Delta E_{\text{tot}}^{I-II} \rangle + \mathbb{F}[\Delta E_{\text{tot}}^{I-II}], \end{aligned} \quad (6.37)$$

where $\mathbb{F}[\Delta E_{\text{tot}}^{I-II}] = \sum_{i \in N_T} \left(s_i - \frac{1}{N_T}\right) \Delta U_i^{I-II}$ is the additional fluctuation term. Considering all the different segments k , the total cross-slip rate becomes

$$R_{XS} = \left(1 - \frac{c}{c^*}\right) \frac{L}{l_{XS}} v_0 \exp\left(-\frac{\Delta G_{XS}^{Mg}}{kT}\right) + v_0 \exp\left(-\frac{\Delta G_{XS}^{Mg} + \frac{1}{N_T} \sum_{i \in N_T} \Delta U_i^{I-II}}{kT}\right) \sum_{k=1}^{\frac{c}{c^*}\frac{L}{l_{XS}}} \exp\left(-\frac{\mathbb{F}^k[\Delta E_{\text{tot}}^{I-II}]}{kT}\right). \quad (6.38)$$

As before, we take a typical fluctuation corresponding to the standard deviation of the energy,

$$\sigma = \sqrt{\frac{1}{N_T} \sum_{i \in N_T} (\Delta U_i^{I-II})^2}. \quad (6.39)$$

The total cross-slip rate is then

$$R_{XS} = \frac{L}{l_{XS}} v_0 \exp\left(-\frac{\Delta G_{XS}^{Mg}}{kT}\right) \left[1 + \frac{c}{c^*} \left\{ \exp\left(-\frac{\frac{1}{N_T} \sum_{(r/s)} g(r/s) \Delta U_{(r/s)}^{I-II} - \sqrt{\frac{1}{N_T} \sum_{(r/s)} g(r/s) (\Delta U_{(r/s)}^{I-II})^2}}{kT}\right) - 1 \right\} \right]. \quad (6.40)$$

The ductility index χ is then computed by setting $R_{XS} = 10^\chi R_{PB}$. This result bridges naturally to the dilute limit and involves no additional quantities. Care must be taken for certain sites, however, as discussed in the next section.

6.5.1 Cross-slip of pyramidal $\langle c + a \rangle$ screw dislocations in the presence of a single solute

In the previous Eq. 6.40, the summation includes all the N_T atomic sites. If the single solute is located in a position such that the energy change is unfavorable for cross-slip ($\Delta U_i^{I-II} = U_i^I - U_i^{II} > 0$), then the cross-slip barrier will always increase by that energy change. Such sites are irrelevant since cross-slip nucleation will occur in some other regions of the dislocation. If the solute is located in a position such that the energy change is favorable for cross-slip ($\Delta U_i^{I-II} = U_i^I - U_i^{II} < 0$), then cross-slip nucleation will begin in the vicinity of this solute. However, if the favorable solute is located at a position that is far from the *initial stages* of the nucleation process, which occurs at the intersection of the pyramidal planes (see below), then such a favorable solute cannot lower the activation barrier below a limiting value, independent of the solute/dislocation interaction energy difference. The relevant sites lying far from the initial cross-slip nucleation are indicated as the cyan-colored sites in Fig. 6.2(c); these are also the sites with the largest negative interaction energy, i.e those having the greatest potential reduction of the cross-slip energy barrier. In spite of their very favorable energies for pyramidal I, these solutes only enter the cross-slip nucleation process in the latter stages when the cross-slipped segment becomes close to, and then envelopes, the solute. The solutes at such sites therefore can not reduce the cross-slip barrier below the intrinsic barrier associated with the initial jog nucleation. The effect of these solutes on the nucleation barrier is then to reduce the barrier down to the value to $\Delta U_{\text{eff}}^{I-II} = \max(\Delta U^{I-II}, \Delta G_{XS,i} - \Delta G_{XS}^{\text{Mg}})$.

To justify the above analysis, we execute the nudged elastic band (NEB) calculations of the cross-slip process in a model Mg-Y alloy containing a single Y atom at selected sites. In the NEB computations, the initial state is a pyramidal II $\langle c + a \rangle$ screw dislocation in a large cylindrical simulation box with dislocation line direction along z axis, obtained by applying the anisotropic Volterra displacement field on all atoms followed by relaxation while holding all atoms within $2r_c$ (r_c being the cutoff radius of the potential) of the outer boundary fixed at the anisotropic Volterra displacements. The final state is a pyramidal I $\langle c + a \rangle$ screw dislocation obtained by first applying a tensile stress of 800 MPa normal to the pyramidal II plane and running a molecular dynamics simulation at $T = 77$ K. This large non-glide stress decreases the energy difference ΔE^{I-II} and favors the pyramidal I over pyramidal II $\langle c + a \rangle$ screw dislocation [230]. After the transition to pyramidal I is achieved, the structure is relaxed at zero stress and zero temperature while continuing to hold the boundary atoms fixed. NEB calculations are carried out using a cylindrical simulation box of radius 150 Å and of axis length $l_z = 150$ Å. Each NEB calculation is performed under stress-free conditions using 64 replicas, and convergence is assumed when the maximum of the force magnitude acting on all of the atoms across all replicas reaches less than or equal to 2×10^{-4} eV/Å.

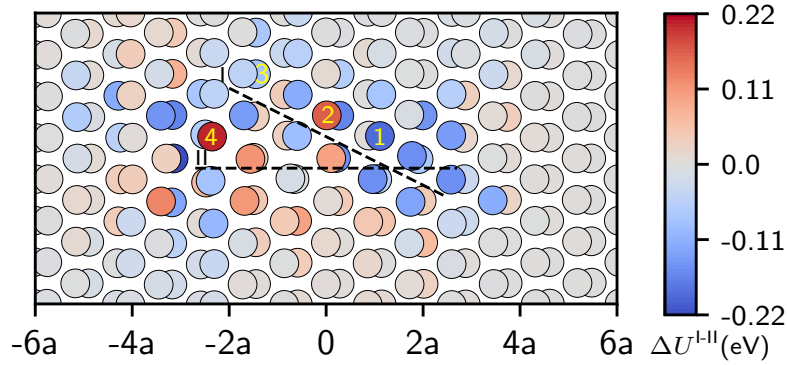


Figure 6.5 – **Map of difference between interaction energy ΔU^{I-II} of Y solute atom with pyramidal I and pyramidal II $\langle c + a \rangle$ screw dislocations.** The dotted lines show the positions of the stacking faults corresponding to initial pyramidal II and final pyramidal I dislocations. Sites marked with 1,2,3 and 4 are substituted with Y atoms for subsequent NEB calculations, and are referred to in Fig. 6.6 and Fig. 6.7.

The Mg-Y potential used in this work, as discussed in Section 3.2, is not perfect, deviating from DFT results for some crucial properties. The potential predictions for the average interaction energy of Y with the Pyramidal I stacking fault is much weaker than DFT values, which renders this potential unsuitable for the investigation of the cross-slip model in general. Nevertheless, the potential can be employed to test the assumptions of the proposed model by carefully selecting individual atomic sites into which Y is substituted for Mg. To this end, we compute the difference $\Delta U^{I-II} = U^I - U^{II}$ of a Y solute at any specified atomic position relative to the cross-slipped pyramidal I and initial pyramidal II $\langle c + a \rangle$ screw dislocations. To compute the interaction energy of Y at a particular site around a dislocation, we first note the energy of the relaxed dislocation structure with Y substituted with Mg at that site. The interaction energy is then the energy of this dislocation structure minus the energy of a reference structure. The energy of the reference structure is obtained by making use of the fact that the interaction of a solute situated far from the core is purely elastic. The dislocation line length is sufficient to avoid any effects of the periodic images of the Y atoms along the line. Fig. 6.5 shows the computed ΔU^{I-II} for all atomic sites around the dislocations. Y solutes at atomic sites having a negative value of ΔU^{I-II} will decrease the energy difference ΔE^{I-II} and thus assist the cross-slip process from pyramidal II to pyramidal I plane. Sites having positive ΔU^{I-II} will increase ΔE^{I-II} and thus suppress the cross-slip process. We refer to sites having negative and positive values of ΔU^{I-II} as favorable and unfavorable sites, respectively. For the NEB calculations of the cross-slip process in Mg-Y alloys, we choose the four atomic sites numbered in Fig. 6.5. Sites #1 and #3 are favorable sites situated, respectively, near and far from the intersection of pyramidal planes. Sites #2 and #4 are unfavorable sites located, respectively, near and far from the pyramidal planes intersection.

Fig. 6.6 shows the transformation of the dislocation cores and Fig. 6.7 shows the corresponding energy changes along the MEP of the cross-slip process from a pyramidal II to a pyramidal I

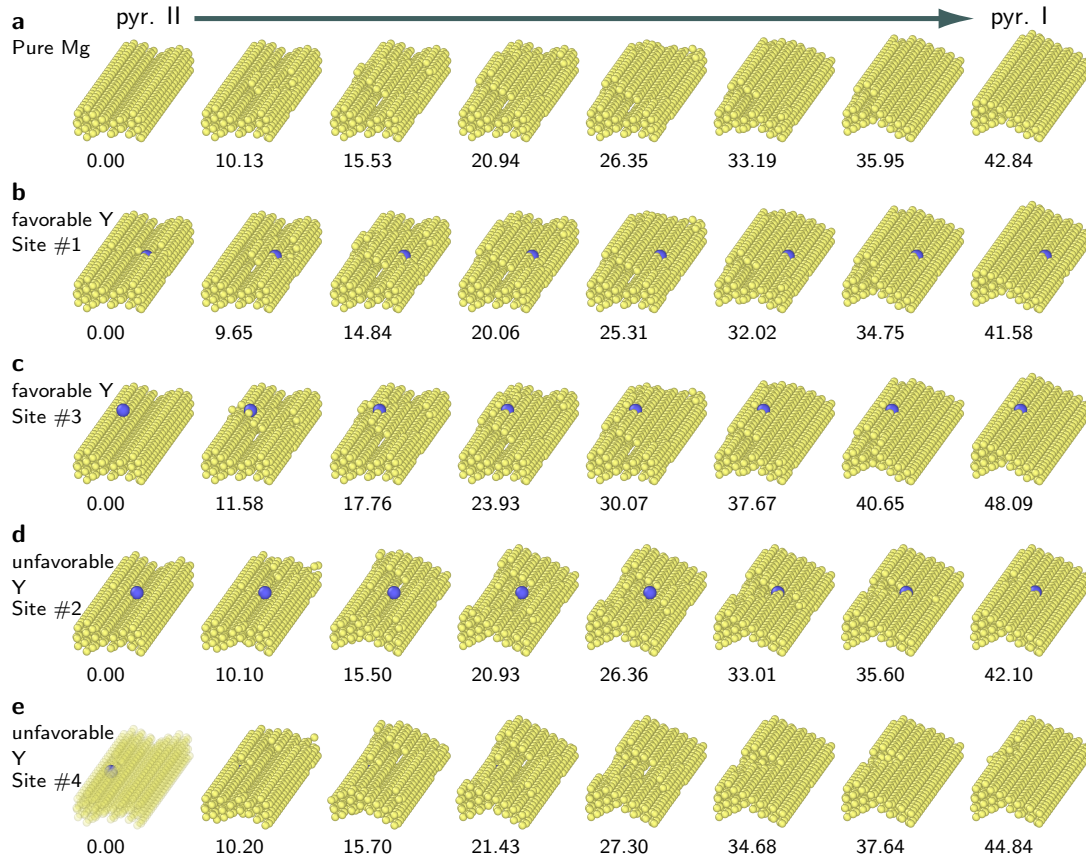


Figure 6.6 – MEPs for the cross-slip of $\langle c + a \rangle$ screw dislocations from pyramidal II to pyramidal I plane in Mg and Mg-Y alloys: (a) pure Mg and (b)-(e) Mg-Y. All the NEB calculations are performed for a dislocation line length of ~ 150 Å. The numbers written below each figure depict the reaction coordinates shown in Fig. 6.7. Only non-hcp atoms are shown to represent the core structures: yellow atoms denote Mg atom and blue atoms denote Y atom. Mg atoms in the first frame of (e) are rendered transparent to show the position of Y atom which is embedded in between the Mg atoms. In (b)-(e), Mg at marked sites, shown in Fig. 6.5, are substituted with Y atoms.

plane, as obtained from the NEB calculations. We now examine the cross-slip evolution for the specific Y solutes #1 - #4. Fig. 6.6 shows that nucleation of the cross-slip process occurs near the solute for favorable solutes #1 and #3, and avoids the solute for unfavorable solutes #2 and #4, as claimed earlier. For the unfavorable solutes, the cross-slipped dislocation only envelops the solute at the very end of the process, which is forced by the imposed final state of full cross-slip. For the favorable solute #1 near the pyramidal I/II intersection, the solute is intimately involved in the early-stage nucleation. For the favorable solute #3 far from the pyramidal I/II intersection, the solute does not influence the initial nucleation process.

The features seen in the atomistic pictures in Fig. 6.6 are reflected in the quantitative results for the energy versus reaction coordinate shown in Fig. 6.7. For the unfavorable solutes #2

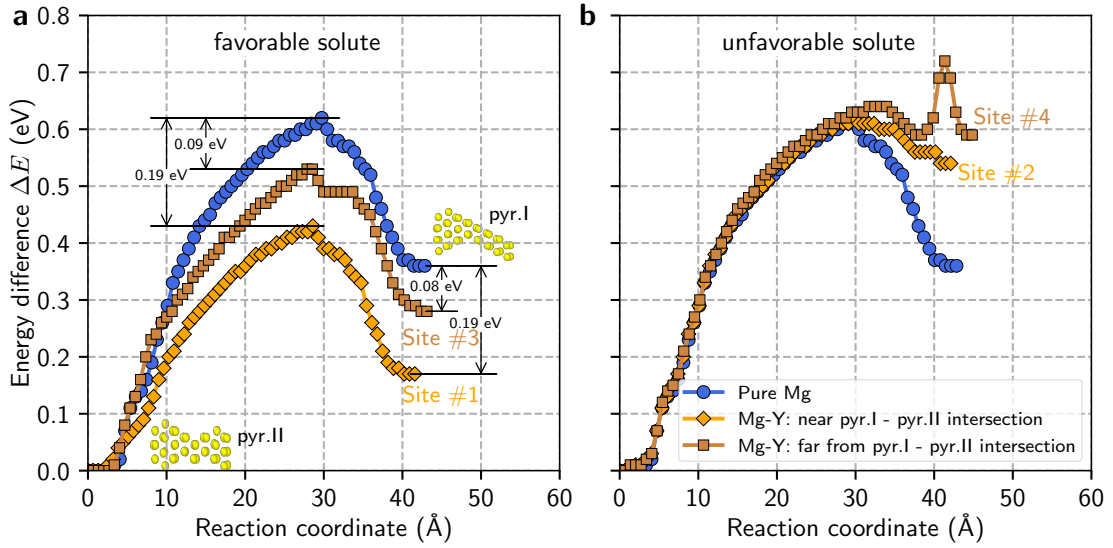


Figure 6.7 – **Energy variation along the MEP associated with the pyramidal II-pyramidal I cross-slip of $\langle c + a \rangle$ screw dislocations in pure Mg and Mg-Y.** Results are shown for a dislocation line length of ~ 150 Å. In all figures, blue curves are for pure Mg, orange curves are for Mg-Y having a Y solute near the pyramidal I-pyramidal II plane intersection, and brown colored curves correspond to Y at a site far from the intersection of the pyramidal planes. Y solutes in (a) are at the favorable sites and in (b) at the unfavorable sites. The energy for each curve is referenced to the initial energy of the solute plus pyramidal II dislocation energy in order to compare the interaction energy difference with the change in the cross-slip barrier. Non-hcp atoms, identified by the common neighbor analysis, comprising core structures of the two pyramidal $\langle c + a \rangle$ screw dislocations in pure Mg are shown in (a). Curves for Mg-Y are labeled with corresponding site numbers of Y shown in Figs. 6.5 and 6.6.

and #4, the first two stages of cross-slip are the same as those in pure Mg, as demonstrated in Fig. 6.7(b). The cross-slip barrier in the presence of the unfavorable solutes either increases or remains the same with respect to pure Mg. Fig. 6.7(a) shows clearly that during cross-slip in presence of favorable solute #1, situated near the pyramidal plane intersection, the energy (orange curve) of cross-slipped structure starts to decrease as compared to pure Mg (blue curve) right from the nucleation stage. Also shown in Fig. 6.7(a) is that the energy curve (brown colored) for site #3, which is far from the pyramidal plane intersection, closely follows the curve for pure Mg (blue colored) till reaction coordinate ~ 10 which coincides with the end of the first nucleation stage of the cross-slip. Therefore, it can be concluded that if a solute is far from the intersection of the pyramidal planes, the favorable solute cannot pay for the intrinsic barrier associated with the initial jog nucleation. Moreover, Fig. 6.7(a) also depicts that the decrease in the cross-slip barrier for the solute in both site #1 and #3 with respect to pure Mg is very close to the interaction energy difference ΔU^{I-II} . This validates the assumption made in the previous model relating total energy change after cross-slip to the change in the activation energy for cross-slip.

6.6 Experimental observation of the solute accelerated pyramidal cross-slip in Mg-Y alloys ¹

We now demonstrate the direct physical evidence for the operation of the pyramidal $\langle c + a \rangle$ cross-slip process accelerated by Y solutes. Fig. 6.8 show the initial $\{0001\}$ and $\{10\bar{1}0\}$ pole figures, stress-strain curves, and TEM observation of dislocation microstructures in pure Mg, Mg-1wt.%(0.28at.%)Y, and Mg-3wt.(0.84at.%)Y solid solution alloys deformed under uniaxial tensile loading at room temperature. All samples are process-controlled to yield similar grain sizes and the strong basal texture typical of pure Mg, with all TEM observations performed in grains having close-to-basal orientation as confirmed by selected area diffraction, making direct comparisons appropriate.

Upon yielding, the alloys have much lower hardening rates that could be due to both the slightly weaker texture (favoring more basal slip) and enhanced $\langle c + a \rangle$ slip. We thus examine the deformation microstructures at the same 3% strain (Fig. 6.8 (b)-(d)). The stress level for pure Mg is much higher than for the two alloys. The alloys exhibit a clear increase in both $\langle c + a \rangle$ dislocation cross-slip and overall $\langle c + a \rangle$ activity: Connected $\langle c + a \rangle$ dislocation segments are increasingly found on both pyramidal I and II planes with increasing Y concentrations, with pyramidal II slip being dominant. This is consistent with earlier observations of slip traces on both pyramidal I and II planes in Mg-3wt.%Y [179]. In pure Mg, the $\langle c + a \rangle$ dislocations are primarily dissociated on the basal plane, with some indications of limited cross-slip involving either pyramidal II or I slip. These observations indicate that, in the alloys, $\langle c + a \rangle$ slip operates and contributes to the lower hardening even at the very early stages of plastic straining, consistent with the theory that posits continued $\langle c + a \rangle$ generation and slip at lower stresses. We attribute the presence of some pyramidal I segments to the high tensile stress level in pure Mg, which is consistent with single-crystal studies [16] and atomistic simulations [230]. The role of easy $\langle c + a \rangle$ slip is perhaps more critical at the later stages of deformation (strain > 10% where further extension twinning is limited). In pure Mg polycrystals with grain sizes > 10 μm , excessive basal slip without $\langle c \rangle$ -axis strain accommodation can quickly build up strain incompatibility and high constraint stresses, leading to damage initiation and limiting ductility [51]. In the Mg-Y alloys, the stress-strain curves clearly have a longer range of stable plastic flow at relatively normal hardening rates, indicating that sufficient plastic deformation mechanisms are activated until the onset of macroscopic plastic instability (e.g., the Considère criterion) is reached. These controlled experiments demonstrate that Y solutes do enhance $\langle c + a \rangle$ dislocation cross-slip, slip, $\langle c \rangle$ -axis strain accommodation, and ductility with increasing Y concentration, in excellent agreement with our predictions.

¹The experimental results presented in this section were provided by Dr. Stefanie Sandlöbes from institut für Metallkunde und Metallphysik at RWTH (Rheinisch- Westfälische Technische Hochschule) Aachen University, Germany.

6.6. Experimental observation of the solute accelerated pyramidal cross-slip in Mg-Y alloys

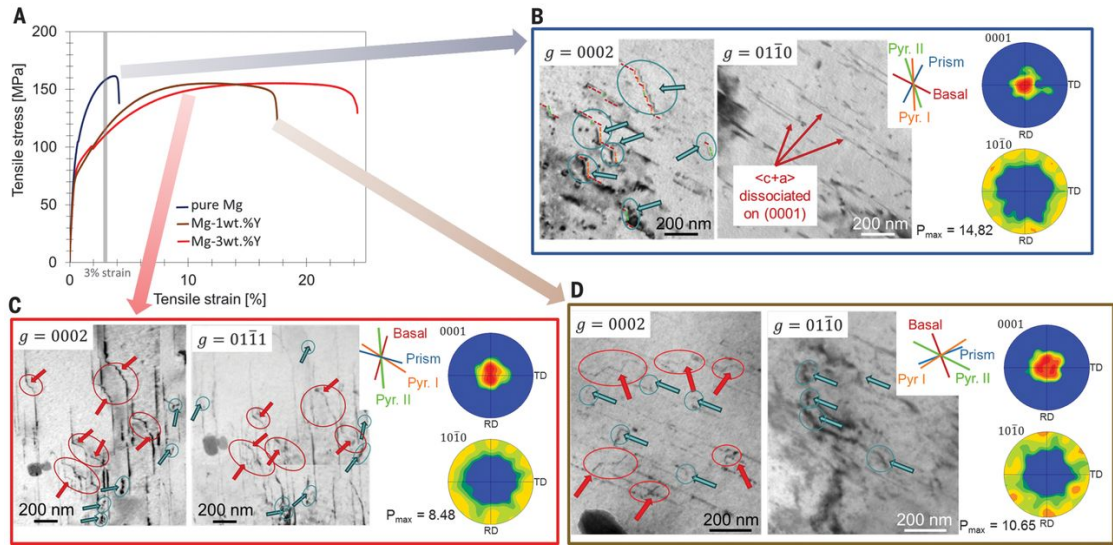


Figure 6.8 – Experimental results for pure Mg and Mg-Y alloys under tensile deformation at room temperature. (a) Stress-strain curves for pure Mg and two Mg-Y solid solution alloys containing 1 wt.% and 3 wt.% Y atoms. (b-d) show initial $\{0001\}$ and $\{10\bar{1}0\}$ pole figures and bright-field TEM of corresponding dislocation microstructures at 3% strain for (b) pure Mg, (c) Mg-3wt.%Y and (d) Mg-1wt.%Y. In (b) to (d), dislocations visible under diffraction vector $\mathbf{g} = 0002$ are $\langle c + a \rangle$ dislocations based on two-beam $\mathbf{g} \cdot \mathbf{b} = 0$ visibility analysis (\mathbf{b} is the Burgers vector); the insets show the corresponding crystallographic plane traces identified using diffraction analysis, enabling determination of the crystal planes of the observed $\langle c + a \rangle$ dislocations. In (b), $\langle c + a \rangle$ dislocation segments are lying on basal and pyramidal II planes; areas, where dislocations change from the pyramidal II to the basal planes, are highlighted by turquoise arrows and circles. In (c) and (d), $\langle c + a \rangle$ dislocation segments are predominantly on pyramidal II planes, with frequent plane changes to either pyramidal I (highlighted by red arrows and circles) or basal (highlighted by turquoise arrows and circles) planes. In (c), for Mg-3wt.% Y, high-frequency $\langle c + a \rangle$ dislocation switching between pyramidal II and I planes (double cross-slip) is evident.

7 Cross-Slip Driven Ductility in Dilute Mg Alloys: Results

This chapter is in part extracted from the following publications

1. Ahmad R., Yin B., Wu Z. and Curtin W. A. (2019). Designing high ductility in magnesium alloys. *Acta Mater.*, 172: 161-184.
2. Ahmad R., Wu Z. and Curtin W. A. (2020). Analysis of double cross-slip of pyramidal I $\langle \mathbf{c} + \mathbf{a} \rangle$ screw dislocations and implications for ductility in Mg alloys. *Acta Mater.*, 183: 228-241.

In this chapter, we present the predictions of the model for ductility in a range of binary, ternary and quaternary solid solution Mg alloys at room temperature $T = 300$ K. We place particular emphasis on the Mg alloys free of RE solute elements. These results presented in this chapter could facilitate the computationally guided search for the compositions of high ductile dilute Mg alloys.

We first discuss the choice of parameters used in making predictions. We then apply the model in the pyramidal II favorable regimes, relevant for low solute concentrations, of Mg alloys, and compare the model predictions with the available experimental observations. Finally, results for pyramidal I favorable regime, relevant for a relatively larger amount of favorable solutes, of Mg alloys are presented and compared with the experiments.

7.1 Determination of model parameters

The ductility condition, Eq. 6.13, requires as inputs the interaction energy of solutes with pyramidal I and pyramidal II $\langle \mathbf{c} + \mathbf{a} \rangle$ screw dislocations, the net cross-slip driving shear stress $\Delta\tau$, and the dislocation energy difference $\Delta E_{\text{Mg}}^{\text{I-II}}$ in pure Mg. In the current model approximations, the solute-dislocation interactions are limited to solute-stacking fault interactions, which are computed accurately using DFT. The energy difference in pure Mg $\Delta E_{\text{Mg}}^{\text{I-II}}$ and net driving stress $\Delta\tau$ are two crucial inputs in the ductility model that are not accessible with high

precision. In this section, we compare model predictions versus experimental observations for various values of $\Delta E_{\text{Mg}}^{\text{I-II}}$ and $\Delta\tau$, and choose that pair which best capture the experimental features related to ductility and pyramidal slip in Mg alloys.

A reasonable range for the net driving shear stress $\Delta\tau$ was discussed in Section 6.4. Values for $\Delta E_{\text{Mg}}^{\text{I-II}}$ have been estimated previously. A DFT calculation [97] using quadrupolar arrangements of pyramidal I or pyramidal II $\langle\mathbf{c} + \mathbf{a}\rangle$ screw dislocation in a small periodic cell leads to an estimated energy difference of $\Delta E_{\text{Mg}}^{\text{I-II}} = 7 \pm 20$ meV/nm. In this calculation the simulation cell is sheared to negate the average shear strain developed by the dislocations [42], creating large stresses throughout the cell which can alter the apparent energies of the dislocations [230]. Such undesirable/extrinsic additional stresses arising from the small periodic cell can be eliminated by simulating a single dislocation in a large simulation cell; this is challenging in DFT because the uncertainty in total energy grows with the number of atoms, making it hard to extract the small difference between the two types of screw dislocations. We instead use the MEAM_I potential of Mg [231] that has been comprehensively tested for various properties related to dislocations. The computed energy difference $\Delta E_{\text{Mg}}^{\text{I-II}} = 27$ meV/nm is within the uncertainty of the DFT calculation. Within the context of the model, if $\Delta E_{\text{Mg}}^{\text{I-II}}$ is too small, then pyramidal I slip could easily occur in pure Mg, which is not broadly observed in experiments. If $\Delta E_{\text{Mg}}^{\text{I-II}}$ is too large, then cross-slip cannot become favorable in various alloys at the concentrations studied experimentally.

To examine the dependence of the model predictions to the above material parameter values, we apply the model to three representative binary Mg alloys Mg-Zn, Mg-Al, and Mg-Y for a range of values of $\Delta E_{\text{Mg}}^{\text{I-II}}$ and $\Delta\tau$. Zn, Al, and Y are chosen as representatives of solutes that are highly unfavorable, intermediate, and highly favorable, respectively, for achieving ductility.

Fig. 6.3(a) shows the effect of the solute concentrations on the average energy difference of pyramidal $\langle\mathbf{c} + \mathbf{a}\rangle$ screw dislocations in Mg alloys. Al and Zn solutes increase the dislocation energy difference and thus hamper the cross-slip process on average. Y is a favorable solute, decreasing the dislocation energy difference and thus accelerating the cross-slip process. The Y concentration at which the average energies of pyramidal I and II $\langle\mathbf{c} + \mathbf{a}\rangle$ screw dislocations become equal depends on $\Delta E_{\text{Mg}}^{\text{I-II}}$. This concentration can be roughly estimated from experiments. The observation of slip traces in single-crystal tensile tests of Mg-Y alloys by Rikihisa et al. [167] indicates that pyramidal I slip becomes predominant in the range of 0.6-1.1at.%Y. Slip traces observed in tensile tests of a Mg-0.9at.%Y polycrystal also indicated higher activity of pyramidal I $\langle\mathbf{c} + \mathbf{a}\rangle$ dislocations than pyramidal II $\langle\mathbf{c} + \mathbf{a}\rangle$ dislocation. On the other hand, over the same concentration range, TEM observations presented in Fig. 6.8 show higher pyramidal II dislocation content. This concentration also cannot be too low, because then at higher Y concentrations where pyramidal I is the lowest-energy plane, the necessary cross-slip from the low-energy pyramidal I onto higher energy pyramidal II would again have a high barrier, enabling the detrimental PB transition on pyramidal I plane to dominate and preventing high ductility. These considerations suggest that the concentration of Y at which $\langle\mathbf{c} + \mathbf{a}\rangle$ screw dislocations become equal on pyramidal I and pyramidal II planes is around 0.6

7.1. Determination of model parameters

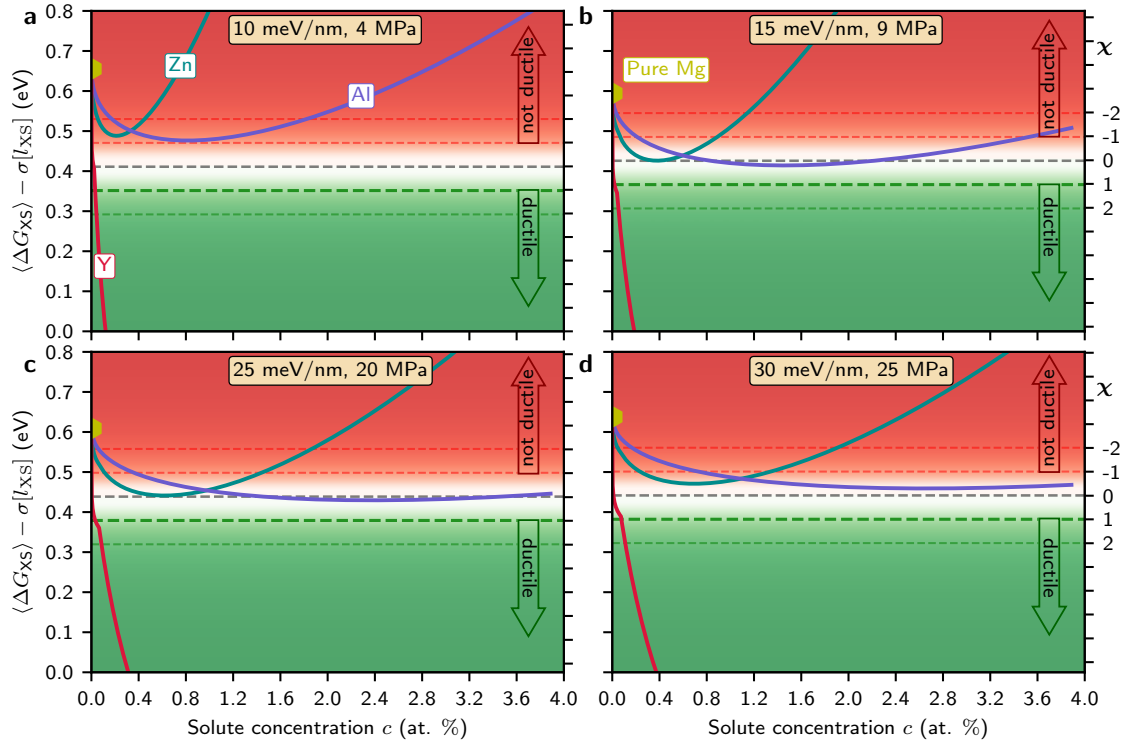


Figure 7.1 – Predictions of the cross-slip barrier ΔG_{XS} , including fluctuation, and ductility index χ in binary Mg alloys, containing Zn, Al, and Y, as function of solute concentration for various values of ΔE_{Mg}^{I-II} and $\Delta\tau$: a) $\Delta E_{Mg}^{I-II} = 10$ meV/nm and $\Delta\tau = 4$ MPa, b) $\Delta E_{Mg}^{I-II} = 15$ meV/nm and $\Delta\tau = 9$ MPa, c) $\Delta E_{Mg}^{I-II} = 25$ meV/nm and $\Delta\tau = 20$ MPa, and d) $\Delta E_{Mg}^{I-II} = 30$ meV/nm and $\Delta\tau = 25$ MPa.

at.%, which, from Fig. 6.3(a) implies that $\Delta E_{Mg}^{I-II} \approx 25$ meV/nm; this is just within the range of the DFT value [97] and close to the MEAM_I value [230]. Thus, values in and around this range are considered.

Table 7.1 – Properties of Mg relevant to the pyramidal I and the pyramidal II stacking faults. b , γ_{Mg} , and A_0 are calculated using DFT [236]. $\Delta G_{XS,i}$ and l_{nuc} are determined from atomistic simulation using the MEAM_I potential [231]. K_{12} is determined in the framework of anisotropic elasticity utilizing the DFT data, and ΔE_{PB} and l_{PB} are computed employing MD simulations using the MEAM_I potential.

Properties	b (Å)	μ (GPa)	ΔE_{Mg} (meV/nm)	$\Delta G_{XS,i}$ (eV)	$\Delta\tau$ (MPa)	γ_{Mg} (mJ/m ²)	K_{12} (eV/Å)	A_0 (Å ²)	ΔE_{PB} (eV)	l_{PB} (Å)	l_{nuc} (Å)	N_T
Pyramidal I	6.09	18	25	0.23	20	163.648	0.159	18.759	0.3	20	25	45
Pyramidal II	6.09	18	25	0.23	20	167.572	0.180	16.833	0.5	20	25	45

Fig. 7.1 shows the predicted cross-slip barrier versus solute concentration for Zn, Al, and Y solutes for four pairs of $(\Delta E_{Mg}^{I-II}, \Delta\tau)$. The net driving stress $\Delta\tau$ are within the estimated range and chosen to produce fairly similar predictions across the four values of energy difference

$\Delta E_{\text{Mg}}^{\text{I-II}}$. All four parameter sets predict that $\chi < -2$ for pure Mg, severely failing to satisfy the ductility criterion. Y solutes are predicted to produce good ductility above some very small concentration. For Zn and Al, $\chi < 1$, such that these alloys can not achieve high ductility in general (submicron polycrystals with weak textures may still show certain ductility). Al is widely used in commercial Mg alloys, with a plethora of experimental studies of Mg-Al alloys. We thus examine Mg-Al more carefully. Mg-Al alloys exhibit wide variability in the room temperature ductility [93] over the concentration range of 2.5-5.5 at.%. This indicates that χ should be close in the range $0 < \chi < 1$, which is the domain where details such as processing routes, textures, grain sizes, etc. could greatly affect the resulting ductility. Huang et al. [93] show that increasing the Al concentration in Mg-0.17at.%Mn alloy from 2.6 at.% to 5.2 at.% weakens the basal texture and increases the ductility, while for higher Al concentrations, the basal texture is increased and ductility begins to decrease. These experimental results are most consistent with $\Delta E_{\text{Mg}}^{\text{I-II}} = 25$ meV/nm and $\Delta\tau = 20$ MPa. Interestingly, this pair match quite well the values estimated by independent considerations. We thus use these values in presenting subsequent results. Additional parameters required in the model are tabulated in Table 7.1.

7.2 Prediction for binary Mg alloys

We now make predictions of the cross-slip energy barrier and ductility index χ for binary Mg-X alloys containing a wide range of solute atoms.

Fig. 7.2 shows the combined average and fluctuation effects of solutes on the cross-slip barrier and ductility index χ . We note that $\chi > 1$, at which the cross-slip rate is ten times the PB transition rate, is taken to be sufficient in achieving ductility. The model predicts that all RE alloys reach $\chi > 1$ at dilute concentrations. Only 0.035 at.% Ce is sufficient for inducing ductility, consistent with the experimental observation of weak basal texture and high ductility [50, 85, 138]. Zr turns out to be quite efficient at low concentrations [40, 154]. Ca and Sr are predicted to be similarly effective in turning Mg ductile at concentrations $c > 0.1$ at.%. This result is consistent with the addition of dilute Ca and Sr inducing weak basal texture and increasing the ductility of Mg alloys [34, 35, 49, 53, 132]. The addition of a small quantity of K is predicted to induce ductility, however, making a Mg-K alloy is challenging on account of the boiling temperature of K being close to the melting temperature of Mg. For Mn, the ductility condition is fulfilled at concentrations > 0.3 at.% in accordance with the observed good ductility and formability at 0.35 at.% [193, 194, 242]. Ductile Mg-Sn alloys require a concentration of Sn more than 0.8 at.% which may be beyond its practical solubility limit. Additions of Li at concentrations more than ~ 2 at.% are expected to be ductile, agreeing with the experiments on $\sim 3, 10, 15$ at.% Li [5, 6]. Binary Mg alloys comprising Zn and Ag never fulfill ductility condition $\chi = 1$, so these alloys are never expected to be sufficiently ductile in general. Another observation is that Ag and Zn solutes are practically the same, and subsequent ternary and quaternary results presented for Zn can also be applied as it is for Ag. For Al, the ductility condition $\chi > 1$ is never achieved and reaches to the maximum value

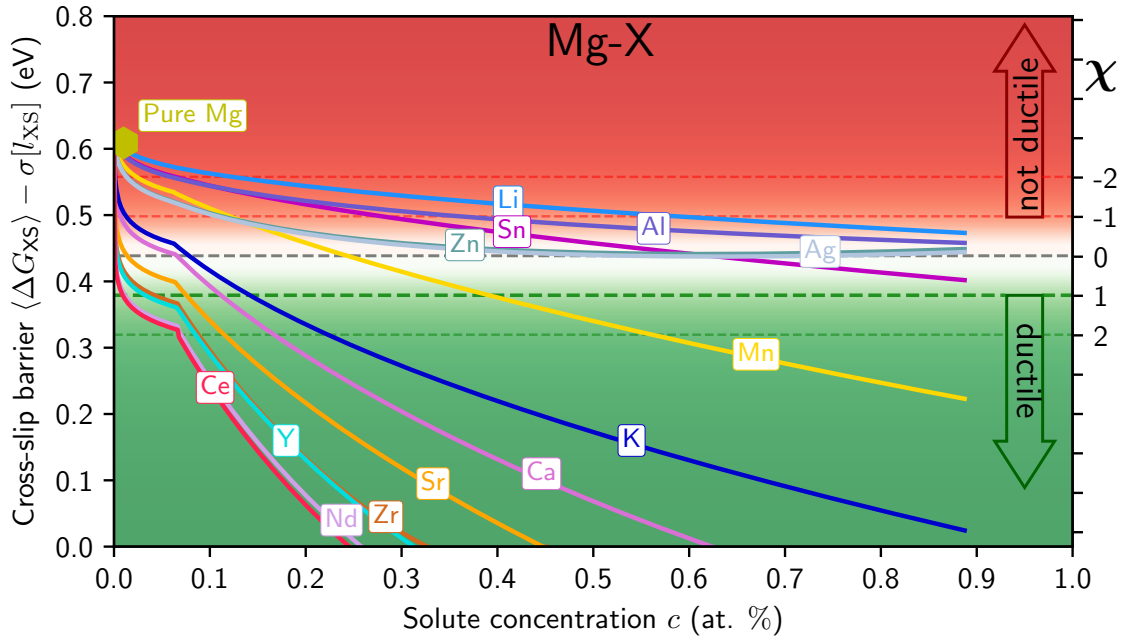


Figure 7.2 – **Variation of the cross-slip barrier, including average and fluctuation, and ductility index χ with the concentration of the solutes in binary alloys.** Sudden change in the slopes of the curves at around 0.08 at.% for REs, Zr, Sr, Ca, and K is the signature of the beginning of the ultra dilute limit.

$\chi = 0.1$ at 2.4 at.% (see Fig. 7.1(c)). Thus Al is expected to have moderate effects consistent with the experimentally observed moderate ductility [41, 52, 53]. We can further identify ductile binary Mg alloys comprising at least 2.5 at.% Li or 1.1 at.% Sn or 0.4 at.% Mn or 0.15 at.% K or 0.12 at.% Ca or 0.07 at.% Sr or 0.04 at.% Zr.

7.3 Predictions for ternary Mg alloys

For Mg alloys to be competitive in structural applications, the ultimate goal is to achieve high ductility and high strength. In Mg, strengthening is best achieved through age-hardening, i.e. precipitation of hard phases that resist dislocation motion. Identifying higher order alloys ductile in the solid solution state thus opens the possibility of subsequent age-hardening processes, as well as delicate control of strength and ductility. Alloy processing may also be facilitated by the addition of some solutes for reasons not directly connected with strength and ductility. Thus, it is valuable to move beyond simple binary alloys and consider ternary and quaternary alloys.

Figs. 7.3 and 7.5 show ductility predictions for a wide range of non-RE ternary Mg alloys, with Al, Zn, and Li as one of the two alloying elements. As shown in Fig. 7.2, since Zn and Al cannot achieve the ductility condition by itself and that these are the main alloying elements used in industrial alloys, we present here the ternary alloys based on Al, Zn, and Li with favorable

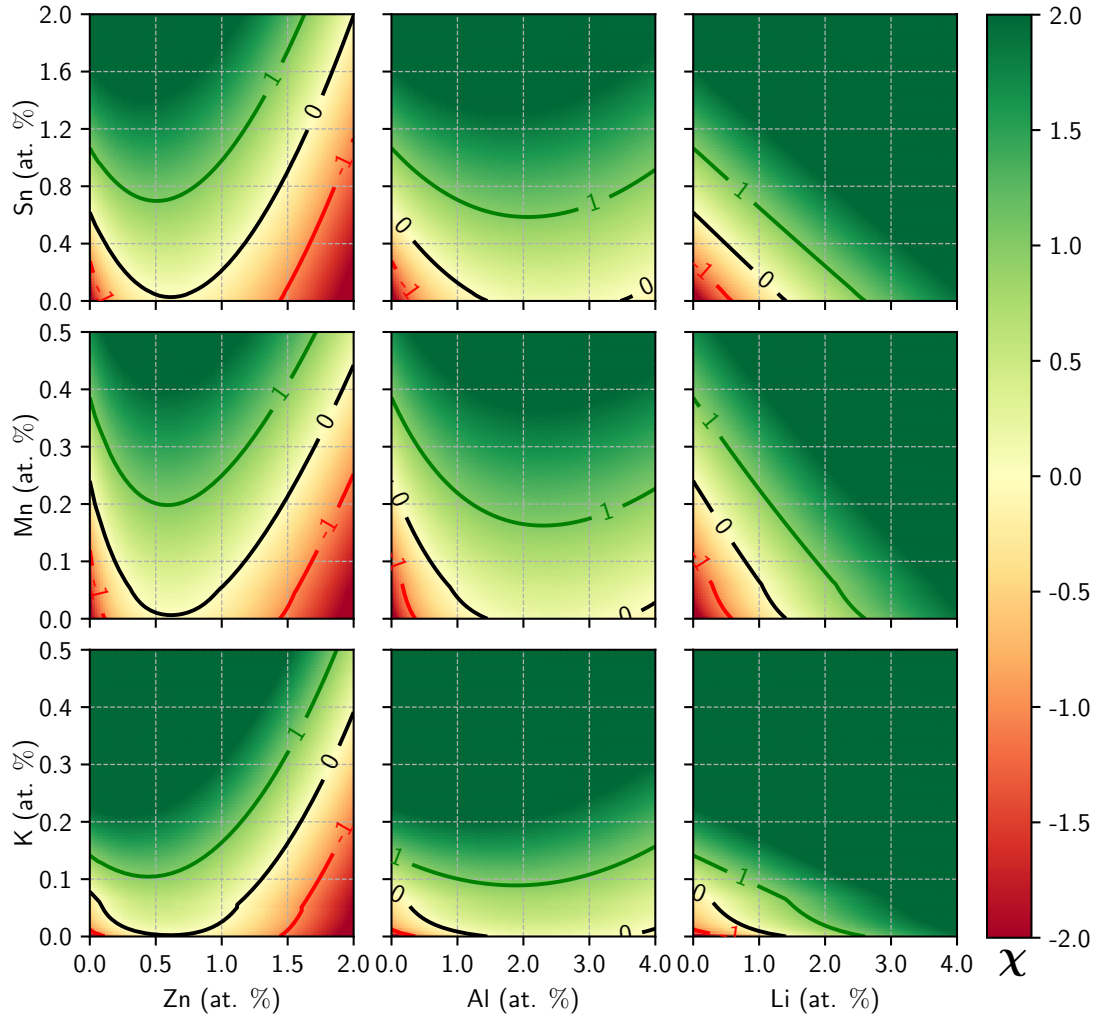


Figure 7.3 – **Variation of ductility index χ as a function of the concentrations of solutes in ternary Mg alloys.** These Al, Zn, and Li based ternary alloys contain one of K, Mn, or Sn as second alloying elements. The compositions of alloys lying in the green region, for which $\chi > 1$, are predicted to be ductile.

solutes K, Mn, Sn, Zr, Ca and Sr. In these figures, the green region ($\chi > 1$) corresponds to the ductile composition and the red region ($\chi < -1$) denotes the composition expected to exhibit poor ductility. The first observation is that as the amount of Zn is increased, the ductility of the resulting alloys starts to decrease, consistent with the experimental trend [40, 53, 123, 194, 247]. Secondly, the addition of ~ 0.4 at.% Zn seems to be optimum which is generally used in industrial alloys. The addition of Mn along with Zn (0.3at.%Zn-0.45at.%Mn, 0.6at.%Zn-0.45at.%Mn, 0.9at.%Zn-0.45at.%Mn) has been shown to increase ductility [192, 194], which is in the predicted ductile range. The addition of Sn and K are predicted to result in ductile alloys. Adding a dilute amount of Ca, Zr and Sr can turn the Mg-Zn alloys ductile and weaken the basal texture which indeed has been observed experimentally [40, 49, 53, 132]. Ca and Sr have similar effects on ductility. From this analysis, we identify Mg0.5Zn0.7Sn, Mg0.5Zn0.2Mn, Mg-

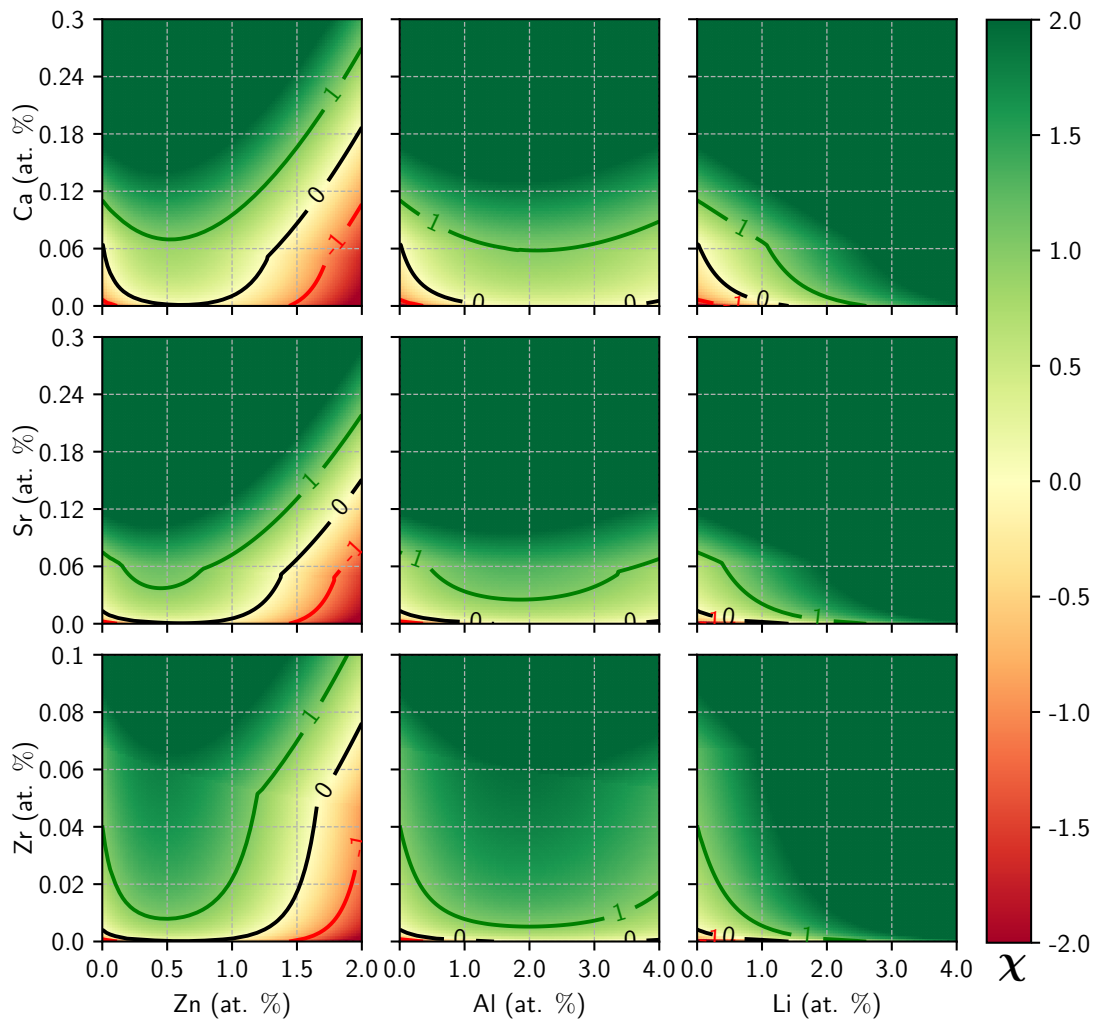


Figure 7.4 – **Variation of ductility index χ as a function of the concentrations of solutes in ternary Mg alloys.** These Al, Zn, and Li based ternary alloys contain one of Zr, Sr, or Ca as second alloying elements. The compositions of alloys lying in the green region, for which ductility $\chi > 1$, are predicted to be ductile. The abrupt change in the slopes of the curves is due to the ultra dilute limit.

0.5Zn0.1K, Mg0.5Zn0.07Ca, Mg0.4Zn0.04Sr, and Mg0.04Zn0.01Zr (concentration in at.%) to be potential ductile ternary Mg alloys containing Zn and optimum amount of second alloying element.

Mg-Al alloys itself remain very close to satisfying the ductility condition, so a small addition of favorable solutes can tip the balance in favor of ductility. Mg-Al-Mn alloys with ~ 0.18 at. % Mn are shown to be ductile over a wide range of Al concentrations [93, 124] and ductility of alloys decreases with Al content at high Al concentrations [93], consistent with the predicted trend. Replacements of Zn with Sn in AZ alloys have been shown to induce higher ductility [198]. Additions of Ca and Sr in Mg-Al alloys have successfully been shown to weaken the basal

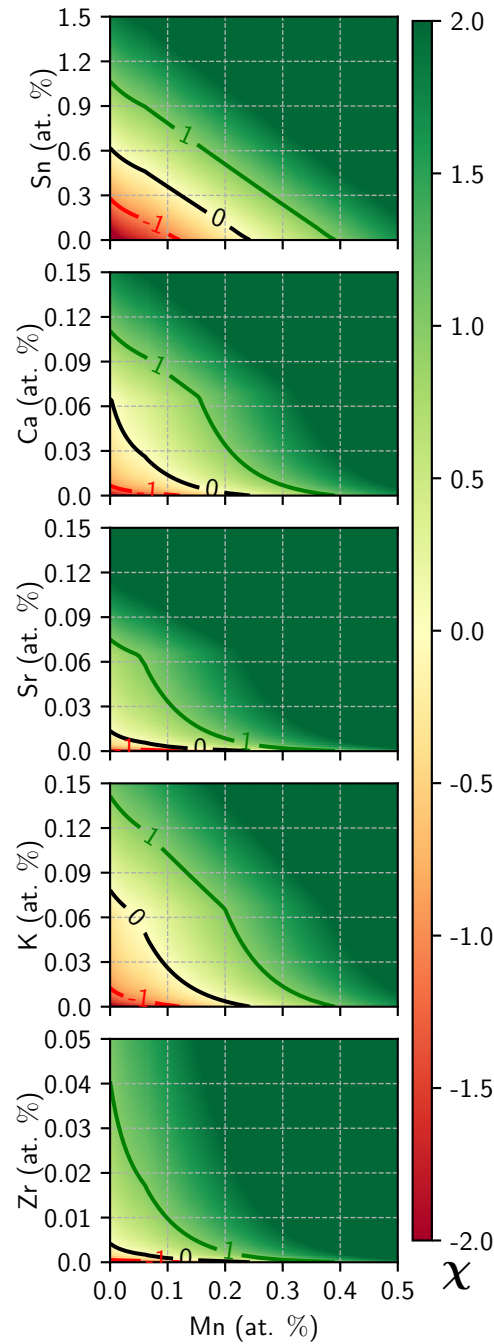


Figure 7.5 – **Variation of ductility index χ as a function of the concentrations of solutes in ternary Mn based Mg alloys.** The second alloying element is one of Sn, Ca, Sr, K, or Zr. The compositions of alloys lying in the green region, for which ductility $\chi > 1$, are predicted to be ductile. Discontinuity in the slopes of the χ curves is due to the ultra dilute limit.

texture and improve ductility [24, 53, 178]. Furthermore, according to the model, $\text{Mg}_2\text{Al}_{0.6}\text{Sn}$, $\text{Mg}_2\text{Al}_{0.17}\text{Mn}$, $\text{Mg}_{1.5}\text{Al}_{0.1}\text{K}$, $\text{Mg}_2\text{Al}_{0.06}\text{Ca}$, $\text{Mg}_2\text{Al}_{0.03}\text{Sr}$, $\text{Mg}_2\text{Al}_{0.005}\text{Zr}$ (concentration in at.%) are predicted to be ductile Al based ternary Mg alloys. Since the χ curves are shallow at around

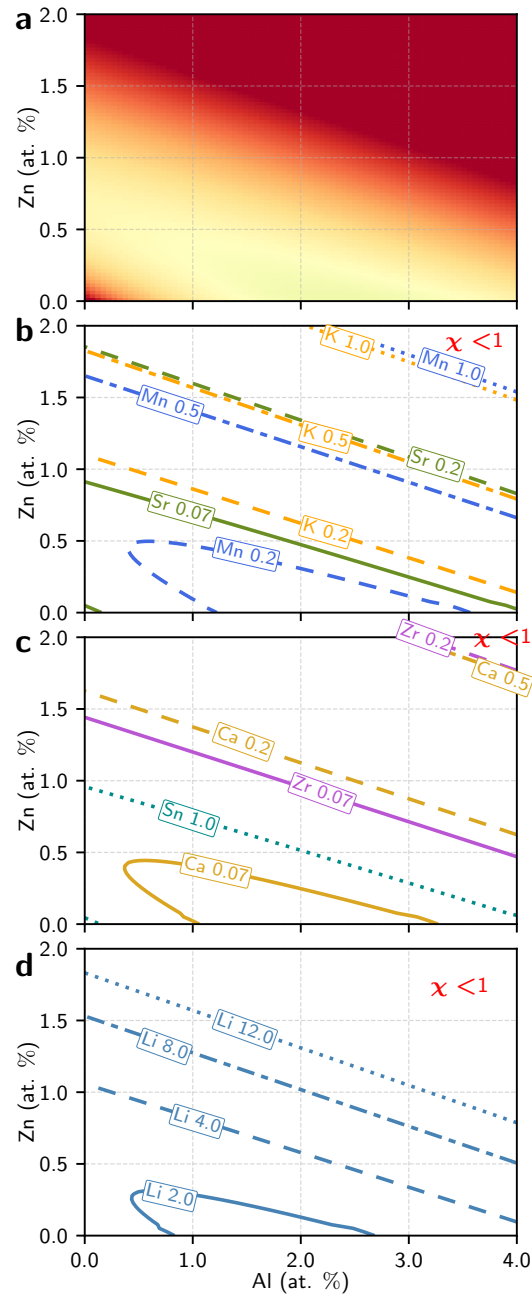


Figure 7.6 – **Prediction of ductility in quaternary alloys based on Al-Zn solutes.** Fig. (a) shows the variation of ductility index χ with Al and Zn concentrations. χ always remains less than 1, indicating not enough ductility for any composition of ternary Mg-Al-Zn alloys. The rest of the figures (b), (c), and (d) show the effect of a third solute (Mn, K, Sr, Zr, Ca, Sn, and Li) on the ductility index. Each line, marked with the atomic concentration (at. %) of the third solute, indicates the compositions at which $\chi = 1$. The compositions of alloys away from $\chi < 1$ in the lower-left region for each line are predicted to yield good room temperature ductility.

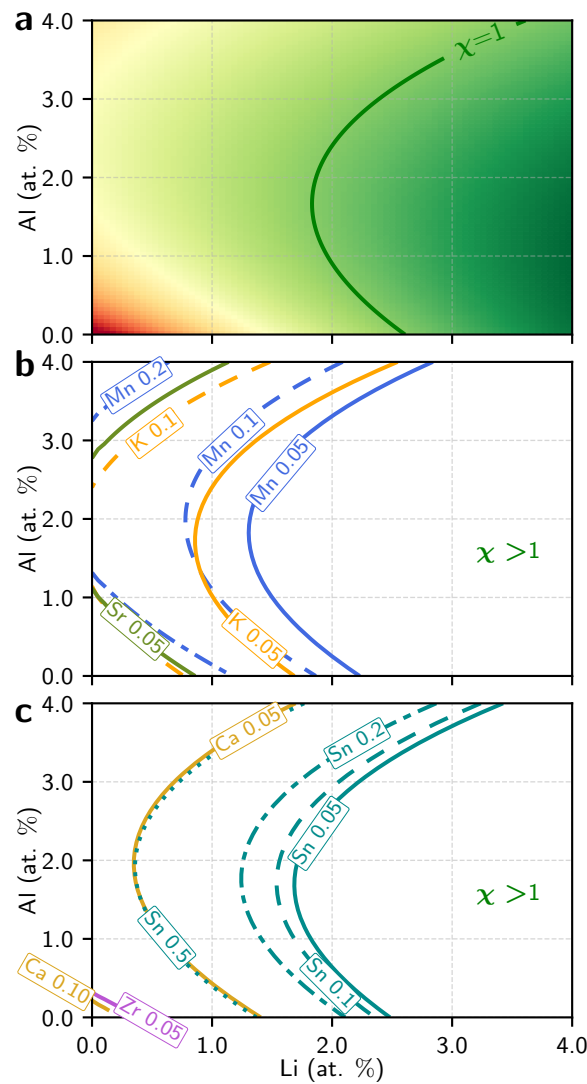


Figure 7.7 – Prediction of ductility in quaternary alloys based on Li-Al solutes. Fig. (a) shows the variation of ductility index χ with Li and Al concentrations. $\chi > 1$ indicates the regions of good ductility. The rest of the figures (b) and (c) show the effect of a fourth solute (Mn, K, Sr, Zr, Ca, and Sn) on the ductility index. Each line, marked with the atomic concentration (at. %) of the third solute, indicates the compositions at which $\chi = 1$. The compositions of alloys towards $\chi > 1$ in the lower-right region for each line are predicted to yield good room temperature ductility.

2 at.% Al concentration, the Al amount in the predicted composition can be varied in the range of 1-3 at.% without much change in the value of χ .

Li is another potential element to be used in forming ductile Mg alloys which, however, exhibit low strength [226] (Li is also currently relatively expensive). The low strength of Mg-Li alloys can be overcome by the additions of ternary elements without sacrificing ductility. Alloying with Al [126, 135, 226], Zn [135, 226], Ag [226], Ca [226] has been shown experimentally to

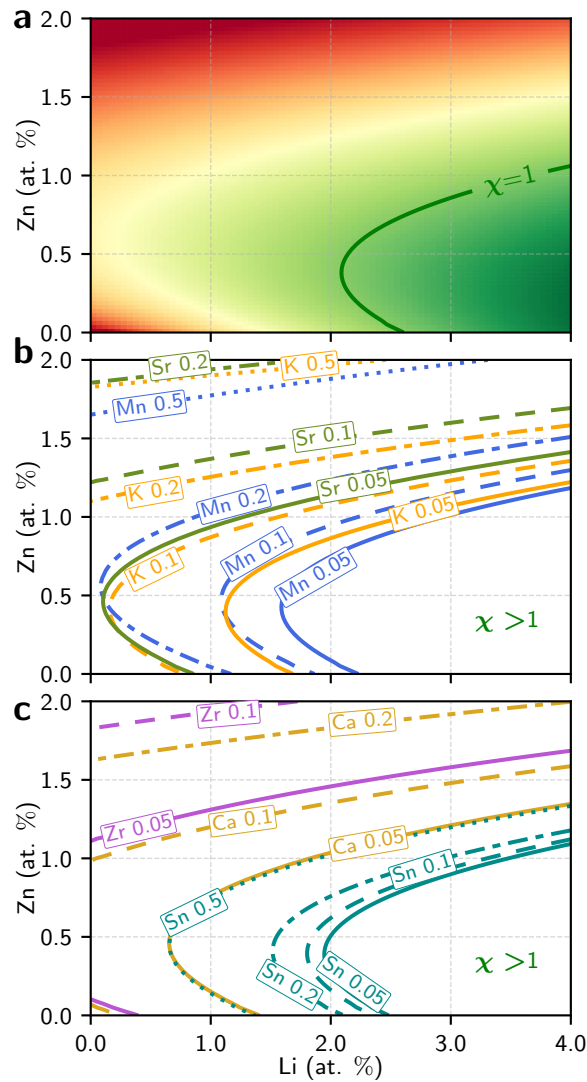


Figure 7.8 – **Prediction of ductility in quaternary alloys based on Li-Al solutes.** Fig. (a) shows the variation of ductility index χ with Li and Zn concentrations. $\chi > 1$ indicates the regions of good ductility. The rest of the figures (b) and (c) show the effect of a third solute (Mn, K, Sr, Zr, Ca, and Sn) on the ductility index. Each line, marked with the atomic concentration (at. %) of the third solute, indicates the compositions at which $\chi = 1$. The composition of alloys towards $\chi > 1$ in the lower-right region for each line are predicted to yield good room temperature ductility.

demonstrate good ductility in the compositions predicted by our theory. The theory also predicts that small addition of effective second alloying elements such as Ca, Sr, Zr in Mg-Li can afford the concentration of Li to be less than 1 at.%. We should also note that Li, if exceeds ~ 19 at.% concentration, can form the bcc β phase in Mg alloys [10] and that the present theory is applicable for solid solution state, the Li level should be below that critical concentration.

Mn as an alloying element is gaining attention to improve the ductility of Mg alloys, which is

discussed above in relation to Mg-Al-Mn, Mg-Zn-Mn, and Mg-Li-Mn alloys. We show in Fig. 7.4 the combination of Mn with other favorable solutes. This shows that two favorable solutes can be mixed together in very small quantity, allowing both to remain in their solubility limits, to achieve good ductility in Mg alloys. Mg0.06Ca0.17Mn, Mg0.03Sr0.1Mn, Mg0.03K0.25Mn, and Mg0.01Zr0.1Mn (concentration in at.%) are a few examples of such potential alloys.

7.4 Predictions for quaternary Mg alloys

Fig. 7.6 shows the predicted ductility index χ and ductility inducing compositions for quaternary alloys based on Al-Zn with favorable solutes Sr, Mn, K, Sn, Ca, and Zr. Fig. 7.6(a) shows the result for ternary alloys, and in the rest of the figures (b), (c), and (d), the plotted lines, corresponding to the labeled amount of third solute element, show the boundary of composition with $\chi = 1$. For any line labeled with the amount of third solute elements, the compositions of the two base solute elements away from $\chi < 1$ in Fig. 7.6 indicate the alloy composition expected to be ductile.

Ternary Al-Zn alloys do not show sufficient ductility, so we show that the addition of a third favorable solute can turn these alloys into ductile. The addition of a small amount of Mn in AZ31 alloys can bring the ductility index $\chi \sim 0$ by negating the detrimental effect of Zn. Many commercially used alloys contain Mn exhibiting good ambient temperature ductility [94, 111, 124, 133] consistent with the theory prediction. The addition of Ca in AZ31 alloy [131] has been used to increase the ductility, in agreement with the prediction of the theory. The theory also predicts that the addition of Li will bring the ductility index $\chi > 1$ producing ductility which is corroborated by experiments [126, 135, 224, 225]. According to the theory, the additions of solute elements Sr, Sn, and Zn can generate ductility in AZ alloys.

Figs. 7.7 and 7.8 show the ductility index χ of quaternary alloys based on Li-Al and Li-Zn. In these figures, (a) shows the result of ternary alloys, and in the rest of the figures (b) and (c), the plotted lines, corresponding to the labeled amount of third solute element, show the boundary of composition with $\chi = 1$. For any line labeled with the amount of third solute elements, the compositions of the two base solute elements towards $\chi > 1$ indicate the alloy composition expected to be ductile. The theory provides the range of compositions that are expected to be ductile. Moreover, the possibility of adding three solute elements provides us with a greater degree of freedom in composition space to optimize the alloy properties specific to the application, such as ductility, strength, toughness, formability, extrudability, density, creep resistance, corrosion resistance, bio-compatibility, and cost to name a few.

7.5 Predictions in pyramidal I favorable regime

Until now, we have presented the results for the dilute concentration of solutes where $\langle c + a \rangle$ screw dislocations, on average, are more stable on pyramidal II than on pyramidal I plane. However, the addition of favorable solutes above a specific amount will reverse the stability order, as

shown in Fig. 6.3, and then cross-slip from the pyramidal I plane to the pyramidal II plane compete with the PB transition of pyramidal I $\langle c + a \rangle$ mixed dislocation. This pyramidal I favorable regime is particularly relevant RE solutes that have a very strong average effect and high enough solubility limit [171].

Fig. 7.9(a) shows the variation of average energy difference between pyramidal I and pyramidal II dislocations with RE solute concentrations. In Fig. 7.9, \bar{c} is the concentration at which the energies of both dislocations become equal in the binary alloys, and in Fig. 7.9(b), the concentration is normalized with respect to \bar{c} for each solute. As we gradually increase the solute concentration up to \bar{c} (Er : 0.62 at.%, Y : 0.61 at.%, Gd : 0.56 at.%, Nd : 0.53 at.%, Ce : 0.53 at.%), the dislocation energy difference decreases, which in turn increases the rate of cross-slip process.

Fig. 7.9(b) shows the predicted cross-slip energy barrier versus solute concentrations. The RE elements lead to a rapid decrease in the pyramidal $\langle c + a \rangle$ cross-slip barrier at low solute concentrations. At concentrations for which $\chi > 1$, the generation of new pyramidal II dislocation loops is deemed sufficiently fast to enhance ductility in spite of the on-going detrimental PB transitions. These predictions were shown to be consistent with a host of experimental studies performed on Mg-RE alloys [5, 84, 138, 167, 179, 181, 182]. At concentrations $c > \bar{c}$, further addition of RE solutes makes pyramidal I more stable and increases the average pyramidal I-II energy difference. The average solute effect will thus drive the cross-slip barrier higher. However, the effect of solute fluctuations is increasing and continues to reduce the overall cross-slip barrier. Ultimately, however, with increasing solute concentrations, the increasing average effect of the solutes counteracts the fluctuation effect and the cross-slip barrier begins to increase again. Since the PB transition of the mixed pyramidal I dislocation has a much lower energy barrier than that of the pyramidal II edge dislocation, the increasing cross-slip barrier re-enters the less-ductile ($\chi < 1$) domain at concentrations $\approx 3 - 3.5$ times the concentrations at which pyramidal I and pyramidal II are energetically equal. Ductility is predicted to be rapidly reduced with the further addition of solutes, as χ decreases toward 0 and further to $\chi = -1$. Therefore, we predict an upper limit to the ductilizing effects of the RE solutes, in the vicinity of 1.5 at% for the RE elements, beyond which the alloys are predicted to have low ductility. This is the main result of the current work, which has practical implications in the future design of new ductile Mg alloys.

We now compare our prediction with some recent experiments on high concentration Mg-RE alloys. Rikihisa et al. [167] investigated the dominant slip systems in designed single-crystal Mg-Y alloys at 0.6 at.%, 0.9 at.%, 1.1 at.%, and 1.3 at.% Y concentrations. Their findings suggest that pure Mg yields by pyramidal II slip while all these Mg-Y alloys yield by pyramidal I slip except the Mg-1.3 at.% Y alloy where yield is evidently dominated by prismatic slip. This is in agreement with the result shown in Fig. 7.9(a), where pyramidal I dislocation becomes more favorable at around 0.6 at.% Y. Furthermore, deformation studies of polycrystal Mg-0.9at.%Y alloy indicate higher activity of pyramidal I $\langle c + a \rangle$ dislocations, with concomitant good ductility, in accordance with the results shown in Fig. 7.9(b).

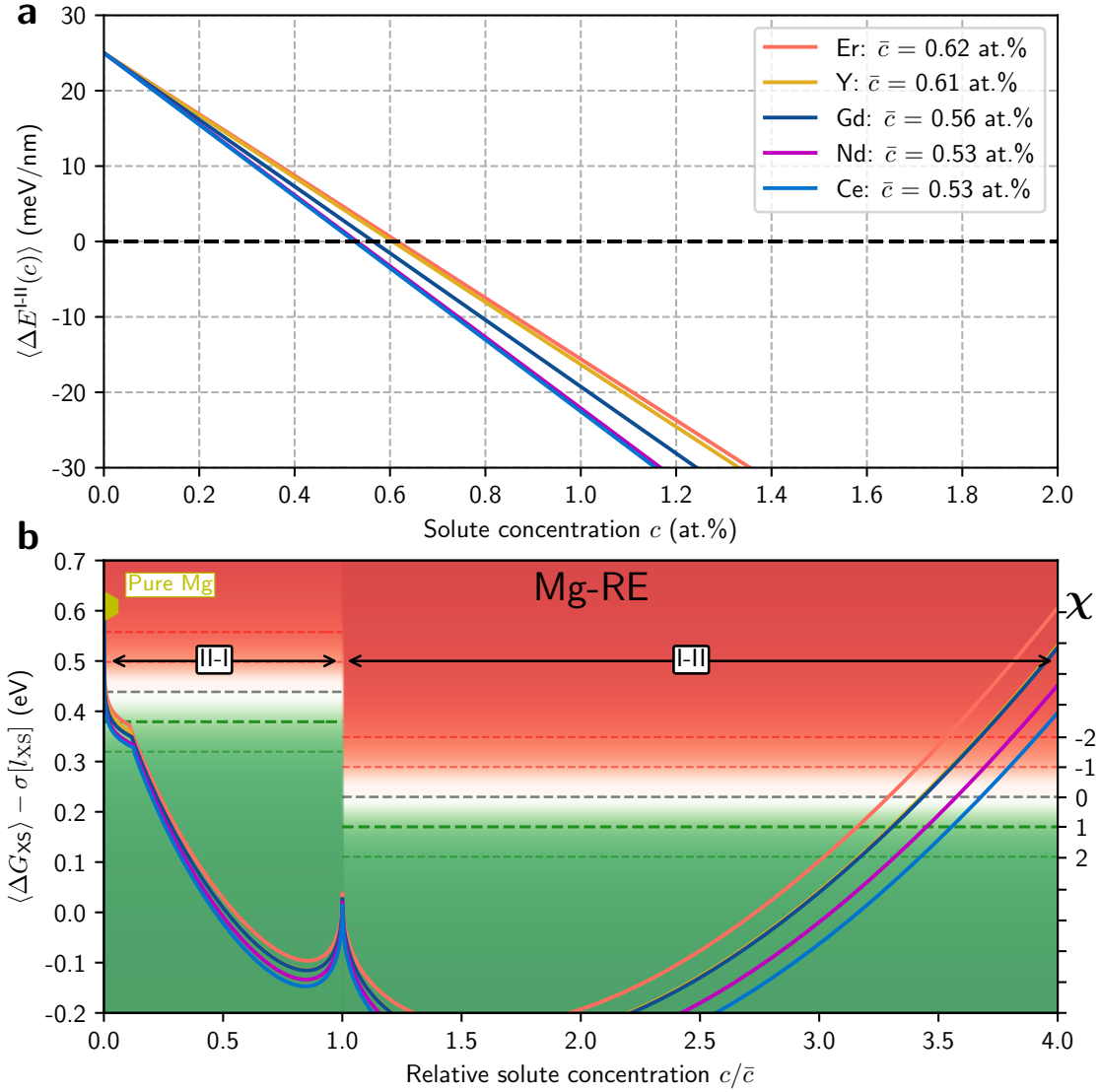


Figure 7.9 – **Prediction of ductility in Mg-RE binary alloys including the pyramidal I favorable regime.** (a) Variation of the average energy difference between the pyramidal I and pyramidal II screw $\langle c + a \rangle$ dislocations as a function of solutes concentrations. (b) Cross-slip barrier, including fluctuation, and ductility index χ as a function of concentrations normalized by \bar{c} at which the energies of the pyramidal I and pyramidal II dislocations become equal. Value of \bar{c} (at.%) - Er : 0.62, Y : 0.61, Gd : 0.56, Nd : 0.53, Ce : 0.53. Mg alloys with $\chi > 1$ (in the green region) are predicted to be ductile, and not ductile with $\chi < 0$ (in the red region). At concentrations lower than \bar{c} , pyramidal II is more stable and cross-slip from the pyramidal II to pyramidal I planes competes with the PB transition of the pyramidal II $\langle c + a \rangle$ edge dislocation (with barrier of $\Delta E_{PB} = 0.5$ eV). Beyond \bar{c} , pyramidal I becomes more stable and now cross-slip from the pyramidal I to pyramidal II planes competes with even faster PB transition of the pyramidal I mixed $\langle c + a \rangle$ dislocation (with barrier of $\Delta E_{PB} = 0.3$ eV).

Gao et al. [78] studied the deformation of solution treated polycrystal Mg-Gd cast alloys and found decreasing ductility with increasing Gd contents. In their experiments, as the Gd concentration is increased from 0.5 at.% to 3.63 at.%, the alloy ductility is reduced with an increase in yield strength. This loss of ductility may, however, be due to normal ductility reduction with increasing strength, according to the Considère criterion. However, the experiments are not inconsistent with our findings. Data from the same work shows low ductility in ternary Mg-1.82Gd-1.02Y(at.%), Mg-1.48Gd-1.13Y(at.%), and Mg-1.07Gd-1.77Y(at.%). Since Gd and Y have similar effects, our binary predictions are approximately appropriate for these ternaries at the total Gd+Y content. All of these alloys have a Gd+Y concentration around 1.6-1.8 at.%, which is above the level where we predict a transition back to low ductility. Nonetheless, caution is needed in interpreting the observation because ductility can also be influenced by other factors such as texture, grain boundary segregation and precipitation, and grain sizes. For example, in these experiments, cast alloys were studied and these microstructures presumably would not have strong texture and presumably basal $\langle a \rangle$ dislocation could accommodate some plastic strain and thus lead to some ductility.

Finally, we discuss the experiment performed by Wang et al. [218] on rolled and extruded Mg-1.8Gd-0.9Y-0.1Zr(at.%) alloys. Again, interpretation of ductility measurements in experiments is not straightforward, since ductility is not an intrinsic material property and depends on many factors. Nevertheless, the experiment shows that the as-rolled and as-extruded alloys have low ductility. This is consistent with our theory since the amount of RE elements is 2.7 at.%, well beyond the ductility limit according to Fig. 7.9(b). This low ductility may also arise due to hard precipitate formation since the excessive formation of hard precipitates would increase yield/flow strength and decrease ductility. However, the alloy ductility increased after aging, which might be due to the depletion of RE solutes in the matrix when forming the precipitates, and restoring the matrix concentration of RE elements back into the ductile range. Thus, the experimental observations here are broadly consistent with the present theory.

8 Discussion and Conclusion

In this thesis, we investigate in detail the underlying atomistic mechanisms operative in certain Mg alloys that circumvent the harmful PB transition of the pyramidal $\langle c + a \rangle$ dislocations, the primary cause for low ductility in pure Mg. We choose the Mg-Y alloy as a model ductile Mg alloys to perform the atomistic simulations, exposing the influence of the favorable solutes on the various mechanisms associated with pyramidal $\langle c + a \rangle$ dislocations. To this end, we develop a new Mg-Y interatomic potential in the MEAM framework for the specific purpose of examining the plastic deformation of this alloy family.

We first test the hypothesis that Y and other favorable solutes might suppress the inimical PB transition by increasing the associated energy barrier and stabilizing the $\langle c + a \rangle$ dislocations on the easy-glide pyramidal planes. Extensive finite temperature MD simulations in random solid solution Mg-3at.%Y alloy show that Y solutes decrease the energies of both initial pyramidal-dissociated and final basal-oriented dislocations, and do not have any appreciable effect on the transition time. The simulation results showing the basal-dissociated core having even lower energy than the pyramidal-dissociated core even suggest a trend toward solutes enhancing the PB transition. Statistically-rare solute fluctuations may exist and these fluctuations may reduce the energy of the basal-dissociated $\langle c + a \rangle$ dislocation even more than seen here. Since the PB transition is a nucleation event, such rare fluctuations somewhere along an extended dislocation line could lead to a faster net PB transition rate than in pure Mg. This would act against ductility, increasing the CRSS for the $\langle c + a \rangle$ slip in single-crystal Mg alloys. Furthermore, the results presented here are in full agreement with the elasticity estimates of the RE solute effects on the PB transition [237], and experimental observation of the profuse $\langle c + a \rangle$ dislocations dissociated on the basal plane in Mg-RE alloys [181, 182].

After establishing that the solute elements are not able to delay the detrimental PB transition, we propose a new mechanism to explain the enhanced activity of the pyramidal $\langle c + a \rangle$ dislocations in ductile Mg alloys. In pure Mg, the energy difference between the low-energy pyramidal II $\langle c + a \rangle$ screw dislocation and the high-energy pyramidal I $\langle c + a \rangle$ screw dislocation leads to very a slow cross-slip process. The favorable solutes, however, reduce the dislocation energy difference, and thus accelerate the cross-slip and double cross-slip process of the pyramidal

$\langle c + a \rangle$ dislocations. The accelerated cross-slip process then acts as a source for generating new dislocation loops rapidly enough to extenuate the harmful effects of the PB transition. The mechanistic theory is accompanied by a mathematical model that identifies and predicts the ductile compositions of Mg alloys based on the DFT computed interaction energies between the solutes and the pyramidal I and the pyramidal II stacking faults. The mechanistic theory has been validated by the experimental observation of increased dislocation cross-slip in Mg-Y alloys, and the predictions of the model have been shown to be in accordance with experimental results for a large number of binary, ternary and higher order of Mg alloys containing a range of solute elements (Ag, Zn, Al, Li, K, Sn, Mn, Sr, Ca, Zr, and RE).

One notable success of the theory is in quantitatively explaining the emergence of good ductility and concomitant weak basal texture in Mg alloys containing trace amounts of REs. Hantzsche et al. [85] and Griffiths [84] show that binary Mg alloys containing a mere ~ 0.01 at.% Ce or ~ 0.02 at.% Nd or ~ 0.06 at.% Y start to show weaker basal texture; both studies confirm Ce to be the most effective and Y to be the relatively least effective solute in terms of amounts required to weaken the basal texture. These concentration limits coincide with the predicted concentrations of corresponding solutes at which $\chi \approx 1$ for Mg-Ce, Mg-Nd, and Mg-Y binary alloys.

Although we mainly focus on the binary and ternary alloys containing Al and Zn where an additional favorable solute is needed to counteract the negative effects of Al and Zn, the ductile Mg alloys comprising many favorable solutes have been examined experimentally and are in accordance with the prediction of the theory. For instance, Mg alloys containing (Sr, Mn, Li, Al) can be inferred from the presented data to be ductile, in agreement with the experiment [233]. Likewise, for alloys made of (Ca,Sr,Mn) [148, 202], (Al,Ca,Mn) [147], (Al,Zn,Mn,Ca) [104] and (Zn,Sr,Mn) [154], the ductility index χ would be more than 1, thus predicting good ductility. This data reaffirms the ability of the theory in suggesting ductile Mg alloy compositions. We could further predict that ternary or higher-order Mg alloys containing a combination of favorable solutes (out of Ca, Sr, Sn, Mn, K, and Zr) in small amounts exhibit good room temperature ductility.

The theory predicts Mg-K binary alloys to be ductile at K concentrations more than 0.15 at.%. In general, the addition of K in other higher-order alloys comprising unfavorable solute produces good ductility. These K containing Mg alloys are hitherto unexplored and could serve as further tests of the predictive power of the mechanistic model. However, because the boiling temperature of K is close to the melting temperature of Mg, manufacturing Mg-K alloys are challenging.

For favorable solutes (reducing the average dislocation energy difference), the situation may arise where beyond a critical solute concentration, the pyramidal I $\langle c + a \rangle$ dislocations become energetically stable compared to the pyramidal II $\langle c + a \rangle$ dislocations. In this scenario, cross-slip from the pyramidal I to the pyramidal II (leading to the $\langle c + a \rangle$ dislocation multiplication) would be required to circumvent the PB transition of the pyramidal I $\langle c + a \rangle$ mixed disloca-

tion. The energy barrier associated with the PB transition of the pyramidal I $\langle c + a \rangle$ mixed dislocations (~ 0.3 eV [229]) is even less than that associated with the PB transition of the pyramidal II $\langle c + a \rangle$ edge dislocation (~ 0.5 eV [228]). All of these point to the existence of a maximum concentration of favorable solute beyond which the resulting alloys are not ductile. This discussion is more relevant to alloys containing RE elements that have strong average effects and moderate/high solubility.

The presence of two different pyramidal I and one pyramidal II planes intersecting each other along a common $\langle c + a \rangle$ direction leads to several cross-slip pathways in the pyramidal I favorable regime. A comparison of energetics among the possible cross-slip routes obtained by NEB calculations reveals that the $\langle c + a \rangle$ dislocation residing on the pyramidal I plane first cross-slips onto a pyramidal II plane and then cross-slips back to a parallel pyramidal I plane. Based on the results gleaned from the NEB computations, we extend the ductility model in the pyramidal I favorable regime, applying it to the binary Mg alloys containing RE solute elements. We find that increasing the RE solute concentration, which increases the stability of the pyramidal I $\langle c + a \rangle$ dislocations relative to the pyramidal II $\langle c + a \rangle$ dislocations, ultimately increases the barrier for cross-slip to levels that are too high for double cross-slip to overcome the detrimental effects from the transition of the pyramidal I mixed dislocations to immobile basal-dissociated structures. Thus, there is an upper limit of approximately 1.5 at.% concentration of RE solutes beyond which high ductility in Mg-RE alloys is lost. This is perhaps a surprising result, but not inconsistent with limited experimental data available. Our findings motivate further experiments on the Mg-RE alloys at higher concentrations, in the solutionized state that have not been probed thoroughly, and where some implications of our findings for the design of strong and ductile Mg alloys have been identified.

An important and sensitive parameter required in this model is the energy difference between the pyramidal I and the pyramidal II $\langle c + a \rangle$ screw dislocations which in this work is inferred by the analysis of experimental studies of ductility of various Mg alloys. Further, the first principles calculations are required to precisely calculate this crucial parameter. The overall success of the theory in predicting broad trends in ductility across various solid solution alloys, however, suggests that the energy difference should be close to that used in this work.

Our analysis is based on the solid solution model and does not consider the solubility of solute elements in Mg. For the cross-slip mechanism to be effective, the solutes at concentrations indicated in the figures in Chapters 6 and 7 must be in a solid solution state. Whether this solid solution concentration range is attainable is determined by alloy thermodynamics. Thermodynamics calculation can be performed to estimate the solute solubility limits in Mg alloys at various temperatures and processing stages, for example before and after precipitation.

Mg alloys suitable for industrial applications must possess both high ductility and high strength. Strength is most effectively achieved through age-hardening/precipitation. Precipitation depletes solutes in the matrix material. However, high ductility according to the present model requires maintenance of sufficient solute concentration in the lattice to accelerate the

cross-slip. Therefore, alloys that are ductile in the solid-solution state may have much lower ductility, although much higher strength, after age-hardening. Thermodynamic calculations on the alloys can be used to estimate residual solute concentrations after aging. The current analysis, which focuses on dilute to ultra dilute solute concentrations, can determine whether the matrix material is expected to remain ductile after aging/peak-aging. The results presented here are useful for identifying alloys that are ductile not only in the solid-solution state but also in the precipitate-strengthened state.

Increasing the alloy strength by increasing the RE solute content is counterproductive in the pursuit of high strength and high ductility alloys. Common alloying elements that can enable ductility, such as Zr, Ca, and Mn, are not soluble at high concentrations and so would not be affected by the present findings. Other high-solubility non-RE elements such as Li and Sn do not cause a transition to pyramidal I dominance at moderate concentrations (10% or less). At moderate concentrations, these solutes could be particularly useful additions for providing good ductility along with some solute strengthening, and with the addition of other dilute solutes that enable precipitate formation might enable strengthening (due to precipitation) while maintaining ductility (due to high remaining Li and Sn concentrations in the Mg lattice).

The research work performed as part of this thesis allows us to gain a mechanistic understanding of the origins of ductility in various solid solution Mg alloys and enables us to identify the different solute elements across the periodic table and their concentrations that can impart ductility in Mg. Along with rationalizing the existing experimental results, this theory also suggests some hitherto untested potential solute elements and compositions. This theory can be used in conjunction with other theories, such as solute strengthening theory [120, 204] to optimize the properties and cost of Mg alloys by combining the different solute elements in suitable proportions. Finally, we note that while the mechanistic theory presented in this thesis can be useful for the design of ductile Mg alloy compositions, the thermo-mechanical processing, and other metallurgical strategies are equally important in achieving technologically useful Mg alloys for structural applications.

9 Outlook

The ductility model presented in this research is successfully validated against experimental observations. The ductility mechanisms based on the solute effect on the pyramidal cross-slip barrier are inherently atomistic in nature, and thus its various aspects could, in principle, be clarified and tested by means of atomistic simulations. The effects of a single solute on the cross-slip barrier have indeed been demonstrated by NEB calculations in this work. However, a complete treatment of the ductility model is not possible at this stage due to the lack of a sufficiently accurate interatomic potential for Mg alloys. The recent surge of interest in a new class of machine learning potentials [25, 29–31, 65, 86, 144, 163] has a potential to fill this gap, especially for alloy systems. Supervised machine learning potentials have been applied successfully to investigate various mechanical properties of metals and alloys [67, 107, 129]. Thus the development of machine learning potential for pure Mg and Mg alloys could be the focus of future studies.

This work sought to unveil the atomic-scale mechanisms associated with a single dislocation. The plastic deformation of a crystal is, however, controlled by the multiscale evolution of a large number of dislocations subject to external stresses. The evolution and patterning of a dislocation network are influenced as much by the short-range atomic-scale mechanisms as by the elastic interactions induced by dislocations situated relatively far away. Due to the heavy computational resources involved, atomistic simulations are unsuitable for probing the evolution of dislocation networks in order to make meaningful observations and prediction of resulting crystal plasticity. Dislocation dynamics (DD) simulations are particularly useful to investigate the mesoscale dislocation plasticity [20, 83, 244]. DD simulations ignore the atomic nature of dislocations and explicitly follow the evolution of individual dislocations represented as line segments interacting elastically with each other. DD simulations, however, are prescriptive as opposed to the descriptive nature of atomistic simulations. The rules for short-range interactions associated with dislocations such as cross-slip, junction formation, junction destruction, dislocation splitting, and PB transition, etc. are described a priori [20, 37, 130, 166]; dislocation evolution and resulting plastic deformation are the output of the DD computations [39, 66, 127]. Essential and important steps towards performing DD simulations

in hcp crystals have been taken by many researchers [21, 47, 140]. Further efforts are, however, needed to incorporate the insights obtained from the atomistic simulations of the thermally activated processes, such as the PB transition and the pyramidal $\langle c + a \rangle$ cross-slip process. DD simulations will then be able to directly show the effect of the competition between the PB transition and cross-slip of the pyramidal $\langle c + a \rangle$ dislocations on the hardening behavior of Mg single crystal under various loading conditions, providing input for higher scale crystal plasticity models.

Another intriguing aspect of Mg plasticity is that the CRSS for the pyramidal II $\langle c + a \rangle$ dislocations drops significantly at higher temperatures beyond around 416 K, [15, 151, 155], and ductility of pure Mg increases [134]. A basic understanding of the mechanisms associated with the high-temperature plastic deformation of Mg is still missing. A number of thermally activated rate-controlling mechanisms may be operative at higher temperatures: activation of the pyramidal $\langle c + a \rangle$ dislocations, cross-slip, and climb of the $\langle a \rangle$ and the $\langle c \rangle$ dislocations, grain boundary sliding, and diffusional flow. The atomistic simulation could play a key role in clarifying the high deformation mechanism in pure Mg [168]. One immediate and important step in this direction is to compute the free energy difference between the pyramidal I and the pyramidal II $\langle c + a \rangle$ dislocations as a function of temperature. This free energy difference controls the efficacy of the cross-slip process in countering the PB transition and activating the pyramidal $\langle c + a \rangle$ dislocation systems. A decrease in the free energy difference indicates the possibility of higher activation of pyramidal $\langle c + a \rangle$ dislocations, softening of the pyramidal slip systems, and increased ductility. More extensive research in the high-temperature behavior of various dislocation types is necessary in order to clarify the high-temperature plastic deformation of pure Mg.

A The MEAM potential framework for elemental and binary alloy system

The MEAM interatomic potential framework was first proposed by Baskes [27, 28] as a modification of the EAM potential method to account for the directionality of near-neighbor atomic bonding. The MEAM was later modified to overcome some critical shortcomings of the original formalism [118, 119], primarily by including second-nearest-neighbor interactions. The description given below draws from Refs. [118, 119].

A.1 Formalism for pure element

Under the framework of the MEAM potential, energy of a atomic system comprising pure element is given as

$$E = \sum_i \left[F(\bar{\rho}_i) + \frac{1}{2} \sum_{j(\neq i)} \phi_{ij}(R_{ij}) \right], \quad (\text{A.1})$$

where F is the embedding function, $\bar{\rho}_i$ is the background electron density at site i , ϕ_{ij} is the pair interaction between atoms at sites i and j with a distance R_{ij} between them. The embedding function takes the form

$$F(\bar{\rho}) = AE_c \frac{\bar{\rho}}{\bar{\rho}^0} \ln \frac{\bar{\rho}}{\bar{\rho}^0}, \quad (\text{A.2})$$

where A is an element-dependent adjustable parameter, E_c is the cohesive energy, and $\bar{\rho}^0$ is the background electron density for a reference structure which is usually the equilibrium structure. The background electron density $\bar{\rho}_i$ comprised spherically symmetric partial contribution $\rho_i^{(0)}$ and angular partial contributions $\rho_i^{(1)}$, $\rho_i^{(2)}$ and $\rho_i^{(3)}$, which are expressed as

$$\left(\rho_i^{(0)}\right)^2 = \left[\sum_{j(\neq i)} \rho_j^{a(0)}(R_{ij}) S_{ij} \right]^2, \quad (\text{A.3a})$$

$$\left(\rho_i^{(1)}\right)^2 = \sum_{\alpha} \left[\sum_{j(\neq i)} \frac{R_{ij}^{\alpha}}{R_{ij}} \rho_j^{a(1)}(R_{ij}) S_{ij} \right]^2, \quad (\text{A.3b})$$

$$\left(\rho_i^{(2)}\right)^2 = \sum_{\alpha, \beta} \left[\sum_{j(\neq i)} \frac{R_{ij}^{\alpha} R_{ij}^{\beta}}{R_{ij}^2} \rho_j^{a(2)}(R_{ij}) S_{ij} \right]^2 - \frac{1}{3} \left[\sum_{j(\neq i)} \rho_j^{a(2)}(R_{ij}) S_{ij} \right]^2, \quad (\text{A.3c})$$

$$\left(\rho_i^{(3)}\right)^2 = \sum_{\alpha, \beta, \gamma} \left[\sum_{j(\neq i)} \frac{R_{ij}^{\alpha} R_{ij}^{\beta} R_{ij}^{\gamma}}{R_{ij}^3} \rho_j^{a(3)}(R_{ij}) S_{ij} \right]^2 - \frac{3}{5} \sum_{\alpha} \left[\sum_{j(\neq i)} \frac{R_{ij}^{\alpha}}{R_{ij}} \rho_j^{a(3)}(R_{ij}) S_{ij} \right]^2, \quad (\text{A.3d})$$

where $\rho_j^{a(h)}(R_{ij})$ denote the atomic electron densities from a site j at a distance R_{ij} from site i , R_{ij}^{α} is the α component of distance vector between atoms at sites j and i , and S_{ij} is the screening between atoms at sites i and j as described below. Several expressions have been proposed to combine the partial electron densities to obtain the total background electron density [26]. We use the following expression in the present work

$$\bar{\rho}_i = \rho_i^{(0)} G(\Gamma_i), \quad (\text{A.4a})$$

$$G(\Gamma) = \frac{2}{1 + \exp(-\Gamma)}, \quad (\text{A.4b})$$

$$\Gamma_i = \sum_{h=1}^3 t^{(h)} \left[\frac{\rho_i^{(h)}}{\rho_i^{(0)}} \right]^2, \quad (\text{A.4c})$$

where $t^{(h)}$ are adjustable parameters. The atomic electron density is computed as

$$\rho_j^{a(h)}(R_{ij}) = \rho_0 \exp \left[-\beta^{(h)} \left(\frac{R_{ij}}{r_e} - 1 \right) \right], \quad (\text{A.5})$$

where ρ_0 is element-dependent density scaling factor, $\beta^{(h)}$ are adjustable parameters, and r_e is the nearest neighbor distance in the equilibrium reference structure.

After determining the embedding function, we turn our attention to the pair potential contribution $\phi(R)$ in the total energy given by Equation A.1. In MEAM, no specific functional form is given to pair potential $\phi(R)$, instead, it is determined from the known values of total energy and embedding function. The energy per atom for the reference structure is obtained from

the universal equation of state by Rose et al. [172] as a function of nearest-neighbor R

$$E^u(R) = -E_{ic}(1 + a^* + da^{*3})\exp(-a^*), \quad (\text{A.6a})$$

$$a^* = \alpha \left(\frac{R}{r_e} - 1 \right), \quad (\text{A.6b})$$

$$\alpha = \sqrt{\frac{9B\Omega}{E_c}}, \quad (\text{A.6c})$$

where d is an adjustable parameter, B is the bulk modulus, and Ω is equilibrium atomic volume. Considering the second nearest-neighbor interaction, energy per atom in the reference structure is written by using A.1

$$E^u(R) = F[\bar{\rho}(R)] + \frac{Z_1}{2}\phi(R) + \frac{Z_2S}{2}\phi(aR), \quad (\text{A.7})$$

where $\bar{\rho}(R)$ is the background electron density, Z_1 and Z_2 are, respectively, number of the first and second nearest-neighbor atoms, a is the ratio between the second and first nearest-neighbor distance, and S is the screening on the second nearest-neighbor interaction. Another function $\psi(R)$ is introduced to write Equation A.7 as

$$E^u(R) = F[\bar{\rho}(R)] + \frac{Z_1}{2}\psi(R), \quad (\text{A.8a})$$

$$\psi(R) = \phi(R) + \frac{Z_2S}{Z_1}\phi(aR). \quad (\text{A.8b})$$

Now, $\psi(R)$ can be calculated as a function of R from Equation A.8a and then, $\phi(R)$ is computed as function of R by using following relation

$$\phi(R) = \psi(R) + \sum_{n=1}^{\infty} (-1)^n \left(\frac{Z_2S}{Z_1} \right)^n \psi(a^n R), \quad (\text{A.9})$$

where summation is performed until the correct value of energy is obtained.

Now we discuss the final component of elemental-MEAM potential, the screening function S_{ij} between the atoms at sites i and j . Screening function is built such that $S_{ij} = 1$ for completely unscreened atoms within the cutoff radius r_c of the potential, and $S_{ij} = 0$ for atom pair completely screened or outside the cutoff radius. For partial screening, it takes a value between 0 and 1. The total screening function is the product of the radial cutoff function and

three body terms. The expression for screening function is

$$S_{ij} = \bar{S}_{ij} f_c \left(\frac{r_c - R_{ij}}{\Delta r} \right), \quad (\text{A.10a})$$

$$\bar{S}_{ij} = \prod_{k(\neq i, j)} S_{ikj}, \quad (\text{A.10b})$$

$$f_c(x) = \begin{cases} 1 & x \geq 1, \\ [1 - (1 - x)^4]^2 & 0 < x < 1, \\ 0 & x \leq 0, \end{cases} \quad (\text{A.10c})$$

where Δr is parameter to smoothen the radial cutoff of potential which has a cutoff radius r_c . Three body screening function S_{ikj} , amount of screening between atoms at i and j due to atom at k , is determined from a simple geometrical construction. Imagine an ellipse in $\mathbf{x} - \mathbf{y}$ plane passing through atoms i, j and k with the atoms i and j on the \mathbf{x} axis

$$x^2 + \frac{y^2}{C} = \left(\frac{R_{ij}}{2} \right)^2, \quad (\text{A.11})$$

where the value of C is computed for every atom k . Two adjustable limiting values C_{\min} and C_{\max} ($C_{\max} > C_{\min}$) are defined for every possible triplet (i, j, k) . If atom k is located outside the ellipse defined by C_{\max} , that is, $C > C_{\max}$, the atom k does not provide any screening. If atom k is inside the ellipse defined by C_{\min} , that is, $C < C_{\min}$, the atom k completely screens the interaction between i and j . On the other hand, if $C_{\min} < C < C_{\max}$, there will be only partial screening. Following is the expression for three body screening function S_{ikj} which satisfies the conditions mentioned above

$$S_{ikj} = f_c \left(\frac{C(i, k, j) - C_{\min}(i, k, j)}{C_{\max}(i, k, j) - C_{\min}(i, k, j)} \right), \quad (\text{A.12})$$

$$C(i, k, j) = 1 + \frac{2(R_{ij}^2 R_{ik}^2 + R_{ij}^2 R_{jk}^2 - R_{ij}^4)}{R_{ij}^4 - (R_{ik}^2 - R_{jk}^2)^2}. \quad (\text{A.13})$$

A.2 Formalism for binary system

Interatomic potential of binary system, under MEAM framework, is constructed upon the potential of individual constituents. In addition to individual elements, pair interaction between different elements is required. Considering an ordered binary intermetallic as the reference structure (here we assume having $\frac{1}{2}i$ atom + $\frac{1}{2}j$ atom), the total energy per atoms $E_{ij}^u(R)$ as a function of nearest-neighbor distance R is given as

$$E_{ij}^u(R) = \frac{1}{2} \left[F_i(\bar{\rho}_i) + F_j(\bar{\rho}_j) + Z_1^{ij} \phi_{ij}(R) + \frac{1}{2} Z_2^{ij} \{ S_i \phi_{ii}(aR) + S_j \phi_{jj}(aR) \} \right], \quad (\text{A.14})$$

where E_{ij}^u is determined from the equation of state [172] using experimentally determined cohesive energy E_c , bulk modulus B , atomic volume Ω and parameter d . The embedding functions F_i and F_j can always be computed. Z_1^{ij} and Z_2^{ij} are, respectively, number of the first and second nearest-neighbor atoms in the reference structure, ϕ_{ii} and ϕ_{jj} are pair interaction, respectively between i atoms and between j atoms, and a is the ratio between the second and first nearest-neighbor distances. Therefore, the pair interaction between the different types of atoms is calculated as

$$\phi_{ij}(R) = \frac{1}{Z_1^{ij}} \left[2E_{ij}^u(R) - F_i(\bar{\rho}_i) - F_j(\bar{\rho}_j) - \frac{1}{2} Z_2^{ij} \{ S_i \phi_{ii}(aR) + S_j \phi_{jj}(aR) \} \right]. \quad (\text{A.15})$$

The values of C_{\max} and C_{\min} are needed to be specified for all possible triplet of atom types. For pure elements, there is only one possible triplet, however, for binary system there are four possible types of triplet. Additionally, the density scaling factor ρ_0 , see Equation A.5, also becomes important for binary alloys. This is an arbitrary value having no effect on the calculation for pure elements. However, for alloy systems, especially for systems where the constituent elements have different coordination numbers, the scaling factor (the ratio of the two values) has a great effect on calculations.

B Ultra Dilute Limit for Higher Order Alloys

In this appendix, we discuss the way to treat the computation of cross-slip rates in ternary and quaternary alloys where at least one solute concentration is in ultra dilute limit, ie. there is not more than one that particular solute in the critical cross-slip length.

B.1 The ultra dilute limit in ternary alloy

Here we consider ternary Mg-alloy having two solute types 1 and 2 with concentrations c_1 and c_2 , respectively. Interaction energies of type 1 solute at site i with pyramidal I and pyramidal II dislocations, respectively, are $U_i^{I,1}$ and $U_i^{II,1}$, and interaction energies of type 2 solute are $U_i^{I,2}$ and $U_i^{II,2}$. The ultra dilute limit in the case of ternary alloy needs to be divided into two regimes: First, only one of the solute types is in the ultra dilute limit; second, both solutes are in the ultra dilute limit. These cases are treated in the following sections.

B.1.1 Type 1 in the dilute and type 2 in the ultra dilute limit ($c_1 \geq c^*$ and $c_2 < c^*$)

In this case we assume that type 1 solute is in the dilute limit, $c_1 \geq c^*$, while concentration of type 2 solute lies in the ultra dilute limit, $c_2 < c^*$. Therefore, as in the case of binary alloy, cross-slip in fraction c_2/c^* of the L/l_{XS} segments occurs in the presence of type 1 solute with concentration c_1 and type 2 solute with effective concentration of c^* , while the remaining fraction $1 - c_2/c^*$ of the L/l_{XS} of cross-slip segments contain only solute of type 1 with concentration c_1 .

For segments containing only type 1 solute, the average and standard deviation of cross-slip barrier, $\langle \Delta G_{XS}^{(1)} \rangle$ and $\sigma^{(1)}[l_{XS}]$, respectively, are calculated using Eqs. 6.8-6.11. Average cross-slip barrier $\langle \Delta G_{XS}^{(12)} \rangle$ of the segments containing both type 1 and type 2 solutes with concentrations c_1 and c^* , respectively, can be computed as

$$\langle \Delta G_{XS}^{(12)} \rangle = \langle \Delta G_{XS}^{(1)} \rangle + \frac{1}{N_T} \sum_i \Delta U_i^{I-II,2}. \quad (B.1)$$

Appendix B. Ultra Dilute Limit for Higher Order Alloys

And, standard deviation results in

$$\sigma[\Delta G_{\text{XS}}(12), l_{\text{XS}}] = \sqrt{\frac{c_1 l_{\text{XS}}}{b} \sum_i \left(\Delta U_i^{\text{I-II},1} \right)^2 + \frac{1}{N_{\text{T}}} \sum_i \left(\Delta U_i^{\text{I-II},2} \right)^2}. \quad (\text{B.2})$$

Thus, total nucleation rate of cross-slip over dislocation line of length L becomes

$$\begin{aligned} R_{\text{XS}} &= \left(1 - \frac{c_2}{c^*}\right) \underbrace{\left[\frac{L\nu_0}{l_{\text{XS}}} \exp\left(-\frac{\langle \Delta G_{\text{XS}}^{(1)} \rangle - \sigma^{(1)}[l_{\text{XS}}]}{kT}\right) \right]}_{\text{having only type 1 solute}} + \frac{c_2}{c^*} \underbrace{\left[\frac{L\nu_0}{l_{\text{XS}}} \exp\left(-\frac{\langle \Delta G_{\text{XS}}^{(12)} \rangle - \sigma^{(12)}[l_{\text{XS}}]}{kT}\right) \right]}_{\text{having both type of solutes}}, \\ &= \frac{L\nu_0}{l_{\text{XS}}} \exp\left(-\frac{\langle \Delta G_{\text{XS}}^{(1)} \rangle}{kT}\right) \left[\left(1 - \frac{c_2}{c^*}\right) \exp\left(\frac{\sigma^{(1)}[l_{\text{XS}}]}{kT}\right) + \frac{c_2}{c^*} \exp\left(-\frac{\frac{1}{N_{\text{T}}} \sum_i \Delta U_i^{\text{I-II},2} - \sigma^{(12)}[l_{\text{XS}}]}{kT}\right) \right]. \end{aligned} \quad (\text{B.3})$$

B.1.2 Both solutes are in the ultra dilute limit ($c_1 < c^*$ and $c_2 < c^*$)

When both solutes are in the ultra dilute limit, critical cross-slip length l_{XS} would encounter either both solutes or one of the solutes or zero solute. Probability of these cases can be calculated as

$$P^{(0)} = \left(1 - \frac{c_1}{c^*}\right) \left(1 - \frac{c_2}{c^*}\right) \quad \text{probability of no solute,} \quad (\text{B.4a})$$

$$P^{(12)} = \frac{c_1 c_2}{(c^*)^2} \quad \text{probability of finding both solutes,} \quad (\text{B.4b})$$

$$P^{(1)} = \frac{c_1}{c^*} \left(1 - \frac{c_2}{c^*}\right) \quad \text{probability of finding only type 1 solute,} \quad (\text{B.4c})$$

$$P^{(2)} = \frac{c_2}{c^*} \left(1 - \frac{c_1}{c^*}\right) \quad \text{probability of finding only type 2 solute.} \quad (\text{B.4d})$$

Next, we need to compute the average and standard deviation of cross-slip energy barrier for the cases listed above. The average cross-slip energy barrier can be obtained as

$$\langle \Delta G_{\text{XS}}^{(0)} \rangle = \Delta G_{\text{XS},i} + \Gamma \Delta s - \Delta \tau b A = \Delta G_{\text{XS}}^{\text{Mg}}, \quad (\text{B.5a})$$

$$\langle \Delta G_{\text{XS}}^{(12)} \rangle = \Delta G_{\text{XS}}^{\text{Mg}} + \frac{1}{N_{\text{T}}} \sum_i \Delta U_i^{\text{I-II},1} + \frac{1}{N_{\text{T}}} \sum_i \Delta U_i^{\text{I-II},2}, \quad (\text{B.5b})$$

$$\langle \Delta G_{\text{XS}}^{(1)} \rangle = \Delta G_{\text{XS}}^{\text{Mg}} + \frac{1}{N_{\text{T}}} \sum_i \Delta U_i^{\text{I-II},1}, \quad (\text{B.5c})$$

$$\langle \Delta G_{\text{XS}}^{(2)} \rangle = \Delta G_{\text{XS},i}^{\text{Mg}} + \frac{1}{N_{\text{T}}} \sum_i \Delta U_i^{\text{I-II},2}. \quad (\text{B.5d})$$

B.2. The ultra dilute limit in quaternary alloy

And the corresponding standard deviations are calculated as

$$\sigma^{(0)}[l_{XS}] = 0 \quad (B.6a)$$

$$\sigma^{(12)}[l_{XS}] = \sqrt{\frac{1}{N_T} \sum_i \left(\Delta U_i^{I-II,1} \right)^2 + \frac{1}{N_T} \sum_i \left(\Delta U_i^{I-II,2} \right)^2}, \quad (B.6b)$$

$$\sigma^{(1)}[l_{XS}] = \sqrt{\frac{1}{N_T} \sum_i \left(\Delta U_i^{I-II,1} \right)^2}, \quad (B.6c)$$

$$\sigma^{(2)}[l_{XS}] = \sqrt{\frac{1}{N_T} \sum_i \left(\Delta U_i^{I-II,2} \right)^2}. \quad (B.6d)$$

Total rate of cross-slip is then the weighted sum of rate of cross-slip of the aforementioned cases

$$R_{XS} = \frac{Lv_0}{l_{XS}} \left[P^{(0)} \exp \left(-\frac{\langle \Delta G_{XS}^{(0)} \rangle - \sigma^{(0)}[l_{XS}]}{kT} \right) + P^{(12)} \exp \left(-\frac{\langle \Delta G_{XS}^{(12)} \rangle - \sigma^{(12)}[l_{XS}]}{kT} \right) \right. \\ \left. + P^{(1)} \exp \left(-\frac{\langle \Delta G_{XS}^{(1)} \rangle - \sigma^{(1)}[l_{XS}]}{kT} \right) + P^{(2)} \exp \left(-\frac{\langle \Delta G_{XS}^{(2)} \rangle - \sigma^{(2)}[l_{XS}]}{kT} \right) \right],$$

$$R_{XS} = \frac{Lv_0}{l_{XS}} \exp \left(-\frac{\Delta G_{XS}^{Mg}}{kT} \right) \left[\left(1 - \frac{c_1}{c^*} \right) \left(1 - \frac{c_2}{c^*} \right) + \frac{c_1 c_2}{(c^*)^2} \exp \left(-\frac{\frac{1}{N_T} \sum_i \Delta U_i^{I-II,1} + \frac{1}{N_T} \sum_i \Delta U_i^{I-II,2} - \sigma^{(12)}[l_{XS}]}{kT} \right) \right. \\ \left. + \frac{c_1}{c^*} \left(1 - \frac{c_2}{c^*} \right) \exp \left(-\frac{\frac{1}{N_T} \sum_i \Delta U_i^{I-II,1} - \sigma^{(1)}[l_{XS}]}{kT} \right) + \frac{c_2}{c^*} \left(1 - \frac{c_1}{c^*} \right) \exp \left(-\frac{\frac{1}{N_T} \sum_i \Delta U_i^{I-II,2} - \sigma^{(2)}[l_{XS}]}{kT} \right) \right]. \quad (B.7)$$

As discussed in the case of binary alloy in Section 6.5, interaction energies of solutes situated near the pyramidal I plane and far from pyramidal II plane are modified since they can not lower the cross-slip barrier in the initial stages of cross-slip nucleation.

B.2 The ultra dilute limit in quaternary alloy

In this section we consider quaternary Mg alloy having three type of solutes 1,2 and 3 with concentrations c_1 , c_2 and c_3 , respectively. We consider here two cases: (i) type 1 in the ultra dilute limit and type 2 and 3 in the dilute limit; (ii) both type 1 and 2 in the ultra dilute limit and type 3 in the dilute limit. Further cases can be dealt with by following the same line of reasoning.

B.2.1 One solute (type 1) in the ultra dilute limit ($c_1 < c^*$, $c_2 \geq c^*$, $c_3 \geq c^*$)

In this case, cross-slip segments would either contain one type 1 solute with effective concentration c^* , type 2 solute with c_2 and type 3 solute with c_3 concentrations, or only type 2 and type 3 solutes with c_2 and c_3 concentrations, respectively. These probabilities can be expressed as

$$P^{(23)} = \left(1 - \frac{c_1}{c^*}\right) \quad \text{probability of finding only type 2 and 3 solutes,} \quad (\text{B.8a})$$

$$P^{(123)} = \frac{c_1}{c^*} \quad \text{probability of finding one type 1 2 and 3 solutes.} \quad (\text{B.8b})$$

The average cross-slip energy is given as

$$\langle \Delta G_{\text{XS}}^{(23)} \rangle = \Delta G_{\text{XS},i} + \frac{c_2 l_{\text{XS}}}{b} \sum_i \Delta U_i^{\text{I-II},2} + \frac{c_3 l_{\text{XS}}}{b} \sum_i \Delta U_i^{\text{I-II},3} + \Gamma \Delta s - \Delta \tau b A, \quad (\text{B.9a})$$

$$\langle \Delta G_{\text{XS}}^{(123)} \rangle = \langle \Delta G_{\text{XS}}^{(23)} \rangle + \frac{1}{N_{\text{T}}} \sum_i \Delta U_i^{\text{I-II},1}. \quad (\text{B.9b})$$

The corresponding standard deviations of the cross-slip energy barrier are

$$\sigma^{(23)}[l_{\text{XS}}] = \sqrt{\frac{c_2 l_{\text{XS}}}{b} \sum_i \left(\Delta U_i^{\text{I-II},2}\right)^2 + \frac{c_3 l_{\text{XS}}}{b} \sum_i \left(\Delta U_i^{\text{I-II},3}\right)^2}, \quad (\text{B.10a})$$

$$\sigma^{(123)}[l_{\text{XS}}] = \sqrt{\frac{1}{N_{\text{T}}} \sum_i \left(\Delta U_i^{\text{I-II},1}\right)^2 + \frac{c_2 l_{\text{XS}}}{b} \sum_i \left(\Delta U_i^{\text{I-II},2}\right)^2 + \frac{c_3 l_{\text{XS}}}{b} \sum_i \left(\Delta U_i^{\text{I-II},3}\right)^2}. \quad (\text{B.10b})$$

Total rate is calculated as

$$R_{\text{XS}} = \frac{L\nu_0}{l_{\text{XS}}} \exp\left(-\frac{\langle \Delta G_{\text{XS}}^{(23)} \rangle}{kT}\right) \left[\left(1 - \frac{c_1}{c^*}\right) \exp\left(\frac{\sigma^{(23)}[l_{\text{XS}}]}{kT}\right) + \frac{c_1}{c^*} \exp\left(-\frac{\frac{1}{N_{\text{T}}} \sum_i \Delta U_i^{\text{I-II},1} - \sigma^{(123)}[l_{\text{XS}}]}{kT}\right) \right]. \quad (\text{B.11})$$

B.2.2 Two solutes (type 1 and 2) in the ultra dilute limit ($c_1 < c^*$, $c_2 < c^*$, $c_3 \geq c^*$)

In this case, critical cross-slip length l_{XS} would encounter either one type 1 (c^*), one type 2 (c^*) and type 3 (c_3) solutes or one of the type 1 or 2 solute along with type 3 or only type 3

solute. Probability of these cases are

$$P^{(3)} = \left(1 - \frac{c_1}{c^*}\right) \left(1 - \frac{c_2}{c^*}\right) \quad \text{probability of finding only type 3 solute,} \quad (\text{B.12a})$$

$$P^{(123)} = \frac{c_1 c_2}{(c^*)^2} \quad \text{probability of finding all three types of solutes,} \quad (\text{B.12b})$$

$$P^{(13)} = \frac{c_1}{c^*} \left(1 - \frac{c_2}{c^*}\right) \quad \text{probability of finding only type 1 and type 3 solute,} \quad (\text{B.12c})$$

$$P^{(23)} = \frac{c_2}{c^*} \left(1 - \frac{c_1}{c^*}\right) \quad \text{probability of finding only type 2 and type 3 solute.} \quad (\text{B.12d})$$

The average cross-slip energy barrier can be obtained as

$$\langle \Delta G_{\text{XS}}^{(3)} \rangle = \Delta G_{\text{XS},i} + \frac{c_3 l_{\text{XS}}}{b} \sum_i \Delta U_i^{\text{I-II},3} + \Gamma \Delta s - \Delta \tau b A, \quad (\text{B.13a})$$

$$\langle \Delta G_{\text{XS}}^{(123)} \rangle = \langle \Delta G_{\text{XS}}^{(3)} \rangle + \frac{1}{N_{\text{T}}} \sum_i \Delta U_i^{\text{I-II},1} + \frac{1}{N_{\text{T}}} \sum_i \Delta U_i^{\text{I-II},2}, \quad (\text{B.13b})$$

$$\langle \Delta G_{\text{XS}}^{(13)} \rangle = \langle \Delta G_{\text{XS}}^{(3)} \rangle + \frac{1}{N_{\text{T}}} \sum_i \Delta U_i^{\text{I-II},1}, \quad (\text{B.13c})$$

$$\langle \Delta G_{\text{XS}}^{(23)} \rangle = \langle \Delta G_{\text{XS}}^{(3)} \rangle + \frac{1}{N_{\text{T}}} \sum_i \Delta U_i^{\text{I-II},2}. \quad (\text{B.13d})$$

And the corresponding standard deviations are calculated as

$$\sigma^{(3)}[l_{\text{XS}}] = \sqrt{\frac{c_3 l_{\text{XS}}}{b} \sum_i \left(\Delta U_i^{\text{I-II},3} \right)^2}, \quad (\text{B.14a})$$

$$\sigma^{(123)}[l_{\text{XS}}] = \sqrt{\frac{1}{N_{\text{T}}} \sum_i \left(\Delta U_i^{\text{I-II},1} \right)^2 + \frac{1}{N_{\text{T}}} \sum_i \left(\Delta U_i^{\text{I-II},2} \right)^2 + \frac{c_3 l_{\text{XS}}}{b} \sum_i \left(\Delta U_i^{\text{I-II},3} \right)^2}, \quad (\text{B.14b})$$

$$\sigma^{(13)}[l_{\text{XS}}] = \sqrt{\frac{1}{N_{\text{T}}} \sum_i \left(\Delta U_i^{\text{I-II},1} \right)^2 + \frac{c_3 l_{\text{XS}}}{b} \sum_i \left(\Delta U_i^{\text{I-II},3} \right)^2}, \quad (\text{B.14c})$$

$$\sigma^{(23)}[l_{\text{XS}}] = \sqrt{\frac{1}{N_{\text{T}}} \sum_i \left(\Delta U_i^{\text{I-II},2} \right)^2 + \frac{c_3 l_{\text{XS}}}{b} \sum_i \left(\Delta U_i^{\text{I-II},3} \right)^2}. \quad (\text{B.14d})$$

Appendix B. Ultra Dilute Limit for Higher Order Alloys

Total rate of cross-slip is then computed as

$$\begin{aligned}
 R_{\text{XS}} = \frac{Lv_0}{l_{\text{XS}}} \exp\left(-\frac{\Delta G_{\text{XS}}^{(3)}}{kT}\right) & \left[\left(1 - \frac{c_1}{c^*}\right) \left(1 - \frac{c_2}{c^*}\right) \exp\left(\frac{\sigma^{(3)}[l_{\text{XS}}]}{kT}\right) \right. \\
 & + \frac{c_1 c_2}{(c^*)^2} \exp\left(-\frac{\frac{1}{N_{\text{T}}} \sum_i \Delta U_i^{\text{I-II},1} + \frac{1}{N_{\text{T}}} \sum_i \Delta U_i^{\text{I-II},2} - \sigma^{(123)}[l_{\text{XS}}]}{kT}\right) \\
 & + \frac{c_1}{c^*} \left(1 - \frac{c_2}{c^*}\right) \exp\left(-\frac{\frac{1}{N_{\text{T}}} \sum_i \Delta U_i^{\text{I-II},1} - \sigma^{(13)}[l_{\text{XS}}]}{kT}\right) \\
 & \left. + \frac{c_2}{c^*} \left(1 - \frac{c_1}{c^*}\right) \exp\left(-\frac{\frac{1}{N_{\text{T}}} \sum_i \Delta U_i^{\text{I-II},2} - \sigma^{(23)}[l_{\text{XS}}]}{kT}\right) \right]. \quad (\text{B.15})
 \end{aligned}$$

Following the same approach, we can calculate the rate of cross-slip for other higher order alloys with some of the solutes in the ultra dilute limit and remaining in the dilute limit.

C DFT Computation and Solute-Stacking Fault Interaction Energy

C.1 Details of DFT computations¹

First-principles calculations are carried out within the DFT framework, as implemented in the Vienna Ab initio Simulation Package (VASP) [112, 113]. The exchange-correlation functional is treated using generalized gradient approximation (GGA) with the Perdew-Burke-Ernzerhof (PBE) parametrization [158] and the core electrons are replaced by the projector augmented wave (PAW) pseudopotentials [33]. The valence states of all elements studied in this work are listed in Table S1A. The valence-electron eigenstates are expanded using a spin-free (except Mn) plane-wave basis set with a cutoff energy 400 eV. A second-order Methfessel-Paxton method [136] with 0.2 eV is used to smear the occupancy of the eigenstates. In reciprocal space, Γ -centered Monkhorst-Pack [139] k-mesh is used. The density of the k-mesh is kept as consistent as possible in various supercell geometries, where the interval between two neighbouring k-mesh points along any reciprocal lattice \mathbf{b}_i is set to be $0.01 \text{ \AA}^{-1} (\mathbf{a}_i \cdot \mathbf{b}_j = \delta_{ij})$, as in Ref. [237]. Atoms are relaxed until the maximum atomic force is below 1 meV/\AA . Further details of the DFT calculations are described in Ref. [237].

C.2 Solute-stacking fault interaction energy

The solute-stacking fault interaction energy depends on the solute position, i.e. the atomic layer d_i relative to the stacking fault plane, as shown in Fig. C.1. This interaction energy, $U_{\text{SF}}(d_i)$, is calculated using DFT for solutes in all possible planes d_i . Details of such calculations, including DFT parameters, method, supercell geometry, and structure optimization, can be found in our recent work [237]. Here we emphasize that the calculation of solute interaction energy with the pyramidal II stacking fault is delicate and requires special procedures. In this case, the stacking fault spontaneously migrates toward or away from the solute when the solute is placed at some sites close to the stacking fault. This prevents calculation of the

¹Most of the first principle DFT computations used in this work were performed by Dr. Binglun Yin who was at the time a postdoctoral researcher in the Laboratory for Multiscale Mechanics Modeling at EPFL, Switzerland.

Appendix C. DFT Computation and Solute-Stacking Fault Interaction Energy

solute-stacking fault interaction energy for all possible solute positions. The easy migration is due to the unique atomic structure of the pyramidal II plane and stacking fault, and is accomplished by small atomic shuffling nearly perpendicular to the slip direction. In order to obtain the interaction energy between a single solute and a flat stacking fault plane for all possible solute positions, constraints must be applied in the calculation. Here, we use a method that fixes the relative distance in selected pairs of atoms below the stacking fault. This constraint prevents stacking fault migration with only small constraint energy. Comparisons with other constraint methods and details are presented in Yin et al. [237]. The final computed DFT results on solute-stacking fault interaction energy are shown in Figs. C.1 and C.2. The properties of the solutes are presented in Table 6.1.

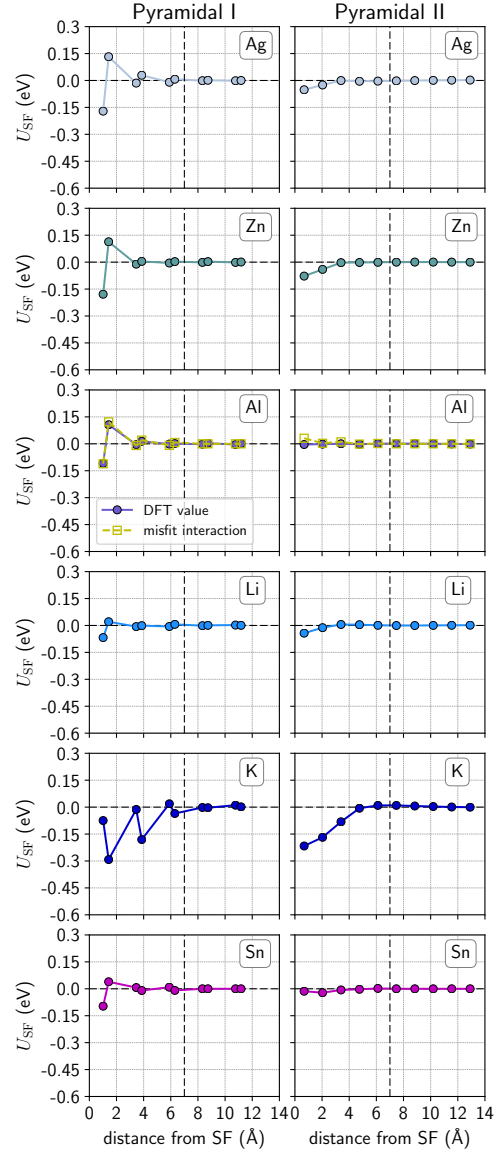


Figure C.1 – The single solute-stacking fault interaction energies U_{SF} with pyramidal I and pyramidal II stacking faults are plotted as a function of the solute-stacking fault distance for Ag, Zn, Al, Li, K, and Sn. Distances are measured from the slip plane situated in the middle of two neighboring atom layers. For Al, both the DFT solute-stacking fault interaction energy (circles) and the solute misfit-stacking fault stress interaction energy (squares) are shown. Determination of the average and fluctuation effect of solutes includes data up to 7 Å (indicated by the vertical thick dashed lines), corresponding to atom layers $d_1 - d_6$ for pyramidal I stacking fault and $d_1 - d_5$ for pyramidal II stacking fault.

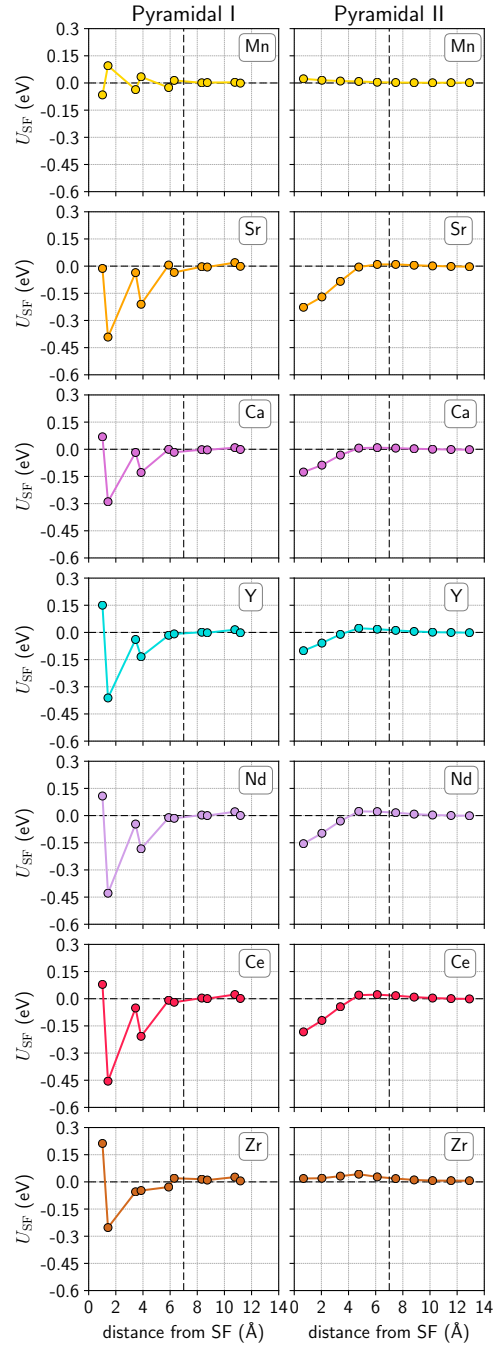


Figure C.2 – The single solute-stacking fault interaction energies U_{SF} with pyramidal I and pyramidal II stacking faults are plotted as a function of the solute-stacking fault distance d_i for Mn, Sr, Ca, Y, Nd, Ce, and Zr. Distances are measured from the slip plane situated in the middle of two neighboring atom layers. Determination of the average and fluctuation effect of solutes includes data up to 7 Å (indicated by the vertical thick dashed lines), corresponding to atom layers $d_1 - d_6$ for pyramidal I stacking fault and $d_1 - d_5$ for pyramidal II stacking fault.

D Dislocation Energy Difference associated with Pyramidal Cross-Slip

We start by considering the total energy E per unit length of a single straight dislocation, either pyramidal I or II, when dissociated into two partial dislocations. As discussed in Section 1.3, total dislocation energy E can be written as a sum of core energies of the partials, elastic energy including self-energy, radial and angular elastic interaction energies of the two partials, and stacking fault energy between the partials [232], i.e.

$$E = [E_{c1}(r_0) + E_{c2}(r_0)] + \left[K \ln \frac{R}{r_0} + K_{12} \ln \frac{r_0}{r_{12}} - E_\theta \right] + \gamma r_{12}, \quad (\text{D.1})$$

where r_0 is the core radius for each partial dislocation, R is the radius of an (arbitrarily large) outer cylindrical domain, r_{12} is the partial dislocation separation, and K and K_{12} are prefactors completely determined by the material elastic constants, dislocation line direction, and Burgers vectors of the partial dislocations. The angular interaction energy E_θ varies with the relative orientation between the two partials in the hcp structure, their Burgers vectors, and the elastic constants. The equilibrium separation between the two partials minimizes the total energy with respect to r_{12} , leading to $r_{12} = K_{12}/\gamma$. Substituting r_{12} into Eq. D.2 and combining the core energy of the two partials give

$$E = E_c(r_0) + K \ln \frac{R}{r_0} + K_{12} \ln \frac{r_0 \gamma}{K_{12}} + K_{12} - E_\theta, \quad (\text{D.2})$$

where $E_c(r_0) = E_{c1}(r_0) + E_{c2}(r_0)$ is the sum of the core energy of the two partials.

Cross-slip of the $\langle \mathbf{c} + \mathbf{a} \rangle$ dislocations from pyramidal II to pyramidal I can be considered as a transformation of the screw dislocation from the pyramidal II initial state to the pyramidal I final state. The energy difference per unit length between the pyramidal I and pyramidal II screw dislocations is then

$$\Delta E^{\text{I-II}} = [E_c^{\text{I}}(r_0) - E_c^{\text{II}}(r_0)] + \left[K_{12}^{\text{I}} \ln \frac{r_0 \gamma^{\text{I}}}{K_{12}^{\text{I}}} - K_{12}^{\text{II}} \ln \frac{r_0 \gamma^{\text{II}}}{K_{12}^{\text{II}}} \right] + [K_{12}^{\text{I}} - K_{12}^{\text{II}}] + [E_\theta^{\text{II}} - E_\theta^{\text{I}}]. \quad (\text{D.3})$$

The long-range elastic field prefactor K is identical for the pyramidal I and the pyramidal II

Appendix D. Dislocation Energy Difference associated with Pyramidal Cross-Slip

$\langle \mathbf{c} + \mathbf{a} \rangle$ screw dislocations and thus does not contribute to the energy difference.

In dilute solute concentrations, the average effects of solute on elastic constants and dislocation Burgers vectors are small [237]. The cores of the $\langle \mathbf{c} + \mathbf{a} \rangle$ screw partials on the pyramidal I and II planes are also similar (42, 44). Therefore, solutes have similar interaction energy with all partial cores. The mean energy differences in the core and angular part of the elastic energy, i.e. the first and last groups in Eq. D.3, are thus approximately independent of solute concentrations. However, solutes change the stacking fault energies as $\gamma(c) = \gamma_{\text{Mg}} + kc$ where γ_{Mg} is the stacking fault energy of pure Mg and k is a solute-dependent constant characterizing the average potency of a solute in changing the stacking fault energy as discussed in Section 3.2.2. Substituting $\gamma(c)$ into Eq. D.3 gives the average dislocation energy difference per unit length due to solute-stacking interactions as a function of solute concentration c in the dilute limit as

$$\begin{aligned}
 \Delta E^{\text{I-II}} &= [E_c^{\text{I}}(r_0) - E_c^{\text{II}}(r_0)] \\
 &\quad + \left[K_{12}^{\text{I}} \ln \frac{r_0 \gamma_{\text{Mg}}^{\text{I}} \left(1 + \frac{k^{\text{I}} c}{\gamma_{\text{Mg}}^{\text{I}}}\right)}{K_{12}^{\text{I}}} - K_{12}^{\text{II}} \ln \frac{r_0 \gamma_{\text{Mg}}^{\text{II}} \left(1 + \frac{k^{\text{II}} c}{\gamma_{\text{Mg}}^{\text{II}}}\right)}{K_{12}^{\text{II}}} \right] \\
 &\quad + [K_{12}^{\text{I}} - K_{12}^{\text{II}}] + [E_{\theta}^{\text{II}} - E_{\theta}^{\text{I}}], \\
 &= [E_c^{\text{I}}(r_0) - E_c^{\text{II}}(r_0)] + \left[K_{12}^{\text{I}} \ln \frac{r_0 \gamma_{\text{Mg}}^{\text{I}}}{K_{12}^{\text{I}}} - K_{12}^{\text{II}} \ln \frac{r_0 \gamma_{\text{Mg}}^{\text{II}}}{K_{12}^{\text{II}}} \right] \\
 &\quad + [K_{12}^{\text{I}} - K_{12}^{\text{II}}] + [E_{\theta}^{\text{II}} - E_{\theta}^{\text{I}}] \\
 &\quad + \left[K_{12}^{\text{I}} \ln \left(1 + \frac{k^{\text{I}} c}{\gamma_{\text{Mg}}^{\text{I}}}\right) - K_{12}^{\text{II}} \ln \left(1 + \frac{k^{\text{II}} c}{\gamma_{\text{Mg}}^{\text{II}}}\right) \right], \\
 &= \Delta E_{\text{Mg}}^{\text{I-II}} + \left[K_{12}^{\text{I}} \ln \left(1 + \frac{k^{\text{I}} c}{\gamma_{\text{Mg}}^{\text{I}}}\right) - K_{12}^{\text{II}} \ln \left(1 + \frac{k^{\text{II}} c}{\gamma_{\text{Mg}}^{\text{II}}}\right) \right], \\
 &\approx \Delta E_{\text{Mg}}^{\text{I-II}} + \left[\frac{K_{12}^{\text{I}} k^{\text{I}}}{\gamma_{\text{Mg}}^{\text{I}}} - \frac{K_{12}^{\text{II}} k^{\text{II}}}{\gamma_{\text{Mg}}^{\text{II}}} \right] c.
 \end{aligned} \tag{D.4}$$

where $\Delta E_{\text{Mg}}^{\text{I-II}}$ is the energy difference in pure Mg.

Bibliography

- [1] Agnew, S. (2012). *2 – Deformation mechanisms of magnesium alloys*. Woodhead Publishing Limited.
- [2] Agnew, S. R., Capolungo, L., and Calhoun, C. A. (2015). Connections between the basal II "growth" fault and $\langle c + a \rangle$ dislocations. *Acta Mater.*, 82:255–265.
- [3] Agnew, S. R. and Duygulu, Ö. (2005). Plastic anisotropy and the role of non-basal slip in magnesium alloy AZ31B. *Int. J. Plast.*, 21(6):1161–1193.
- [4] Agnew, S. R., Horton, J. A., and Yoo, M. H. (2002). Transmission electron microscopy investigation of $\langle c + a \rangle$ dislocations in Mg and α -solid solution Mg-Li alloys. *Metall. Mater. Trans. A*, 33(13):851–858.
- [5] Agnew, S. R., Senn, J. W., and Horton, J. A. (2006). Mg sheet metal forming: Lessons learned from deep drawing Li and Y solid-solution alloys. *Jom*, 58(5):62–69.
- [6] Agnew, S. R., Yoo, M. H., and Tome, C. N. (2001). Application of texture simulation to understanding mechanical behavior of Mg and solid solution alloys containing Li or Y. *Acta Mater.*, 49(20):4277–4289.
- [7] Akhtar, A. (1975). Prismatic slip in zirconium single crystals at elevated temperatures. *Metall. Trans. A*, 6(6):1217–1222.
- [8] Akhtar, A. and Teghtsoonian, E. (1975). Prismatic slip in α -titanium single crystals. *Metall. Mater. Trans. A*, 6(12):2201–2208.
- [9] Alaneme, K. K. and Okotete, E. A. (2017). Enhancing plastic deformability of Mg and its alloys—A review of traditional and nascent developments. *J. Magnes. Alloy*, 5(4):460–475.
- [10] Alexandra, R., Pavel, L., and Stanislav, K. (2005). Thermal Properties of Mg-Li and Mg-Li-Al Alloys. In *Magnesium*, chapter 15, pages 106–109. Wiley-Blackwell.
- [11] Allen, M. P., Allen, M. P., Tildesley, D. J., ALLEN, T., and Tildesley, D. J. (1989). *Computer Simulation of Liquids*. Oxford Science Publ. Clarendon Press.
- [12] Anciaux, G., Junge, T., Hodapp, M., Cho, J., Molinari, J. F., and Curtin, W. A. (2018). The Coupled Atomistic/Discrete-Dislocation method in 3d part I: Concept and algorithms. *J. Mech. Phys. Solids*, 118:152–171.

Bibliography

- [13] Anderson, P. M., Hirth, J. P., and Lothe, J. (2017). *Theory of dislocations*. Cambridge University Press, New York, NY, 3rd edition.
- [14] Ando, S., Gotoh, T., and Tonda, H. (2002). Molecular Dynamics simulation of $\langle c+a \rangle$ dislocation core structure in hexagonal-close-packed metals. *Metall. Mater. Trans. A*, 33(March):823–829.
- [15] Ando, S., Harada, N., Tsushida, M., Kitahara, H., and Tonda, H. (2007). Temperature Dependence of Deformation Behavior in Magnesium and Magnesium Alloy Single Crystals. *Key Eng. Mater.*, 345-346:101–104.
- [16] Ando, S., Kodera, A., Fukushima, K., Tsushida, M., and Kitahara, H. (2014). Tensile Deformation of Magnesium and Magnesium Alloy Single Crystals. *Mater. Sci. Forum*, 783-786:341–345.
- [17] Ando, S. and Tonda, H. (2000). Non-Basal Slips in Magnesium and Magnesium-Lithium Alloy Single Crystals. *Mater. Sci. Forum*, 41(9):1188–1191.
- [18] Ando, S., Tsushida, M., and Kitahara, H. (2010). Deformation Behavior of Magnesium Single Crystal in $\langle c \rangle$ -Axis Compression and $\langle a \rangle$ -Axis Tension. *Mater. Sci. Forum*, 654-656:699–702.
- [19] Argon, A. (2008). *Strengthening Mechanisms in Crystal Plasticity*. Osmm Series. Oxford University Press, Inc.
- [20] Arsenlis, A., Cai, W., Tang, M., Rhee, M., Oppelstrup, T., Hommes, G., Pierce, T. G., and Bulatov, V. V. (2007). Enabling strain hardening simulations with dislocation dynamics. *Model. Simul. Mater. Sci. Eng.*, 15(6):553–595.
- [21] Aubry, S., Rhee, M., Hommes, G., Bulatov, V. V., and Arsenlis, A. (2016). Dislocation dynamics in hexagonal close-packed crystals. *J. Mech. Phys. Solids*, 94:105–126.
- [22] Bacon, D. J., Barnett, D. M., and Scattergood, R. O. (1980). Anisotropic continuum theory of lattice defects. *Prog. Mater. Sci.*, 23(C):51–262.
- [23] Bacon, D. J. and Vitek, V. (2002). Atomic-scale modeling of dislocations and related properties in the hexagonal-close-packed metals. *Metall. Mater. Trans. A*, 33(13):721–733.
- [24] Baril, E., Labelle, P., and Pekguleryuz, M. (2003). Elevated temperature Mg-Al-Sr: Creep resistance, mechanical properties, and microstructure. *Jom*, 55(11):34–39.
- [25] Bartók, A. P., Payne, M. C., Kondor, R., and Csányi, G. (2010). Gaussian approximation potentials: The accuracy of quantum mechanics, without the electrons. *Phys. Rev. Lett.*, 104(13):1–4.
- [26] Baskes, M. (1997). Determination of modified embedded atom method parameters for nickel. *Mater. Chem. Phys.*, 50(2):152–158.

-
- [27] Baskes, M. I. (1987). Application of the Embedded-Atom Method to Covalent Materials: A Semiempirical Potential for Silicon. *Phys. Rev. B*, 59(3):2666–2669.
- [28] Baskes, M. I. (1992). Modified embedded-atom potentials for cubic materials and impurities. *Phys. Rev. B*, 46(5):2727–2742.
- [29] Behler, J. (2014). Representing potential energy surfaces by high-dimensional neural network potentials. *J. Phys. Condens. Matter*, 26(18).
- [30] Behler, J. (2016). Perspective: Machine learning potentials for atomistic simulations. *J. Chem. Phys.*, 145(17).
- [31] Behler, J. and Parrinello, M. (2007). Generalized neural-network representation of high-dimensional potential-energy surfaces. *Phys. Rev. Lett.*, 98(14):1–4.
- [32] Bettles, C. J. and Gibson, M. A. (2005). Current wrought magnesium alloys: Strengths and weaknesses. *Jom*, 57(5):46–49.
- [33] Blöchl, P. E. (1994). Projector augmented-wave method. *Phys. Rev. B*, 50(24):17953–17979.
- [34] Borkar, H., Hoseini, M., and Pekguleryuz, M. (2012a). Effect of strontium on flow behavior and texture evolution during the hot deformation of Mg-1wt%Mn alloy. *Mater. Sci. Eng. A*, 537:49–57.
- [35] Borkar, H., Hoseini, M., and Pekguleryuz, M. (2012b). Effect of strontium on the texture and mechanical properties of extruded Mg-1%Mn alloys. *Mater. Sci. Eng. A*, 549:168–175.
- [36] Buey, D., Hector, L. G., and Ghazisaeidi, M. (2018). Core structure and solute strengthening of second-order pyramidal $\langle c+a \rangle$ dislocations in Mg-Y alloys. *Acta Mater.*, 147:1–9.
- [37] Bulatov, V., Abraham, F. F., Kubin, L., Devincere, B., and Yip, S. (1998). Connecting atomistic and mesoscale simulations of crystal plasticity. *Nature*, 391(6668):669–672.
- [38] Bulatov, V. and Cai, W. (2006). *Computer Simulations of Dislocations (Oxford Series on Materials Modelling)*. Osmm Series. Oxford University Press, Inc., USA.
- [39] Bulatov, V. V., Hsiung, L. L., Tang, M., Arsenlis, A., Bartelt, M. C., Cai, W., Florando, J. N., Hiratani, M., Rhee, M., Hommes, G., Pierce, T. G., and de la Rubia, T. D. (2006). Dislocation multi-junctions and strain hardening. *Nature*, 440(7088):1174–1178.
- [40] Cáceres, C. H. and Blake, A. (2002). The strength of concentrated Mg – Zn solid solutions. *Phys. Status Solidi*, 194(1):147–158.
- [41] Cáceres, C. H. and Rovera, D. M. (2001). Solid solution strengthening in concentrated Mg-Al alloys. *J. Light Met.*, 1(3):151–156.
- [42] Cai, W., Bulatov, V. V., Chang, J., Li, J., and Yip, S. (2003). Periodic image effects in dislocation modelling. *Philos. Mag.*, 83(December 2012):37–41.

Bibliography

- [43] Cai, W., Bulatov, V. V., Justo, J. F., Argon, A. S., and Yip, S. (2000). Intrinsic mobility of a dissociated dislocation in silicon. *Phys. Rev. Lett.*, 84(15):3346–3349.
- [44] Cai, W. and Nix, W. D. (2016). *Imperfections in Crystalline Solids*. MRS-Cambridge Materials Fundamentals. Cambridge University Press.
- [45] Caillard, D. (2010). Kinetics of dislocations in pure Fe. Part II. In situ straining experiments at low temperature. *Acta Mater.*, 58(9):3504–3515.
- [46] Caillard, D. and Martin, J. L. (2003). *Thermally Activated Mechanisms in Crystal Plasticity*, volume 8 of *Pergamon Materials Series*. Pergamon.
- [47] Capolungo, L. (2011). Dislocation junction formation and strength in magnesium. *Acta Mater.*, 59(8):2909–2917.
- [48] Chang, J. P., Cai, W., Bulatov, V. V., and Yip, S. (2002). Molecular dynamics simulations of motion of edge and screw dislocations in a metals. *Comput. Mater. Sci.*, 23:111–115.
- [49] Chino, Y., Huang, X., Suzuki, K., and Mabuchi, M. (2010a). Enhancement of Stretch Formability at Room Temperature by Addition of Ca in Mg-Zn Alloy. *Mater. Trans.*, 51(4):818–821.
- [50] Chino, Y., Huang, X., Suzuki, K., Sassa, K., and Mabuchi, M. (2010b). Influence of Zn concentration on stretch formability at room temperature of Mg-Zn-Ce alloy. *Mater. Sci. Eng. A*, 528(2):566–572.
- [51] Chino, Y., Kado, M., and Mabuchi, M. (2008). Compressive deformation behavior at room temperature - 773 K in Mg-0.2 mass%(0.035at.%)Ce alloy. *Acta Mater.*, 56(3):387–394.
- [52] Chino, Y., Kado, M., Ueda, T., and Mabuchi, M. (2011a). Solid solution strengthening for Mg-3.0 Mass Pct (2.71 At. Pct)Al and Mg-0.06 mass Pct (0.036 At. Pct)Ca alloys. *Metall. Mater. Trans. A Phys. Metall. Mater. Sci.*, 42(7):1965–1973.
- [53] Chino, Y., Ueda, T., Otomatsu, Y., Sassa, K., Huang, X., Suzuki, K., and Mabuchi, M. (2011b). Effects of Ca on Tensile Properties and Stretch Formability at Room Temperature in Mg-Zn and Mg-Al Alloys. *Mater. Trans.*, 52(7):1477–1482.
- [54] Clouet, E., Garruchet, S. S., Nguyen, H., Perez, M., and Becquart, C. S. (2008). Dislocation interaction with C in α -Fe: A comparison between atomic simulations and elasticity theory. *Acta Mater.*, 56(14):3450–3460.
- [55] Cottrell, A. (1965). *Dislocations and Plastic Flow in Crystals*. International series of monographs on physics. Clarendon Press.
- [56] Couret, A. and Caillard, D. (1985a). An in situ study of prismatic glide in magnesium-I. The rate controlling mechanism. *Acta Metall.*, 33(8):1447–1454.

-
- [57] Couret, A. and Caillard, D. (1985b). An in situ study of prismatic glide in magnesium-II. Microscopic activation parameters. *Acta Metall.*, 33(8):1455–1462.
- [58] Couret, A., Caillard, D., Püschl, W., and Schoeck, G. (1991). Prismatic glide in divalent h.c.p. metals. *Philos. Mag. A*, 63(5):1045–1057.
- [59] Curtin, W. A. (2017). The X-Mechanics Toolbox to Solve Y-Mechanics Problems. *Procedia IUTAM*, 21:2–10.
- [60] Curtin, W. A. and Miller, R. E. (2003). Atomistic / continuum coupling in computational. *Model. Simul. Mater. Sci. Eng.*, 11:R33.
- [61] Curtin, W. A. and Miller, R. E. (2017). A perspective on atomistic-continuum multiscale modeling. *Model. Simul. Mater. Sci. Eng.*, 25(7).
- [62] Daw, M. S. and Baskes, M. I. (1984). Embedded-atom method: Derivation and application to impurities, surfaces, and other defects in metals. *Phys. Rev. B*, 29(12):6443–6453.
- [63] Daw, M. S., Foiles, S. M., and Baskes, M. I. (1993). The embedded-atom method: a review of theory and applications. *Mater. Sci. Reports*, 9(7-8):251–310.
- [64] Deo, C. S., Srolovitz, D. J., Cai, W., and Bulatov, V. V. (2005). Kinetic Monte Carlo method for dislocation migration in the presence of solute. *Phys. Rev. B - Condens. Matter Mater. Phys.*, 71(1):1–12.
- [65] Deringer, V. L., Caro, M. A., and Csányi, G. (2019). Machine Learning Interatomic Potentials as Emerging Tools for Materials Science. *Adv. Mater.*, 31(46):1–16.
- [66] Devincre, B., Kubin, L., and Hoc, T. (2006). Physical analyses of crystal plasticity by DD simulations. *Scr. Mater.*, 54(5):741–746.
- [67] Dragoni, D., Daff, T. D., Csányi, G., and Marzari, N. (2018). Achieving DFT accuracy with a machine-learning interatomic potential: Thermomechanics and defects in bcc ferromagnetic iron. *Phys. Rev. Mater.*, 2(1):1–16.
- [68] E, W., Ren, W., and Vanden-Eijnden, E. (2002). String method for the study of rare events. *Phys. Rev. B*, 66(5):52301.
- [69] Esteban-Manzanares, G., Martínez, E., Segurado, J., Capolungo, L., and LLorca, J. (2019a). An atomistic investigation of the interaction of dislocations with Guinier-Preston zones in Al-Cu alloys. *Acta Mater.*, 162:189–201.
- [70] Esteban-Manzanares, G., Santos-Güemes, R., Papadimitriou, ., Martínez, E., and LLorca, J. (2019b). Influence of the stress state on the cross-slip free energy barrier in Al: an atomistic investigation. *Acta Mater.*, 184:109–119.
- [71] Eyring, H. (1935). The activated complex in chemical reactions. *J. Chem. Phys.*, 3:107.

Bibliography

- [72] Faken, D. and Jónsson, H. (1994). Systematic analysis of local atomic structure combined with 3D computer graphics. *Comput. Mater. Sci.*, 2(2):279–286.
- [73] Finnis, M. (2010). *Interatomic Forces in Condensed Matter*. Interatomic Forces in Condensed Matter. OUP Oxford.
- [74] Fisher, J. C. and Johnston, W. G. (1957). *Dislocations and Mechanical Properties of Crystals: An International Conference Held at Lake Placid Sept. 6-8 1956*. General Electric.
- [75] Frenkel, D. and Smit, B. (2001). *Understanding Molecular Simulation: From Algorithms to Applications*. Computational science. Elsevier Science.
- [76] Friák, M., Hickel, T., Grabowski, B., Lymperakis, L., Udyansky, A., Dick, A., Ma, D., Roters, F., Zhu, L. F., Schlieter, A., Kühn, U., Ebrahimi, Z., Lebensohn, R. A., Holec, D., Eckert, J., Emmerich, H., Raabe, D., and Neugebauer, J. (2011). Methodological challenges in combining quantum-mechanical and continuum approaches for materials science applications. *Eur. Phys. J. Plus*, 126(10):1–22.
- [77] Friedrich, H. and Schumann, S. (2001). Research for a "new age of magnesium" in the automotive industry. *J. Mater. Process. Technol.*, 117(3):276–281.
- [78] Gao, L., Chen, R. S., and Han, E. H. (2009). Effects of rare-earth elements Gd and Y on the solid solution strengthening of Mg alloys. *J. Alloys Compd.*, 481(1-2):379–384.
- [79] Geng, J., Chisholm, M., Mishra, R., and Kumar, K. (2015). An electron microscopy study of dislocation structures in Mg single crystals compressed along [0 0 0 1] at room temperature. *Philos. Mag.*, 95(35):3910–3932.
- [80] Geng, J., Chisholm, M. F., Mishra, R. K., and Kumar, K. S. (2014). The structure of <c+a> type dislocation loops in magnesium. *Philos. Mag. Lett.*, 94(6):377–386.
- [81] Ghazisaeidi, M., Hector, L. G., and Curtin, W. A. (2014a). First-principles core structures of <c+a> edge and screw dislocations in Mg. *Scr. Mater.*, 75:42–45.
- [82] Ghazisaeidi, M., Hector, L. G., and Curtin, W. A. (2014b). Solute strengthening of twinning dislocations in Mg alloys. *Acta Mater.*, 80:278–287.
- [83] Giessen, E. V. D. and Needleman, A. (1995). Discrete dislocation plasticity: a simple planar model. *Model. Simul. Mater. Sci. Eng.*, 3(5):689–735.
- [84] Griffiths, D. (2015). Explaining texture weakening and improved formability in magnesium rare earth alloys. *Mater. Sci. Technol.*, 31(1):10–24.
- [85] Hantzsche, K., Bohlen, J., Wendt, J., Kainer, K. U., Yi, S. B., and Letzig, D. (2010). Effect of rare earth additions on microstructure and texture development of magnesium alloy sheets. *Scr. Mater.*, 63(7):725–730.

-
- [86] Hellström, M. and Behler, J. (2020). *Neural Network Potentials in Materials Modeling*, pages 661–680. Springer International Publishing, Cham.
- [87] Henkelman, G. and Jónsson, H. (2000). Improved tangent estimate in the nudged elastic band method for finding minimum energy paths and saddle points. *J. Chem. Phys.*, 113(22):9978–9985.
- [88] Henkelman, G., Uberuaga, B. P., and Jónsson, H. (2000). Climbing image nudged elastic band method for finding saddle points and minimum energy paths. *J. Chem. Phys.*, 113(22):9901–9904.
- [89] Hirth, J. P. (1985). A brief history of dislocation theory. *Metall. Trans. A*, 16(12):2085–2090.
- [90] Hodapp, M., Anciaux, G., and Curtin, W. A. (2019). Lattice Green function methods for atomistic/continuum coupling: Theory and data-sparse implementation. *Comput. Methods Appl. Mech. Eng.*, 348:1039–1075.
- [91] Hodapp, M., Anciaux, G., Molinari, J. F., and Curtin, W. A. (2018). Coupled atomistic/discrete dislocation method in 3D Part II: Validation of the method. *J. Mech. Phys. Solids*, 119:1–19.
- [92] Horstemeyer, M. F., Potirniche, G. P., Marin, E. B., and Dynamics, B. D. (2005). 3.5 - Crystal Plasticity. In Yip, S., editor, *Handb. Mater. Model. Methods*, pages 1133–1149. Springer Netherlands.
- [93] Huang, X., Suzuki, K., Chino, Y., and Mabuchi, M. (2015a). Influence of aluminum content on the texture and sheet formability of AM series magnesium alloys. *Mater. Sci. Eng. A*, 633:144–153.
- [94] Huang, X., Suzuki, K., Chino, Y., and Mabuchi, M. (2015b). Texture and stretch formability of AZ61 and AM60 magnesium alloy sheets processed by higherature rolling. *J. Alloys Compd.*, 632:94–102.
- [95] Huang, Y., Gan, W., Kainer, K. U., and Hort, N. (2014). Role of multi-microalloying by rare earth elements in ductilization of magnesium alloys. *J. Magnes. Alloy*, 2(1):1–7.
- [96] Hull, D. and Bacon, D. J. (2011). *Introduction to dislocations*. Butterworth-Heinemann, Oxford.
- [97] Itakura, M., Kaburaki, H., Yamaguchi, M., and Tsuru, T. (2016). Novel Cross-Slip Mechanism of Pyramidal Screw Dislocations in Magnesium. *Phys. Rev. Lett.*, 116(22):1–5.
- [98] Jackson, P. J. (1985). Dislocation modelling of shear in f.c.c. crystals. *Prog. Mater. Sci.*, 29(1-2):139–175.
- [99] Jin, C., Ren, W., and Xiang, Y. (2010). Computing transition rates of thermally activated events in dislocation dynamics. *Scr. Mater.*, 62(4):206–209.

Bibliography

- [100] Jónsson, H., Mills, G., and Jacobsen, K. W. (1998). Nudged elastic band method for finding minimum energy paths of transitions. In Berne, B. J., Ciccotti, G., and Coker, D. F., editors, *Class. Quantum Dyn. Condens. Phase Simulations*, inbook 16, pages 385–404. World Scientific, singapore edition.
- [101] Kang, K., Yin, J., and Cai, W. (2014). Stress dependence of cross slip energy barrier for face-centered cubic nickel. *J. Mech. Phys. Solids*, 62(1):181–193.
- [102] Kim, K. H., Jeon, J. B., and Lee, B. J. (2015). Modified embedded-atom method interatomic potentials for Mg-X (X=Y, Sn, Ca) binary systems. *Calphad Comput. Coupling Phase Diagrams Thermochem.*, 48:27–34.
- [103] Kim, K. H. and Lee, B. J. (2017). Modified embedded-atom method interatomic potentials for Mg-Nd and Mg-Pb binary systems. *Calphad Comput. Coupling Phase Diagrams Thermochem.*, 57(March):55–61.
- [104] Kim, W. J., Lee, H. W., Park, J. P., Kim, M. G., and Yoon, U. S. (2009a). Forging of Mg-3Al-1Zn-1Ca alloy prepared by high-frequency electromagnetic casting. *Mater. Des.*, 30(10):4120–4125.
- [105] Kim, Y. M., Kim, N. J., and Lee, B. J. (2009b). Atomistic Modeling of pure Mg and Mg-Al systems. *Calphad Comput. Coupling Phase Diagrams Thermochem.*, 33(4):650–657.
- [106] Ko, W.-S. and Lee, B.-J. (2009). Modified embedded-atom method interatomic potentials for pure Y and the V-Pd-Y ternary system. *Acta Mater.*, 57(11):3140–3147.
- [107] Kobayashi, R., Giofré, D., Junge, T., Ceriotti, M., and Curtin, W. A. (2017). Neural network potential for Al-Mg-Si alloys. *Phys. Rev. Mater.*, 1(5):1–11.
- [108] Kocks, U. F., Argon, A. S., and Ashby, M. F. (1975). *Thermodynamics and Kinetics of slip*, volume 19 of *Progress in Materials Science*. Elsevier.
- [109] Kocks, U. F., Tomé, C. N., Wenk, H. R., Beaudoin, A. J., and Mecking, H. (1998). *Texture and Anisotropy: Preferred Orientations in Polycrystals and Their Effect on Materials Properties*. Cambridge University Press.
- [110] Koehler, J. S. (1952). The nature of work-hardening. *Phys. Rev.*, 86(1):52–59.
- [111] Koike, J., Kobayashi, T., Mukai, T., Watanabe, H., Suzuki, M., Maruyama, K., and Higashi, K. (2003). The activity of non-basal slip systems and dynamic recovery at room temperature in fine-grained AZ31B magnesium alloys. *Acta Mater.*, 51(7):2055–2065.
- [112] Kresse, G. and Furthmüller, J. (1996). Efficient iterative schemes for ab initio total-energy calculations using a plane-wave basis set. *Phys. Rev. B - Condens. Matter Mater. Phys.*, 54(16):11169–11186.
- [113] Kresse, G. and Joubert, D. (1999). From ultrasoft pseudopotentials to the projector augmented-wave method. *Phys. Rev. B - Condens. Matter Mater. Phys.*, 59(3):1758–1775.

- [114] Kubin, L. (2013). *Dislocations, Mesoscale Simulations and Plastic Flow*. Oxford Series on Materials Modelling. OUP Oxford.
- [115] Kulekci, M. K. (2008). Magnesium and its alloys applications in automotive industry. *Int. J. Adv. Manuf. Technol.*, 39(9-10):851–865.
- [116] Kuramoto, E., Aono, Y., and Kitajima, K. (1979). Thermally activated slip deformation of high purity iron single crystals between 4.2 K and 300 K. *Scr. Metall.*, 13(11):1039–1042.
- [117] Lapovok, R. and Estrin, Y. (2012). 4 - Superplasticity in magnesium alloys by severe plastic deformation. In Bettles, C. and Barnett, M., editors, *Adv. Wrought Magnes. Alloy*, Woodhead Publishing Series in Metals and Surface Engineering, pages 144–185. Woodhead Publishing.
- [118] Lee, B. J., Baskes, M., Kim, H., and Koo Cho, Y. (2001). Second nearest-neighbor modified embedded atom method potentials for bcc transition metals. *Phys. Rev. B*, 64(18):184102.
- [119] Lee, B. J. and Baskes, M. I. (2000). Second nearest-neighbor modified embedded-atom-method potential. *Phys. Rev. B - Condens. Matter Mater. Phys.*, 62(13):8564–8567.
- [120] Leyson, G. P. M., Curtin, W. A., Hector, L. G., and Woodward, C. F. (2010). Quantitative prediction of solute strengthening in aluminium alloys. *Nat. Mater.*, 9(9):750–755.
- [121] Leyson, G. P. M., Hector, L. G., and Curtin, W. A. (2012). Solute strengthening from first principles and application to aluminum alloys. *Acta Mater.*, 60(9):3873–3884.
- [122] Liu, X.-Y., Adams, J. B., Ercolessi, F., and Moriarty, J. A. (1996). EAM potential for magnesium from quantum mechanical forces forces. *Model. Simul. Mater. Sci. Eng.*, 4:293.
- [123] Luo, A. A., Mishra, R. K., and Sachdev, A. K. (2011). High-ductility magnesium-zinc-cerium extrusion alloys. *Scr. Mater.*, 64(5):410–413.
- [124] Luo, A. A. and Sachdev, A. K. (2007). Development of a new wrought magnesium-aluminum-manganese alloy AM30. *Metall. Mater. Trans. A Phys. Metall. Mater. Sci.*, 38(6):1184–1192.
- [125] Luo, A. A. and Sachdev, A. K. (2012). 12 - Applications of magnesium alloys in automotive engineering. In Bettles, C. and Barnett, M., editors, *Adv. Wrought Magnes. Alloy*, Woodhead Publishing Series in Metals and Surface Engineering, pages 393–426. Woodhead Publishing.
- [126] Mackenzie, L. W. and Pekguleryuz, M. (2008). The influences of alloying additions and processing parameters on the rolling microstructures and textures of magnesium alloys. *Mater. Sci. Eng. A*, 480(1-2):189–197.
- [127] Madec, R., Devincre, B., and Kubin, L. P. (2002). From dislocation junctions to forest hardening. *Phys. Rev. Lett.*, 89(25):255508.

Bibliography

- [128] Maras, E., Trushin, O., Stukowski, A., Ala-Nissila, T., and Jónsson, H. (2016). Global transition path search for dislocation formation in Ge on Si(001). *Comput. Phys. Commun.*, 205:13–21.
- [129] Maresca, F., Dragoni, D., Csányi, G., Marzari, N., and Curtin, W. A. (2018). Screw dislocation structure and mobility in body centered cubic Fe predicted by a Gaussian Approximation Potential. *npj Comput. Mater.*, 4(1).
- [130] Martinez, E., Marian, J., Arsenlis, A., Victoria, M., and Perlado, J. M. (2008). Atomistically informed dislocation dynamics in fee crystals. *J. Mech. Phys. Solids*, 56(Dd):869–895.
- [131] Masoudpanah, S. M. and Mahmudi, R. (2009). Effects of rare-earth elements and Ca additions on the microstructure and mechanical properties of AZ31 magnesium alloy processed by ECAP. *Mater. Sci. Eng. A*, 526(1-2):22–30.
- [132] Masoumi, M. and Pekguleryuz, M. (2011). The influence of Sr on the microstructure and texture evolution of rolled Mg-1%Zn alloy. *Mater. Sci. Eng. A*, 529(1):207–214.
- [133] Masoumi, M., Zarandi, F., and Pekguleryuz, M. (2011). Microstructure and texture studies on twin-roll cast AZ31 (Mg-3wt.%Al-1wt.%Zn) alloy and the effect of thermomechanical processing. *Mater. Sci. Eng. A*, 528(3):1268–1279.
- [134] Máthis, K., Nyilas, K., Axt, A., Dragomir-Cernatescu, I., Ungár, T., and Lukáč, P. (2004). The evolution of non-basal dislocations as a function of deformation temperature in pure magnesium determined by X-ray diffraction. *Acta Mater.*, 52(10):2889–2894.
- [135] Meng, X., Wu, R., Zhang, M., Wu, L., and Cui, C. (2009). Microstructures and properties of superlight Mg-Li-Al-Zn wrought alloys. *J. Alloys Compd.*, 486(1-2):722–725.
- [136] Methfessel, M. and Paxton, A. T. (1989). High-precision sampling for Brillouin-zone integration in metals. *Phys. Rev. B*, 40(6):3616–3621.
- [137] Mishin, Y. (2005). *Interatomic Potentials for Metals*, pages 459–478. Springer Netherlands, Dordrecht.
- [138] Mishra, R. K., Gupta, A. K., Rao Rama, P., Sachdev, A. K., Kumar, A. M., and Luo, A. A. (2014). Influence of Cerium on Texture and Ductility of Magnesium Extrusions. *Essent. Readings Magnes. Technol.*, 59:363–368.
- [139] Monkhorst, H. J. and Pack, J. D. (1977). "special points for Brillouin-zone integrations"-a reply. *Phys. Rev. B*, 16(4):1748–1749.
- [140] Monnet, G., Devincre, B., and Kubin, L. P. (2004). Dislocation study of prismatic slip systems and their interactions in hexagonal close packed metals: Application to zirconium. *Acta Mater.*, 52(14):4317–4328.
- [141] Mordike, B. L. and Ebert, T. (2001). Magnesium Properties - applications - potential. *Mater. Sci. Eng. A*, 302(1):37–45.

- [142] Moriarty, J. A., Vitek, V., Bulatov, V. V., and Yip, S. (2002). Atomistic simulations of dislocations and defects. *J. Comput. Mater. Des.*, 9(2):99–132.
- [143] Mott, N. F. (1958). A theory of the origin of fatigue cracks. *Acta Metall.*, 6(3):195–197.
- [144] Mueller, T., Hernandez, A., and Wang, C. (2020). Machine learning for interatomic potential models. *J. Chem. Phys.*, 152(5).
- [145] Murr, L. E. (2015). *Line Defects: Dislocations in Crystalline Materials*. Springer International Publishing.
- [146] Nakano, A. (2008). A space-time-ensemble parallel nudged elastic band algorithm for molecular kinetics simulation. *Comput. Phys. Commun.*, 178(4):280–289.
- [147] Nakata, T., Xu, C., Ajima, R., Shimizu, K., Hanaki, S., Sasaki, T. T., Ma, L., Hono, K., and Kamado, S. (2017). Strong and ductile age-hardening Mg-Al-Ca-Mn alloy that can be extruded as fast as aluminum alloys. *Acta Mater.*, 130:261–270.
- [148] Nakaura, Y., Watanabe, A., and Otori, K. (2006). Effects of Ca,Sr Additions on Properties of Mg-Al Based Alloys. *Mater. Trans.*, 47(4):1031–1039.
- [149] Nguyen, L. D., Baker, K. L., and Warner, D. H. (2011). Atomistic predictions of dislocation nucleation with transition state theory. *Phys. Rev. B - Condens. Matter Mater. Phys.*, 84(2):1–8.
- [150] Nöhring, W. G. and Curtin, W. A. (2017). Dislocation cross-slip in fcc solid solution alloys. *Acta Mater.*, 128:135–148.
- [151] Obara, T., Yoshinga, H., and Morozumi, S. (1973). {1122} <1123> Slip system in magnesium. *Acta Metall.*, 21(7):845–853.
- [152] Orowan, E. (1934). Zur Kristallplastizität. I. *Zeitschrift für Phys.*, 89:614–633.
- [153] Owen, D. R. J. and Hinton, E. (1980). *Finite Elements in Plasticity: Theory and Practice*. Pineridge Press.
- [154] Pan, H., Ren, Y., Fu, H., Zhao, H., Wang, L., Meng, X., and Qin, G. (2016). Recent developments in rare-earth free wrought magnesium alloys having high strength: A review. *J. Alloys Compd.*, 663:321–331.
- [155] par Jean François Stohr and Poirier, J. P. (1972). Etude en microscopie electronique du glissement pyramidal {1122} <1123> dans le magnesium. *Philos. Mag. A J. Theor. Exp. Appl. Phys.*, 25(6):1313–1329.
- [156] Pei, Z., Zhu, L. F., Friák, M., Sandlöbes, S., Von Pezold, J., Sheng, H. W., Race, C. P., Zaefferer, S., Svendsen, B., Raabe, D., and Neugebauer, J. (2013). Ab initio and atomistic study of generalized stacking fault energies in Mg and Mg-Y alloys. *New J. Phys.*, 15:1–19.

Bibliography

- [157] Pekguleryuz, M. O. (2012). 1 - Current developments in wrought magnesium alloys. In Bettles, C. and Barnett, M., editors, *Adv. Wrought Magnes. Alloy.*, Woodhead Publishing Series in Metals and Surface Engineering, pages 3–62. Woodhead Publishing.
- [158] Perdew, J. P., Burke, K., and Ernzerhof, M. (1996). Generalized gradient approximation made simple. *Phys. Rev. Lett.*, 77(18):3865–3868.
- [159] Plimpton, S. (1995). Fast Parallel Algorithms for Short-Range Molecular Dynamics. *J. Comput. Phys.*, 117(1):1–19.
- [160] Polanyi, M. (1934). Über eine Art Gitterstörung, die einen Kristall plastisch machen könnte. *Zeitschrift für Phys.*, 89:660–664.
- [161] Pollock, T. M. (2010). Weight loss with magnesium alloys. *Science.*, 328:986–987.
- [162] Proville, L. and Rodney, D. (2018). Modeling the Thermally Activated Mobility of Dislocations at the Atomic Scale. In Andreoni, W. and Yip, S., editors, *Handb. Mater. Model.*, pages 1–20. Springer International Publishing.
- [163] Pun, G. P., Batra, R., Ramprasad, R., and Mishin, Y. (2019). Physically informed artificial neural networks for atomistic modeling of materials. *Nat. Commun.*, 10(1):1–10.
- [164] Puschl, W. (2002). Models for dislocation cross-slip in close-packed crystal structures: A critical review. *Prog. Mater. Sci.*, 47(4):415–461.
- [165] Rao, S. I., Dimiduk, D. M., El-Awady, J. A., Parthasarathy, T. A., Uchic, M. D., and Woodward, C. (2009). Atomistic simulations of cross-slip nucleation at screw dislocation intersections in face-centered cubic nickel. *Philos. Mag.*, 89(34-36):3351–3369.
- [166] Rhee, M., Zbib, H. M., Hirth, J. P., Huang, H., and T., d. I. R. (1998). Models for long- / short-range interactions and cross slip in 3D dislocation simulation of BCC single crystals. *Model. Simul. Mater. Sci. Eng.*, 6(698):467–492.
- [167] Rikihisa, H., Mori, T., Tsushida, M., Kitahara, H., and Ando, S. (2017). Influence of yttrium addition on plastic deformation of magnesium. *Mater. Trans.*, 58(12):1656–1663.
- [168] Ritzo, M. A., Bhattacharyya, J. J., Lebensohn, R. A., and Agnew, S. R. (2020). An Investigation into the Role of Dislocation Climb During Intermediate Temperature Flow of Mg Alloys. In Jordon, J. B., Miller, V., Joshi, V. V., and Neelameggham, N. R., editors, *Magnes. Technol. 2020*, pages 115–122, Cham. Springer International Publishing.
- [169] Rodney, D. (2007). Activation enthalpy for kink-pair nucleation on dislocations: Comparison between static and dynamic atomic-scale simulations. *Phys. Rev. B - Condens. Matter Mater. Phys.*, 76(14):1–9.
- [170] Rodney, D. and Bonneville, J. (2014). *Dislocations*.

- [171] Rokhlin, L. L. (1998). Dependence of the rare earth metal solubility in solid magnesium on its atomic number. *J. Phase Equilibria*, 19(2):142–145.
- [172] Rose, J. H., Smith, J. R., Guinea, F., and Ferrante, J. (1984). Universal features of the equation of state of solids. *Phys. Rev. B*, 29(6):2963–2969.
- [173] Rosenfield, A. R. and Institute, B. M. (1968). *Dislocation Dynamics*. Batelle Institute materials science colloquia. McGraw-Hill.
- [174] Roters, F., Eisenlohr, P., Bieler, T. R., and Raabe, D. (2011). *Crystal Plasticity Finite Element Methods: in Materials Science and Engineering*. Wiley.
- [175] Roters, F., Eisenlohr, P., Hantcherli, L., Tjahjanto, D. D., Bieler, T. R., and Raabe, D. (2010). Overview of constitutive laws, kinematics, homogenization and multiscale methods in crystal plasticity finite-element modeling: Theory, experiments, applications. *Acta Mater.*, 58(4):1152–1211.
- [176] Ryu, S., Kang, K., and Cai, W. (2011a). Entropic effect on the rate of dislocation nucleation. *Proc. Natl. Acad. Sci.*, 108(13):5174–5178.
- [177] Ryu, S., Kang, K., and Cai, W. (2011b). Predicting the dislocation nucleation rate as a function of temperature and stress. *J. Mater. Res.*, 26(18):2335–2354.
- [178] Sandlöbes, S., Friák, M., Korte-Kerzel, S., Pei, Z., Neugebauer, J., and Raabe, D. (2017). A rare-earth free magnesium alloy with improved intrinsic ductility. *Sci. Rep.*, 7(1):10458.
- [179] Sandlöbes, S., Friak, M., Neugebauer, J., and Raabe, D. (2013). Basal and non-basal dislocation slip in Mg-Y. *Mater. Sci. Eng. A*, 576:61–68.
- [180] Sandlöbes, S., Friák, M., Zaefferer, S., Dick, A., Yi, S., Letzig, D., Pei, Z., Zhu, L. F., Neugebauer, J., and Raabe, D. (2012). The relation between ductility and stacking fault energies in Mg and Mg-Y alloys. *Acta Mater.*, 60(6-7):3011–3021.
- [181] Sandlöbes, S., Pei, Z., Friak, M., Zhu, L. F., Wang, F., Zaefferer, S., Raabe, D., and Neugebauer, J. (2014). Ductility improvement of Mg alloys by solid solution: Ab initio modeling, synthesis and mechanical properties. *Acta Mater.*, 70:92–104.
- [182] Sandlöbes, S., Zaefferer, S., Schestakow, I., Yi, S., and Gonzalez-Martinez, R. (2011). On the role of non-basal deformation mechanisms for the ductility of Mg and Mg-Y alloys. *Acta Mater.*, 59(2):429–439.
- [183] Saroukhani, S., Nguyen, L. D., Leung, K. W., Singh, C. V., and Warner, D. H. (2016). Harnessing atomistic simulations to predict the rate at which dislocations overcome obstacles. *J. Mech. Phys. Solids*, 90:203–214.
- [184] Saroukhani, S. and Warner, D. H. (2017). Investigating dislocation motion through a field of solutes with atomistic simulations and reaction rate theory. *Acta Mater.*, 128:77–86.

Bibliography

- [185] Schoeck, G. (1980). Thermodynamics and Thermal Activation of Dislocations. In Nabarro, F. R. N., editor, *Dislocations Solids (Vol 3)*, pages 65–163. North-Holland Publishing Company.
- [186] Schoeck, G. (2000). *Thermal Activation in Plastic Deformation*, pages 33–56. Springer Netherlands, Dordrecht.
- [187] Sheppard, D., Terrell, R., and Henkelman, G. (2008). Optimization methods for finding minimum energy paths. *J. Chem. Phys.*, 128(13):1–10.
- [188] Shin, I. and Carter, E. A. (2012). Orbital-free density functional theory simulations of dislocations in magnesium. *Model. Simul. Mater. Sci. Eng.*, 20(1).
- [189] Shinzato, S., Wakeda, M., and Ogata, S. (2019). An atomistically informed kinetic Monte Carlo model for predicting solid solution strengthening of body-centered cubic alloys. *Int. J. Plast.*, 122(November 2018):319–337.
- [190] Sillekens, W. H. and Bormann, D. (2012). 13 - Biomedical applications of magnesium alloys. In Bettles, C. and Barnett, M., editors, *Adv. Wrought Magnes. Alloy.*, Woodhead Publishing Series in Metals and Surface Engineering, pages 427–454. Woodhead Publishing.
- [191] Singh, C. V., Mateos, A. J., and Warner, D. H. (2011). Atomistic simulations of dislocation-precipitate interactions emphasize importance of cross-slip. *Scr. Mater.*, 64(5):398–401.
- [192] Sivakesavam, O. and Prasad, Y. V. (2003). Hot deformation behaviour of as-cast Mg-2Zn-1Mn alloy in compression: A study with processing map. *Mater. Sci. Eng. A*, 362(1-2):118–124.
- [193] Somekawa, H., Kinoshita, A., and Kato, A. (2017). Great room temperature stretch formability of fine-grained Mg-Mn alloy. *Mater. Sci. Eng. A*, 697(March):217–223.
- [194] song Yin, D., lin Zhang, E., yan Zeng, S., song Yin, D., lin Zhang, E., and yan Zeng, S. (2008). Effect of Zn on mechanical property and corrosion property of extruded Mg-Zn-Mn alloy. *Trans. Nonferrous Met. Soc. China (English Ed.)*, 18(4):763–768.
- [195] Staiger, M. P., Pietak, A. M., Huadmai, J., and Dias, G. (2006). Magnesium and its alloys as orthopedic biomaterials: A review. *Biomaterials*, 27(9):1728–1734.
- [196] Stukowski, A. (2010). Visualization and analysis of atomistic simulation data with OVITO-the Open Visualization Tool. *Model. Simul. Mater. Sci. Eng.*, 18(1).
- [197] Stukowski, A. (2012). Structure identification methods for atomistic simulations of crystalline materials. *Model. Simul. Mater. Sci. Eng.*, 20(4).
- [198] Suh, B. C., Kim, J. H., Bae, J. H., Hwang, J. H., Shim, M. S., and Kim, N. J. (2017). Effect of Sn addition on the microstructure and deformation behavior of Mg-3Al alloy. *Acta Mater.*, 124:268–279.

- [199] Sun, D. Y., Mendelev, M. I., Becker, C. A., Kudin, K., Haxhimali, T., Asta, M., Hoyt, J. J., Karma, A., and Srolovitz, D. J. (2006). Crystal-melt interfacial free energies in hcp metals: A molecular dynamics study of Mg. *Phys. Rev. B - Condens. Matter Mater. Phys.*, 73(2):1–12.
- [200] Syed, B., Geng, J., Mishra, R. K., and Kumar, K. S. (2012). [0 0 0 1] Compression response at room temperature of single-crystal magnesium. *Scr. Mater.*, 67(7-8):700–703.
- [201] Tadmor, E. B. and Miller, R. E. (2011). *Modeling Materials: Continuum, Atomistic and Multiscale Techniques*. Cambridge University Press.
- [202] Tang, A., Pan, F., Yang, M., and Cheng, R. (2008). Mechanical Properties and Microstructure of Magnesium-Aluminum Based Alloys Containing Strontium. *Mater. Trans.*, 49(6):1203–1211.
- [203] Taylor, G. I. (1934). The Mechanism of Plastic Deformation of Crystals . Part I . Theoretical. *Proc. R. Soc. London Ser. A*, 145(855):362–387.
- [204] Tehranchi, A., Yin, B., and Curtin, W. A. (2018). Solute strengthening of basal slip in Mg alloys. *Acta Mater.*, 151:56–66.
- [205] Ting, T. C. T. (1996). *Anisotropic Elasticity: Theory and Applications*. Oxford Engineering Science Series. Oxford University Press.
- [206] Tonda, H. and Ando, S. (2002). Effect of temperature and shear direction on yield stress by {1122}<1123> slip in hcp metals. *Met. Mater. Trans. A*, 33(March):831–836.
- [207] Trinkle, D. R. and Woodward, C. (2005). The Chemistry of Deformation : How Solutes Soften Pure Metals The Chemistry of Deformation : How Solutes Soften Pure Metals. 1665(December).
- [208] Truhlar, D. G., Garrett, B. C., and Klippenstein, S. J. (1996). Current status of transition-state theory. *J. Phys. Chem.*, 100(31):12771–12800.
- [209] Tsuzuki, H., Branicio, P. S., and Rino, J. P. (2007). Structural characterization of deformed crystals by analysis of common atomic neighborhood. *Comput. Phys. Commun.*, 177(6):518–523.
- [210] Tuckerman, M. E. (2011). *Statistical Mechanics: Theory and Molecular Simulation*. Oxford graduate texts. Oxford University Press.
- [211] Van Der Giessen, E., Schultz, P. A., Bertin, N., Bulatov, V. V., Cai, W., Csányi, G., Foiles, S. M., Geers, M. G., González, C., Hütter, M., Kim, W. K., Kochmann, D. M., Llorca, J., Mattsson, A. E., Rottler, J., Shluger, A., Sills, R. B., Steinbach, I., Strachan, A., and Tadmor, E. B. (2020). Roadmap on multiscale materials modeling. *Model. Simul. Mater. Sci. Eng.*, 28(4).
- [212] Vanden-Eijnden, E. and Venturoli, M. (2009). Revisiting the finite temperature string method for the calculation of reaction tubes and free energies. *J. Chem. Phys.*, 130(19):1–17.

Bibliography

- [213] Varvenne, C., Bruneval, F., Marinica, M. C., and Clouet, E. (2013). Point defect modeling in materials: Coupling ab initio and elasticity approaches. *Phys. Rev. B*, 88(13):1–7.
- [214] Vegge, T., Rasmussen, T., Leffers, T., Pedersen, O. B., and Jacobsen, K. W. (2000). Determination of the of Rate Cross Slip of Screw Dislocations. *Phys. Rev. Lett.*, 85(18):3866–3869.
- [215] Vineyard, G. H. (1957). Frequency factors and isotope effects in solid state rate processes. *J. Phys. Chem. Solids*, 3(1-2):121–127.
- [216] Vitek, V. (1968). Intrinsic stacking faults in body-centred cubic crystals. *Philos. Mag. A J. Theor. Exp. Appl. Phys.*, 18(154):773–786.
- [217] Vitek, V. (1970). Multilayer stacking faults and twins on {211} planes in B.C.C. metals. *Scr. Metall.*, 4(9):725–732.
- [218] Wang, R., Dong, J., Fan, L. K., Zhang, P., and Ding, W. J. (2008). Microstructure and mechanical properties of rolled Mg-12Gd-3Y-0.4Zr alloy sheets. *Trans. Nonferrous Met. Soc. China (English Ed.)*, 18(SPEC. ISSUE 1):s189–s193.
- [219] Wang, Y. N. and Huang, J. C. (2003). Texture analysis in hexagonal materials. *Mater. Chem. Phys.*, 81(1):11–26.
- [220] Warner, D. H. and Curtin, W. A. (2009). Origins and implications of temperature-dependent activation energy barriers for dislocation nucleation in face-centered cubic metals. *Acta Mater.*, 57(14):4267–4277.
- [221] Warner, D. H., Curtin, W. A., and Qu, S. (2007). Rate dependence of crack-tip processes predicts twinning trends in f.c.c. metals. *Nat. Mater.*, 6(11):876–881.
- [222] Weinberger, C. R. and Tucker, G. J. (2016). *Multiscale Materials Modeling for Nanomechanics*. Springer Series in Materials Science. Springer International Publishing.
- [223] Weiner, J. H. (2002). *Statistical Mechanics of Elasticity*. Dover Books on Physics. Dover Publications.
- [224] Wu, L., Cui, C., Wu, R., Li, J., Zhan, H., and Zhang, M. (2011). Effects of Ce-rich RE additions and heat treatment on the microstructure and tensile properties of Mg-Li-Al-Zn-based alloy. *Mater. Sci. Eng. A*, 528(4-5):2174–2179.
- [225] Wu, L. B., Liu, X. H., Wu, R. Z., Cui, C. L., Zhang, J. H., and Zhang, M. L. (2012). Microstructure and tensile properties of Mg-Li-Al-Zn based alloys with Ce addition. *Trans. Nonferrous Met. Soc. China (English Ed.)*, 22(4):779–785.
- [226] Wu, R. Z., Qu, Z. K., and Zhang, M. L. (2010). Reviews on the influences of alloying elements on the microstructure and mechanical properties of aluminum alloys and aluminum alloy composites. *Rev. Adv. Mater. Sci.*, 24:35–43.

- [227] Wu, Z. and Curtin, W. A. (2015a). Brittle and ductile crack-tip behavior in magnesium. *Acta Mater.*, 88:1–12.
- [228] Wu, Z. and Curtin, W. A. (2015b). The origins of high hardening and low ductility in magnesium. *Nature*, 526:62–67.
- [229] Wu, Z. and Curtin, W. A. (2016a). Intrinsic structural transitions of the pyramidal I $\langle c + a \rangle$ dislocation in magnesium. *Scr. Mater.*, 116:104–107.
- [230] Wu, Z. and Curtin, W. A. (2016b). Mechanism and energetics of $\langle c + a \rangle$ dislocation cross-slip in hcp metals. *PNAS*, 113(40):11137–11142.
- [231] Wu, Z., Francis, M. F., and Curtin, W. A. (2015). Magnesium interatomic potential for simulating plasticity and fracture phenomena. *Model. Simul. Mater. Sci. Eng.*, 23(1):15004.
- [232] Wu, Z., Yin, B., and Curtin, W. A. (2016). Energetics of dislocation transformations in hcp metals. *Acta Mater.*, 119:203–217.
- [233] Xu, T. C., Peng, X. D., Jiang, J. W., Xie, W. D., Chen, Y. F., and Wei, G. B. (2014). Effect of Sr content on microstructure and mechanical properties of Mg-Li-Al-Mn alloy. *Trans. Nonferrous Met. Soc. China (English Ed.)*, 24(9):2752–2760.
- [234] Yasi, J. A., Hector, L. G., and Trinkle, D. R. (2010). First-principles data for solid-solution strengthening of magnesium: From geometry and chemistry to properties. *Acta Mater.*, 58(17):5704–5713.
- [235] Yasi, J. A., Nogaret, T., Trinkle, D. R., Qi, Y., Hector, L. G., and Curtin, W. A. (2009). Basal and prism dislocation cores in magnesium: Comparison of first-principles and embedded-atom-potential methods predictions. *Model. Simul. Mater. Sci. Eng.*, 17(5).
- [236] Yin, B., Wu, Z., and Curtin, W. A. (2017a). Comprehensive first-principles study of stable stacking faults in hcp metals. *Acta Mater.*, 123:223–234.
- [237] Yin, B., Wu, Z., and Curtin, W. A. (2017b). First-principles calculations of stacking fault energies in Mg-Y, Mg-Al and Mg-Zn alloys and implications for $\langle c + a \rangle$ activity. *Acta Mater.*, 136:249–261.
- [238] Yoo, M. H. (1981). Slip, twinning, and fracture in hexagonal close-packed metals. *Metall. Trans. A*, 12(3):409–418.
- [239] Yoo, M. H., Agnew, S. R., Morris, J. R., and Ho, K. M. (2001). Non-basal slip systems in HCP metals and alloys: Source mechanisms. *Mater. Sci. Eng. A*, 319-321:87–92.
- [240] Yoo, M. H., Morris, J. R., Ho, K. M., and Agnew, S. R. (2002). Nonbasal Deformation Modes of HCP Metals and Alloys : Role of Dislocation Source and Mobility. 33(March):813–822.
- [241] You, S., Huang, Y., Kainer, K. U., and Hort, N. (2017). Recent research and developments on wrought magnesium alloys. *J. Magnes. Alloy*, 5(3):239–253.

Bibliography

- [242] Yu, Z., Tang, A., Wang, Q., Gao, Z., He, J., She, J., Song, K., and Pan, F. (2015). High strength and superior ductility of an ultra-fine grained magnesium-manganese alloy. *Mater. Sci. Eng. A*, 648:202–207.
- [243] Yuasa, M., Miyazawa, N., Hayashi, M., Mabuchi, M., and Chino, Y. (2015). Effects of group II elements on the cold stretch formability of Mg-Zn alloys. *Acta Mater.*, 83:294–303.
- [244] Zbib, H. M. (1998). ON PLASTIC DEFORMATION 3D DISLOCATIONS. *Int. J. mech. Sci.*, 40:113–127.
- [245] Zepeda-Ruiz, L. A., Stukowski, A., Oppelstrup, T., and Bulatov, V. V. (2017). Probing the limits of metal plasticity with molecular dynamics simulations. *Nature*, 550(7677):492–495.
- [246] Zhang, D., Jiang, L., Wang, X., Beyerlein, I. J., Minor, A. M., Schoenung, J. M., Mahajan, S., and Lavernia, E. J. (2019). In situ transmission electron microscopy investigation on $\langle c + a \rangle$ slip in Mg. *J. Mater. Res.*, pages 1–10.
- [247] Zhang, E., Yin, D., Xu, L., Yang, L., and Yang, K. (2009). Microstructure, mechanical and corrosion properties and biocompatibility of Mg-Zn-Mn alloys for biomedical application. *Mater. Sci. Eng. C*, 29(3):987–993.
- [248] Zhang, X., Lu, G., and Curtin, W. A. (2013). Multiscale quantum/atomistic coupling using constrained density functional theory. *Phys. Rev. B - Condens. Matter Mater. Phys.*, 87(5):1–10.
- [249] Zhu, T., Li, J., Samanta, A., Leach, A., and Gall, K. (2008). Temperature and strain-rate dependence of surface dislocation nucleation. *Phys. Rev. Lett.*, 100(2):1–4.

Rasool Ahmad

CONTACT INFORMATION	PhD Student	e-mail: rasool.ahmad@epfl.ch
	Laboratory for Multiscale Mechanics Modeling Institute of Mechanical Engineering École Polytechnique Fédérale de Lausanne Lausanne, 1015, Switzerland	e-mail: rasoolahmad.a@gmail.com Mobile: +41 0786681260 OrcID: 0000-0002-4154-6902 Google Scholar: ujjgd08AAAAJ
RESEARCH INTERESTS	Computational materials science, dislocation mechanics, atomistic simulation, plasticity	
EDUCATION	École Polytechnique Fédérale de Lausanne, Lausanne, Switzerland	
	Ph.D. in Mechanical Engineering Advisor: Dr. William Curtin	Aug 2016 - Present
	Indian Institute of Technology, Kanpur, India	
	B.Tech.-M.Tech. Dual Degree in Mechanical Engineering	Jul 2011 - Jul 2016
PUBLICATIONS	R. Ahmad, S. Paul and S. Basu, "Characterization of entanglements in glassy polymeric ensembles using the Gaussian linking number", <i>Phys. Rev. E</i> 101 (2020) 022503.	
	R. Ahmad, Z. Wu and W. A. Curtin, "Analysis of double cross-slip of pyramidal I $\langle c + a \rangle$ screw dislocations and implications for ductility in Mg alloys", <i>Acta Mater.</i> 183 (2020) 228-241.	
	R. Ahmad, B. Yin, Z. Wu and W. A. Curtin, "Designing high ductility in magnesium alloys", <i>Acta Mater.</i> 172 (2019) 161-184.	
	R. Ahmad, Z. Wu, S. Groh and W. A. Curtin, "Pyramidal II to basal transformation of $\langle c + a \rangle$ edge dislocations in Mg-Y alloys", <i>Scr. Mater.</i> 155 (2018) 114-118.	
	R. Ahmad, S. Groh, M. Ghazisaeidi and W. A. Curtin, "Modified embedded-atom method interatomic potential for Mg-Y alloys", <i>Modelling Simul. Mater. Sci. Eng.</i> 26 (2018) 065010.	
	Z. Wu, R. Ahmad, B. Yin, S. Sandlbes and W. A. Curtin, "Mechanistic origin and prediction of enhanced ductility in magnesium alloys", <i>Science</i> 359 (2018) 447-452.	
CONFERENCE/ SUMMER SCHOOL	R. Ahmad, Z. Wu, and W. A. Curtin, "Pyramidal $\langle c + a \rangle$ cross-slip mediated ductility in Mg alloys ductility", <i>The Minerals, Metals & Materials Society (TMS)</i> (2020) San Diego, USA.	
	W. A. Curtin, R. Ahmad, B. Yin and Z. Wu, "Design of Ductile Rare-Earth-Free Magnesium Alloys", <i>Magnesium Technology 2020</i> , 19-24	
	R. Ahmad, Z. Wu, S. Groh and W. A. Curtin, "Pyramidal II to basal transformation of $\langle c + a \rangle$ edge dislocations in Mg-Y alloys and its implication for ductility", <i>Euromat</i> (2019) Stockholm, Sweden.	
	<i>Mechanics and Physics of Stretchable Objects</i> (2018) Corsica, France.	
RESEARCH EXPERIENCES	Atomic scale investigations into the origins of ductility in Mg alloys	
	Ph.D. Thesis École Polytechnique Fédérale de Lausanne, Lausanne, Switzerland Advisor: Dr. William Curtin	Aug 2016-Present
	Investigation into disentanglement of polymer chains in a glassy amorphous polymer through molecular dynamics simulations	
	M.Tech. Thesis Indian Institute of Technology, Kanpur, India Advisor: Dr. Sumit Basu	Jul 2015 - Jun 2016

ACADEMIC PROJECTS	Kinetic Monte Carlo simulation of screw dislocation mobility in BCC metals		Feb - Jun '19
	Updated Lagrangian Finite Element Formulation		Aug - Nov '14
	Effect of Initial Stresses on the Wave Propagation in Arteries		Aug - Nov '14
	Static Equilibrium of a Red Blood Cell		Aug - Nov '14
	Wave Propagation in Initially Stressed Elastic Solids		Aug-Nov '14
	Minimum Energy Path of a Reaction Using Nudge Elastic Band Method		Jan-Apr '14
RELEVANT COURSES	<ul style="list-style-type: none"> - Non-Linear Vibration - Fracture Mechanics - Topics in Topology - Wave Propagation in Elastic Solid - Finite Element Method - Theory of Elasticity - Linear Algebra and Ordinary Diff Eqns - Real Analysis and Calculus - Fourier Analysis and Boundary Value Problems 		
	<ul style="list-style-type: none"> - Rheology and Structure of Complex Fluids - Molecular Modelling in Chemistry - Non-Linear Finite Element Method - Mechanics of Biological Membrane - Advanced Mechanics of Solid - Vibration and Control - Complex Analysis and Partial Diff Eqns - Nature and Properties of Materials - Computational Multiscale Modeling of Solid 		
TEACHING EXPERIENCES	Teaching Assistant, EPFL		
	<ul style="list-style-type: none"> - Solid Mechanics - Introduction to Structural Mechanics 		Spring Semesters 2018, 2019, 2020 Spring Semester 2017
	Teaching Assistant, IIT Kanpur		
	<ul style="list-style-type: none"> - Basic Electrical Engineering - Engineering Graphics and Design 		Fall Semesters 2016 Spring Semester 2015